A Recoil Resilient Luminal Support

by

Arash Mehdizadeh

B. Sc. (Computer Systems Engineering, Honours)
Amirkabir University of Technology (Tehran Polytechnic), Iran, 2005

M. Sc. (Computer Architecture Engineering, First Class)
Amirkabir University of Technology (Tehran Polytechnic), Iran, 2008

Thesis submitted for the degree of

Doctor of Philosophy

in

School of Electrical & Electronic Engineering
Faculty of Engineering, Computer & Mathematical Sciences
The University of Adelaide, Australia

April 2014

Supervisors:

Dr Said Al-Sarawi, School of Electrical & Electronic Engineering

Prof. Derek Abbott, School of Electrical & Electronic Engineering

Centre for
Biomedical Engineering
(CBME)

THE UNIVERSITY *of* ADELAIDE

Contents

Contents i

Abstract v

Statement of Originality ix

Acknowledgments xi

Conventions xv

Publications & Awards xvii

List of Symbols xix

Abbreviations xxv

List of Figures xxvii

List of Tables xxxi

Chapter 1. Introduction and Motivation 1

1.1 Abstract 2

1.2 Atherosclerosis and Luminal Occlusion 3

1.3 Non-surgical Treatments 5

1.4 Surgical Treatments 6

1.4.1 Coronary Artery Bypass Grafting 6

1.4.2 Endarterectomy 7

1.4.3 Percutaneous Transluminal Angioplasty 8

1.4.4 Stenting 9

1.4.5 Atherectomy 11

1.5 Stents Current Status and the Future 13

1.5.1 Materials and Expansion Mechanism 15

1.5.2 Material Form 19

1.5.3 Fabrication Method 20
1.5.4 Design and Geometrical Features 23
I. Coil Stents 23
II. Spiral Stents 24
III. Woven Stents 25
IV. Modular (sequential) Stents 25
1.5.5 Stent Coatings and Surface Treatments 29
1.5.6 Stenting Limitations and Mitigation Efforts 31
I. Stent Recoil 31
I. Stent Thrombosis 32
II. Restenosis 33
1.6 Chapter Summary 35
1.7 Thesis Overview 37
1.7.1 Thesis Structure and Original Contributions 37
Chapter 2. A Recoil Resilient Luminal Support 41
2.1 Abstract 42
2.2 Introduction 43
2.3 Design and Modelling 47
2.3.1 Free Expansion Analysis 47
I. Materials and Methods 47
II. Results 51
2.3.2 Radial Strength 52
2.3.3 Axial Strength and Feasible Improvements 54
2.4 Fabrication 60
2.4.1 Machining 60
2.4.2 Shaping 61
I. Surface Profile 62
II. RRR Patency 63

2.4.3 Experimental Results 64
2.5 Chapter Summary 69
Chapter 3. Hemodynamic Risk Assessment by Computational Fluid Dynamics 71
3.1 Abstract 72
3.2 Introduction 73
3.3 Materials and Methods 75
3.3.1 Models Development 78
3.3.2 Discretisation 79
3.3.3 Dimensional Analysis 81
3.4 Results and Discussion 83
3.4.1 Part 1 – Unbranched Fluid Domain 83
I. LWSS in Unbranched Fluid Domains 83
II. Drag Force in the Unbranched Domains 92
3.4.2 Part 2 – Branched Fluid Domain 94
I. LWSS in Branched Fluid Domains 94
II. Drag Force and Output Flow Rate 96
3.4.3 Part 3 – Dimensional Analysis 103
I. Dimensional Assumptions and LWSS 104
II. Dimensional Assumptions, Drag Force and Flow Supply 106
III. Dimensional Assumptions, Final Notes 112
3.5 Chapter Summary 113
Chapter 4. Thermal Actuation of the Recoil Resilient Ring.....117
4.1 Abstract 118
4.2 Introduction 118
4.3 Materials and Methods 121
4.4 Theoretical Analysis 124
4.4.1 Results 134
4.5 Numerical Analysis: Uniform Heat Transfer 136

4.5.1 Materials and Methods 137
4.5.2 Results 139
4.6 Numerical Analysis: Conjugate Heat Transfer 143
4.6.1 Materials and Methods 143
4.6.2 Results 147
4.7 Experimental Results 154
4.7.1 Heat-induced Actuation *in vitro* 157
4.7.2 Heat-induced Actuation in Free Expansion 158
4.7.3 Heat-induced Actuation Force 160
4.8 Electro-Thermal Actuation 164
4.8.1 Theoretical Framework 165
4.8.2 Numerical Analysis 169
I. Materials and Methods 169
II. Results 172
4.9 Chapter Summary 176
Chapter 5. Conclusion and Future Directions 179
5.1 Introduction 180
5.2 Contributions and Conclusions 181
5.3 Recommendations for Future Work 187
5.4 Closing Comments 188
Bibliography 189
Index 209
Biography 215
Scientific Genealogy 216

Abstract

Cardiovascular disease (CVD) refers to a class of diseases affecting normal function of cardiovascular system and its momentous role to carry oxygenated blood to the entire body. Taking lives of more than 17 million people in 2008, CVD has yet remained as the primary cause of deaths around the world. Statistics from World Health Organisation in 2002 associated CVD with 10% of the disability-adjusted life years lost in low/middle-income countries and 18% in high-income countries.

Atherosclerosis, as one of the primary causes of CVD, refers to the thickening of vascular walls due to deposition of fatty materials wherein it can lead to impeded or completely occluded blood flow. Obstruction of coronary arteries, referred to as coronary heart disease (CHD), is estimated to become the single leading health problem by 2020. Occurrence and further development of CHD is associated with a number of biological and environmental factors such as an individual's genetic predisposition, lifestyle, climate conditions, exercise habits and emotions to name a few.

Treatment and management of vascular constrictions consists of a combination of non-surgical and surgical methods. The former includes approaches such as healthy lifestyle changes and pharmacological interventions while the later includes bypass grafting, balloon angioplasty with or without deployment of a stent and atherectomy. Stents are mechanical devices that provide a chronic support against internal walls of occluded vessels to restore their normal luminal patency. In the past decade, stenting has prevailed as the conventional treatment option in management of CVD, exceeding current number of bypass grafting procedures, owing this success to its proven efficacy in short and long-term treatment of occluded vessels. Common stent structures are simply made of a metal mesh, e.g. stainless steel, and deployed in a blood vessel such as an artery during a percutaneous coronary intervention procedure, also known as angioplasty. Several attempts to meet the often self-competing objectives of stents such as high radial strength, low elastic recoil, axial flexibility, trackability in tortuous paths, biocompatibility and radio-

pacity gave birth to a multitude of different stent design and improvement iterations to date. The acute luminal gain after stenting is often compromised by the two most common post intervention complications, namely in-stent thrombosis (formation of blood clot) and restenosis (re-narrowing of the lesion). Induced trauma during stent deployment is proven to play a key role in the occurrence of these complications. Elastic recoil of stents after deployment due to the intrinsic material properties and the compressive forces from a vessel accounts for both acute and chronic luminal loss after stent deployment. Mitigation measures such as over-expansion in balloon-expandable (BE) stents and use of self-expandable (SE) stents so far have proven to aggravate vascular trauma leading to thrombosis and restenosis. Pharmacological approaches such as systemic administration of blood-thinners or localized drug release in drug-eluting (DE) stents aim to control these complications by inhibition of an accentuated inflammatory response from the body. Despite the promising results in reduction of restenosis after use of DE stents, increased rate of late thrombosis raised concerns about efficacy of these stents in comparison with bare-metal (BM) stents. Moreover, it is important to note that in these approaches the mechanical aspect of the problem still stands. As a result, to meet the often-competing aforementioned imperatives of stents, a new design paradigm is called for.

To address the issue of recoil and extend capability of current stents to controlled and incremental expansion steps with alternative expansion mechanisms, in this thesis a novel recoil resilient stent is proposed and developed. The proposed luminal support called a recoil resilient ring (RRR) is an open ring with overlapping ends and asymmetrical sawtooth structures from the two ends that are intermeshed. Utilized as a standalone support or integrated with other stent structures, upon expansion of the RRR, the teeth from opposite ends can slide on top of each other, yet interlock step-by-step in the opposite direction so to keep the final expanded state against compressive forces that normally cause recoil.

Design, fabrication and compatibility of the proposed stent with current state-of-the-art stent deployment procedures and its superior radial strength in comparison with commercial stents are extensively studied in this thesis through finite element modelling (FEM) and experimental studies. The RRR is fabricated from Nitinol sheets with transformation temperatures well above typical body temperature ensuring martensite mode

of operation of the device after deployment. Fabrication is carried out by linear patterning of Nitinol sheets of 200-μm thickness utilizing μEDM technology. Superior radial strength of the RRR in comparison with a commercial stent composed of the stiffer material, stainless steel, is demonstrated via experimental and numerical studies.

Hemodynamic risk assessment of the proposed design as a standalone and integrated support compared with a typical commercial stent is then carried out by transient computational fluid dynamics (CFD). Subject to a realistic pulsatile blood flow, spatial and temporal restenosis risk indicators of three luminal supports are extensively studied utilizing CFD. These luminal supports include a standalone RRR, a nominal BE stent and an RRR-integrated stent. Risk factors including extension of areas subject to low wall shear stress as the primary risk factor of restenosis after deployment, tendency of supports to migrate in response to fluid drag forces as well as flow supply changes to side branches are extensively investigated. Furthermore, sensitivity of the results to the dimensional assumptions of the deployment domain, branching vessels and patency of the supports is studied. Our results indicate superior hemodynamic performance of the standalone RRR compared with the others. In addition, close correspondence of the performance indicators of RRR-integrated stent and the standalone stent demonstrates minimal hemodynamic footprint of the proposed RRR highlighting its merit as a viable luminal support given its superior radial strength.

Attractive attributes such as shape memory effect of Nitinol, the thermally trained expanded shape of the RRR, its unique incremental slide and lock expansion mechanism and its higher transformation temperature compared to the body temperature, bring new potential for alternative controlled and incremental actuation of the RRR. These alternative expansion methods, by application of direct or electrically-induced heat are further explored through extensive analytical, multi-field numerical and experimental studies. The knowledge and contributions made in the current work, in addition to the design, development, experimental and multi-field numerical results provide a general engineering framework applicable to other biomedical luminal supports in the future.

This page is left blank intentionally

Statement of Originality

This work contains no material that has been accepted for the award of any other degree or diploma in any university or other tertiary institution and, to the best of my knowledge and belief, contains no material previously published written by another person, except where due reference has been made in the text.

I give consent to this copy of my thesis, when deposited in the University Library, being made available for loan and photocopying, subject to the provisions of the Copyright Act 1968.

I also give permission for the digital version of my thesis to be made available on the web via the University's digital research repository, the Library catalogue, the Australasian Digital Thesis Program (ADTP) and also through web search engines, unless permission has been granted by the University to restrict access for a period of time.

Signed _____ Date _____

This page is left blank intentionally

Acknowledgments

Now that the multidisciplinary journey of this research has come to a conclusion, I truly understand the power of collaboration and its momentous role to realise the wildest of dreams. I am thrilled to have this opportunity to express my gratitude and acknowledgement to those around me, to only some of whom it is possible to give particular mention here. All the people who shed light on different aspects of my personal and academic life in this period undoubtedly deserve a big cheer.

First and foremost, I would like to express my sincerest gratitude to my principal supervisor **Dr Said Al-Sarawi** from the school of Electrical and Electronic Engineering at the University of Adelaide. His open mind and receptive attitude towards new ideas, taught me how to let ideas fly beyond boundaries and consider nothing as being off-limits. While continuously providing support to improve my critical thinking and make progress on the set milestones, every single meeting with Dr Al-Sarawi was an absolute joy. His investigative and progressive approach towards other branches of science gave me the drive to feed my curious mind and plunge into different disciplines such as biology, optimization, micro-electronics, and mechanical engineering all of which equipped me with the necessary skills to tackle the present work. He has been a genuine mentor to me on this journey and I sincerely thank him for that.

My special gratitude is extended to my co-supervisor **Prof. Derek Abbott** from the School of Electrical and Electronic Engineering at the University of Adelaide who laid the foundation for the commencement of my research at this university. Prof. Abbott's unsurpassed friendly, supportive and informative attitude was very apparent even before I met him in person. His initiative to provide guidance in administrative and collaborative efforts provided me with invaluable experiences and lessons that I will carry for the rest of my life. His meticulous and critical eye enriched the content of this thesis for which I am grateful.

Physical implementation of the proposed designs in this thesis could have not been realized without the support and extensive help of **Dr Kenichi Takahata** from the department of Electrical and Computer Engineering at the University of British Columbia (UBC), Vancouver, Canada. His venerated expertise on stents and MEMS research and his influential and supportive mentorship during my visit to Microsystems and Nanotechnology Group (MiNa) at UBC provided me with invaluable direction and technical support to accomplish key components of this research. Also, I would like to acknowledge the friendly and insightful advice that I have received from Prof. York Hsiang from Vascular Surgery Department at the University of British Columbia, Vancouver, Canada.

In this vein, I would like to extend my gratitude to my dear friends and colleagues in UBC who assisted me during this period to feel at home and part of a great scientific taskforce. I acknowledge help and support of (in a random order) Dr Mohamed Sultan Mohamed Ali for his assistance on fabrication of microdevices and his critical and technical reviews and enlightening suggestions, Dr Reza Rashidi for his critical yet encouraging support on development of stents, Mr Masoud Dahmardeh for being an incredible friend during my visit to Canada and his indispensable help on micromachining and physical evaluation of prototypes, and Mr Babak Assadsangabi for his insightful ideas on structural analysis of the proposed structures in COMSOL.

I would also like to convey my gratitude to The University of Adelaide for the funding and support provided for this research to make it a success. This project would have not been accomplished without the financial assistance via the international postgraduate scholarship (ASI) and travel grants including Research Abroad Scholarship, University of Adelaide and BUPA Postgraduate Travel Grant and AUGU/RC Heddle Award that facilitated my visit to UBC. I acknowledge the support and expertise of Mr Simon Doe and Mr Dapankar Chugh at Ian Wark Research Institute at the University of South Australia for providing access to optical profilometer. Numerical analysis has been an integral part of this thesis and I am pleased to thank the helpful support of Leap Australia, Australia and CMC Microsystems, Canada support teams for their guidance on finite element modelling packages ANSYS and COMSOL.

Constant support and help of the academic and professional staff at the School of Electrical and Electronic Engineering at the University of Adelaide, undeniably, deserves a special thanks. Especially, I would like to mention Mrs. Ivana Rebellato, Mrs. Rose-Marie Descalzi, Mr Stephen P. Guest and Mr Danny Di Giacomo form the administration team in addition to Mr David Bowler, Mr Mark Innes, Mr Greg Pullman and Mr Ryan King from IT and technical support for their unlimited support and patience with the multitude of requests that I had in this period. I also wish to express my thanks to Mr Ian Linke for his insightful technical suggestions and assistance for macro-fabrication of the first prototype. I also enjoyed being a proud member of our schools team in a number of athletic events to experience their cooperative spirit yet in another level.

I am deeply grateful to all my colleagues and good friends as they enriched my life during this journey by their motivational encouragement and helpful suggestions. Particularly, I wish to thank my dearest friends, who in fact have become my family in Australia, Mr Nikan Rostamzadeh Torghabeh and Dr Pawel Kuklik, for both their insightful directions into different theoretical aspects of my thesis and most importantly making life in Adelaide an unforgettable joy. I will always remember our countless hours of discussions, often turning into arguments, on subjects such as electromagnetism, fluid mechanics and even the cosmos that, albeit the following headaches and disagreements, challenged us constantly. My gratitude is extended especially to Nikan for his invaluable help and friendly dedication during our extensive discussions on fluid mechanics and computational fluid dynamics (CFD) that were indispensable to the accomplishment of this project.

Among my fellow postgraduate students, I would like to thank Dr Muammar Kabir for his kind help, valuable friendship and encouraging conversations that we had together, Dr Don W. Dissanayake for his expertise on biomedical implants and our fruitful discussions on pilot studies and Mr Shaoming Zhu, Mr Henry Ho and Dr Gretel M. Png for providing such a friendly and pleasant environment to work in.

Above all, I would like to convey my endless appreciation to my family for their unconditional love, perpetual support and patience throughout my life. A special expression of gratitude goes to my dearest parents Shahnaz and Majid for the sacrifices they made in their lives to empower me become who I am today.

In the end I dedicate this thesis to my grandfathers whose vision for excellence reverberated through generations and beyond.

Arash Mehdizadeh

Conventions

Formatting: For typesetting and image production of this thesis, Microsoft (MS) Office suite 2010 is used. Plots and images were generated using Matlab 10.0 (Mathworks Inc.) and MS Excel 2010.

Spelling: Australian English spelling is adopted, as defined by the Macquarie English Dictionary (Delbridge 2001).

Referencing: IEEE style is used for referencing and citations in this thesis managed by Endnote X6 (Thomson Reuters).

This page is left blank intentionally

Publications & Awards

Journal Articles

- **A. Mehdizadeh**, M. S. M. Ali, K. Takahata, S. Al-Sarawi, and D. Abbott, "A recoil resilient lumen support, design, fabrication and mechanical evaluation," *Journal of Micromechanics and Microengineering*, vol. 23, art. no. 065001, 2013.
- M. K. Kopaei, **A. Mehdizadeh**, D. C. Ranasinghe, and S. Al-Sarawi, "A novel hybrid approach for wireless powering of biomedical implants," *IEEE Sensors Journal*, 2013 (Submitted, Under Review).
- A. Mirsepahi, **A. Mehdizadeh**, L. Chen, and B. O'Neill, "A comparative approach between intelligent techniques and conventional methods for inverse heat transfer modelling of an irradiative dryer," *Journal of International Communications in Heat and Mass Transfer*, 2013 (Submitted).

Conferences

- M. K. Kopaei, **A. Mehdizadeh**, D. C. Ranasinghe, and S. Al-Sarawi, "A novel hybrid approach for wireless powering of biomedical implants," in *2013 IEEE Eighth International Conference on Intelligent Sensors, Sensor Networks and Information Processing*, , 2013, pp. 455-460.
- **A. Mehdizadeh**, S. Al-Sarawi, K. Takahata, and D. Abbott, "A novel stent for recoil resilience," presented at *the Australian Biomedical Engineering Conference (ABEC)*, Brisbane, Queensland, 2012.
- **A. Mehdizadeh**, A. K. Horestani, S. F. Al-Sarawi, and D. Abbott, "An efficient 60 GHz resonator using Harmony Search," in *2011 IEEE Conference on Recent Advances in Intelligent Computational Systems (RAICS)*, 2011, pp. 369-372.
- **A. K. Horestani**, A. Mehdizadeh, S. Al-Sarawi, C. Fumeaux, and D. Abbott, "Quality factor optimization process of a tapered slow-wave coplanar strips resonator in CMOS technology," in *Microwave Conference Proceedings (APMC), 2011 Asia-Pacific*, 2011, pp. 45-48.

- **A. Mehdizadeh**, A. Miremadi, S. Al-Sarawi, M. Arjomandi, S. Mehdizadeh, B. Dally, and D. Abbott, "Optimal design of an offset strip fin heat sink using harmony search," in *38th Chemeca 2010: Engineering at the Edge,* Hilton Adelaide, South Australia, 2010, pp. 848-858.
- **A. Miremadi**, A. Mehdizadeh, M. Arjomandi, S. Al-Sarawi, M. Kahrom, B. Dally, and D. Abbott, "Taguchi based performance analysis or an offset strip fin heat sink," in *38th Chemeca 2010: Engineering at the Edge,* Hilton Adelaide, South Australia, 2010, pp. 1-10.

Awards

- Young Biomedical Engineer Prize awarded by Engineers Australia at the 12th Australian Biomedical Engineering Conference (ABEC), Brisbane, Australia, 2012.
- Research Abroad Scholarship travel grant to visit Microsystems and Nanotechnology (MiNa) research group at the University of British Columbia (UBC), Vancouver, Canada, awarded by University of Adelaide, 2011.
- BUPA Postgraduate Travel Grant and AUGU/RC Heddle Award travel scholarship to visit Microsystems and Nanotechnology (MiNa) research group at the University of British Columbia (UBC), Vancouver, Canada, 2011.
- Selected runner for the 3-Minute thesis competition, Faculty of Engineering Computer Science & Mathematical Sciences, School of Electrical & Electronic Engineering, The University of Adelaide, 2010.
- Postgraduate research Scholarship (ASI) towards doctoral studies, The University of Adelaide, Nov 2008.

List of Symbols

Notation	Description
CSA_{pre}	Luminal cross-sectional area before deflation of balloon
CSA_{post}	Luminal cross-sectional area after deflation of balloon
ρ_0	Initial density
V_0	Initial volume
$V(t)$	Current volume
m_0	Initial mass
ρ	Density
t	Time
σ_{ij}	Stress tensor component *ij*
$\ddot{x}$	Acceleration component in the *x* direction
$\ddot{y}$	Acceleration component in the *y* direction
$\ddot{z}$	Acceleration component in the *z* direction
b_i	Body acceleration in the direction of axis *i*.
ε_{ij}	Strain tensor component *ij*
m	Mass
F	Force
$\dot{x}_i$	Velocity in the *i* direction
$\{x\}$	Nodal displacement vector
$[K]$	Stiffness matrix
$\{F\}$	Nodal force vector
$D_{effective}$	Effective internal diameter of a scaffold
$D_{dilated}$	Average external diameter of a scaffold
D_{lost}	Diameter loss due to strut thickness

Notation	Description
T_s	Strut thickness
G_P	Patency gain
A_C	Average cross-sectional area patent to fluid
A_T	Mean cross-sectional area of a deployed scaffold
$T_{s,avg}$	Average strut thickness
$T_{s,flat}$	Fabricated RRR thickness with no sawtooth
t_h	RRR sawtooth height
t_l	RRR sawtooth length
O_l	RRR overlap length
R_l	RRR total length
$\mathbf{V}$	Fluid velocity vector
p	Fluid pressure
μ	Dynamic viscosity
$\mathbf{D}$	Rate of deformation tensor
μ_∞	Viscosity at zero shear rate
μ_0	Viscosity at infinite shear rate
$\dot{\gamma}$	Shear rate
u	Velocity component in the direction of x axis
v	Velocity component in the direction of y axis
w	Velocity component in the direction of z axis
$D_{in,avg}$	Mean inner diameter of a scaffold
W_s	Strut width
T_s	Strut thickness
D_{in_m}	Main vessel diameter
D_{in_m}	Branching vessel diameter
$L_{Prox,Stent}$	Boundary layer initial length, proximal end of stent
$L_{Dist,Stent}$	Boundary later initial length, distal end of stent
$L_{Prox,RRR\text{-}Stent}$	Boundary layer initial length, proximal end of RRR-stent
$L_{Dist,RRR\text{-}Stent}$	Boundary later initial length, distal end of RRR-stent

Notation	Description
F_{wh}	Scaffolding withholding force
F_{d}	Fluid drag force
$f_{i,support}$	Branch *i* outlet flow rate, main branch scaffolded
f_{in}	Inlet flow rate
FR_{i}	Outlet/Inlet flow rate ratio
$f_{i,healthy}$	Branch *i* outlet flow rate, main branch unscaffolded
FD_{i}	Outlet/Inlet flow rate ratio deviation
$A_{RRR\text{-}Stent}$	Area subject to low wall shear stress, RRR-stent
A_{Stent}	Area subject to low wall shear stress, stent
A_{s}	SMA starting transformation temperature
A_{f}	SMA finishing transformation temperature
$L_{sty,r}$	Axial length of Styrofoam rings
$L_{sty,c}$	Axial length of Styrofoam cap
L_{rod}	Axial length of heat transfer rod
r_{1}	Radius of heat transfer rod
$L_{air,r}$	Axial length of air cylinder trapped, Styrofoam rings
$L_{air,d}$	Axial length of air cylinder at the deployment area
r_{2}	Mock vessel internal diameter
$T_{sty,r}$	Thickness of Styrofoam rings
L_{mock}	Axial length of mock vessel
L_{RRR}	Total length of RRR
t_{RRR}	RRR average thickness
W_{RRR}	RRR width
V_{flow}	Approach velocity
k_{rod}	Thermal conductivity of heat transfer rod
k_{sty}	Thermal conductivity of Styrofoam
k_{air}	Thermal conductivity of air
ν	Kinematic viscosity

Notation	Description
Re	Reynolds number
Pr	Prandtl number
$\dot{Q}$	Heat transfer rate
T	Temperature
R_{thermal}	Thermal resistance
R_{cond}	Conduction thermal resistance
R_{conv}	Convective thermal resistance
h	Convective heat transfer coefficient
R_{rad}	Radiation thermal resistance
h_{rad}	Radiation heat transfer coefficient
T_{s}	Surface temperature
T_{surr}	Surrounding temperature
$R_1 = R_{\text{cond\_ins}}$	Conductive thermal resistance of air and Styrofoam rings
$R_2 = R_{\text{cond\_mock}}$	Conductive thermal resistance of mock vessel
$R_3 = R_{\text{conv}}$	Convective thermal resistance of crossflow
k_{ins}	Thermal conductivity of insulation layer
Nu	Nusselt Number
$\dot{q}_{\text{conv}}$	Convective heat flux rate
$\dot{q}_{\text{cond}}$	Conductive heat flux rate
h_{flow}	Effective heat transfer coefficient of crossflow
L_{chr}	Characteristic length
Nu_{cyl}	Nusselt number of cylinder in crossflow
T_1	Temperature at internal walls of mock vessel
$T_{\infty 1}$	Constant rod temperature
R_{total}	Total thermal resistance
$\dot{Q}_{\text{in}}(x)$	Heat transfer rate into the differential volume at distance x
$\dot{Q}_{\text{out}}(x)$	Heat transfer rate out of the diff. volume at distance x
$\dot{Q}_{\text{comb}}(x)$	Heat transfer rate out of the diff. volume in radial direction
R_{comb}	Combined thermal resistance of insulation layer

Notation	Description
A_c	Cross-sectional area of heat transfer rod
L_{total}	Total length of the thermal model of heat transfer rod
L_{added}	Added length to the thermal mode of heat transfer rod
$\dot{Q}_{out,tip}$	Heat transfer rate from the tip of heat transfer rod
x_{tip}	Axial distance from base to tip of heat transfer rod
$\dot{Q}_{added}$	Heat transfer from added length of heat transfer rod
$T_{rod}(x)$	Temperature of rod at axial distance x from the base
R_{total_tip}	Total thermal resistance at the tip of the rod
R_{ins}	Thermal resistance of the insulation at the top section of mock-rod assembly
$A_{c,ins}$	Cross-sectional area of Styrofoam cap
$k_{ins,top}$	Thermal conductivity of insulation at the top section of mock-rod assembly
h_{top}	Heat transfer coefficient at the top of mock rod assembly
R_{top}	Thermal resistance at the top of mock-rod assembly
L_{top}	Axial length of the top section of the mock-rod assembly
P_{mock}	Periphery of the mock vessel
$A_{c,mock}$	Cross-sectional area of mock vessel
$\dot{p}$	Heat transfer rate per unit length
R_{mock}	Effective thermal resistance of mock vessel
$[K]$	Matrix of thermal conductance
$\dot{Q}_{electric}$	Electric power consumption
I	Electric current
$R_{electric,plate}$	Electrical resistance of heating plate
$\dot{Q}_{thermal}$	Thermal heat transfer rate
$R_{thermal,\ plate}$	Thermal resistance of heating plate
T_{plate}	Heating plate temperature
T_{room}	Room temperature

Notation	Description
δ_{linear}	Coefficient of linear thermal expansion
$L_{initial}$	Initial length of a solid
$V_{electric}$	Electric potential
$I_{electric}$	Electric current
T_{RRR}	RRR body temperature
T_{body}	RRR's surrounding tissue (human body) temperature
$R_{thrm,body}$	Thermal resistance tissue surrounding RRR
$R_{thrm,blood}$	Effective thermal resistance of blood
$R_{elec,RRR}$	Electrical resistance of RRR
V_{in}, V_{out}	Input and output voltage
$R_{cond,parylene}$	Conduction thermal resistance of parylene
$R_{conv,blood}$	Convective thermal resistance of blood
$L_{coating}$	Thickness of parylene-C layer
$k_{parylene}$	Thermal conductivity of parylene
$A_{RRR,conv}$	RRR area subject to blood flow
h_{blood}	Convective heat transfer coefficient of blood
$\rho_{elec,Nitinol}$	Electrical resistance of Nitinol
$A_{RRR,cs}$	RRR strut cross-sectional area
$V_{avg,blood}$	Average blood velocity
ρ_{blood}	Blood density
μ_{blood}	Average blood viscosity
P_{RRR}	Cross-sectional periphery of RRR
$\mathbf{f}$	Fluid body forces

Abbreviations

Notation	Description
μEDM	Micro Electro-Discharge Machining
3D	Three-Dimensional
ACE	Angiotensin-Converting Enzyme
ARB	Angiotensin II Receptor Antagonist
BE	Balloon-Expandable
BM	Bare-Metal
CABG	Coronary Artery Bypass Grafting
CAD	Computer-Assisted Design
CFD	Computational Fluid Dynamics
CHD	Coronary Heart Disease
CNT	Carbon Nanotube
Co-Cr	Cobalt Chromium
CSA	Cross-Sectional Area
CTE	Coefficient of Thermal Expansion
CU	Copper
CVD	Cardiovascular Disease
DE	Drug-eluting
Fe	Iron
FEA	Finite Element Analysis
FEM	Finite Element Modelling
HT	Heat transfer Rod
IR	Infrared
ISR	In-Stent Restenosis
LDL	Low Density Lipoproteins
LWSS	Low Wall Shear Stress
Mg	Magnesium

Notation	Description
MRI	Magnetic Resonance Imaging
Ni-Ti	Nickel-Titanium (Nitinol)
PCI	Percutaneous Coronary Intervention
PCTA	Percutaneous Transluminal Angioplasty
PET	Polyethylene Terephthalate
PEVA	Polyethylene-*co*-Vinyl Acetate
PGA	Polyglycolid Acid
PLA	Polylactic Acid
PLGA	Poly-l-Glycolic Acid
PMBA	Poly-n-Butyl Methacrylate
Pt-Cr	Platinum Chromium
Pt-Ir	Platinum Iridium
PU	Polyurethane
RF	Radio-Frequency
RRR	Recoil Resilient Ring
SE	Self-Expandable
SIBS	Styrene-*b*-Isobutylene-*b*-Styrene
SMA	Shape Memory Alloy
SS 316L	Stainless Steel 316L
SST	Shear Stress Transport
STD	Standard Deviation
Ti	Titanium
TiBN	Titanium-Boron-Nitride
VLSI	Very Large Scale Integration

List of Figures

Chapter 1 ..... **1**

Figure 1.1 . Composition of arterial walls. 4

Figure 1.2 . Occurrence and growth of atherosclerosis. 5

Figure 1.3 . Coronary artery bypass grafting. 7

Figure 1.4 . Carotid artery endarterectomy. 8

Figure 1.5 . Percutaneous transluminal angioplasty (PCTA). 8

Figure 1.6 . Dissection after percutaneous coronary angioplasty. 9

Figure 1.7 . Balloon expansion of a coronary stent. 10

Figure 1.8 . Common atherectomy techniques. 12

Figure 1.9 . Stent classification map. 16

Figure 1.10 . Expansion of balloon and self-expandable stents. 17

Figure 1.11 . Coil stents. 24

Figure 1.12 . Spiral stents. 25

Figure 1.13 . Woven stents. 26

Figure 1.14 . Closed-cell modular stent. 26

Figure 1.15 . Stent with flexible bridges. 27

Figure 1.16 . Closed-cell stent with flexible bridges. 28

Figure 1.17 . Open cell modular stent. 28

Figure 1.18 . Fish scaling and plaque prolapse in open cell stents. 29

Figure 1.19 . Stent thrombosis in a DE stent. 32

Figure 1.20 . In-stent restenosis. 34

Figure 1.21 . Overview of thesis structure. 38

Chapter 2 ..... **41**

Figure 2.1 . Recoil Resilient Ring (RRR) luminal support. 45

Figure 2.2 . Finite element model of the simplified RRR. 50

Figure 2.3 . Radial displacement and stress results during expansion. 51

Figure 2.4 . Plastic strain results of the teeth. 52

Figure 2.5 . BE stent resilience against compression. 53
Figure 2.6 . RRR resilience against compression. 54
Figure 2.7 . Computational model of RRR in axial loading analysis. 55
Figure 2.8 . Axial loading results of the RRR without axial support. 56
Figure 2.9 . Axial harnesses. 57
Figure 2.10 . Use of axial harnesses in the fully expanded state. 58
Figure 2.11 . Discretised 3D model of RRR with axial harnesses. 58
Figure 2.12 . Axial loading results of the RRR with axial harnesses. 59
Figure 2.13 . Plastic deformation of axial harnesses. 59
Figure 2.14 . Straight RRR, μEDM patterned from a 200-μm-thick Nitinol sheet. 60
Figure 2.15 . RRR shaping and thermal treatment setup. 61
Figure 2.16 . RRR after shaping and thermal treatment. 62
Figure 2.17 . Surface profile of RRR 63
Figure 2.18 . Balloon expansion of RRR *in vitro* 65
Figure 2.19 . Radial loading test setup. 66
Figure 2.20 . Radial loading test results, free-holding. 68
Figure 2.21 . Radial loading test results, *in vitro*. 69

Chapter 3 71

Figure 3.1 . Geometry of the three different supports. 77
Figure 3.2 . Fluid domain configurations of the CFD analysis. 79
Figure 3.3 . Inlet flow profile. 80
Figure 3.4 . Discretization of the fluid domain. 80
Figure 3.5 . Dimensional configurations of the dimensional analysis. 82
Figure 3.6 . LWSS distribution in unbranched fluid domains. 84
Figure 3.7 . Temporal average of LWSS in unbranched fluid domains. 84
Figure 3.8 . Selected time instances of third cardiac cycle. 85
Figure 3.9 . Inverse relation of the dynamic viscosity and shear rate, standalone stent. 86
Figure 3.10 . Inverse relation of the dynamic viscosity and shear rate, RRR-integrated stent. 86
Figure 3.11 . LWSS contour plots, deployment area of unbranched domains, instances 1–3. 87
Figure 3.12 . LWSS contour plots, deployment area of unbranched domains, instances 4–6. 88
Figure 3.13 . LWSS contour plots, entire area of unbranched fluid domains, instances 1–3. 89
Figure 3.14 . LWSS contour plots, entire area of unbranched fluid domains, instances 4–6. 90

Figure 3.15 . Radial gradient of velocity and shear strain rate 91
Figure 3.16 . Velocity magnitudes along a radial path. 92
Figure 3.17 . Drag force comparison in a unbranched fluid domain. 93
Figure 3.18 . LWSS distribution in branched fluid domains. 95
Figure 3.19 . Drag force comparison of the scaffolds in branched domains. 96
Figure 3.20 . LWSS contour plots, deployment area of branched domains, instances 1–3. 97
Figure 3.21 . LWSS contour plots, deployment area of branched domains, instances 4–5. 98
Figure 3.22 . LWSS contour plots, entire area of branched fluid domains, time instances 1–3. 99
Figure 3.23 . LWSS contour plots, entire area of branched fluid domains, time instances 4–6. 100
Figure 3.24 . Flow rate comparison of proximal, distal and main branches. 101
Figure 3.25 . Mean absolute flow deviation from a healthy branched vessel. 102
Figure 3.26 . Temporal average values of hemodynamic indicators. 103
Figure 3.27 . LWSS in the deployment area of cases 1–8. 105
Figure 3.28 . LWSS in the entire fluid domains of case 1–8. 106
Figure 3.29 . Drag Force Comparison, cases 1–8. 107
Figure 3.30 . Proximal branch to inlet flow rate ratio, cases 1–8. 108
Figure 3.31 . Distal branch to inlet flow rate ratio, cases 1–8. 109
Figure 3.32 . Main branch to inlet flow rate ratio, cases 1–8. 110
Figure 3.33 . Mean absolute flow deviation. 111
Figure 3.34 . Temporal average values of hemodynamic indicators, cases 1–8. 111
Figure 3.35 . Temporal distribution of the mean LWSS ratios, cases 1–8. 112
Figure 3.36 . Temporal distribution of mean drag force, cases 1–8. 113
Figure 3.37 . Temporal mean flow ratios, cases 1–8. 114

Chapter 4 117

Figure 4.1 . Stress-strain curve of a shape memory alloy. 120
Figure 4.2 . Heat transfer setup model. 122
Figure 4.3 . Cross-sectional overview of the mock-rod assembly. 125
Figure 4.4 . Fin analysis of the heat transfer assembly. 129
Figure 4.5 . Thermal resistance network at the top section of mock-rod assembly. 131
Figure 4.6 . Temperature distribution along walls of mock vessel. 134
Figure 4.7 . Temperature distribution along heat transfer (HT) rod. 135
Figure 4.8 . Temperature distribution along walls of mock vessel, high temperature input. 136

Figure 4.9 . Geometry of the 3D thermal analysis model. 138
Figure 4.10 . Discretised mock-rod domain. 139
Figure 4.11 . Temperature distribution in the axial direction of the rod. 140
Figure 4.12 . Heat flux in the mock-rod assembly. 141
Figure 4.13 . Temperature distribution along internal walls of mock vessel. 142
Figure 4.14 . Temperature distribution in the simplified RRR. 143
Figure 4.15 . FEA model of the mock-rod assembly in a fluid chamber. 144
Figure 4.16 . Discretization of the fluid solid domain for conjugate heat transfer. 147
Figure 4.17 . Convergence plots of the conjugate heat transfer analysis. 148
Figure 4.18 . Temperature distribution along the rod, conjugate heat transfer. 149
Figure 4.19 . Velocity profile at the horizontal cross-section of the fluid chamber. 150
Figure 4.20 . Velocity profile at the vertical cross-section of the fluid chamber. 151
Figure 4.21 . Temperature on mock vessel internal walls, conjugate heat transfer. 152
Figure 4.22 . Temperature on mock vessel external walls, conjugate heat transfer. 153
Figure 4.23 . Temperature distribution in the RRR, conjugate heat transfer. 154
Figure 4.24 . Heat transfer setup. 155
Figure 4.25 . Temperature of the external surface of mock vessel, base. 156
Figure 4.26 . Temperature of the external surface of mock vessel, deployment area. 157
Figure 4.27 . *In vitro* thermal expansion of the RRR. 158
Figure 4.28 . Free expansion of the RRR under heat stimuli. 159
Figure 4.29 . Average external diameter of RRR vs. temperate. 159
Figure 4.30 . Actuation force measurement setup. 160
Figure 4.31 . Temperature distribution on the heating plate and RRR. 163
Figure 4.32 . Expansion forces of thermal actuation. 164
Figure 4.33 . Electro-thermal actuation of the RRR. 166
Figure 4.34 . Geometry of the electro-thermal analysis, deployment area. 170
Figure 4.35 . Discretization of the fluid solid domain, electro-thermal analysis. 172
Figure 4.36 . Convergence plots of electro-thermal analysis 173
Figure 4.37 . Temperature distribution in RRR, electro-thermal analysis. 174
Figure 4.38 . Parametric study of electro-thermal analysis. 174
Figure 4.39 . Shear thinning effect of blood, electro-thermal analysis 175

List of Tables

Chapter 1 ..... **1**

Table 1.1 . Mechanical properties of common stent materials. 18

Table 1.2 . Common materials used for fabrication of stents. 21

Table 1.3 . Common stent surface enhancement strategies. 30

Chapter 2 ..... **41**

Table 2.1 . Material and geometrical characteristics of a typical BE stent and RRR. 50

Table 2.2 . Surface roughness measurement parameters and values. 63

Table 2.3 . Properties of RRR and commercial stent samples for compression test. 67

Chapter 3 ..... **71**

Table 3.1 . Material and geometrical characteristics of the three luminal supports. 78

Table 3.2 . Dimensional configurations of the fluid domain for sensitivity study. 81

Table 3.3 . Drag and withholding forces comparison in an unbranched fluid domain. 94

Chapter 4 ..... **117**

Table 4.1 . Geometrical and material properties of the mock-rod assembly. 123

Table 4.2 . Vertical expansion of components in heat-induced actuation setup. 162

Table 4.3 . Material properties of blood and parylene-C 167

This page is left blank intentionally

Chapter 1

Introduction and Motivation

Cardiovascular disease is the primary cause of death in the developed and developing countries, every year taking lives of millions around the world. In this chapter an overview of the risk factors leading to this disease are first introduced, followed by the common non-surgical and surgical treatment options. Among the occlusive vascular disease surgical treatments, balloon angioplasty with adjunct stenting is the most prevalent method.

Stents are mechanical tubular structures that are delivered to an occluded site in a crimped state, wherein they expand and provide a permanent support against luminal walls to re-establish normal fluid flow. As the main focus of this chapter, a review of current stent structures, designs and their often self-competing requirements are provided. Having recognized advantages and disadvantages of each class, current design gaps are recognized that are considered for the development of a proposed novel transluminal scaffolding device in subsequent chapters.

1.1 Abstract

The human heart is a small fist-sized organ that beats about 70 times per minute at rest, humbly reviving itself and all other parts of the body bestowing them oxygen and nutrient-rich blood. As an integral part of the cardiovascular system, the vessels facilitate this process by providing the pathways between the heart and its descendants. Though resilient to the myriad of different conditions of its owner, this marvel of creation may yet fall shy of its responsibilities by the slightest nuance of a blockage endangering our existence. Cardiovascular disease (CVD), taking lives of more than 17 million people in 2008, has yet remained the greatest culprit for deaths around the globe as of today [1].

Statistics from the World Health Organisation and US Centre for Disease Control and Prevention (2002) show that cardiovascular disease is responsible for 10% of the disability-adjusted life years lost in low and middle-income countries, and 18% in high-income countries. Accounting as one of the primary causes of CVD, atherosclerosis refers to the thickening of internal layers of vessels due to accumulation of fatty materials. This chronic inflammatory disease can lead to narrowing or total occlusion of any of the arteries negatively affecting the downstream organs such as the heart (coronary artery disease), the brain and peripheral organs.

Coronary heart disease is estimated to become the single leading health problem by 2020 [1]. In Australia, based on statistics in 2001, CVD accounted for 38% of all Australian deaths; 26% of these were due to coronary heart diseases, while the rest (9%) were stroke related. In addition, this disease is responsible for 7.5% of all hospital operations, costing $7.8 billion of the total Australian health expenditure in 2002, and becoming the most costly health condition. Some of the commonly recognized causes of this disease include genetic predisposition, unhealthy lifestyle, cold weather, lack of exercise and strong emotions [2]. Treatment and management of vascular constrictions consists of a combination of non-surgical approaches such as healthy lifestyle changes, pharmacological approaches as well as the more invasive surgical methods among which bypass grafting, balloon angioplasty, stenting and atherectomy are the most common.

A stent is a mechanical structure that provides a chronic support against internal walls of an occluded vessel to restore its luminal cavity. Having proved its efficacy in short- and long-term treatment of occluded vessels, stenting has become the mainstream approach

in management of CVD surpassing the number of bypass grafting procedures every year. Common stent structures are simply made of a metal mesh, e.g. stainless steel, and deployed in a blood vessel such as an artery during a percutaneous coronary intervention procedure, also known as angioplasty. Despite promising acute luminal gain after stenting, thrombosis (formation of blood clots) and restenosis (renarrowing of the lesion) have yet remained as the most important post-intervention complications that limit the effectiveness of this procedure.

In this chapter, after an introduction on atherosclerosis and its contributing factors, common treatment options are discussed. Stenting as the main focus of this thesis is then expanded providing a review of current structures and improvements since deployment of the very first vascular stent. Iterating the advantages and shortcomings of each of the designs and important attributes of stents, then the design gap is recognized. Finally, a summary of the thesis and original contributions are outlined.

1.2 Atherosclerosis and Luminal Occlusion

Major blood vessels of the body are comprised of three distinct layers including, the *tunica intima*, the *tunica media* and the *tunica adventitia*. From the innermost layer to the outermost, the *tunica intima* consists of the thin internal layer adjacent to the luminal cavity. This layer acts as a barrier between the luminal fluid and the rest of the vessel engaging in mediation of coagulation, platelet adhesion, immune function and controlling the content and amount of intravascular and extravascular fluids [3]. In a healthy vessel, this layer comprises a thin layer of endothelial cell and connective tissue. The mechanical action of this layer is provided by the smooth muscles cells of the *tunica media* that are enclosed by a network of collagen and elastic fibres. These two first layers are covered by a protective layer of primarily elastin and collagen that consists of *tunica adventitia*. Figure 1.1 shows the cross-sectional view of an artery with a detailed view of the three layers. The cavity at the centre of a vessel that is normally filled with flowing blood is referred to as the lumen.

One of the most prevalent pathological indications of abnormal vessels is an inflammatory phenomenon referred to as atherosclerosis. Development of atherosclerosis is majorly associated with early appearance of fibrotic fatty depositions between the *tunica media*

and *intima* [4, 5]. Despite the widespread agreement on the relevance of atherosclerosis and the inflammatory response of the endothelial layer to injuries [6, 7], this complex phenomenon is yet to be understood completely.

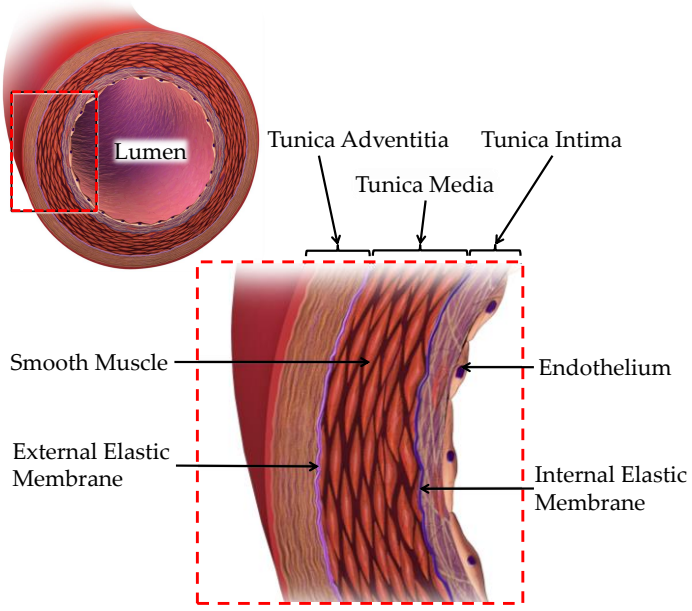

Figure 1.1. Composition of arterial walls. Main three layers incorporating, *tunica intima*, *tunica media* and *tunica adventitia* from the innermost to the outer layer in order. Atherosclerosis is triggered by endothelium dysfunction. Typical luminal diameter of healthy human coronary arteries ranges from 1.5 to 5.5 mm [8, 9]. Image reproduced from [10].

Deposition of plaques is usually preceded by an abnormality in the function of endothelial layer [11, 12] succeeded by proliferation of low density lipoproteins (LDL) between *tunica intima* and *media*, which eventually leads to oxidation of these sediments. Prevalence of oxidized LDL triggers accumulation of plaques, and in turn, phospholipids, which induce regeneration of endothelial cells [5, 13, 14]. This process, at the initial phases, causes an increase in the external diameter of a vessel that eventually leads to internal narrowing or complete occlusion referred to as stenosis [5, 15]. Figure 1.2 depicts the evolution of atherosclerosis into a luminal constriction in different stages.

Risk factors such as genetic predisposition, age, hepercholesteromia, hypertension (high blood pressure), diabetes and smoking contribute to the prevalence of atherosclerosis [4, 16-18]. Being one of the leading causes of death in the world [16], atherosclerosis and, in the severe case, stenosis (narrowing) of vessels have grave consequences for their downstream organs that is typically due to the obstructed oxygen delivery. By occasional breakage of small particles of plaques, the situation can escalate into a complete blockage

leading to necrosis of vital organs such as the heart (heart attack) and/or brain (stroke). In less life-threatening situations atherosclerotic plaques can cause peripheral artery disease typically leading to pain in legs, poor wound healing and even amputations. Depending on the severity of plaque deposition in terms of volume, content and its risk of rupture, different treatment protocols are adopted by clinicians as detailed in the following sections.

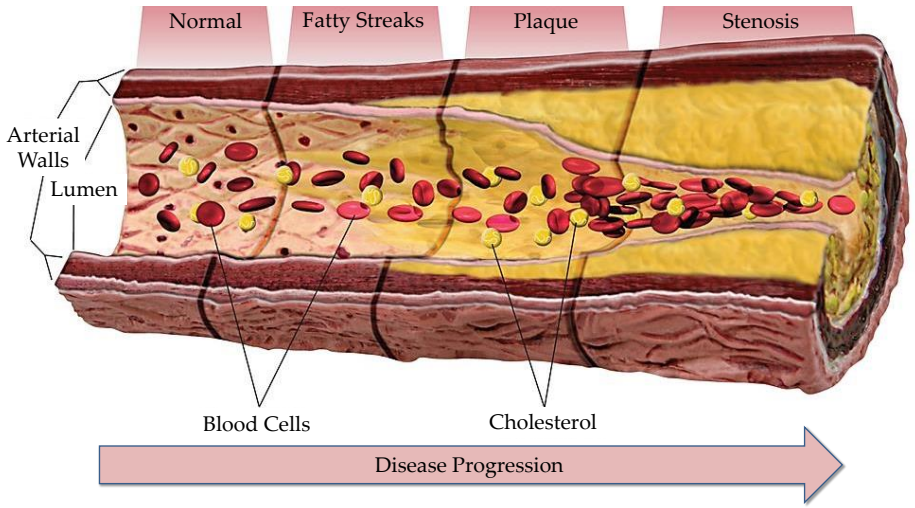

Figure 1.2. Occurrence and growth of atherosclerosis. Healthy artery at left followed by the atherosclerotic artery at early stages with increased external diameter in the middle, and severe narrowing (stenosis) of the lumen due to accumulation of atherosclerosis at right. Typical luminal diameter of healthy human coronary arteries ranges from 1.5 to 5.5 mm [8, 9]. Image reproduced from [19].

Due to the complex and patient-specific nature of atherosclerosis and luminal constrictions resulting in different classification of the progression of the disease, a number of approaches have been adopted over the years for its treatment. These approaches may be classified into two major groups of non-surgical and surgical methods. The non-surgical methods are mostly applied in less severe cases, though vastly adjoined with the surgical methods, to prolong their acute benefits [7].

1.3 Non-surgical Treatments

Non-surgical methods aim to relieve (or at least decrease) symptoms of progression of atherosclerosis by first reducing risk factors in an effort to cease or slow down plaque growth. These methods can be administered at any stages of the disease even as an adjunct to other treatment methods. General healthy lifestyle changes such as adopting a

healthy diet low in cholesterol, sugar and salt, more frequent physical activities, lowering stress, quitting smoking and maintaining a healthy weight are of outmost importance as the first line of defence for prevention or alleviation of atherosclerosis [2]. Pharmacological interventions may also be applicable at the early stages of the disease and as an adjunct treatment. At this stage a single or combination therapy of medications mainly addressed to lower blood pressure, lower cholesterol levels and blood thinners are administered [20-23]. Typical antihypertensive medications including but not limited to beta blockers, angiotensin-converting enzyme (ACE) inhibitors and the more recent angiotensin II receptor antagonists (ARB) [24, 25] reduce the high stress levels and inflammation of arteries that lead to poor vascular performance [20, 21]. Cholesterol-lowering medications (statins) attempt to control further sedimentation of fatty cells in the atherosclerotic lesion. Blood thinners, including anticoagulants such as heparin or warfarin and antiplatelet agents such as aspirin can assist the fight against atherosclerosis progression by reducing thrombus formations yet increase the risk of excessive bleeding in individuals with low platelet levels [22, 26].

1.4 Surgical Treatments

In severe cases of stenosis, surgical methods are employed to physically push or remove the atherosclerotic plaque away from the lumen and restore blood flow. These methods can further be classified into two groups of invasive and minimally-invasive. The two dominant invasive approaches include bypass grafting, and endarterectomy that are explained later in this section. In addition to the older invasive methods, the more recent transluminal methods such as angioplasty with or without stent deployment and atherectomy have become more dominant in the past decade. Long-term clinical results of the transluminal methods are improved even beyond the more invasive methods by the advent of site-specific drug administration using DE stents and DE balloons.

1.4.1 Coronary Artery Bypass Grafting

Coronary artery bypass grafting (CABG) entails cultivation of a healthy blood vessel from some other part of the body such as legs, chest or arms and using that to establish an alternative path for the stenosed (constricted) section of an artery as demonstrated in Figure 1.3.

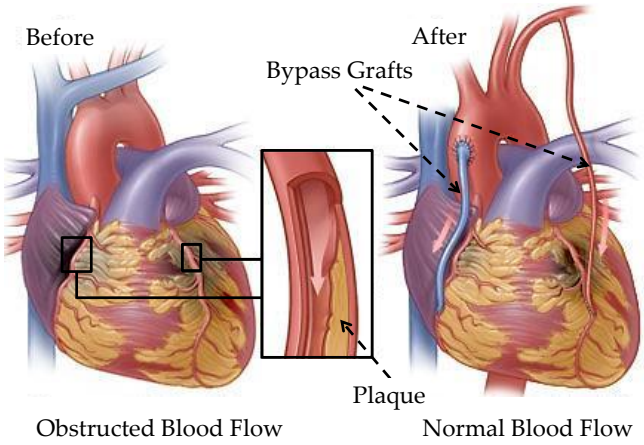

Figure 1.3. Coronary artery bypass grafting. Blood flow of stenosed coronary arteries is rerouted via alternative vessels from the aorta. Image reproduced from [27].

Undergoing CABG requires general anaesthesia and the recovery time is the longest amongst other treatment options [28, 29]. One streamlined method for CABG is referred to as arrested heart surgery (conventional bypass surgery) wherein the heart is stopped and a heart-lung machine replaces the circulatory system. The second method referred to as off-pump or beating heart surgery discards the need for the heart-lung machine yet entails certain equipment to facilitate operation on a beating heart [28, 30]. General complications of this method include those of any open surgery such as infection, internal bleeding in addition to circulatory-specific problems such as clot formation or acute closure of arteries leading to heart attack or stroke [29, 31].

1.4.2 Endarterectomy

Endarterectomy is a surgical procedure to manually remove the atheromatous plaque. First introduced by the Portuguese surgeon J. Cid Dos Santos in 1946 on a femoral artery, nowadays, it is mostly used on the superficially accessible arteries, such as carotid arteries [32]. During the procedure, after exposing the affected artery, a shunt is placed across the lesion to provide temporary blood flow while the arterial wall is incised and the plaque is removed manually. The artery is then sutured after removing the shunt, Figure 1.4. Having similar complications to CABG, carotid endarterectomy can potentially result in production or aggravation of neurological problems [32, 33]. Minimally invasive techniques such as percutaneous transluminal angioplasty (PCTA) with or without a stent proved to be viable alternatives to the more invasive CABG over the years [34] boasting shorter recovery times and similar long-term benefits [35].

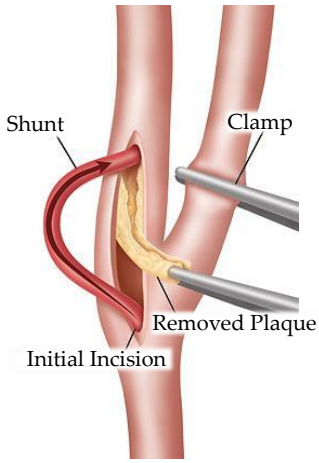

Figure 1.4. Carotid artery endarterectomy. Temporary shunt provides blood flow to the brain during the surgery and is removed after removal of the atherosclerotic plaque. Image reproduced from [36].

1.4.3 Percutaneous Transluminal Angioplasty

First introduced by Andreas Gruentzig in 1977 [37], PCTA has become widely accepted for treatment of obstructed lumens where the target stenosis is dilated by the inflation of a balloon. As demonstrated by Figure 1.5, the procedure includes insertion of a deflated balloon catheter through a point incision typically in the femoral or brachial artery [38].

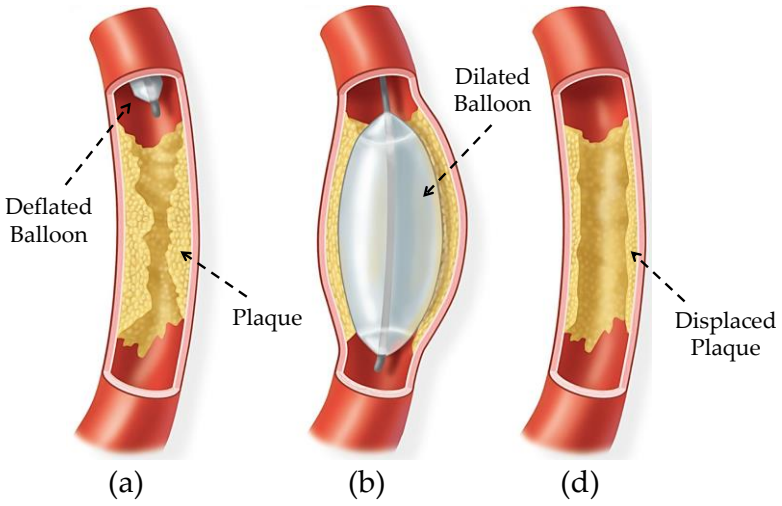

Figure 1.5. Percutaneous transluminal angioplasty (PCTA). a) A deflated balloon is guided to the lesion site via a catheter, b) then dilated by increasing the hydraulic pressure inside displacing the atherosclerotic protrusions away from the lumen, d) to restore the blood flow. Typical luminal diameter of healthy human coronary arteries ranges from 1.5 to 5.5 mm [8, 9]. Image reproduced from [39].

After reaching the target site, the balloon is inflated by running pressurized water inside it with which the balloon dilates the constricted lumen. Then the balloon is deflated and

retracted with the catheter leaving the displaced (and compressed) plaque in lesion. Although limited in the final luminal diameter gains, PCTA favours GABG by shorter recovery time and lower cost. Major complications arising from PCTA include abrupt closure and arterial dissection. Dissection, as shown in Figure 1.6, is a small tear within the inner layers of arterial walls allowing the blood separate these layers leading to a condition also known as pseudo-aneurysm [40]. It usually occurs from either inadvertent guide wire punctures or over-inflation of the balloon in inelastic lesions.

Another important limitation of PCTA includes late loss of luminal area gradually eroding the acute beneficial gains shortly after this procedure. This renarrowing (restenosis) process is often triggered by early recoil of the elastic stenotic lesion (primarily made of fibrotic tissue) and is continued by late proliferation of the intimal cells referred to as neointimal hyperplasia [41].

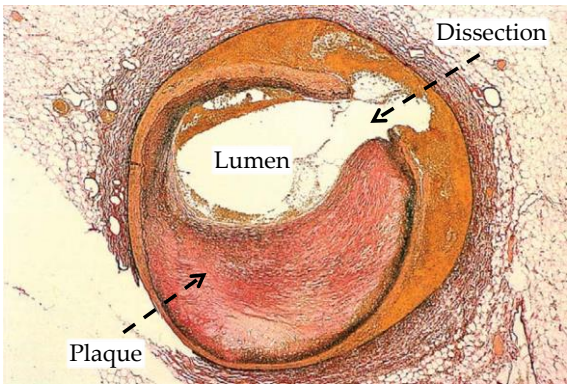

Figure 1.6. Dissection after percutaneous coronary angioplasty. Image reproduced from [42].

To overcome these shortcomings of PCTA, and more specifically high restenosis rates, stents where introduced as a complimentary scaffolding during percutaneous coronary intervention (PCI) since 1990 [43].

1.4.4 Stenting

Stents are mechanical devices that provide chronic support against diseased walls of a vessel to minimize elastic recoil and the need for potentially detrimental high pressure angioplasty dissections [44, 45]. Apart from their primary use in coronary artery disease [44], they have found application in other cavities of the body over the years [46-48]. Delivery and deployment of stents is performed in a very similar manner to the PCTA. A crimped stent either mounted on top of a balloon catheter or inside a sheath catheter is first routed to the target lesion and then expanded either by increasing pressure inside

an angioplasty balloon or by releasing the stent from a restraining sheath. Stents expanded by the former and later methods of expansion are respectively referred to as balloon-expandable (BE) and self-expandable (SE) stents. Majority of the stents in the current market fit in the first category where the diameter of the crimped stent is gradually increased by inflation of the balloon while the alloy-based stent undergoes plastic deformation. After being satisfied by the final diameter of the stent, the clinician deflates the balloon and retracts the catheter with the expanded stent left at the lesion to restore and maintain normal blood flow, Figure 1.7.

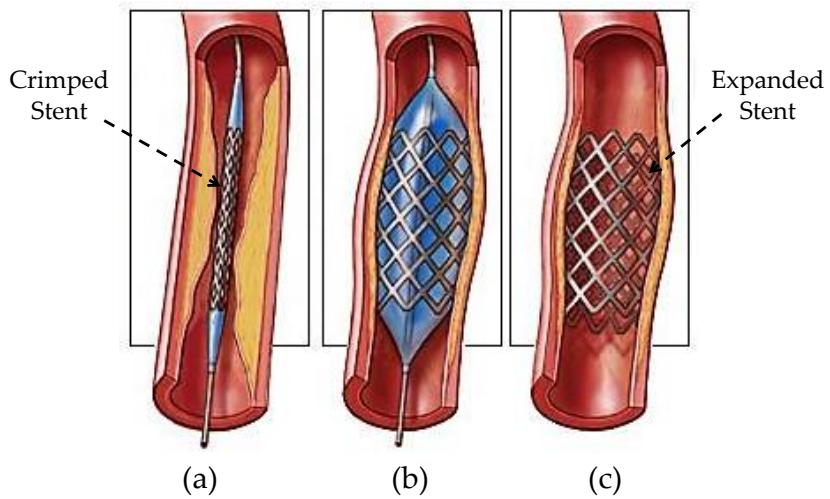

Figure 1.7. Balloon expansion of a coronary stent. a) Crimped stent that is threaded by the deflated balloon catheter is delivered to the lesion, b) then by increasing the hydraulic pressure balloon is dilated expanding the stent with it, c) the plastically deformed stent remains in the vessel while the balloon and catheter are retracted at the end of the procedure. Typical luminal diameter of healthy human coronary arteries ranges from 1.5 to 5.5 mm [8, 9]. Image reproduced from [49].

Despite initial luminal gain shortly after PCTA, restenosis (renarrowing) rates in 6 months follow-up can reach as high as 30–40%, leading to the use of stents as chronic mechanical scaffolds against compressive forces of the lumen. This resulted in lower rates of restenosis 20–30% [45, 50]. Limitations and complications of stenting, mostly being similar to PCTA, include thrombosis, haemorrhagic and vascular complications such as renarrowing of the lesion, acute stent recoil and the need for reintervention [41, 51].

Considering clinical and angiographic complications of current stenting procedures, a number of requirements for ideal stenting could be recognized. Apart from procedural and physiological objectives, stent design plays a key role in optimization of the final

outcomes namely, less re-interventional therapy due to renarrowing of the a treated lesion. In Section 1.5 after giving a brief introduction to the "ideal" stent design considerations, an overview of the current stent technology is provided. The objective of this section is to recognize the shortcomings of current design paradigms then attempting to address those, proposing a novel design that is outlined and evaluated in the subsequent chapters.

1.4.5 Atherectomy

One of the major shortcomings of PCTA and stenting is their very limited ability to dilate heavily calcified, thus hardened, lesions. At these areas, even high hydraulic pressures were demonstrated to be ineffective to reach a target inner diameter [52, 53]. More importantly, over-pressurization and over-inflation can aggravate the risk of vessel dissection while not even achieving the desired expanded diameter leading to incomplete stent deployment thereby increased risk of restenosis and thrombosis [54-56]. In order to overcome these issues, atherectomy devices were developed to remove the heavily calcified or fibrotic plaques. Contrary to the angioplasty expansion where luminal gain is achieved through displacement of atherosclerotic tissue, in atherectomy these depositions are actually ablated from the lesion [57, 58]. So far, several atherectomy devices have been developed including directional, high-speed rotational, transluminal excision and laser atherectomy as depicted in Figure 1.8.

In directional atherectomy, the device catheter is first routed to the lesion then the scraping blade is pushed towards the plaque by assistance of an inflatable balloon. The excised plaque fragments are collected in a chamber at the tip of the device. The catheter is then rotated in all directions to ensure an even surfacing of the lesion.

Rotational atherectomy devices are equipped with a diamond coated burr that rotates at high speeds (more than 60,000 rpm). When placed at the target site the burr selectively pulverizes the inelastic tissue (i.e. plaque) into fine particles of 5–10 μm in diameter that are released into the downstream blood flow. These particles are then removed from the body through phagocytosis (destruction by white cells) in the liver, spleen and lung [59]. The differential cutting mechanism of the burr ensures maintaining integrity of the elastic normal tissue rendering application of this technique most effective in hard lesions rather than soft and thrombus-containing ones [58, 60].

Transluminal excision (extraction), similar to the rotational atherectomy, replaces the diamond coated burr with a set of stainless steel blades. Moreover, the hollow tubular catheter in transluminal excision atherectomy collects the ablated fragments through vacuum suction instead of releasing them into the bloodstream.

Laser atherectomy, most often adjunct to balloon angioplasty and stenting, vaporises the plaque by delivery of 308-nm wavelength energy (excimer laser) to target lesions allowing selective ablation of thrombus and atherosclerotic plaque [61-63]. The primary objective of this method is to convert complex angiographic cases into more manageable ones referred to as laser assisted revascularization [61].

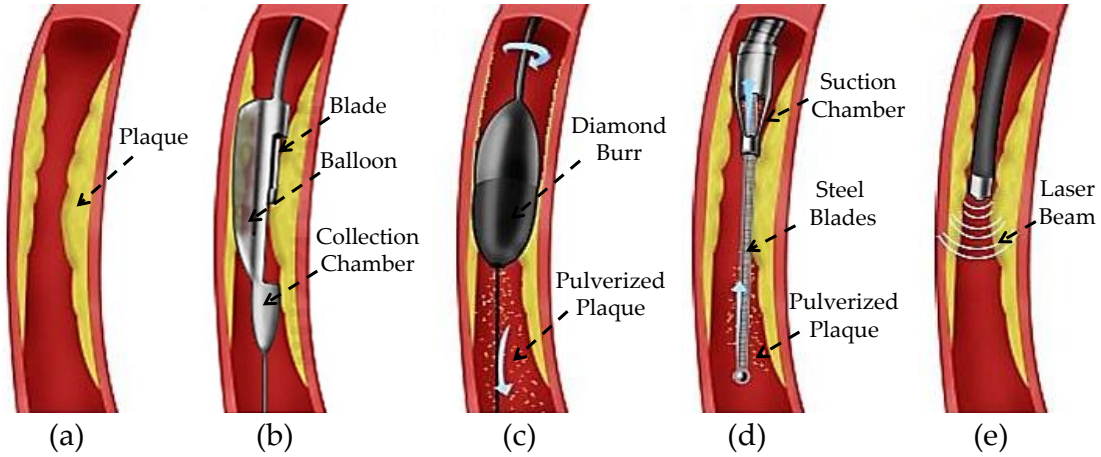

Figure 1.8. Common atherectomy techniques. a) Stenosed artery, b) directional atherectomy, the balloon expands to expose the cutting blade to the plaque, scraped plaque is collected at the collection chamber, c) rotational atherectomy, the rotating diamond-coated tip disintegrates the plaque into microscopic fragments that are released downstream, d) transluminal excision, the rotating stainless steel blades grind the plaque that is collected by vacuum suction, e) laser atherectomy, laser vaporizes the plaque, [64]. Typical luminal diameter of healthy human coronary arteries ranges from 1.5 to 5.5 mm [8, 9].

Atherectomy and other debris removal techniques such as thrombectomy (removal of clots) and embolic protection (capturing embolic debris) can all be used in conjunction with balloon angioplasty and coronary stenting to augment their beneficial results [57]. Particularly, where concerns regarding proper expansion of a stent in a heavily calcified lesion are escalated, combination of rotational ablation followed by stenting has proven to be useful. This is due to the better compliance of the lesion following atherectomy, which results in better stent expansion [65-68]. One of the most indicative application areas of atherectomy, more specifically rotational atherectomy, is management of chronic

in-stent restenosis (ISR). Contrary to the elastic recoil mechanism of restenosis in PCTA, ISR is mainly due to neointimal proliferation that is most likely in response to the presence of a foreign object, the stent and intravascular trauma during deployment. Restenosis management, solely by re-application of angioplasty exhibited very high rates (up to 85%) of recurrent restenosis [69]. This is due to the inability of the balloon to efficiently displace the high volume of stenotic tissue. For these reasons, pre-treatment with an atheroablative technique before balloon dilation is proposed [70-75].

1.5 Stents Current Status and the Future

The word "stent" is derived from a dental prosthesis developed by the 19th century English dentist Charles Stent. Nowadays, it refers to any mechanical device that is to expand and provide support inside a cavity in the body [41]. Mostly indicated in vascular occlusions [41, 44], these devices have found their way in other ducts of the body [46-48]. Today's market is replete with numerous stents amounting to a 3-billion-dollar industry. General characteristics and requirements of stents are reiterated abundantly in the literature [76-80]. These often competing ideal stent specifications can be classified as follows:

- *High radial strength*: to withstand the compressive forces imposed by the often atherosclerotic vessel walls to retain the lumen.
- *Low elastic recoil*: elastic recoil of stents that is due to the intrinsic material properties of the stent ought to be accounted for during deployment to achieve optimal luminal diameter. The higher the recoil, the higher is the need for over-expansion of the stent to compensate for luminal loss due to recoil, which in turn results in induction of more vascular injury leading to subsequent proliferative response from the body.
- *High axial flexibility*: increases the vascularization success rate at tortuous and distal lesions. Low axial flexibility results in lesion straightening and non-homogenous stress distribution on the vessel walls potentially leading to excessive vascular injury at the proximal and distal ends of the stent.
- *High crimped to expanded ratio*: increases trackability of the deployment catheter to pass through narrow and tortuous paths when the stent is crimped while providing good scaffolding upon expansion of the stent.

- *Minimal foreshortening*: foreshortening refers to the reduction in the axial length of stent upon radial expansion that is a common attribute of stents. For optimal scaffolding of the lesion and plaque coverage, foreshortening must be minimized.
- *Optimum wall coverage*: in order to reduce plaque prolapse (protrusion of stenotic tissue between the stent struts). This objective contradicts the requirement for minimal contact surface area between the vessel walls and the stent due to potential aggressive inflammatory response of the body to the foreign object (stent).
- *Material specific requirements*:
    - *Bio and hemocompatibility*: Drastic reactions from the body such as platelet formation that can lead to recurrent occlusions are highly undesired. Hemocompatibility concerns such as resistance of the material against corrosion, hydrophobicity for reduced traction between the blood and the stent surface are also highly desired.
    - *Fatigue resistance*: refers to the failure resistance of the stent against cyclic contractions of the vessels over its normal mission period (at least 10 years).
    - *Radiopacity*: for better visibility of the stent that has beneficial effect through more precise positioning of the stent during deployment and follow-up evaluations under fluoroscopic imaging.

Other ideal characteristics such as superelastic behaviour are more tailored for specific applications and areas where crushing or dynamic bending may occur, such as carotid and popliteal arteries [76, 81]. Apparently meeting all these majorly self-competing requirements calls for challenging trade-offs and optimization processes. In numerous efforts to achieve an optimum balance between these objectives, stent designers spawned a plethora of stents through a complicated process of adopting different materials, geometrical stent designs and manufacturing processes.

A rather comprehensive review of stents based on their engineering aspects is presented by Stoeckel *et al.* in [77]. In general, stents can be classified based on their material composition, originating material form, fabrication method, geometrical design, deployment method that is directly dependent on the material composition (balloon or self-expansion), mission period (permanent or degradable), clinical use (vascular or non-

vascular) and some other specific finishing attributes such as coatings, surface preparation and radiopacity [41]. Primary clinical drivers in the new generations of stents included radial strength, biocompatibility and radiopacity [82]. At the early stages of stent development much attention was given to address these requirements through different stent designs. On the other hand, in recent years, by the introduction of drug-eluting (DE) stents, the focus has been around the merit of these stents. In light of their early promising yet later controversial clinical outcomes, further attention is given to different stent surface treatment strategies, their long term efficacy and pharmacological comparison [82, 83]. As outlined by O'Brien and Carrol, as more and more clinical results on long-term performance of DES and absorbable stents are surfacing, arguments in support of bare metal stents and refocusing on their development are getting stronger [82].

A general map of the classification of stents is presented in Figure 1.9. For better recognition of current status of stenting and its shortcomings, in the following sections, these commonly-interrelated concepts of stent design and manufacturing are elaborated and complimented with some state-of-the-art commercial examples.

1.5.1 Materials and Expansion Mechanism

Majority of the stents in the current market are made of alloys in addition to a number of polymer based stents [79, 82] and the rather new advent of stent structures developed from carbon nanotubes (CNT) [84]. Specific characteristics of different materials such as elastic modulus, density, yield and tensile strength greatly influence subsequent attributes such as expansion mechanism and geometrical design [79]. Apart from expansion mechanism, a further classification of stents can be drawn depending on their absorption by the body into biostable and bioabsorbable stents. Biostable alloy-based stents, as the current mainstream standard, are intended to reside in a vessel permanently. Conversely, biodegradable stents exhibit the advantage of degradation or absorption (bioabsorbable stent) after their scaffolding mission period is lapsed [82, 85]. The rationale behind degradable stents is the short-term need for scaffolding within a vessel, hence avoiding potential chronic complications of the presence of a foreign structure inside the body (complications of stenting are elaborated later in this chapter) [86]. Biodegradable materials may also be used as coatings and vehicles of localized drug release at the lesion site giving rise to drug-eluting (DE) stents [87, 88].

Figure 1.9. Stent classification map. Detailed classification according to clinical indications is not in the scope of current chapter. Bln-expandable refers to balloon-expandable stents.

Degradable stents specifically prove more useful for scaffolding of vessels in growing infants whose vessels undergo geometrical changes over time [82, 85, 88-90]. Despite their promising potential, production and application of these stents are still in their in-

fancy lacking convincing favourable outcomes in comparison with their biostable counterparts. For instance, development of a low profile biodegradable stent with high radial strength for a predefined period that does not incur an excessive inflammatory response from the body is a long-standing challenge [79, 88, 89].

Ductile alloys such as stainless steel 316L are predominantly used in BE stents that can undergo plastic deformation during balloon inflation. In these structures, after deflation of the balloon the residual plastic strain in the material enables the stent to retain its expanded shape despite the initial elastic recoil. As a result the ideal material for these stents is required to exhibit low yield stress, to enable the stent undergo expansion at low pressures, and at the same time high elastic modulus, to reduce the elastic recoil of stent under compressive forces from the vessel. Apparently, these two requirements are contradictory for the majority of ductile metals.

Crimped BE stents are first mounted on a deflated balloon at the tip of a guide catheter. Being delivered to the target lesion, the balloon is inflated by increasing the hydraulic pressure inside with which the stent is also expanded, Figure 1.10 (a).

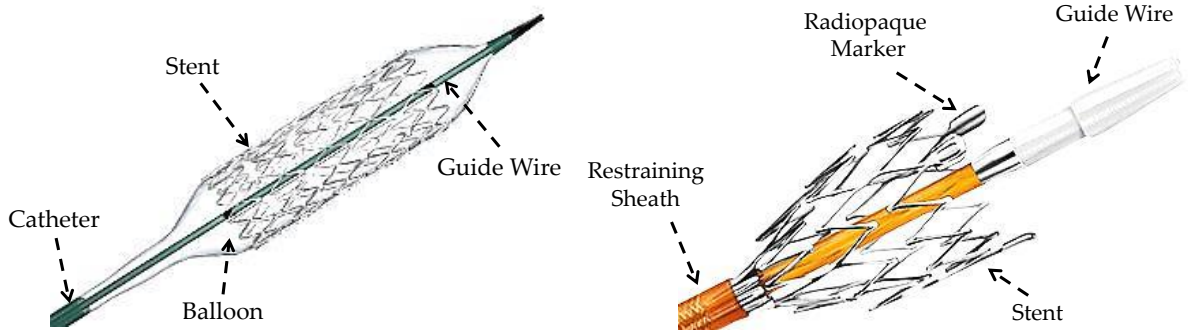

Figure 1.10. Expansion of balloon and self-expandable stents. a) BE stent. These stents are primarily made of plastically deformable alloys such as stainless steel 316L in a crimped state, then mounted on an angioplasty balloon for expansion and deployment. Image reproduced from [91], b) SE stent made of superelastic alloys that can undergo large deformations without reaching the plastic state. These stents are manufactured in the expanded shape then crimped and constrained by a sheath. Upon retraction of the sheath the stent recovers its expanded shape in response to body heat. Radiopaque markers are to enhance visibility in fluoroscopic imaging. Image reproduced from [92].

Conversely, SE stents rely on high elasticity or the shape-memory effect of certain alloys. These normally expanded stents are first crimped and constrained inside a sheath while

being delivered via the catheter to the lesion site. Upon retraction of the sheath, stent reverts to its predefined expanded form pushing plaque and the arterial walls away from the lumen [80, 93], Figure 1.10 (b). Consequently, materials for the SE stents are required to have large elastic recovery capability, such as the superelastic austenite Ni-Ti (Nitinol) alloys [94]. Being used in a majority of biomedical implants [94-96], Nitinol owes this popularity to attractive characteristics such as large recovery of elastic deformations up to 10%, biocompatibility and high fatigue resistance. This relatively large elastic range, referred to as superelastic region, is due to the stress-induced changes between austenite (harder) and martensite (softer) crystallographic phases. Further details on these phases of Nitinol are given in Chapter 4. Mechanical properties of common alloys used in fabrication of stents are presented in Table 1.1.

Table 1.1. Mechanical properties of common stent materials.

Material	Elastic Modulus GPa	Yield Strength MPa	Tensile Strength MPa	Density g/cc
SS 316L [79, 97]	190	331	586	7.9
Tantalum [79]	185	138	207	16.6
Pure Ti grade-1 [98]	102.7	170	240	4.5
Nitinol (Austenite) [79]	83	195–690	895	6.7
Nitinol (Martensite) [79]	28–41	70–140	895	6.7
Co-Cr (ASTM F90) [79]	210	448–648	951–1220	9.2
Fe [79, 99, 100]	211.4	120–150	180–210	7.87
Mg Alloy (WE43) [79]	44	162	250	184

One of the most important inherent defects of current stents is acute recoil. It refers to the reduction in the diameter of the stent immediately after deflation of the balloon due to the elastic recoil of the stent material. Recoil has been recognized as the primary culprit of stents failure to reach their nominal expanded diameter thereby increasing the risk of restenosis [101, 102]. This phenomenon is relatively common amongst the majority of balloon expandable stents [103].

In contrast, the constant leniency of SE stents to grow in diameter virtually eliminates this effect. Nevertheless, this situation is very different when the stent is deployed inside a vessel where it is under constant compressive vascular forces, consequently resulting in higher recoil in both types of stents. Experimental results revealed less recoil being associated with BE stents in comparison with the SE stents [81]. This result can also be intuitively deducted comparing the elastic modulus of stainless steel 316L as the primary

material for BE stents and the austenite Nitinol that forms the majority of today's SE stents. This superiority in radial strength is one of the primary reasons that BE stents are still the preferred modality for treatment of coronary and renal lesions [81]. Nevertheless, one of the strongest arguments in support of SE stents is their malleability rendering them suitable for more tortuous paths. Moreover, their inherent self-expansion tendency results in a low chronic outward force opposing the plaque and stenotic tissue in long-term [77, 81, 94, 96, 104].

Considering the benefits and shortcomings of BE and SE stents, results from a large randomized study including 1,096 patients with native coronary artery disease comparing effectiveness of the aforementioned two types of stents revealed similar clinical and angiographic outcomes at 9 months. More particularly, in spite of the late luminal gain as a result of the chronic outward force of the SE stents, this force also increased incidence of neointimal hyperplasia likely due to the continued induced stress on the arterial walls [104]. A further difficulty arises from accurate placement of SE stents as they tend to advance from the sheath during expansion, which makes them unsuitable for treating ostial lesions or stenoses adjacent to side branches [80]. A number of rather comprehensive reviews of stent materials and coatings are given in [79, 82, 105]. Table 1.2 presents an overview of the common materials used in current biostable and biodegradable stent fabrication technology outlining the advantages and disadvantages of each for better comparison along with some examples [77, 79].

1.5.2 Material Form

The raw materials from which the stents are manufactured mainly come in tubes, wires and flat sheets. Tubular BE stents are manufactured in a crimped or nearly crimped state when cut, then expanded using the angioplasty balloon. On the other hand, the tubular SE stents are manufactured in the expanded or slightly over-expanded state then crimped and constrained by the catheter to be released in the lesion site [81]. Wire braided, or woven meshes that are mainly used for fabrication of SE stents, are commonly used for non-vascular or peripheral artery disease applications including but not limited to the cobalt alloy-based WallStent (Boston Scientific, Massachusetts, USA), and Nitinol based CraggStent (MinTec, Bahamas) [96], Expander Stent (Medicorp, S. A., Villers les Nancy, France) [106], Symphony and Ultraflex stents (Boston Scientific, Massachusetts,

USA) and ZA biliary stent (Cook Group Inc., Indiana, USA) [96]. Some examples of BE wire stents are the stainless steel-based AVE: Bridge, S7, S660, S670 (Medtronic, Minneapolis, USA), the tantalum-based Strecker (Boston Scientific, Massachusetts, USA) and platinum-iridium based AngioStent (Angio-Dynamics, NY, USA) [107]. Stents from planar sheet metals require an additional rolling step to form the planar shape into the tubular stent structure. The two free ends of the sheet metal may be conjoined through welding or mechanical locking, such as ZR1 (formerly Navius, San Diego, USA) and EndoTex (Endotex Interventional Systems, CA, USA) stents [77, 108].

1.5.3 Fabrication Method

The raw material form greatly influences the fabrication method as well. Stents from tubes are mainly manufacture by laser (Nd:YAG) cutting. Although this method offers low profile kerf widths of less than 20 μm, it produces a heat-affected zone near the cut regions. For better performance of the stent, these edges need to be removed via deburring and passivation techniques. In order to reduce or eliminate the extension of heat-affected zones other cutting methods such as waterjet and (micro electro-discharge machining) μEDM have also been adopted [77, 103, 109, 110]. The early slotted-tube Palmaz stent is one of good examples of use of EDM in stent design.

On the other hand, wire-based stents can be formed through coiling, braiding or knitting. One of the earliest, and most probably, simplest geometries of stents include coil stents. The majority of currently marketed coil stents are made of SE Nitinol [77, 96] with very few experimental BE models [111]. To increase radial and axial stiffness of wire stents, multiple strands of wires may either be knitted or braided, which allows continuous production of long stent tubes. Moreover, adjacent wires can be welded at different spots to create closed-cell wire stents.

To increase batch processing of stents, photochemical etching techniques from very large scale integrated (VLSI) circuit fabrication methodologies have also been utilized. Although available for tubular structures, this method is deemed more beneficial in production of planar sheet based stents. Planar sheet processing techniques such as photochemical etching and 2D μEDM are most suited in mass production of micro structures despite the additional shaping (rolling) step involved [77, 109, 112].

Table 1.2. Common materials used for fabrication of stents. SS 316L refers to stainless steel grade 316L. Pt-Ir refers to the alloy of Platinum-Iridium, Ni-Ti refers to the alloy of Nickel-Titanium and Co-Cr refers to Cobalt-Chromium alloy.

Material	Advantages	Disadvantages	Examples
	Biostable Metallic Stents		

SS 316L and its derivatives	• Excellent corrosion resistance
	• Suitable mechanical properties (Table 1.1)
	  ○ Low recoil due to high elastic modulus
	  ○ High deformity due to low yield strength
	• Can be coated by more biocompatible materials
	  ○ Tantalum
	  ○ Ti-nitride-oxide
		• Ferromagnetic making it non-MRI compliant
		• Low density resulting in low fluoroscopic visibility
		  ○ Can be improved by addition of platinum and chromium to the alloy content
		• Potential allergic and reaction to nickel
		  ○ Can be improved by passivation, coating and alloying techniques
			Majority of BE stents including
			• Biodiv Ysio AS (Biocompatibles Cardiovascular Inc., US)
			• BeStent2 (Medtronic Inc., US)
			• TAXUS Express, and Liberte Monorail (Boston Scientific Crp., USA)

Pt-Ir Alloy	• Excellent radiopacity • High visibility in MRI images • Iridium can be used for fabrication of radioactive stents (radioactive therapy). • Excellent corrosion resistance • Inducing less inflammatory response from body	• Poor mechanical properties (Table 1.1) ○ High recoil • No clinical data is available on biocompatibility and hemocompatibility.	• Gamma Radioactive stent by Bhargava et al [113] • Used to make fluoroscopy markers in Symphony stent (Boston Scinetific, US) [96] • AngioStent (AngioDynamics, US)

Tantalum	• Excellent corrosion resistance due to the highly stable surface oxide layer
	• Excellent fluoroscopic visibility due to high density (Table 1.1)
	• MRI compatible due to non-ferromagnetic properties
	• Good biocompatibility
		• Poor mechanical properties (Table 1.1)
		  ○ Yield strength is very close to tensile strength rendering the structures brittle.
		  ○ Recoil prone due to low deployment pressure requirements
			• Wiktor (Medtronic, US)
			• 1st generation CrossFelx (Cordis, USA)
			• Strecker (Boston Scientific, US)

Titanium	• Excellent biocompatibility due to the highly stable surface oxide layer • Excellent hemocompatibility • Suitable for forming alloys with other metals	• Poor mechanical properties (Table 1.1) ○ Low tensile strength rendering it prone to mechanical failure during expansion	Used mainly as coating for other stents or in forming alloys

Ni-Ti (Nitinol)	• Shape memory effect rendering it suitable for SE stents
	• Plastically deformable at low temperatures (martensite state) see Table 1.1
	• Superelastic properties at high temperatures, up to 11% strain recovery(austenite state) see Table 1.1
	• Corrosion resistant
	• MRI Visible
		• Toxicity of nickel content is debated; to overcome this issue the surface is passivated to increase the Ti oxide concentration at the surface.
		  ○ Plasma-immersion ion implantation
		  ○ Nitric acid treatment
		  ○ Heat treatment
		  ○ Electropolishing
		• Poor fluoroscopic visibility
			Majority of SE stents

Material	Advantages	Disadvantages	Examples
Co-Cr Alloy	• High elastic modulus and radial strength (Table 1.1) ○ Lower profile stents may be made of these alloys • Good radiopacity • MRI compatible	• Requires higher balloon deployment pressures (15 atm) compared with stainless steel (12 atm) thereby increasing chances of vessel wall injury [102, 114], see Table 1.1	• DRIVER stent (Medtronic Inc) • L-605 Multi-Link Vision (Guidant) • SE WallStent (Boston Scientific)
Pt-Cr	• Better fluoroscopic visibility than Co-Cr • High radial strength	• Potential nickel compound toxicity	• PROMUS Element stent (Boston scientific, US)
	Biodegradable Metallic Stents		

Pure Fe	• High radial strength (Table 1.1)
	  ○ High elastic modulus
	• Biodegradation via oxidation into ferrous and ferric ions dissolvable into blood stream.
	  ○ Ferrous ions inhibit neointimal hyperplasia
		• Fracture-prone
		  ○ Close values of yield and tensile strength
			Stents used in experimental studies: [115, 116]

Mg Alloy AE21 and WE43	• Visible to MRI • Corrodes into soluble Mg hydroxide, Mg chloride and hydrogen • Reduces neointimal proliferation	• Poor mechanical and corrosion properties of pure Mg • Even the alloy has poor radial strength (Table 1.1) ○ Thicker stent struts are required • Fracture-prone due to low ductility • Radiolucent (not visible in X-rays) • Premature results calls for more clinical trials	• Lekton Magic Stent (Biotronik, Switzerland)
	Biostable Polymeric Materials		
Polyethylene terephthalate (PET)	• Comparable radial force to SS 316L	• Causes chronic inflammatory response from body ○ Neointimal hyperplasia and complete occlusion • Pool fluoroscopic visibility	Experimental stents in [117-119]

Polyurethane (PU)	• Highly biocompatible
	  ○ Suitable for coating other stents
	  ○ Corrosion resistant
		• Has been associated with intense inflammatory response	Nasolacrimal stents in [120, 121]

	Biodegradable Polymeric Materials		
Poly-l-glycolic acid (PLGA)	• Slow biodegradation rendering it suitable for drug delivery	• Limited luminal application so far ○ Clinical trials for use in coronary arteries are required	Experimental urological stents [122-124]
	Other Biostable Materials		
Carbon nanotubes (CNT)	• Micropatterned pyrolytic carbon • Attractive chemical, electrical and mechanical properties • Highly biocompatible1	• No mechanical or clinical data on the tubular stents	Novel experimental stent by Jones et al. [84]

1.5.4 Design and Geometrical Features

Due to the competing nature of objectives such as axial flexibility, radial strength and minimal luminal profile, the early stent designs were only able to meet some of these criteria while sacrificing the others. For instance, despite the favourable axial conformity of the clamshell design of the first wire stent by Gianturco-Roubin, it exhibited low radial and axial strength and was associated with a rather high rate of tissue prolapse and restenosis (47%) due to its widely spaced struts [41, 80]. To overcome these limitations, in a second attempt this design incorporated a longitudinal spine to enhance both radial and longitudinal strength. Nevertheless, due to the poor clinical results of this structure in a comparative clinical trial, it was decommissioned shortly after [80].

On the other hand, the slotted tube Palmaz stent showed superior radial stiffness and wall coverage (scaffolding). However, its lack of longitudinal flexibility leading to arterial straightening and occasional stent dislodgment *en route* to the lesion rendered it challenging for deployment in tortuous arteries. In an attempt for improving the longitudinal flexibility of this sent, it was split into two segments connected with flexible bridges. Further attempts incorporated decreasing the length of these interconnected segments to reach a balance between radial strength and axial flexibility.

In order to establish an optimal trade-off between the aforementioned competing imperatives, several iterations of design modifications were applied resulting in the multitude of stents in the current market. Stent designs may generally be classified into the following categories, coil, helical spiral, woven, modular closed cell and modular open cell designs that are further elaborated below [77, 80].

I. Coil Stents

Due to the superior longitudinal flexibility and easy retrieval after deployment, coil stents are mainly appointed for non-vascular indications. Conversely, because of their low expansion ratio and the resultant high profile, these stents are not suited for narrow tortuous paths. Owing to this shortcoming, coil stents are mostly made of SE ol, Figure 1.11. Another limiting factor for application of coil stents in vascular lesions is their inferior scaffolding capabilities compared to other designs. This is due to the extensive spacing between the stent struts and potential increased risk of tissue prolapse [80]. In recent years with the promising attributes of miniaturized microelectronics, coil struc-

tures regained some popularity due to their suitable shape for radio-frequency (RF) interrogation capabilities such as sensing [111, 125, 126].

Dogboning, referred to the early expansion of the two ends of the stent prior to the mid-section, is one of the potential complications of BE stents that leads to excessive luminal injury at the distal and proximal ends of the stent, Figure 1.11 (a). This phenomenon can often be observed with other BE stent designs as well [127]. Figure 1.11 (b) shows one of the very first SE coil stents used by Dotter in peripheral arteries [128].

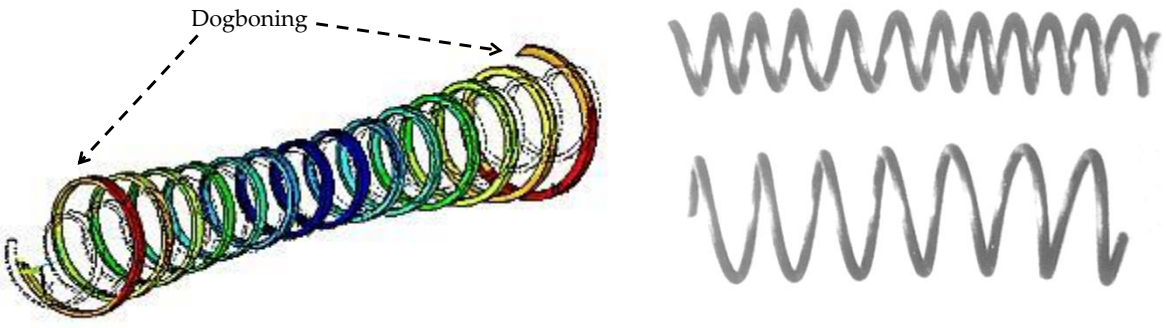

(a) (b)

Figure 1.11. Coil stents. a) Finite element model of a partially expanded coil stent with the early expansion at proximal and distal ends of the stent during expansion (dogboning), image reproduced from [127], b) an early SE Nitinol stent by Dotter et al [128], when crimped before deployment (up) and after expansion (down). Typical luminal diameter of healthy human coronary arteries ranges from 1.5 to 5.5 mm [8, 9].

Their austenite temperature being higher than the body temperature (60˚C), these coils were expanded by injection of heated saline solution through the catheter. In addition to the vascular ducts, Dotter suggested use of these structures in the cerebral aqueduct, bladder neck, biliary system and tracheobronchial tree based on the promising results that he acquired at 4 weeks follow-up [128, 129]. Some commercial examples of coil stents include the SE Nitinol based Horizon Prostatic (Endocare, USA), the peripheral arteries stent IntraCoil (SulzerIntraTheraputics, USA) and the EsophaCoil (InStent, USA).

II. Spiral Stents

Very similar to the structure of coil stents, these stents usually provide minimal connection between subsequent loops thus exhibit high axial flexibility while simultaneously suffering from axial stability. Therefore, these stents are very prone to inadvertent elongation or compression on delivery that results in irregular luminal coverage [77, 80]. To

enhance the longitudinal stiffness, a reasonable first attempt was to establish some connection points between loops leading to loss of flexibility while gaining stability and control over cell size. Figure 1.12 (a) demonstrates a number of early SE spring spirals made of steel that were used by Maass et al [130]. By application of torque to the ends of these spirals, the number of coils increases as the diameters decrease and upon release they spring back to the predefined expanded shape apposing against luminal walls. Due to the limitation of crimping to the extent of yielding strength of these structures, thus the resultant bulky crimped shape, these structures were implanted in larger vessels such as aorta and *vena cava* [130]. Another BE stainless steel helical coil stent with no additional inter-strut connections is demonstrated in Figure 1.12 (b).

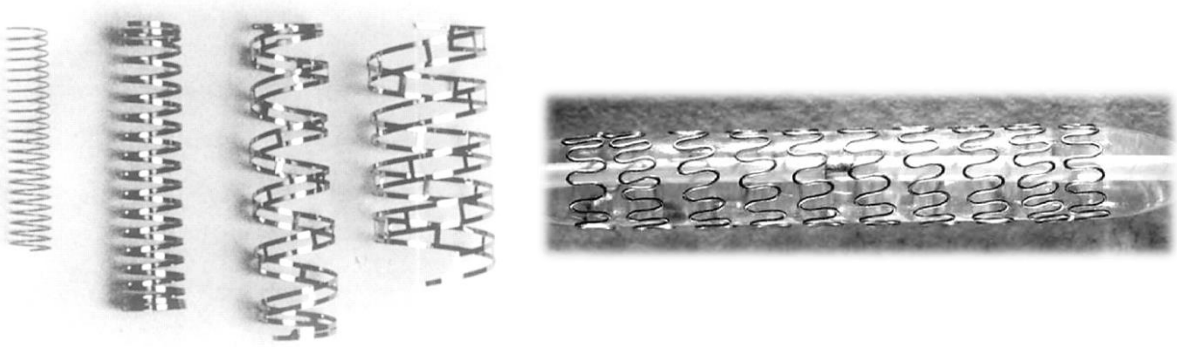

(a) (b)

Figure 1.12. Spiral stents. a) Spiral spring stents used by Maass et. al in canine aortae and *vena cava* [130], b) Crossflex, a helical spiral stent with minimal connections [77].

III. Woven Stents

Produced by inter-shaping of wires these stents may be manufactured using either braiding or knitting. Foreshortening (reduction in longitudinal size) is most prominent in these stents while providing excellent vessel coverage [12]. A removable SE braided stent for treatment of bleeding oesophageal varices is shown Figure 1.13 (a). A knitted BE stent made of tantalum wires is shown in Figure 1.13 (b).

IV. Modular (sequential) Stents

Accounting for the majority of today's commercial stent designs, modular refers to any of the designs that are composed of repeatable geometrical structures. These repeated structures, referred to as Z-rings due to their shape, are most apparent in the slotted tube stents such as the Palmaz stent where they are interconnected at their peak points as demonstrated in Figure 1.14. Depending on the priority of radial strength vs. axial flexi-

bility or vice versa, different sub-designs are born depending on the periodicity and flexibility of the connecting elements between the Z-rings. This design paradigm gave rise to the two general subclasses of closed cell and open cell designs. In closed cell stents, all struts are heavily interconnected to their neighbouring struts whereas in open cell some of these connections are sacrificed to improve axial flexibility.

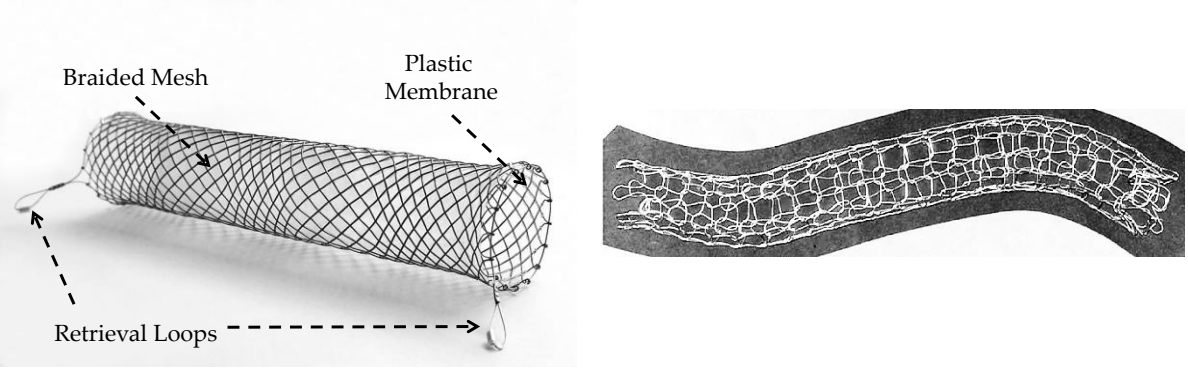

(a) (b)

Figure 1.13. Woven stents. a) SE braided Nitinol stent for deployment in esophagus, SX-ELLA stent. Luminal side of the stent is covered by a plastic membrane. Retrieval loops are used for decommissioning the stent out of the body. Image reproduced from [131] , b) Strecker Stent, a tantalum knitted BE stent. Image reproduced from [77].

In order to enhance flexibility of stents with little sacrifice of the scaffolding properties, hybrid designs with non-homogenous mid-strut to mid-strut bridges that obscure the definitions and differences of open cell and closed cell designs (mote details below) are also proposed, Figure 1.15.

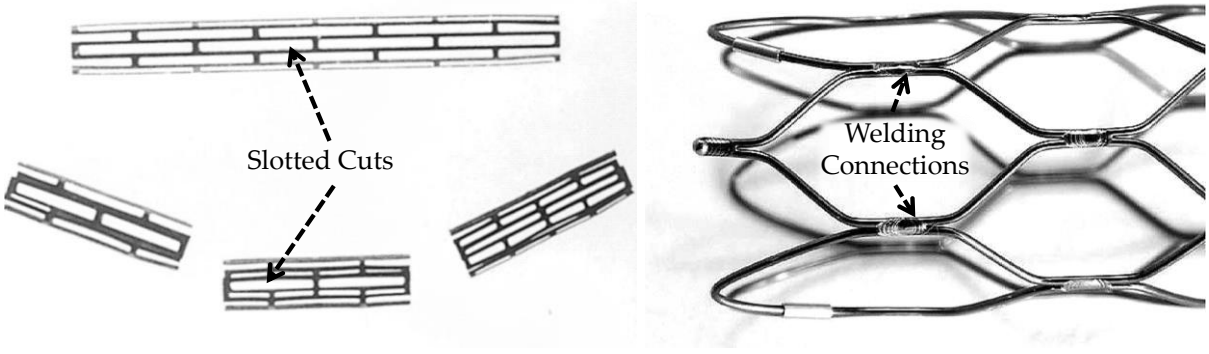

(a) (b)

Figure 1.14. Closed-cell modular stent. a) Early Palmaz stent, one of the first BE stents, made of stainless steel slotted tube [129], b) SE wire welded Symphony stent made of Nitinol [77]. Adjacent cells of both stents are connected at peaks.

Closed-cell modular design: refers to the stents wherein the internal inflection points of adjacent Z-rings are all connected. The early slotted tube Palmaz stent or the welded

Symphony stent, shown in Figure 1.14, are good examples of such structures with robust inter-strut connections. These designs provide strong radial integrity yet lack longitudinal flexibility. To increase conformity of these stents in the axial direction, in later efforts, flexible strut-to-strut bridges were introduced. With a number of different designs, V-, U-, N- or S-shaped as shown in Figure 1.16, these elements can undergo plastic deformation when the stent is expanded or bent axially [77].

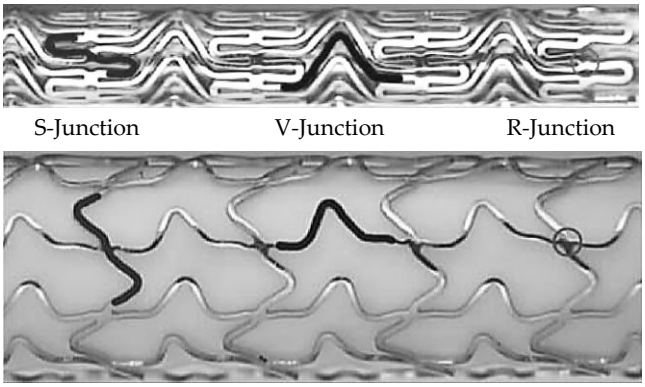

Figure 1.15. Stent with flexible bridges. BeStent2 (MEDTRONIC AVE, Inc., Galway, Ireland) with flexible bridges between the loops, before expansion (top), and after expansion (bottom). R-Junction refers to a rotational junction [80].

Primary advantage of closed-cell stents is their superior vessel wall coverage and radial strength compared to the other geometrical configurations; nevertheless, even the improved flex models lack the axial flexibility of the coil or open cell designs [80]. Moreover, further post-deployment studies observed increased plaque prolapse at the site of longer flex segments due to the compromised scaffolding of fewer struts [76].

Open cell design: demand for flexibility of stents in hard to reach areas such as distal lesions or tortuous paths led to disconnection of some or even all of the connecting bridges between struts creating the so-called *open cell* stents. Buckling due to axial bending is significantly reduced in these stents. Augmented by their crimped-state low profile, these stents are best suited for bending distal paths. Early open cell designs proved to be very flexible, though lack of enough longitudinal reinforcement resulted in poor radial strength [76]. To improve connectivity of adjacent struts, periodic (possibly with different frequencies) peak to peak, valley to valley, peak to valley and mid-strut to mid-strut connections or a combination of all may also be implemented. Figure 1.17 (a) shows the rigid peak to valley connections in a SE stent. The benefit of these connections is more pronounced in reducing foreshortening during expansion leading to better scaffolding

results. Moreover, Figure 1.17 (b) demonstrates an open cell BE stent with flex peak to peak inter-strut connections.

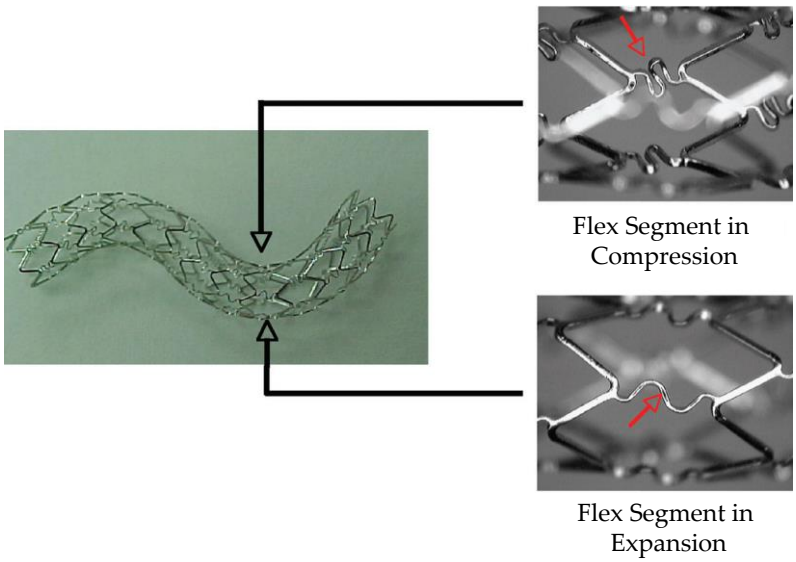

Figure 1.16. Closed-cell stent with flexible bridges. Flexible bridges provide axial compliance to the stent structure. Image reproduced from [76].

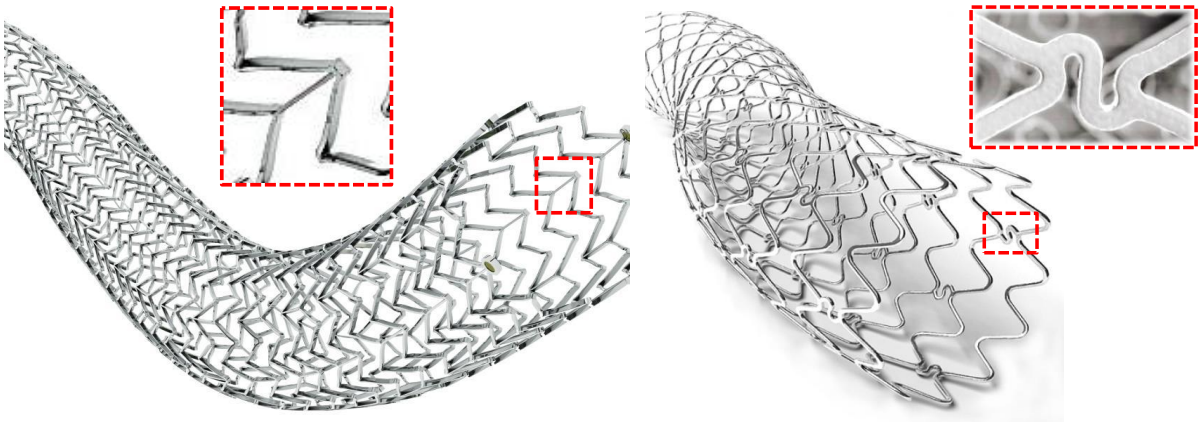

Figure 1.17. Open cell modular stent. a) Open cell SE stent design with peak to valley sequential connections, ZILVER PTX (Cook Group Inc., Indiana, USA), image reproduced from [132], b) open cell BE stent with peak to peak sequential connections, SUN (SINO Medical Sciences Technology, Inc., Tianjin, China), image reproduced from [133].

Despite their intriguing attributes such as flexibility and low deployment profile, performance of open cell stents are often associated with some critical potential challenges including plaque prolapse and fish scaling. Fish scaling refers to the excessive protrusion of the stent struts into the vessel that may induce vascular trauma leading to restenosis, dissections or even perforations. This situation is more common at the sharp angles of tortuous paths where there is often no supporting bridge in the axial length between

subsequent struts [76], Figure 1.18. Plaque prolapse, which is the protrusion of plaque between stent struts into the luminal space, depends on the wall coverage by a stent. As demonstrated by Figure 1.18 (a), this phenomenon is more prominent with open cell designs vs. closed cell. Nevertheless, the clinical and numerical data in the literature is non-uniform, contradictory and inconclusive on the inferiority of open cell vs. closed cell designs in this paradigm that calls for more extensive clinical trials [76, 134-138].

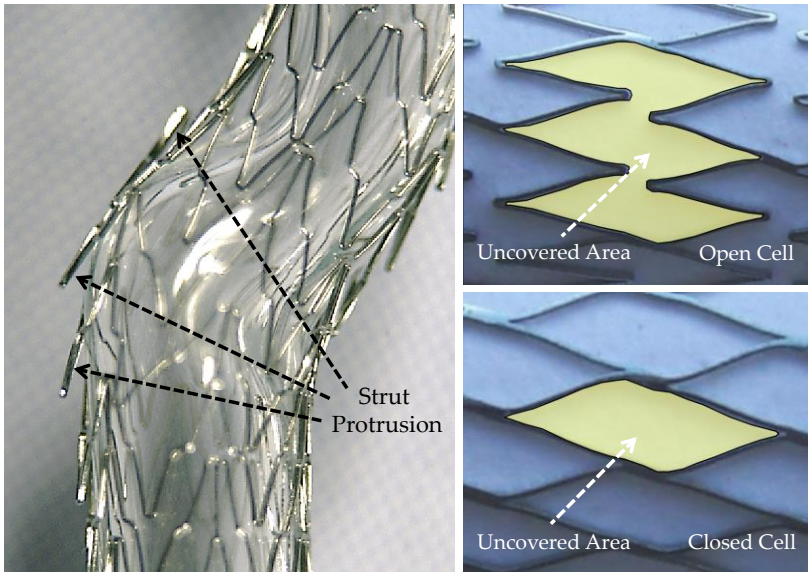

Figure 1.18. Fish scaling and plaque prolapse in open cell stents. a) Fish scaling, protrusion of stent struts into the arterial walls in tortuous lesions due to lack of bridging elements, image reproduced from [76], b) low plaque and vessel wall coverage by open cell stents vs. closed cell theoretically increases chances of plaque prolapse in open cell stents, image reproduced from [139].

1.5.5 Stent Coatings and Surface Treatments

So far fundamental scaffolding aspects of stents are discussed. As mentioned earlier, biocompatibility, accurate deployment during procedure in addition to ease of later diagnostic angiography are also important factors determining overall success of this procedure. Radiopacity referred to as impermeability of a structure to radiation, determines visibility and trackability of a stent during deployment [82]. Strategies such as fabrication of stents from high density alloys or integration with radiopaque markers and/or coatings have been explored so far [79, 82, 105].

Concurrent with the efforts to improve radiopacity and material strength, there has been growing attention devoted to increasing biocompatibility of stents by optimizing their

surface characteristics [82, 105]. As a result, a wide range of surface modifications and coatings are being explored over the years to meet objectives such as reduced surface thrombogenicity, reduced metal ion release and improved texturing to facilitate drug elution and promote endothelialisation [82, 105].

In general implant materials with stable corrosion-resistant oxide surfaces such as titanium oxide or chromium oxide provide better biocompatibility through minimization of metal ion release at the lesion site [82]. Chemical and physical strategies for stent surface modification possibly in conjunction with deposition of new materials on the base platform are among the most common approaches to improve hemo and biocompatibility of stents [105]. Table 1.3 present an overview of common surface treatment strategies to enhance biocompatibility and more recently drug delivery. As mentioned by Mani et al it is impossible to find a single material that possesses all requirements and each material or method hat its own merit [79].

Table 1.3. Common stent surface enhancement strategies.

Surface Treatment	Properties
	Surface Modification Strategies
Radiofrequency plasma treatment	• Alters surface properties of bulk material via [105] o Chemical molecular modification o Grafting other functional materials to the base o Enable drug delivery
Plasma or chemical based etching, sanding, polishing, or microblasting	• Modify surface topography and enhance surface roughness [105] o Reduced metallic ion release o Improved endothelial cell adherence o Enable drug delivery
Thin films deposition	• Using chemical or physical vapour deposition, sputtering etc. [105, 140]. o Strong adherence to stent surface o Improve hemocompatibility o Enhance corrosion resistance o Enable drug delivery
	Biostable Inorganic Coatings
Carbon coatings including Diamond-like Carbon, Pyrolytic Carbon, and Carbon Nanotubes (CNT)	• Used extensively in other biomedical implants [82, 105, 141-143] o Attractive electrical, mechanical and chemical properties o Reduced thrombogenicity o Reduced ion release o Excellent biocompatibility o CNTs are also used to produce stent meshes entirely o Good for loading drugs onto DE stents
Titanium-nitride-oxide	• Titanium oxide is generally very stable and biocompatible • Nitric oxide is important by playing a key role in [82, 144]: o Regulating endothelial function o Helping suppress platelet aggression o Increasing cellular adhesion o Inhibition of smooth muscle cells proliferation

Surface Treatment	Properties
Titanium-boron-nitride (TiBN)	• Mostly used for medical and surgical tools ○ Low thrombogenicity ○ High biocompatibility ○ Better overall performance than CNT coatings [141]
Iridium oxide	• Used extensively for coating of neural stimulating electrodes ○ Excellent barrier against metal ions ○ Exhibits a catalytic effect disrupting smooth muscle cell growth [82]
Nanoporous aluminium oxide	• First porous surface for loading of drugs onto stent surfaces [82] ○ Good vascular compatibility [145] ○ No promising clinical results [146]
Hydroxyapatite ceramic coating	• Widely used in orthopaedic applications ○ Ability to tune porosity for local drug delivery ○ Durable integration with base stent material is still in question [82]
	Polymer based coatings
Biomimetic phosphorlycholine-based	• Mimics the phospholipids on the outer surfaces of red blood cells [82] ○ Reduce thrombogenicity ○ No significant reduction in restenosis rates ○ Suitable for drug delivery
	Polymer based Coatings (Continued)
Parylene **Polyethylene-*co*-vinyl acetate** **Poly-*n*-butyl methacrylate** **SIBS triblock copolymer**	• First and second generation polymers and co-polymers in DE stent [82] ○ Superior drug adhesion and elution ○ Reduced rate of restenosis compound with drug elution ○ Increased risk of late thrombosis
Polylactic acid (PLA) **Polyglycolid acid (PGA)** **PLGA**	• Biodegradable [82] ○ Suitable carriers for drug delivery ○ Reduce thrombogenicity by shorter exposure to blood

1.5.6 Stenting Limitations and Mitigation Efforts

Despite the favoured long-term clinical outcomes of coronary artery bypass grafting [147], with the improvements in technique and equipment, PCI has prevailed as the mainstream revascularization method [1, 34, 38]. Nevertheless, like any other surgical treatment, it is faced with some complications limiting the acute improvements achieved shortly after treatment. The three most important post-stenting complications include acute stent recoil that refers to the loss of luminal diameter due to spring-back of stent, stent thrombosis referring to the formation of blood clots at the lesion site, and in-stent restenosis referring to the renarrowing of the lesion. Attempts to address or mitigate these complications led to a number of improvements in pre-, during and post-stenting design considerations and treatment procedures.

I. Stent Recoil

Both the intrinsic elastic recoil of materials used in production of stents and the compressive forces from the vessels result in some degree of reduction in the gained luminal di-

ameter shortly after stent expansion that is referred to as stent recoil. Highly dependent on the stent design, recoil in coil stents may reach as high as 30% and 16% in modular stents [101]. Natural to any stenting procedure, reduction of this effect is of outmost importance for long-term integrity of the treated lesion. Over-expansion of stents by an over-inflated balloon after deployment has been a historic compensation measure widely adopted by clinicians [80]. Nevertheless, in an atherosclerotic (and very often hardened) lesion, this method results in subsequent problems such as inflicting excessive injury to the vessel walls leading to dissections, negative remodelling and inflammatory response from the vessel [41, 80]. Other recoil mitigation measures include better selection of materials and design methodologies.

I. Stent Thrombosis

Acute in-stent thrombosis is considered as one of the most serious short-term complications of stenting revealing itself between 1–4 days after the procedure with no prior clinical indications. Late stent thrombosis (between 30 days and 2 year) is less common with bare-metal (BM) stents and is more feared with the new line of DE stents, which delay endothelialisation [80, 148, 149], Figure 1.19. Thrombotic events remain as the primary cause of death after percutaneous interventions [148, 150].

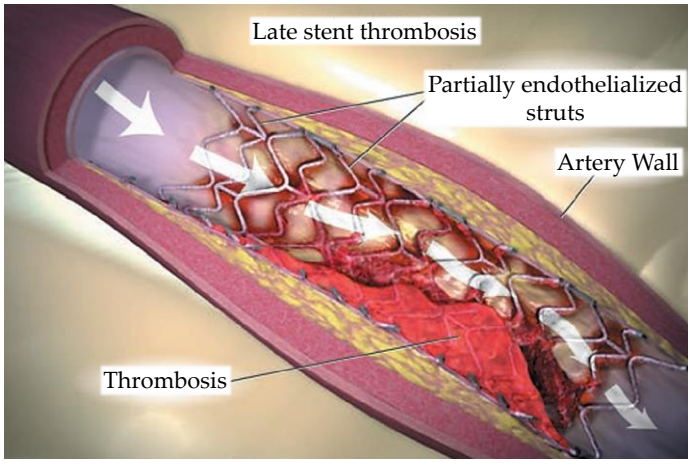

Figure 1.19. Stent thrombosis in a DE stent. Delayed endothelialisation over the sturts of the stent increases risk of platelet and thrombi accumulation leading to thrombosis. Image reproduced from [151].

Common mechanical risk factors of stent thrombosis include stent underexpansion (low luminal gain after procedure), residual dissection, stent malpositioning, significant inflow or outflow stenosis and stent length. Apart from mechanical design improvements

to enhance luminal gain and scaffolding, adjunct chemical and pharma-cological approaches have also been adopted. One of the earliest, yet continuing, modalities is prescription of antiplatelet and anticoagulant agents prior to and after deployment.

Another approach is coating of stents with inert materials to improve surface properties resulting in less platelet adhesion and aggressive coagulation. The primary mission of coatings was to increase biocompatibility and hemocompatibility of stents, yet later they became a platform for local drug delivery to inhibit intimal proliferation [79]. Historically gold is accepted as a biocompatible alloy among clinicians and has been used for a number of biomedical implants. Its use for increasing fluoroscopic visibility of stents has also been endorsed for a long time. Nevertheless, large clinical trials show greater incidence of neointimal hyperplasia in lesions treated with gold coated stents compared with uncoated stents [80, 152, 153]. Some of the other clinically tested coatings to reduce thrombogenicity and restenosis include carbon, silicon carbide and the antithrombotic drug, heparin. Other metallic and polymeric compounds used for coatings are summarized in Table 1.2. An intuitive approach towards mitigation of late thrombosis is utilization of bioabsorbable/biodegradable stents. Such structures theoretically reduce risk of thrombus formation after providing short-term scaffolding to the lesion site then disappearing through corrosion or absorption. Nevertheless due to practical limitations such as simultaneously providing enough scaffolding, having low profile and inducing low inflammatory response from the body, development of these stents experienced a sluggish pace [86, 88, 89].

Early stent deployment results reported thrombosis incidents as high as 24% after 6 months. Nevertheless, improvements such as post-treatment antiplatelet regimens, better stent design, better implantation techniques such as complimentary high-pressure expansions after initial deployment effort and better coatings reduced the rates to as low as 0.5–2% [41, 154]. In case of occurrence and early detection, stent thrombosis can be treated with emergency balloon angioplasty or thrombectomy (removal of thrombi) joined with pharmacological treatments.

II. Restenosis

Restenosis refers to the effect of a complex proliferative healing process of intimal layer after deployment of stents that leads to the renarrowing of a treated lesion [102, 155] as

shown by Figure 1.20. This effect often occurs 1–6 months after stenting with a minority of incidents occurring after 6–12 months [41]. Frequency of restenosis post deployment of BM stents (a stent with no active drug agent as a coating) has been reported between 10% up to values even higher than 60% in [41, 102]. As concluded from the literature, in-stent restenosis (ISR) is related to a combination of factors including the inflammatory response of arterial walls to the foreign object in addition to the sustained injury during and after stent deployment [105, 156, 157] and local hemodynamic changes such as distribution of luminal wall shear stress [158-160]. Apart from the physiological attributes of the lesion, stent design plays an important role in the severity of ISR [93, 161-166]. In addition to the global ISR, localized restenosis might also occur at the proximal and distal edges of the stent most likely owing to the negative vascular re-modelling [167].

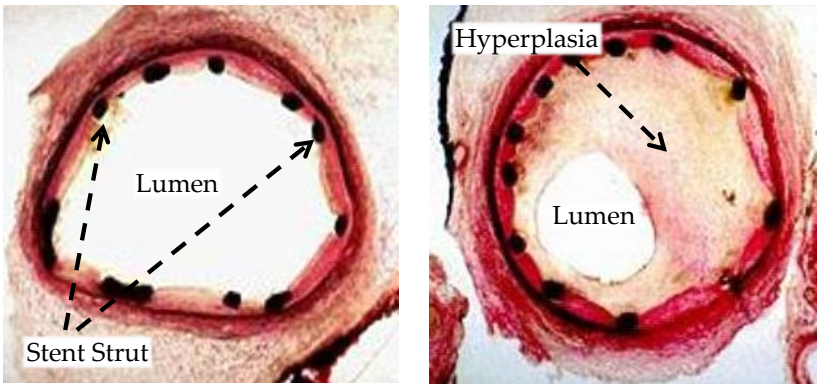

Figure 1.20. In-stent restenosis. a) Coronary artery cross-section after stent deployment, b) cross-section of the coronary artery 6 months after deployment showing significant proliferation of endothelial cells into the lumen. Images reproduced from [168].

With the advent of DE stents that release antiproliferative agents at the target lesion, early clinical results promised a marked drop in the restenosis rate compared with the BM stents from around 50% to 10% [34, 169-172]. The most clinically tested DE stents include the first generation heparin (an anticoagulation agent), Sirolimus (an immunosuppressant) and Paclitaxel (a chemotherapy agent) eluting stents.

Some of the major drawbacks of DE stents include the need for prolonged antiplatelet therapy, and an increasing concern on increased risk for late in-stent thrombosis [105, 169, 173-177]. Late thrombus formation is most likely due to late re-endothelialisation (reformation of the inner layer of the arteries) and endothelial dysfunction after implantation of the DE stents [34, 169, 178, 179]. Despite numerous current attempts to improve

drugs, stent coatings and treatments to lower acute and late thrombosis [105, 180], one should note that utilization of DE stents does not eliminate the inflicted mechanical injury during percutaneous interventions.

In a randomized trial with 2313 patients requiring stenting in large coronary arteries (≥3 mm in diameter), Kaiser et al. [181] compared use of two DE stents, sirolimus-eluting and everolimus-eluting, vs. bare-metal stents. Their results indicated no significant difference between the DE and bare-metal stents with respect to the primary comparison factors including the number of combined deaths from cardiac causes and non-fatal myocardial infarctions in a 2-year follow-up. According to Indermuhle [34], there has not been an optimal and widely accepted treatment for in-stent restenosis yet. This applies for both the BM and DE stents [34]; making clinicians resort to methods such as revascularization of the lesion by a combination of angioplasty and stenting. The most recent approach incorporates application of DE balloons that are coated with antiproliferative substances [34].

1.6 Chapter Summary

Having remained as a significant cause of mortality, CVD annually takes lives of millions of the young and the old. Atherosclerosis as one of the most important precursors to CVD is a complex process that presents itself with a deposition of plaque and fatty streaks between the innermost and the middle layers of vessels gradually constricting or even blocking blood flow. Reduced (or occluded) blood flow to downstream organs has serious consequences mainly stemming from lack of oxygen supply. Apart from the pharmacological interventions and healthy lifestyle mediations, clinicians have tried to alleviate luminal occlusions using surgical methods such as bypass grafting, balloon angioplasty, stenting and atherectomy. Balloon angioplasty tries to re-establish blood flow by inflation of a balloon inside the lesion that consequently pushes the atherosclerotic plaque away from the lumen thereby increasing its diameter on its way.

Despite the acute luminal gain shortly after inflation of the balloon, renarrowing of the lumen is shown to be very prevalent. As a result, stents that are mechanical scaffolds that provide a constant support against the internal walls of vessels came to the rescue. As of today, the number of PCIs has surpassed any other interventional procedures for treat-

ment of occluded vessels including CABG. Proven clinical benefits such as shorter procedure time, faster recovery and long luminal patency after surgery added to the popularity of this method over the more invasive methods such as CABG.

Since the introduction of first generation stents, they have undergone several improvement iterations. Attempts to satisfy the often self-competing stenting objectives such as high radial strength and low elastic recoil in addition to expandability, conformity, high axial flexibility, trackability, biocompatibility and radiopacity all influenced stent design and development giving rise to hundreds of stents on the current market. Apart from their clinical use (deployment region), stents can generally be classified according to their material, initial material form, fabrication method, geometrical design and some final improvement steps such as coatings and capability for in-site drug release. Despite the numerous attempts and the proven stent improvements over the years, stent recoil, stent thrombosis (formation of blood clots) and restenosis remain the most important post intervention complications that limit the outcomes of stenting procedure and its primary objective to maintain a patent treated lesion in long-term.

One of the most important predictors of the aforementioned two complications is the level of trauma induced to the vessel during deployment and the hemodynamic changes to the blood flow after deployment. Elastic recoil of stents after deployment due to the intrinsic properties of alloys often used in stent fabrication in addition to the compressive forces from a vessel, accounts for both acute and chronic luminal loss after deployment. Mitigation measures such as over-expansion in BE stents and use of SE stents, so far have proven to aggravate vascular trauma that leads to thrombosis and restenosis. Pharmacological approaches such as systemic administration of blood-thinners or localized drug release, such as DE stents, try to control these complications by inhibition of an exaggerated inflammatory response from the body. Despite the promising results in reduction of restenosis after deployment of DE stents, increased rate of late thrombosis raised concerns about long-term efficacy of these stents in comparison with BM ones. Moreover, it is important to note that despite these approaches, the mechanical aspect of the problem still stands that calls for a new design paradigm. This statement is further supported by the significant amount of research in the literature emphasizing the role of stent design in the overall performance of stents after deployment.

1.7 Thesis Overview

To meet the often competing imperatives of stents mentioned above, a new design paradigm is called for. To address this shortcoming from a design and engineering perspective, a new recoil resilient luminal support is proposed in this thesis with different aspects of design, deployment procedure and hemodynamic implications as well as alternative actuation methods elaborated in the subsequent chapters. A summary of the thesis structure and contributions made are summarised in the next section.

1.7.1 Thesis Structure and Original Contributions

Key research components and contributions of this thesis are compiled into separate chapters at each significant stage of the research. An overview of the thesis structure is presented in Figure 1.21. Having recognized current stenting design gaps in control and reduction of recoil in Chapter 1 and to address them, a novel luminal support is proposed in Chapter 2. This device, referred to as a recoil resilient ring (RRR), is utilized standalone or potentially integrated with existing stents to address the problem of recoil. The proposed structure aims to minimize the need for high-pressure over-expansion that can induce intra-luminal trauma and excess growth of vascular tissue causing later restenosis. The RRR is an open ring with overlapping ends and asymmetrical sawtooth structures from the two ends that are intermeshed. While radially expanded, these teeth can slide on top of each other, but interlock step-by-step so to keep the final expanded state against compressive forces that normally cause recoil. The RRRs thus deliver balloon expandability and when integrated with a stent, they bring both radial rigidity and longitudinal flexibility to the stent structure.

In Chapter 2, design and development of the RRR is first elaborated by extensive numerical analysis, followed by fabrication and experimental studies. Compliance of the proposed design with current balloon angioplasty expansion mechanics while maintaining structural integrity is studied by finite element modelling (FEM) in an explicit dynamic framework. Superior radial strength of the RRR in withstanding against compressive forces and recovery of its initial shape after retraction of these forces in comparison to a typical BE stent is demonstrated using FEM. The numerical analysis is then extended to evaluate axial strength of RRR, following which improvement measures are proposed and validated.

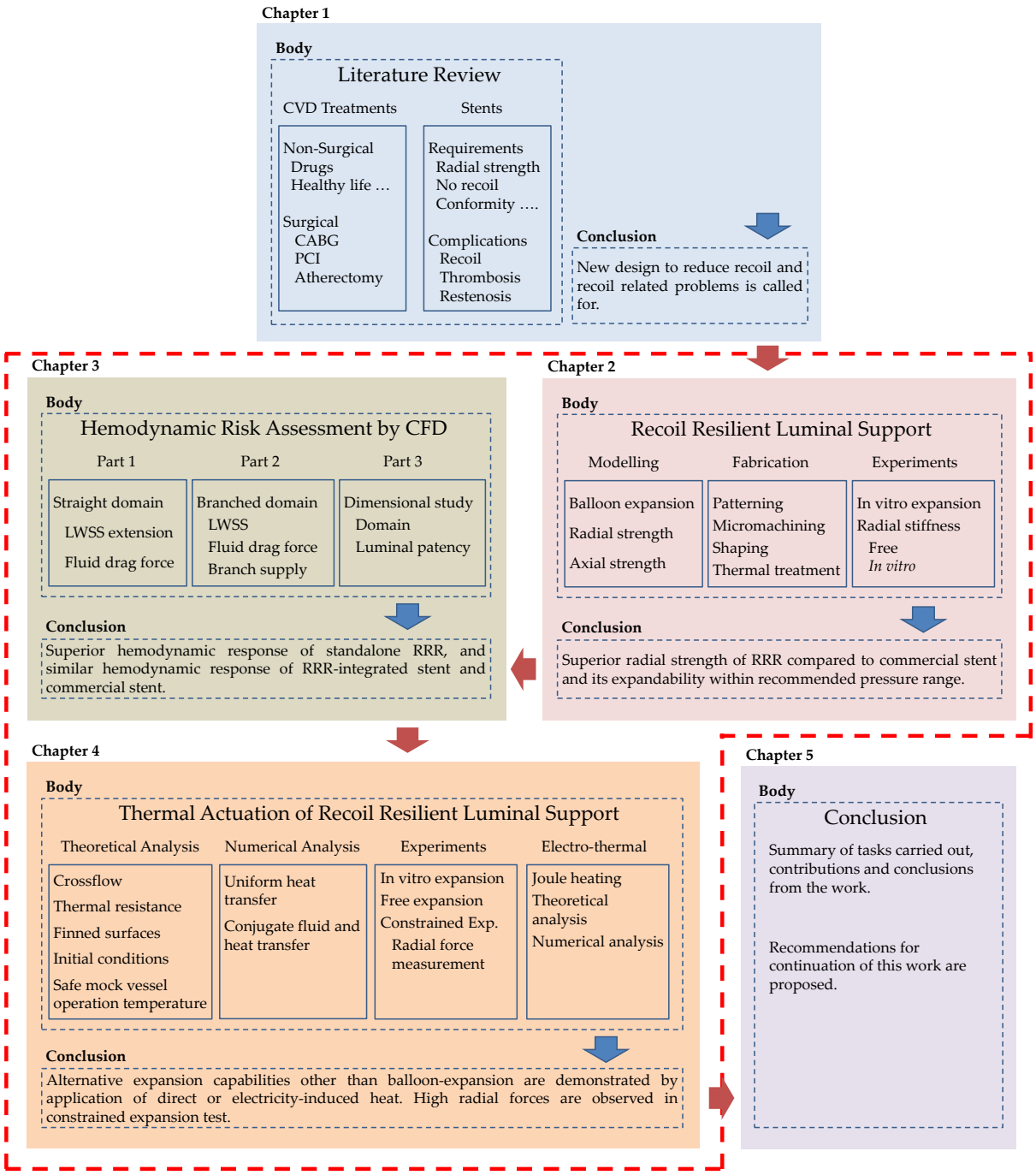

Figure 1.21. Overview of thesis structure. Chapters 2, 3 and 4 outlined by the dashed red line contain original contributions to the design and development of the recoil resilient luminal support.

Utilizing μEDM technology, the RRR is micromachined from a shape memory alloy (SMA) sheet, Nitinol, after which it undergoes shaping and thermal treatment. The novel planar description of the design and subsequent shaping and thermal treatment steps to fabricate the final prototype, enables batch processing and mass production of a number of these devices from planar sheets of material. As the transformation temperature of the

chosen Nitinol is considerably higher, around 80°C, than the typical human body temperature, the RRR normally operates in the martensite state of the material facilitating conformity and easy expansion of the RRR by undergoing large plastic deformations. Moreover, the superior radial strength of the RRR in comparison with a stainless steel commercial stent, made of the considerably stiffer stainless steel 316L, lies in the proposed interlock design numerically validated as outlined above.

These numerical results are complimented by *in vitro* expansion mechanics and radial force measurements carried out in experimental studies, demonstrating expandability of the RRR with balloon pressures well within the recommended *in vivo* range, and its significantly higher radial strength compared to a commercial stainless steel stent.

Apart from the acute mechanical changes and effects such as luminal gain and vessel wall injury, following their deployment, stents introduce changes to the fluid regime. These effects can potentially result in abnormal biological effects such as restenosis. In Chapter 3, rigorous computational fluid dynamic (CFD) models are utilized to study and compare the effect of deployment of three different luminal supports that are subject to a physiological pulsatile fluid flow. These supports include a nominal BE stent, a standalone RRR and an RRR-integrated BE stent. Utilizing a transient analysis framework, spatial and temporal distribution of wall shear stress as the primary indicator of restenosis, fluid drag force and the outlet flow rate of the branching arteries were investigated. The results are compared with corresponding un-scaffolded healthy vessels with uniform internal diameters. The fluidic response of a healthy vessel represents the reference behaviour of a vessel that may be used as a benchmark for hemodynamic comparison of luminal supports after deployment.

Superior hemodynamic performance of the standalone RRR in comparison with the other two is demonstrated by the transient and time-averaged results from these analyses. Moreover, comparable, and in some cases even better, hemodynamic indicators of the RRR-integrated stent compared to the standalone BE stent supports merit of the former as an alternative to the later given the RRR's superior radial strength. In the end, in a dimensional analysis study, sensitivity of the results to dimensional assumptions of the fluid domains such as the main and side branch luminal diameters in addition to different overlap lengths from the two ends of the RRR is studied. Results for this section can

provide other designers a predictive guideline for future hemodynamic analysis of different supports and the effect of deployment domain assumptions on the final results.

The shape memory properties of Nitinol used for fabrication of the RRR, the RRR's thermally trained expanded shape, and its novel incremental interlock expansion mechanism may further be utilized to explore alternative methods of actuation. These methods may include application of direct or electrically-induced heat. Having a transformation temperature, higher than the deployment region (body) temperature, it is possible to transform the normally martensite RRR into austenite and exert high dilating radial forces. In Chapter 4 these possibilities are explored through theoretical, numerical and experimental studies. To study expansion of the RRR in response to heat stimuli in a novel *in vitro* setup, and to ensure exposure of the mock vessel to a safe range of temperature, first a novel theoretical framework based on the theory of thermal resistance and crossflow over cylindrical structures is developed. Based on these models, necessary initial conditions (temperatures) required for thermal actuation of the RRR, and their thermodynamic implications are calculated. Validation of the results from the theoretical analysis framework is carried out by a series of novel heat transfer and multi-field conjugate fluid and heat transfer numerical analyses. Good agreement of the theoretical and numerical results demonstrates the validity of our approach for prediction of initial conditions and their effect on the deployment domain.

Expansion of the RRR in response to heat stimuli is then experimentally studied, in a novel *in vitro* setup complimented by observations from a free expansion study. Moreover, radial forces exerted by a constrained and partially crimped RRR while undergoing martensite to austenite phase transformation in response to heat are experimentally measured and presented. In the end, using the results from the first two parts, a novel alternative actuation mechanism by application of electrical-currents is proposed and examined through theoretical and numerical studies. In the final chapter, a summary of the research carried out in this thesis is provided followed by further suggestions for continuation of this work in the future.

The knowledge and contributions made in the current work, in addition to the design, development, experimental and multi-field numerical results, provide a general engineering framework applicable to future biomedical luminal supports.

Chapter 2

A Recoil Resilient Luminal Support

After the introduction on stents given in Chapter 1, recognizing the pros and cons of each, current design gaps from an engineering perspective are now identified. Elastic recoil and its subsequent complications account for a majority of stent failures thus necessitating careful attention to overcome this issue. Mechanical compensation measures such as stent over-expansion and self-expandable (SE) stents in addition to pharmacological approaches such as use of drug-eluting (DE) stents have not been able to completely eradicate the source of this problem so far.

Moreover, to meet the often competing stent objectives such as high radial strength and flexibility a new design paradigm is called for. As a result, in this chapter, a novel recoil resilient luminal support is introduced. The development steps including design, fabrication, mechanical and numerical evaluations are detailed in this chapter.

2.1 Abstract

In Chapter 1, a comprehensive introduction is given on stents and their current variants to this date. Stents are artificial implants that provide scaffolding to a cavity inside the body. Improvements and drawbacks of each are also presented, in Chapter 1, to elucidate the requirements for current stenting procedure. In the present chapter, after a short introduction, a new luminal device for reducing the mechanical failure of stents due to recoil, which is one of the most important stenting complications, is introduced. This device, referred to as a recoil-resilient ring (RRR), is utilized standalone or potentially integrated with existing stents to address the problem of recoil. The proposed structure aims to minimize the need for high-pressure over-expansion that can potentially induce intraluminal trauma and excess growth of vascular tissue causing later restenosis. The RRR is an open ring with overlapping ends and asymmetrical sawtooth structures from the two ends that are intermeshed. While radially expanded, these teeth can slide on top of each other, but interlock step-by-step so to keep the final expanded state against compressional forces that normally cause recoil. The RRRs thus deliver balloon expandability and high radial strength. Moreover, when integrated with a stent, they bring both radial rigidity and longitudinal flexibility to the stent structure. The design of the RRR in this chapter is first investigated through finite element analysis (FEA), next a prototype device is fabricated using micro electro-discharge machining of 200-μm Nitinol sheets. The standalone RRR is balloon expandable *in vitro* by 5 to 7 atm in pressure, which is well within the recommended *in vivo* pressure ranges for stenting procedures. FEA compression tests indicate a 13× reduction in the loss of luminal cross-sectional area (CSA) of the RRR compared with a typical stainless steel stent under compressive forces. These results also show perfect elastic recovery of the RRR after removal the pressure compared to the remaining plastic deformations of the stainless steel stent. On the other hand, experimental loading tests show that the fabricated RRR exhibits 2.8× greater radial stiffness compared to a two-column section of a commercial stent while exhibiting comparable elastic recovery. Furthermore, testing of *in vitro* expansion in a mock vessel shows around 2.9% recoil, approximately 5–11× smaller than the recoil reported for commercial stents. These experimental results demonstrate the effectiveness of the device design for the targeted luminal support and stenting applications.

2.2 Introduction

After the introduction of interventional cardiology in 1977, this discipline has been primarily driven forward by advances in stents since 1990 [43]. Stents are mechanical implants that provide chronic support against the internal walls of their deployment site [44]. Further to their major use in the coronary artery disease [44], they are also widely used in ducts and lumens from other parts of the body [46-48, 182-184].

There are over 100 different stent designs on the market today, though they can be classified into general groups by their intended deployment area, and manufacturing process. The general manufacturing process can be classified based on the (i) materials used, (ii) the primary form in which the materials come such as tubes, sheets or wires, (iii) the fabrication method including but not limited to laser machining, wire knitting and braiding or micro electrical discharge machining (μEDM), (iv) geometry of the structures including coils, wire meshes and slotted-tubes, and (v) some additional steps to enhance radiopacity and biocompatibility such as surface treatment and coatings [77].

Balloon-expandable (BE) stents are made of plastically deformable materials. After expansion, the stent retains its shape after losing some of its luminal CSA through elastic recoil of its composing materials [77, 101]. Elastic recoil defined by Equation (2.1) refers to the change in the mean CSA of a stent just before deflation of the balloon at its highest pressure and after deflation and retraction of the balloon [185] expressed by:

$$R_{\text{elastic}} = \frac{\text{CSA}_{\text{pre}} - \text{CSA}_{\text{post}}}{\text{CSA}_{\text{pre}}}. \qquad \textbf{(2.1)}$$

In this relation, CSA_{pre} and CSA_{post} refer to the luminal CSA before and after deflation of the balloon at its peak expansion pressure respectively. Consequently, the ideal material and structures for BE stents should have a low yield stress to allow the stent to transform into its required shape, as well as high elastic modulus for minimal recoil and high radial strength [41, 77, 80, 186]. Clearly these two requirements are somewhat contradictory resulting in a challenge in stent design.

Despite the widespread use of high-pressure coronary stents in today's vascular interventions, these implants usually fail to achieve 60% to 80% of the nominal diameter of their expanding balloon [101]. In ideal situations with compliant lumens, with no signs

of atherosclerosis, recoil has been reported to be the predominant mechanism causing failure of stents to achieve their nominal CSA [101]. The magnitude of recoil in stents is highly dependent on the design of the stent and ranges from 30% in coil stents, to 16% in slotted-tube stents [101] increasing the risk of in-stent restenosis (ISR) [102, 187]. As of today, restenosis also known as renarrowing of the treated vessels is the most dominant post-intervention complication that limits the effectiveness of stenting; it has been reported to occur at rates up to 60% [102].

To improve stenting outcomes, several approaches have been adopted since the introduction of bare-metal (BM) stents, including but not limited to drug-eluting (DE) stents [188-192], SE stents [96], and over-expansion techniques [101]; however each tend to lead to different complications.

A meta-analysis concluded that DE stents were associated with a greater mortality rate compared to that of BM stents due to late stent thrombosis [193]. Balloon-expandable (BE) stents are delivered in a crimped state then morphed to a required dilated state. In order to compensate for the elastic recoil, clinicians often resort to over-expansion of the stent. This over-expansion may lead to complications such as early proliferation of endothelial cells around the distal points [194], as those points are the first to open in a typical angioplasty balloon expansion and thus induce more trauma to the arterial walls. Furthermore, clinical studies are indicative of a direct relation between occurrence and severity of restenosis and the degree of vascular trauma during stent deployment that is determined by the anatomic depth to which the stent strut penetrates vascular walls [187, 189]. Induced trauma and the resultant restenosis are also highly influenced by the stent design itself [164].

Relying on the superelasticity of materials such as austenite nickel-titanium alloys (Nitinol), SE stents are mostly delivered in a constrained state to the deployment site then released for expansion [96]. They are fabricated to a diameter slightly larger than that of the target site and upon expansion, they exert a low ‘chronic’ outward force against the luminal walls as the body temperature is beyond their transformation temperature (typically ~30°C) [96, 195]. Although these stents can potentially be custom-manufactured for a wide range of vessels, it is still difficult to tailor them to each individual patient’s diseased vessels specifications that are often subject to different patterns of hardening and

constriction. Furthermore, as mentioned in Chapter 1, the inherent ever-expanding property of these devices may induce a chronic level of trauma, though very low, leading to increasing risk of restenosis [104].

Considering the limitations and requirements outlined above, there are shortcomings to address in order to improve the recoil related complications by targeting the design step of stent manufacturing. A new structure may be introduced to withstand large radial forces from both elastic recoil of the lumen and the stent itself while not sacrificing flexibility. Due to the availability of a vast number of state-of-the-art designs, however, it is even more important to be able to harness the proven benefits of previously devised designs, while addressing their shortcomings with minimal introduction of new manufacturing or stent delivery techniques.

To address these, in this chapter a recoil resilient luminal support (RRR) is introduced as seen in Figure 2.1 (a). The RRRs are micro-fabricated from biocompatible alloy sheets to be used in their martensitic state[1] while inside the body. The design of the RRR is arranged to accommodate integration of an array of the device with a vast range of today's state-of-the-art stents as an add-on to provide radial resilience. Such a design preserves longitudinal flexibility of stents while minimally affecting their production and deployment procedure, Figure 2.1 (b).

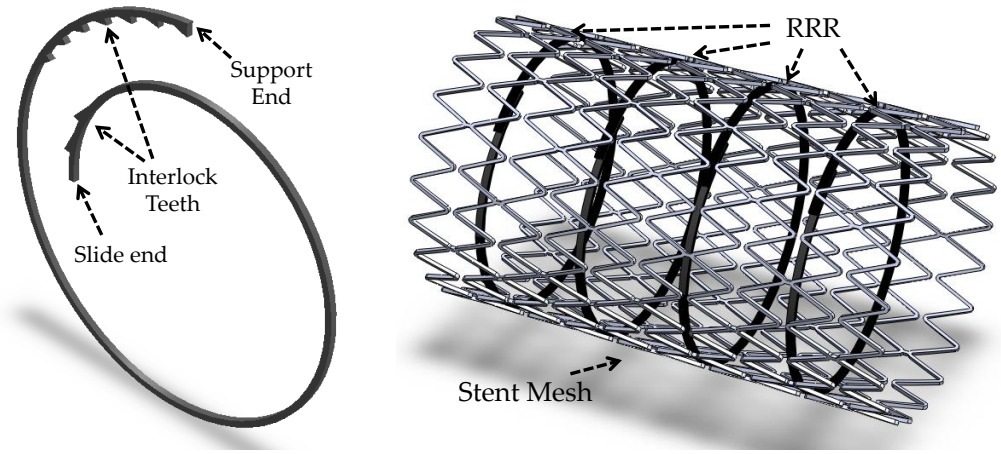

Figure 2.1. Recoil Resilient Ring (RRR) luminal support. a) Conceptual standalone model, b) hosted by a commercial stent, RRRs are connected to the stent mesh by a single welding point. Stent mesh adopted from Open Stent Design [196].

[1] Body and room temperatures lie well below the transformation temperature of Nitinol.

In this study, the RRR devices are fabricated from Nitinol, a nickel-titanium shape-memory alloy (SMA) that is widely adopted in today's medical implants and devices [94, 95] including SE stents [96, 195]. In this work, Nitinol is used in its martensitic state to accommodate low-stress plastic deformations thus expansion by a balloon. Though widely used for SE stents, Nitinol alloy is also used in its martensitic form for construction of BE stents [77]. That is due to its high biocompatibility, corrosion resistance and radiopacity [77, 79]. For a more comprehensive review of materials used in stent fabrication please refer to Chapter 1.

It is important to note that the choice of the material at this stage is not because of its shape memory effect, but rather its *in vivo* benefits and flexibility in the martensitic state. Moreover, this brings potential for other possible expansion methods such as application of heat or electric current as well as remote actuation [197-199]. These possibilities are discussed in more detail in Chapter 4.

Over the years, the demand towards production of non-traditional microstructures using μEDM has increased [112, 200, 201]. This method is used to produce microparts with sizes ranging from a few micro meters to several 100's μm. Being a thermal process, μEDM is used to cut electrically conductive materials utilizing intense heat provided by high-frequency pulses of miniaturized electrical discharge, enabling high precision and burr-free micromachining in any metal or alloy [109, 112]. Moreover, the material biocompatibility of the machined pieces are not impaired by the μEDM thermal treatment [202]. Due to these benefits, μEDM has gained popularity in biocompatible micro-devices such as stents [77, 110, 203]. In this work, we exploited these features of μEDM to fabricate the proposed RRRs.

The rest of this chapter is organized as follows. The design and modelling of RRR is first discussed where topics such as balloon expansion, radial and axial strength of the structure is evaluated. Following this section, the fabrication methodology, including shaping and heat treatment stages are then elaborated. Next, the experimental results of the mechanical evaluation of the fabricated structure in comparison with a commercial stent are given, followed by the chapter summary.

2.3 Design and Modelling

The fabrication approach selected was μEDM of Nitinol sheets of 200 and 300-μm in thickness, to produce a planar strip of the material that is to be shaped into the RRR. The RRR is an open overlapped ring. The two overlapping ends have a number of asymmetrical sawtooth structures facilitating sliding on top of each other in one direction when the RRR is opening. Upon compressive forces the teeth interlock so they keep the final expanded state. The design challenges are to develop a layout describable in a planar fashion to be patterned using Nitinol sheets and a standard μEDM process, and then shape it according to the required description such that it resembles a ring for later crimping and deployment in a vessel. It is also crucial to achieve various key mechanical characteristics including high radial stiffness for recoil resilience and low-pressure expandability. These features eliminate the need for high-pressure balloon expansion or over-expansions that are often employed to compensate for elastic recoil of BE stents. Prior to any fabrication steps, structural FEA studies are conducted to investigate the effect of balloon expansion on the structural integrity of the RRR. The effect of the proposed structure on the hemodynamic risk indicators, such as distribution of low wall shear stress as a predictors of later restenosis [204, 205], after deployment is extensively studied in Chapter 3 utilizing rigorous computational fluid dynamics (CFD) analyses.

2.3.1 Free Expansion Analysis

As mentioned earlier, one of the first objectives of any luminal support is deliverability and deployment capabilities. Deployment calls for expansion of a crimped stent into the luminal site that is commonly performed by an external device such as an angioplasty balloon. To study the mechanics and compliance of the proposed RRR with the current angioplasty methodology, in this section a detailed numerical analysis is presented. In this study a limited radial expansion of the RRR is investigated through structural analysis simulations.

I. Materials and Methods

To simulate the expansion mechanics, the simplified design of the RRR with a short section of an elastic tube representing the angioplasty balloon, as shown in Figure 2.2 is studied in a free expansion model [206] disregarding the vessel wherein the RRR is expanded as a stand-alone luminal support. The simulation is conducted by ANSYS finite

element package (ANSYS Inc., Canonsburg PA, USA) using a three-dimensional (3D) solid mechanics model solved by an explicit solver. For simulations involving large deformations and strains as well as abrupt contact changes, explicit solvers are better suited. In these solvers, basic equations of conservation of mass, momentum and energy are solved for in Lagrange coordinates. Combined with the material model, boundary and initial conditions define a complete framework to acquire the solution to the problem. One of the benefits of Lagrange formulations is the capability of the discretisation mesh to distort and move with material it models where conservation of mass is automatically satisfied. Therefore, density at any place in a given time can be determined from the initial mass of the place and its current volume expressed by:

$$\rho = \frac{m_0}{V(t)} = \frac{\rho_0 V_0}{V(t)} \qquad \textbf{(2.2)}$$

where ρ_0 refers to the initial density of a region, V_0 and $V(t)$ refer to the initial and current volume of the zone at time t respectively. Conservation of momentum can be expressed by the following set of expressions relating acceleration to the stress tensor:

$$\begin{aligned}
\rho\ddot{x} &= b_x + \frac{\partial \sigma_{xx}}{\partial x} + \frac{\partial \sigma_{xy}}{\partial y} + \frac{\partial \sigma_{xz}}{\partial z} \\
\rho\ddot{y} &= b_y + \frac{\partial \sigma_{yx}}{\partial x} + \frac{\partial \sigma_{yy}}{\partial y} + \frac{\partial \sigma_{yz}}{\partial z} \\
\rho\ddot{z} &= b_z + \frac{\partial \sigma_{zx}}{\partial x} + \frac{\partial \sigma_{zy}}{\partial y} + \frac{\partial \sigma_{zz}}{\partial z}
\end{aligned} \qquad \textbf{(2.3)}$$

where ρ refers to the density at any given time determined from Equation (2.2) above, σ_{ij} refers to the components of the stress tensor, $\ddot{x}$, $\ddot{y}$, $\ddot{z}$ refer to the acceleration components in the corresponding x, y and z directions, and b_x, b_y and b_z refer to the x, y and z component of body acceleration at any given time. Moreover, conservation of energy can be expressed by:

$$\dot{e} = \frac{1}{\rho}\left(\sigma_{xx}\dot{\varepsilon}_{xx} + \sigma_{yy}\dot{\varepsilon}_{yy} + \sigma_{zz}\dot{\varepsilon}_{zz} + 2\sigma_{xy}\dot{\varepsilon}_{xy} + 2\sigma_{yz}\dot{\varepsilon}_{yz} + 2\sigma_{zx}\dot{\varepsilon}_{zx}\right) \qquad \textbf{(2.4)}$$

where ε_{ij} refers to the components of the strain tensor. At a given time step, based on the values acquired from the previous time step, equations (2.2), (2.3) and (2.4) are solved simultaneously for each element using a central difference time integration method re-

ferred to as the leapfrog method. Nodal forces that are determined from boundary conditions, internal stress or contact are first computed. Next, acceleration for each node can be derived from:

$$\ddot{x}_i = \frac{F_i}{m} + b_i \qquad \textbf{(2.5)}$$

where the subscript *i*, refers to the three coordinate axes of *x*, *y* and *z*. In this relation *m* is the mass of each node while *F* and *b* refer to the magnitude of force and body acceleration. Having known the acceleration and velocity at earlier time steps, velocity and displacements at later time intervals can be determined using the following estimation expressions:

$$\dot{x}_{i,n+1/2} = \dot{x}_{i,n-1/2} + \ddot{x}_{i,n}\,\Delta t_n \qquad \textbf{(2.6)}$$

$$x_{i,n+1/2} = x_{i,n} + \dot{x}_{i,n+1/2}\,\Delta t_{n+1/2}\,. \qquad \textbf{(2.7)}$$

To develop the model, the ring and balloon assembly are first developed in SolidWorks (SolidWorks Corp, Velizy, France) then imported into ANSYS. In order to decrease the complexity of the model and for improved convergence using the explicit solver, only two teeth of the ring are modelled in this study. The detailed geometrical characteristics of the model assembly are presented in Figure 2.2. The width of the RRR in the Z direction is 200 μm (thickness of Nitinol sheet used for fabrication of RRR) whereas the balloon width is 0.5 mm with a thickness of 50 μm. The balloon is deployed inside the RRR so that it protrudes by 0.15 mm from the two lateral sides of the RRR that are parallel to the X-Y plane.

For the simplified RRR, the material properties of Nitinol in the martensite state were chosen from the Nitinol sheet manufacturer (Memry Corp., Germany) in a bilinear elasto-plastic material model summarized in Table 2.1 in comparison with stainless steel 316L that is commonly used for fabrication of BE stents [207, 208]. This table also presents the geometrical characteristics of the RRR model and a nominal BE stent [196]. The von Mises yield criterion and bilinear isotropic hardening rules are adopted here.

Simulation of a realistic tri-folded angioplasty balloon calls for very high computational power, while also causing convergence problems. This is due to the need for a very refined mesh of the balloon and the introduction of self-contact in the balloon. To avoid these complexities, without sacrificing the accuracy of the RRR deformation results, a

simple elastic tube model is adopted. The presence of this tube is accounted for the time-varying exposure of surfaces of the RRR to pressure during expansion.

Table 2.1. Material and geometrical characteristics of a typical BE stent and RRR.

	Unit	RRR	BE Stent
		Material Properties	
Material	--	Martensite Nitinol	Stainless Steel 316L
Density	g/cc	6.5	8
Modulus of Elasticity	MPa	40	193
Poisson's Ratio	--	0.3	0.3
Yield Stress	MPa	142	290
Tangent Modulus	MPa	714	2500
Tensile Strength	MPa	754	480
		Geometrical Characteristics	
Number of Columns	--	1	2–10
Struts/Column	--	1 – Regular Ring	42 Z-Shaped
Strut Width (W_s)	µm	200	80
Strut Thickness (T_s)	µm	100	110

Material properties of the balloon in a linear isotropic model include density = 0.95 g/cc, modulus of elasticity = 11 MPa, and Poisson's ratio = 0.42.

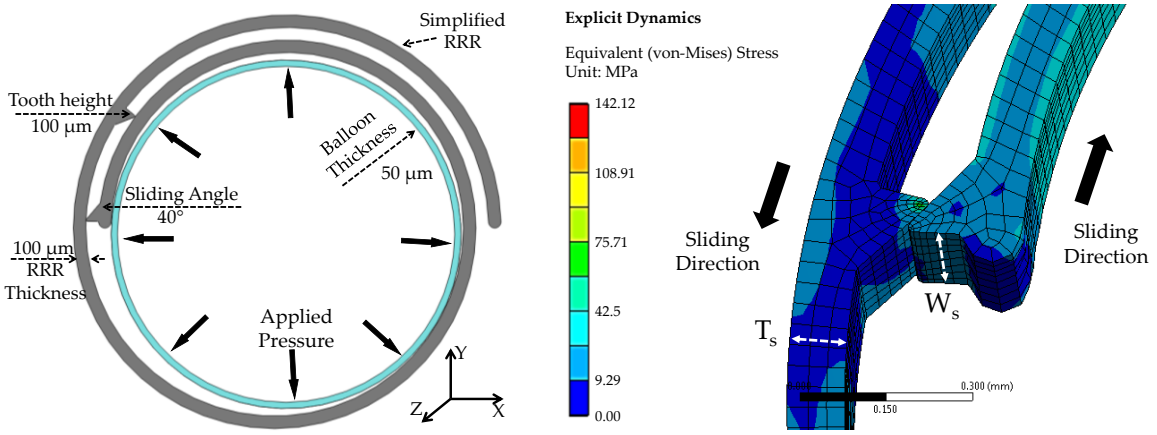

Figure 2.2. Finite element model of the simplified RRR. a) Flexible tube represents the angioplasty balloon. Radial outward pressure is applied to the internal walls of the balloon during expansion. Both the RRR and balloon are fixed in axial direction (Z axis) while free in all other directions, b) expansion of the balloon causes the teeth to slide on each other at about 100 KPa in pressure facilitating expansion of the RRR. Balloon is hidden for better visibility of the RRR.

Frictional forces between surfaces of the simplified RRR and the balloon are neglected for simplicity in the first order calculations. A ramped pressure of 150 KPa is applied to the inner walls of the balloon over 10 ms in a pseudo-static explicit analysis. These pres-

sure levels are well below the typical inflation pressures of angioplasty balloons. The mean inner and outer diameters of the ring before expansion were 2.9 and 3.2 mm respectively and only a limited range of expansion is studied here. Both the balloon and the RRR are free to move radially (in the X-Y direction) while being constricted axially (fixed in the Z direction). This is to restrain the teeth going off-plane with respect to each other. Axial integrity of the ring and methods to improve it are discussed in more detail later in this chapter.

II. Results

Figure 2.3 (a) presents the mean inner diameter of the RRR as a result of the balloon pressure during expansion. Figure 2.2 (b) shows the von Mises stress distribution plots around the teeth during tooth traversal. As indicated by Figure 2.3 (a), tooth traversal starts at around 90 KPa (point A) and finishes at 100 KPa (point B) followed by a smooth increase in the diameter of the RRR over time leading to final mean inner and outer diameters of 3.6 and 3.84 mm respectively. Furthermore, this figure presents the max von Mises stresses developed in the RRR over time during the expansion process. Figure 2.3 (b) shows stress distribution plots over deformed body of the RRR at the end of the expansion process. As demonstrated, the final status of the ring indicates the maximum stress levels well below the tensile strength of Nitinol (Table 2.1).

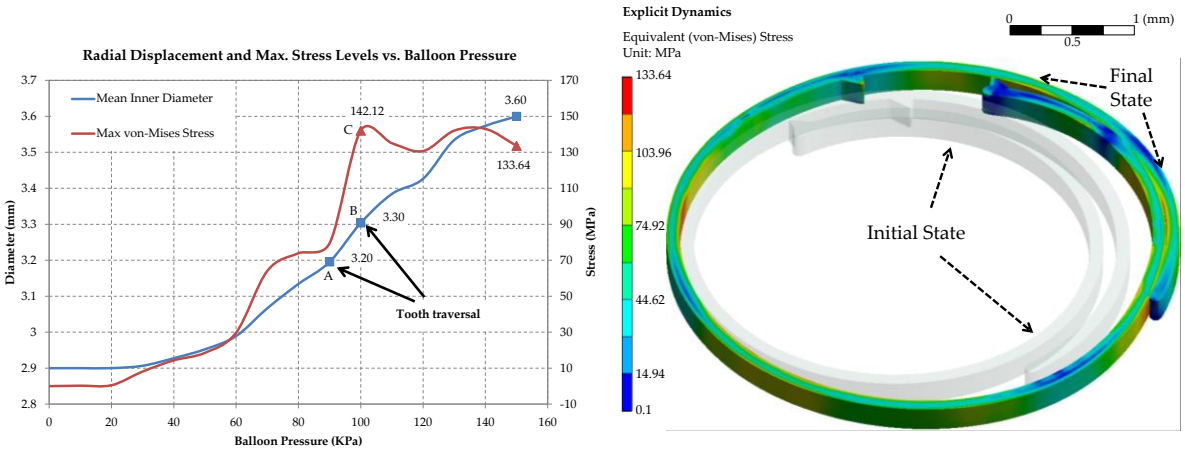

(a) (b)

Figure 2.3. Radial displacement and stress results during expansion. a) Mean inner diameter of the RRR vs. balloon pressure, and maximum von Mises stress vs. pressure during the expansion period. Complete tooth traversal is observed at about 100 KPa pressure, (b) von Mises stress contour plots of the expanded RRR at pressure 150 KPa.

In Figure 2.3 (a), the peak stress marked by point C, followed by a decrease in the stress levels, indicates occurrence of permanent plastic deformations in the RRR structure. To ensure safe interlock operation and ruling out excessive disfigurements of the teeth during expansion, plastic strains of these areas are studied more closely. For this reason histogram of the distribution of equivalent plastic deformation of the elements of the teeth is presented in Figure 2.4 (a).

As shown, about 85% of the elements in the teeth have less than 4% strain rate, despite the higher number of elements at the tip and concentration of elements with higher strain rates at this area as shown in Figure 2.4 (b). Considering the very small average strain rate of 3% for the teeth elements, it is evident that the plastic deformations have minimal effect on the overall structural integrity of the sawtooth structures. This statement is further confirmed by the deformed equivalent plastic strain plots of one of the teeth after completion of tooth traversal shown in Figure 2.4 (b).

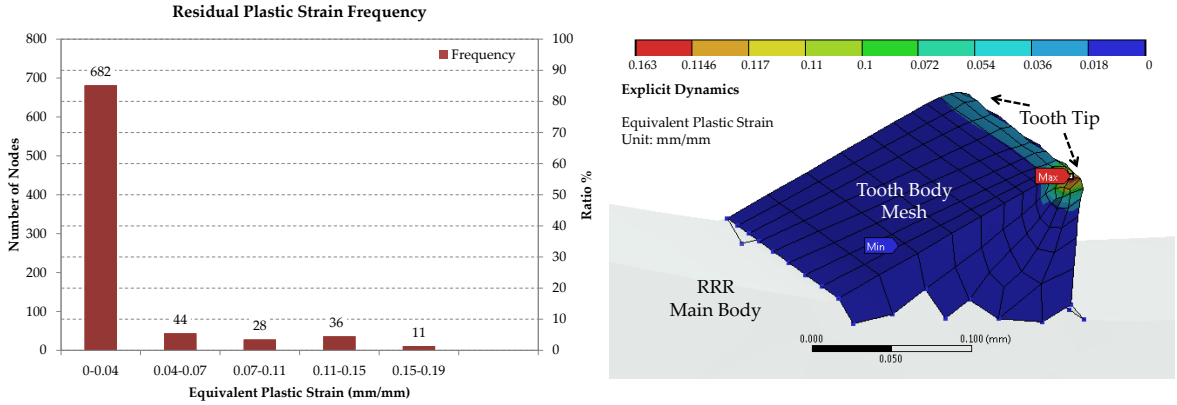

(a) (b)

Figure 2.4. Plastic strain results of the teeth. a) Histogram of the distribution of plastic strain rate in 801 nodes of the elements of the teeth. Majority of elements undergo negligible plastic strain, (b) equivalent plastic strain plot of one of the teeth after completion of tooth traversal. Higher numbers of elements are concentrated at the tip where element size decreases.

2.3.2 Radial Strength

As mentioned earlier in Chapter 1, one of the most important objectives of a stent includes high radial strength (stiffness) after deployment [77]. In this section a comparative analysis on the radial stiffness of the proposed RRR and a two-column typical BE stent (Table 2.1), subject to a circumferential compressive pressure is conducted. The expanded

geometries of both the BE stent (Figure 2.5, b) and the RRR (Figure 2.6, b) with mean inner diameters of 4 mm are first imported into a 3D static structural analysis. In a linear static structural analysis, displacements of the nodes denoted by the vector $\{x\}$ are calculated using the following matrix equation:

$$[K]\{x\} = \{F\} \qquad \textbf{(2.8)}$$

where $[K]$ and $\{F\}$ represent the matrix of stiffness and force vector respectively [209]. Using the principle of superposition, it is possible to solve complex cases applying forces gradually over several substeps. A uniform compressive pressure of 135 KPa is applied to the outer surfaces of the geometries increased linearly over the first solution time step. In the second step, the pressure is linearly decreased to 0 KPa as shown in Figure 2.5 (a). Each one of the solution time steps is solved by a series of 100 substeps.

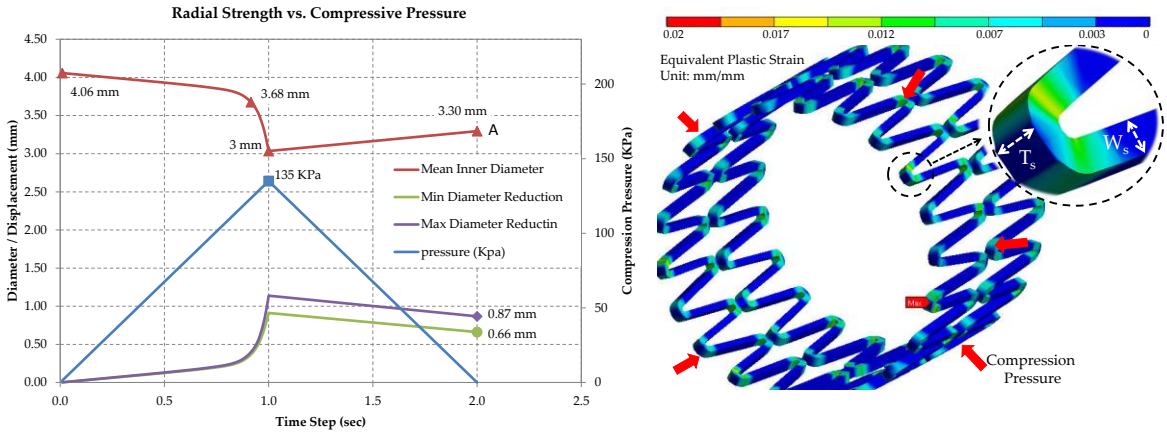

(a) (b)

Figure 2.5. BE stent resilience against compression. a) Change of mean internal diameter, pressure, min and max diameter reduction over time, b) residual plastic strain contour plots post compression (after removal of compression pressure).

As the results in Figure 2.5 (a) show, the mean inner diameter of BE stent reduces linearly down to about 3.7 mm while the pressure is increasing. This trend is followed by a relatively much faster reduction in the diameter despite the linear increase of the pressure, which is an indication of plastic flow. At the pressure of 135 KPa, about 44% of the CSA of the stent is lost due to the compression. By complete removal of the pressure, as noted by point A in (a), the stent still did not recover to its initial expanded state leading to about 34% loss of the initial CSA. Figure 2.5 (b) shows the remaining plastic deformation plots of the stent after removal of the compression pressure at time step 2.

Conversely, as presented in Figure 2.6 (a), subject to the same pressure profile, the RRR exhibits significantly lower levels of radial loss. At pressure 135 KPa, the RRR has lost only 0.07 mm of the initial diameter leading to about 3.4% reduction in CSA that is about 13× less than that of the BE stent. The lost diameter is all recovered after removal of the pressure leading to no loss of CSA. This is also confirmed by the max von Mises stress trend presented over time in Figure 2.6 (a). As indicated by Figure 2.6 (a) and (b), the stress levels over the loading and unloading periods are well below the yielding stress levels of the martensite Nitinol (Table 2.1) ensuring the RRR withholding its structural and radial integrity under compressive loads such as the ones by lumens.

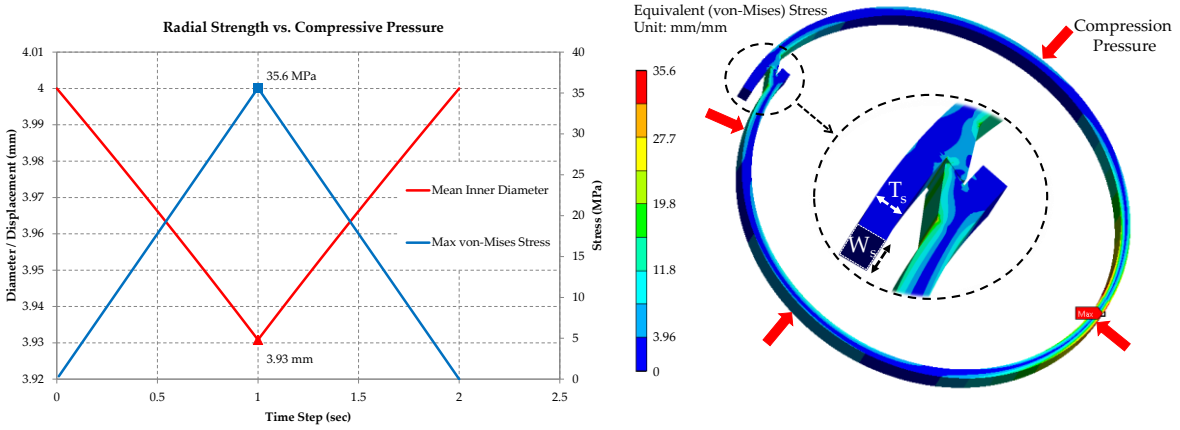

Figure 2.6. RRR resilience against compression. a) Mean inner diameter and max von Mises stress over time, b) residual plastic strain contour plots of the deformed model after removal of the pressure.

The modelling results in this section are limited as the interactions between the simplified models of the RRR and the BE stent, and the surrounding vessels are not modelled. Nevertheless, these results are complimented by the experimental *in vitro* results in the next section by the inclusion of the effect of a silicon-based mock vessel.

2.3.3 Axial Strength and Feasible Improvements

Due to the overlapping open design of the RRR and its limited width (0.2 mm), axial misalignment of the teeth from the two opposite ends is potentially possible and detrimental to its radial integrity. To evaluate strength of the structure against this complication and propose improvement measures, in this section, further numerical studies are conducted. The 3D model of a partially expanded RRR and its boundary conditions are demonstrated in Figure 2.7. The RRR is fixed at the very end of the support end in order

to stabilize the solution in an implicit, static structural analysis. This fixed support may also represent the effect of a single welding point where the RRR is integrated with a stent mesh, Figure 1.1 (b). The RRR in Figure 2.7 is partially expanded up to a mean inner diameter of 3.8 mm leaving 6 steps to a fully expanded state. All other material and dimensional characteristics of this model correspond with the data given in Table 2.1.

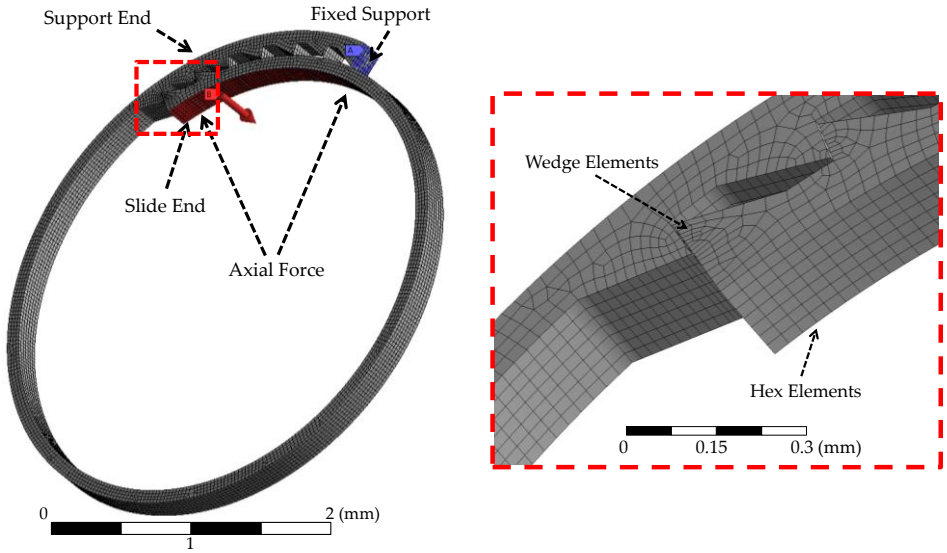

Figure 2.7. Computational model of RRR in axial loading analysis. a) Overview of model, RRR is partially expanded with a mean inner diameter of 3.8 mm. Axial load is applied to a short section of the slide end in the direction of the red arrow. Teeth and strut dimensions are in accordance with Table 2.1, b) close-up view of the interlocking region outlining use of hex and wedge elements in discretising the model.

At the partially expanded state of Figure 2.7 the two teeth from the slide end are interlocked inside the two teeth from the support end providing radial resilience against compressive forces. Nevertheless, upon an axial force, such as the one represented by the red arrow in Figure 2.7 (a), applied to a short section of the slide end, this radial resilience may be compromised. Given the axial displacement of the slide end exceeds the width of the RRR, the intermeshed teeth from opposite ends will completely lose touch that leads to considerably lower radial strength.

To ensure accuracy of the results, a mesh sensitivity analysis is conducted prior to reporting final results. Multiple consecutive mesh refinement levels are defined. Each level increases the number of elements from the previous level by roughly a factor of two where critical results such as axial displacement of the slide end and maximum von Mis-

es stress were closely observed. Given the difference of these key indicators between two successive refinement levels fell below 3%, the last step was chosen to report the results. Final discretised model of the RRR with refined elements across the thickness and width of the ring consists of around 72,000 nodes and 14,000 elements majority of which include hexahedral elements and a limited number of wedge elements used around the angled features of the sawtooth structures, Figure 2.7. Furthermore, for better convergence of the results, axial load is gradually increased to 4-mN in a series of 10 substeps. Results from this study indicate that further refinement of loading steps would yield no benefit in convergence or accuracy of the results. Contact between interlocking teeth is defined as frictionless for simplicity of calculations. Total deformation plots at the last axial loading step (force = 4 mN) is demonstrated in Figure 2.8 where it leads to complete axial misalignment of the interlocked teeth from opposite ends.

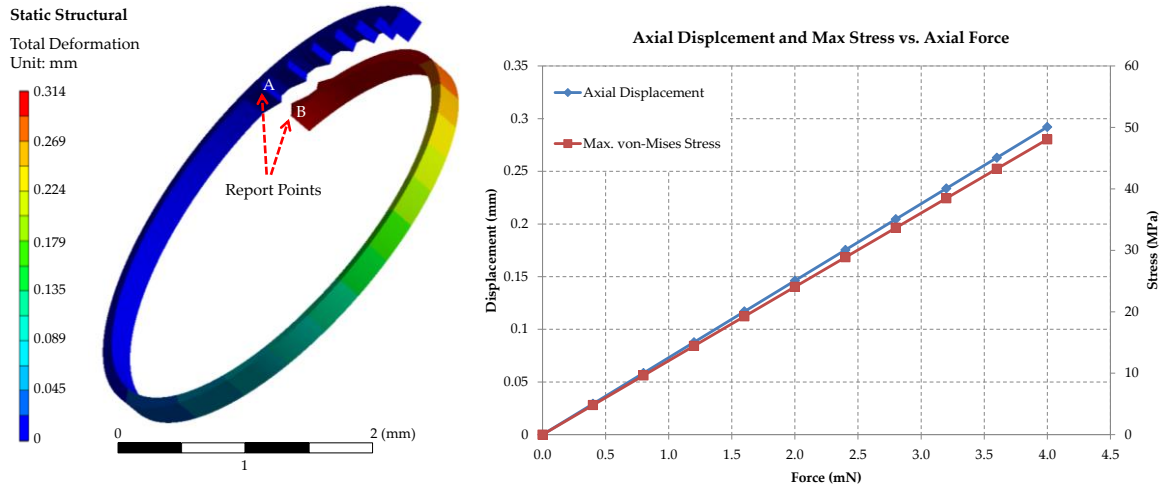

(a) (b)

Figure 2.8. Axial loading results of the RRR without axial support. a) Total deformation contour plots at final loading step, b) relative axial displacement of points A and B and max von Mises stress vs. axial load.

Axial displacement of a report point at the edge of the slide end (denoted by point B in Figure 2.8, a) with respect to a point from opposite end along with the highest values of von Mises stress vs. axial force are presented in Figure 2.8 (b). As confirmed by these results, at axial load of 4 mN, the axial displacement of around 0.3 mm exceeds the RRR's width leading to axial dislodgment of the interlocked teeth. Maximum von Mises stress values are all below the yield and tensile stress levels of Nitinol ensuring structural integrity of the material in all loading steps.

To address this limitation, axial harnesses may be mounted at furthest points of both the slide and the support ends. Being bonded to one end (via spot welds), these harnesses can slide on the lateral faces of the other end providing virtually a straight channel for 2D slide-and-lock movements of the teeth from opposite ends. Figure 2.9 demonstrates these harnesses from the two ends of the RRR when the RRR is flattened.

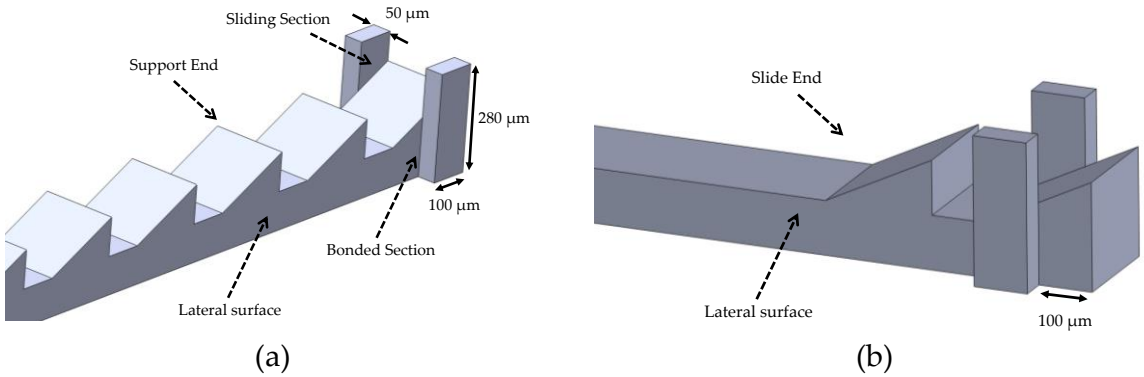

Figure 2.9. Axial harnesses. a) Axial harnesses close to the very end of the support end, and b) the slide end. The height of harnesses is chosen so they will not protrude into the lumen or vascular walls. The 100-μm offset from the right edge of the slide end in part (b) provides a locking mechanism against harnesses of the support end to maintain interlocking at the fully expanded state in the direction of further expansion, Figure 2.10.

This planar description of the RRR is later used in this chapter to conduct machining on a Nitinol sheet for fabrication of RRR. The 100-μm offset distance of the slide end harnesses from the edge limits the expansion range of the RRR to at least one overlapping tooth as demonstrated by Figure 2.10.

Subject to the similar boundary conditions of Figure 2.7 (a), the axial force in this case is increased up to 200 mN. The contact region at the bonded sections is defined by a bonded contact, whereas the contact between overlapping teeth and the harness and lateral surfaces of the RRR and the sliding sections is defined by a frictionless contact for simplicity of calculations. To ensure accuracy of the results, a similar mesh sensitivity analysis as outlined earlier is conducted. This resulted in a discretised model comprised of about 88,000 nodes and 37,000 elements majority of which include tetrahedral elements in the RRR's main body and the more refined hexahedral elements at the axial harness domains as shown in Figure 2.11. The axial force is increased gradually over 10 substeps. Adoption of more substeps did not result in any improvements in accuracy or conversion of the solution.

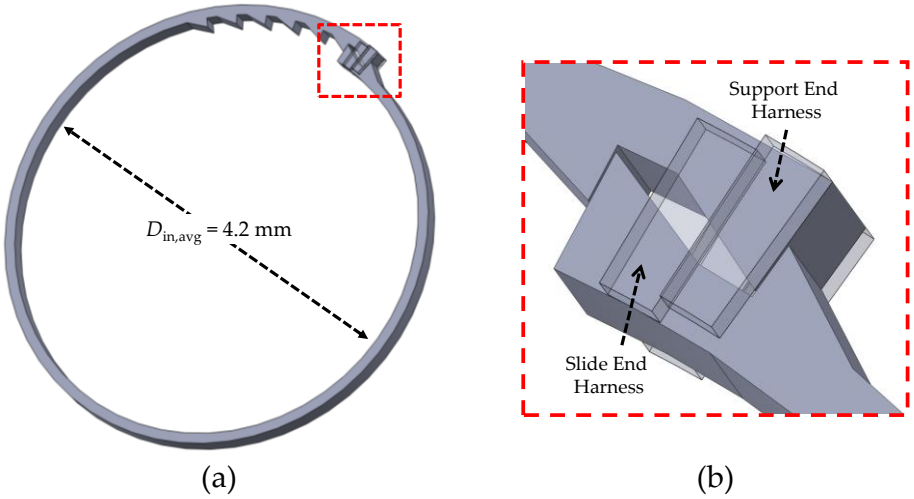

Figure 2.10. Use of axial harnesses in the fully expanded state. a) Overview of RRR at fully expanded state with an average inner diameter of 4.2 mm, b) close-up image at the interlock region, harnesses from opposite ends restrain the ring from over-expansion and loosing contact between teeth. Harnesses are made transparent for better visibility of other features.

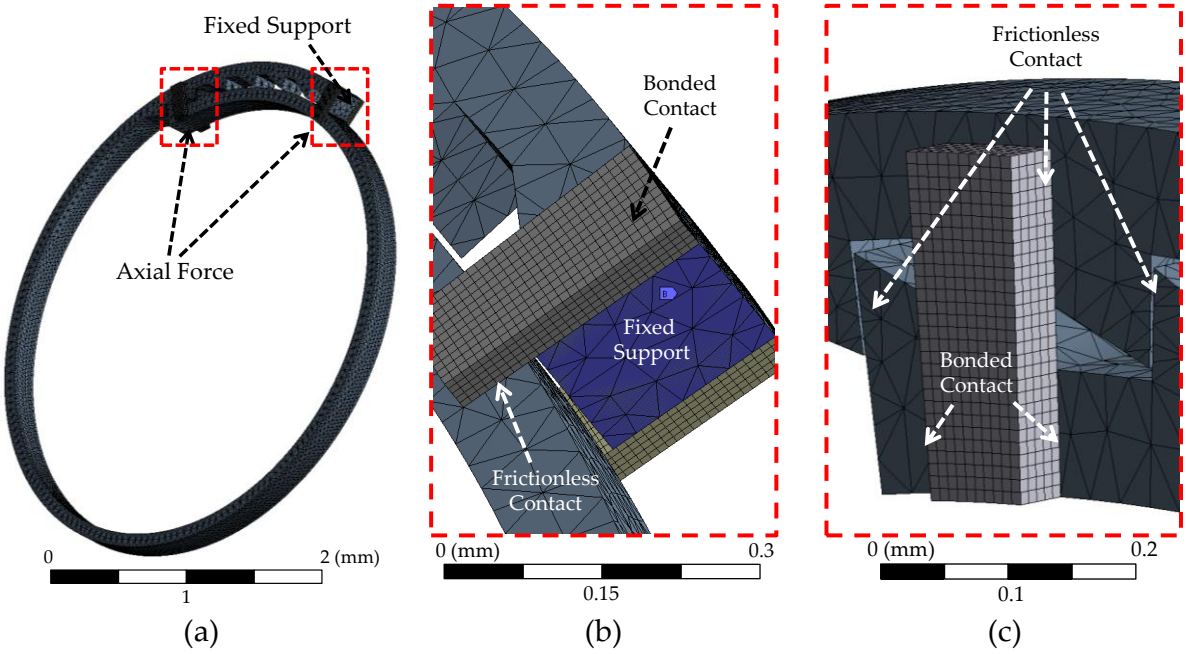

Figure 2.11. Discretised 3D model of RRR with axial harnesses. a) Overview of the model, axial force is applied in the direction of the red arrow as in Figure 2.7, b) close-up view at the support end, c) close-up view at the slide end.

Stress level contour plots at the last loading step of the axial force are demonstrated in Figure 2.12 (a). Furthermore, displacement values of the reporting point A on the slide end with respect to the opposite point B on the support end in different load values along with the maximum stress levels of the structure are presented in Figure 2.12 (b). As indicated by these figures, no significant axial dislodgment of the teeth with respect to

each other is observed. This is despite the significantly (50×) larger axial load being used in these set of analysis compared to the previous.

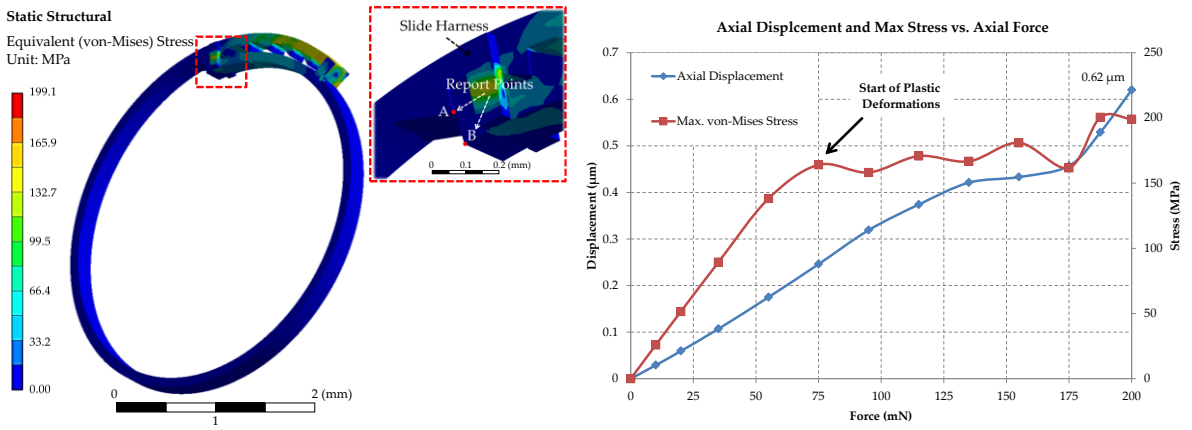

(a) (b)

Figure 2.12. Axial loading results of the RRR with axial harnesses. a) Stress distribution contour plots at axial load = 200 mN, b) relative axial displacement of points A and B, and highest von Mises stress levels over different values of axial force. Immediate decrease in stress levels after axial force of 75 mN indicates occurrence of permanent plastic deformations.

Moreover, highest von Mises stress values in Figure 2.12 (b) lie well below the tensile strength of Nitinol (Table 2.1) indicating microscopic integrity of the RRR and the axial harnesses in entirety in all loading steps.

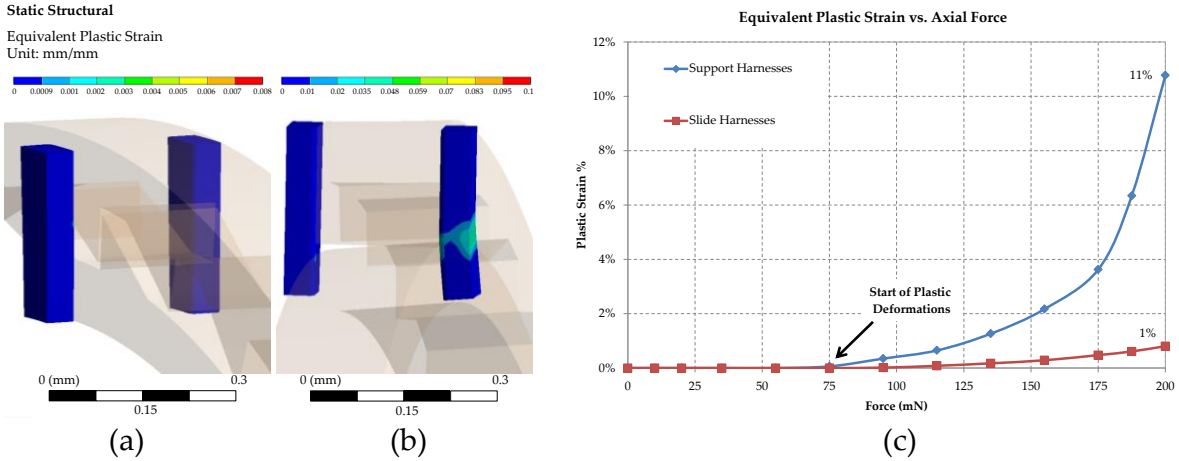

(a) (b) (c)

Figure 2.13. Plastic deformation of axial harnesses. Equivalent plastic strains at the last loading substep in, a) axial harnesses of the slide end with minimal residual plastic strain, and b) axial harnesses of the support end with relatively larger residual plastic strains, c) highest values of equivalent plastic strain over axial loading.

The slight decrease in stress levels immediately after axial force of 75 mN is an indication of plastic deformations that are in agreement with the yield stress levels of Nitinol given

in Table 2.1. This can be further confirmed by the equivalent plastic strain results of the axial harnesses presented in Figure 2.13. In order to limit residual plastic deformations, which are undesirable effects, axial loads are to be maintained below 200 mN to keep the structural integrity of the RRR at all times.

2.4 Fabrication

As discussed earlier, the RRR devices are fabricated from Nitinol sheets with a thickness of 200 μm using a commercial μEDM system (EM203, Smaltec International, IL, USA). Although by the use of a rotational axis available in μEDM, it is possible to realize 3D designs such as the proposed final structure in Figure 2.1 (a), to reduce the likelihood of geometrical errors and follow the policy of minimal technology complexity, we feed a planar structure to the μEDM. The machined piece can later be transformed to the desired final shape with a number of repeatable steps. By decreasing the time of machining, less potential sources of error (X, Y, and Z axis movements vs. X, Y, Z, and angular movements) and less material waste this, process makes mass bulk machining of RRRs realizable using sheet materials.

2.4.1 Machining

The μEDM patterning is conducted in oil with the conventional scanning method using cylindrical tungsten electrodes of approximately 150-μm-thick in diameter. The scanning sequence is programmed to create the planar structure discussed earlier. Figure 2.14 shows the two ends of the 15-mm long planar structure of the device.

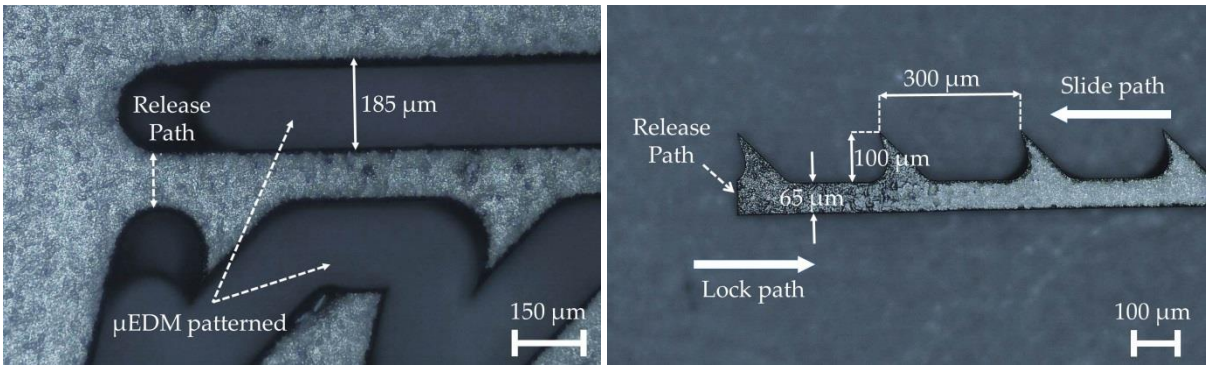

(a) (b)

Figure 2.14. Straight RRR, μEDM patterned from a 200-μm-thick Nitinol sheet. a) Overview of the through-hole structure close to the slide end before release from the primary Nitinol sheet, b) overview of the support end of the RRR strip after release from the sheet.

Four up-right sliding teeth are arranged at the slide end of the strip with the addition of seven other teeth facing down at the support end. Due to the relatively large structure to be patterned, the process used the largest level of discharge energy available with the system. The time required to machine one RRR using machining conditions of voltage level = 100 V, capacitance = 3.3 nF, tool rotation speed = 3000 rpm and feed rate = 10 mm/min is approximately 12 hours. This is quite slow due to the use of single tip electrode, but the planar fabrication allows potential use of batch-mode μEDM [210] in the future to enable volume production of the device so drastically decreasing fabrication time per RRR structure.

2.4.2 Shaping

To shape the planar strip to a ring structure, the setup in Figure 2.15 (a) is prepared and used. It is comprised of a stainless steel base on top of which a 4-mm-thick, 4-cm long stainless steel rod is fixed. The strip is wound around the bottom of the rod where it meets the plane of the base, Figure 2.15 (b). This is to ensure winding within the plane and to eliminate chances of torsional deformation within the structure during thermal training. The ring is fixed to the rod by an adhesive, yet to provide constant mechanical support in high treatment temperatures (around 500°C), a stainless steel cap is used to encompass and lock the ring in its position. The final structure after thermal treatment is demonstrated in Figure 2.16 (a) showing the ring in its fully dilated state with a mean inner diameter of 4 mm.

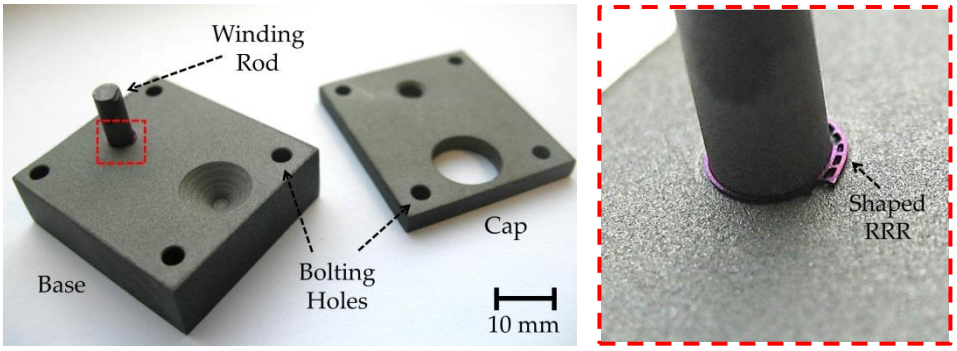

Figure 2.15. RRR shaping and thermal treatment setup. a) Preview of the setup with the base and the cap, b) close-up image around the RRR, the micromachined planar strip is wound around the 4-mm in diameter rod then constrained by a cap bolted to the base.

The teeth A and B from the slide end will be removed from a final design resulting in a design resembling that of Figure 2.1 (a). This is to provide a smooth surface at the cir-

cumference of the RRR, where it contacts the inner walls of the lumen at the expanded state when the RRR is used as a stand-alone support. In this state, all the teeth from the support end will be facing inwards, and the teeth from the slide end are covered by the support end. For the prototype design at this stage, these teeth are included to compensate for the loss of any of the teeth due to possible fabrication defects. Integration of the RRR with a hosting stent may be realized via a single welding point to the stent mesh as demonstrated in Figures 2.1 (b) and 2.16 (b).

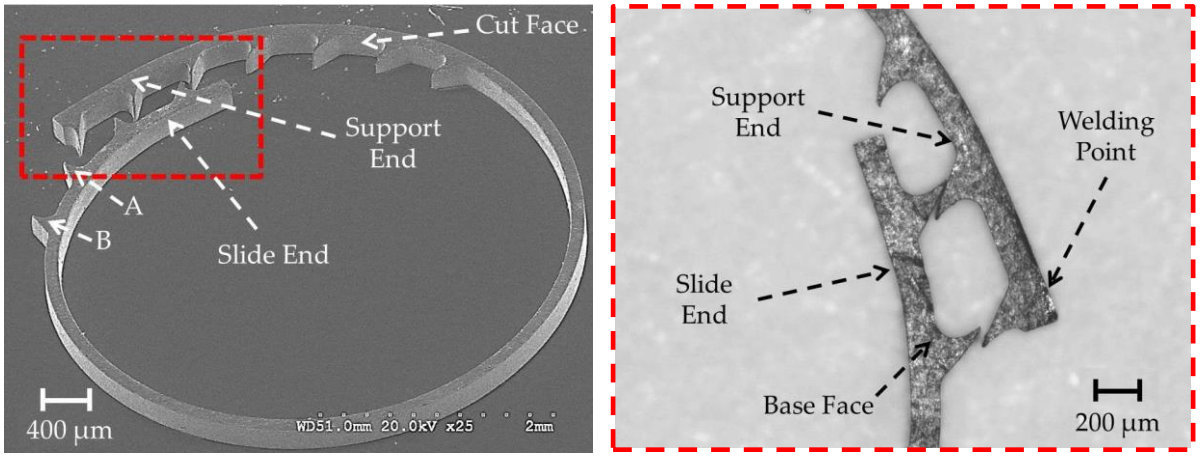

Figure 2.16. RRR after shaping and thermal treatment. a) Full preview, teeth A and B are removed from a final design, b) close-up image around the overlapping ends. Teeth from opposite ends can slide over each other facilitating radial expansion while interlock in the radial compression direction. The RRR can be integrated inside a hosting stent by a single welding point between the stent mesh and the support end. Cut and base surfaces are used for surface profiling as outlined in the next section.

This is to provide enough support to stop migration of the RRR inside the stent while keeping the contact profile between the stent and the lumen intact. Upon exertion of compressive forces on the circumference of the RRR, such as the condition within a vessel, at least two of the teeth, one from the slide end and the other from the support end, interlock and provide a strong scaffold to withstand the forces preventing recoil as described in the previous section. On the other hand, from a crimped state, upon balloon inflation the teeth can slide over each other facilitating radial expansion of the ring.

I. Surface Profile

The surface roughness of the shaped unpolished RRR in Figure 2.16 is measured by an optical profiler (Wyko NT9100, Veeco) and compared with that of an unpolished BE stent

laser cut from stainless steel 316L (Evasc Medical Systems Co., BC, Canada). Surface roughness of the RRR is measured for one cut face, where the machining is performed, and one base (lateral) face that is the surface of the Nitinol sheet used for fabrication (Figure 2.16, b). Measurements for the unpolished stent are performed on a base face. Table 2.2 presents the measurement parameters and the roughness measurements of these surfaces.

Table 2.2. Surface roughness measurement parameters and values.

Measurement Parameters			
Measurement Length (µm)	158		
Measurement Width (µm)	118		
Measurement Mode	Vertical Scanning Interferometry (VSI)		
Surface Measurements			
	RRR		**BE Stent**
	Cut Surface	*Base Surface*	
R_a (nm)	580	560	433
R_q (nm)	734	713	555

Figure 2.17 shows the 3D surface profile of parts of the cut and the base surface areas of the RRR. As indicated by the average roughness measure (Ra), both the cut surface and the base surface exhibit similar roughness. Moreover, these values correspond with those of the unpolished BE stent.

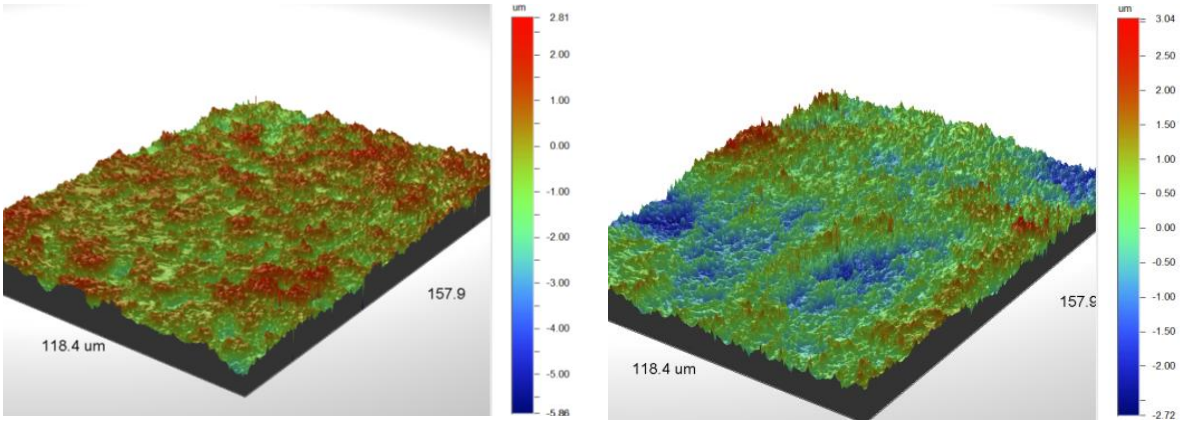

(a) (b)

Figure 2.17. Surface profile of RRR. a) On the cut surface, b) on the base surface.

II. RRR Patency

In order to evaluate the patency of the RRR in an expanded state, a comparison between the cross-sectional impact of the RRR and a typical commercial stent (TAXUS Liberte

coronary stent, Boston Scientific, Boston, USA) is drawn in the following. The average effective diameter of a scaffold $D_{\text{effective}}$ may be expressed by:

$$D_{\text{effective}} = D_{\text{dilated}} - D_{\text{lost}} \quad \textbf{(2.9)}$$

where D_{dilated} refers to the average external diameter of a scaffold (RRR or the commercial stent) in the expanded state, and D_{lost} refers to the average diameter lost as a result of the thickness of the strut (T_s). Given this relation, the patency gain, as a measure of the efficiency of the device to accommodate fluid flow, can be defined by:

$$G_P = \frac{A_C}{A_T} = \left(\frac{D_{\text{effective}}}{D_{\text{dilated}}} \right)^2 \times 100\% \quad \textbf{(2.10)}$$

where A_C is the average CSA patent to fluid flow, and A_T is the mean cross-sectional area of the implanted scaffold. According to our experimental measurements, for which more detail is provided in the next section, the average truss height of the commercial stent loop is 107 μm, which is in correspondence with the average strut thickness of 100 μm available in the literature [207]. This results in a patency gain of G_P = 90.603% for the commercial stent.

For the RRR, given it retains a fully or nearly fully expanded state after deployment, a high estimate on the average strut thickness can be calculated. Accounting for the extra strut thickness from an overlap length and teeth height, this estimate is calculated by:

$$T_{\text{s,avg}} = \left(T_{\text{s,flat}} + \frac{n t_h t_l}{2R_l} \right) \times \left(1 + \frac{O_l}{R_l} \right) \quad \textbf{(2.11)}$$

where $T_{\text{s,flat}}$ = 0.065 mm is the thickness of the fabricated RRR strip where it does not have any teeth (Figure 2.14), n = 9 is the total number of teeth in a final structure, $t_h = 0.1$ mm is the height a tooth, $t_l = 0.1$ mm is the length of a tooth, O_l is the overlapping length of the two ends of the ring (~0.54 mm) and R_l = 15 mm is the total length of the RRR. Substitution into equations (2.11), then (2.9) and (2.10) results in the patency gain G_P = 93.67% that shows a 3.3% improvement over the commercial stent.

2.4.3 Experimental Results

As mentioned in the previous section, two of the most important and competing trade-offs of an effective stent design are firstly high radial resistance against compressive forc-

es, and secondly expandability within rated angioplasty pressures [76, 77]. In this section, the expandability of the fabricated RRR by an angioplasty balloon and its resilience against recoil are experimentally evaluated. For these tests, the RRR is first manually down crimped to a mean outer diameter of 3 mm so that it can be easily inserted into a commercially available silicone-based mock vessel (Dynatek Dalta Scientific Instruments, MO, USA). A mock vessel with an inner diameter of 4 $\pm$0.2 mm and radial compliance of 6–8%, comparable to human arteries, is used for this experiment. Next, the ring is threaded by a deflated balloon (TAXUS Liberte MONORAIL, Boston Scientific, Boston, USA) with a nominal expanded diameter of 4.5 mm. Having this ensemble residing inside the mock vessel, the balloon is gradually inflated by increasing the hydrostatic pressure inside while measuring the outer diameter of the mock vessel at the deployment site of the RRR. These measurements are implemented with a calliper (ABSOLUTE Digimatic, Mitutoyo, USA) taking the average of four measurements at each pressure stage up to 7 atm. Figure 2.18 shows the RRR, balloon, mock vessel assembly at different conditions imaged during this test.

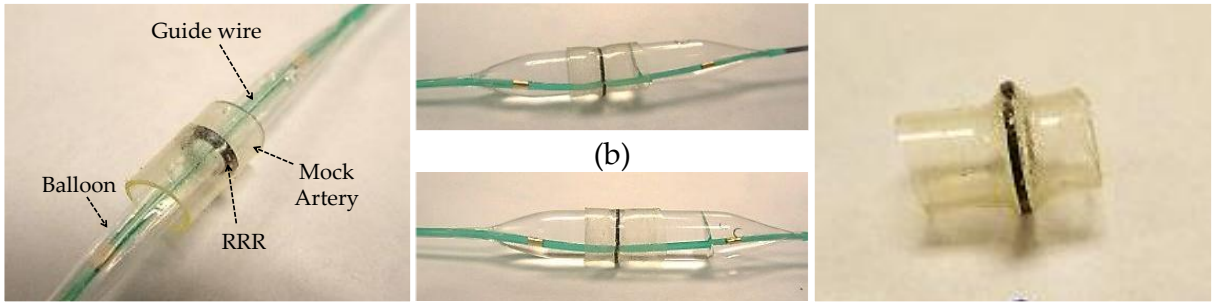

Figure 2.18. Balloon expansion of RRR *in vitro* a) Pre-inflation state, showing the RRR inside the mock vessel threaded by the balloon, b) Balloon filled with deionized water, inflated by raising the pressure to 3 atm resulting in 4.7-mm mean outer diameter, c) Pressure raised to a maximum of 7 atm resulting in 5-mm mean outer diameter, d) Balloon deflated and retracted from the mock vessel resulting in 4.93-mm mean outer diameter.

Average values of the RRR and the mock vessel diameter obtained from measurements just before (5 mm) and after the deflation (4.93 mm) of the balloon indicate less than 3% recoil in the CSA, significantly lower than those of commercial stents reported in the literature reaching as high as 16–30% [101] or 13% [185].

As indicators of performance, radial stiffness and bending compliance of stents are of paramount importance [76]. As per the RRRs, bending compliance is highly dependent

on the hosting stent structure. Over the past decade, a number of methods to evaluate the radial strength of stents have been reported [211, 212]. To assess the radial stiffness of the RRR, a sample with the mean outer diameter of 4.6 mm is tested using the set-up shown in Figure 2.19. The reaction forces of the sample from radial deformations imposed by a force probe are measured using a digital force gauge (DS2-2, Imada Inc., IL, USA) with 1-mN resolution held on a precision vertical linear stage.

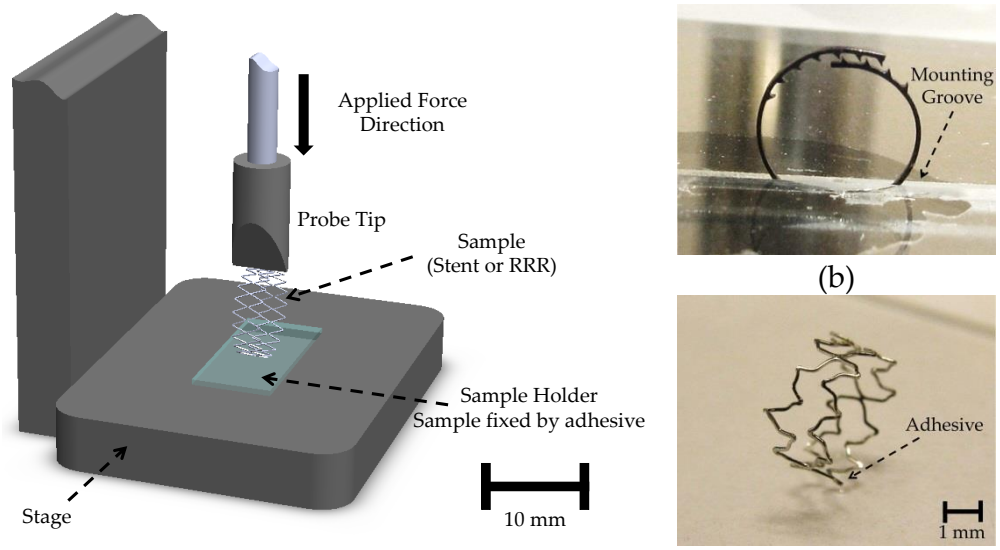

Figure 2.19. Radial loading test setup. a) Vertical positioning of the sample under the force probe, b) RRR mounted in a groove of the sample holder to constrain it from axial tilting, c) two-column sample of the commercial stent mounted on the sample holder by adhesive.

At the first step, the sample is compressed by the probe up to 500 μm in 10-μm displacement substeps while recording the reaction forces. In the next step, the relaxing forces are recorded while reversing the displacement of the probe. For comparison, a short section of a commercial BE stainless steel 316L stent (TAXUS Liberte coronary stent, Boston Scientific, Boston, USA) is also tested using the same set-up and loading procedure. This section contains two loops of the original stent mesh. The reason for comparison between a single RRR and two loops of a commercial stent is to draw a fair comparison between two scaffolds with same effective widths that include a scaffold comprised of two columns of around 100-μm-thick commercial stent and a single loop of 200-μm-thick RRR. Therefore, while minimizing the effect of difference in strut width, other differentiating factors between the two structures including material properties and design, as outlined in Table 2.3, are considered.

The thickness and width values in Table 2.3 include mean value of four measurements conducted under microscope. As both samples in this set-up are not encompassed by any vessel, it is referred to as the free-holding test.

Table 2.3. Properties of RRR and commercial stent samples for compression test.

	RRR	Commercial Stent
Number of Columns	1	2
Avg. External Diameter	4.6	4.57
Max Expansion Pressure (Atm)	7	8
Strut Width (μm)	200	113
Strut Thickness (μm)	65	107
Material	Martensite Nitinol	Stainless Steel 316L, drug Coated
Modulus of Elasticity (GPa)	40	193
Loop Design	Sliding ring with interlocking teeth.	Z-shaped slotted tube, alternating bridges between adjacent loops.

The reaction force vs. displacement measurement results for the RRR and the commercial stent are presented in Figure 2.20. As indicated, the RRR demonstrates significantly higher radial stiffness overall, despite the fact that martensite Nitinol is considerably softer than stainless steel 316L, Table 2.3. At 500 μm displacement, the reaction force from the RRR is ~2.8× greater than that of the commercial stent. Comparing highest slopes of the two trends during exertion of forces, it is also noticeable that the RRR exhibits early rigidity against the compressive forces causing rapid increase of reaction forces vs. displacements compared with the commercial stent trend. Additionally, as observed, the RRR exhibits a comparable elastic recovery to the commercial stent.

An important observation from this experiment is that before the loading cycle, there was a small gap between the two outmost interlocking teeth of the RRR, Figure 2.19 (b). This gap causes the fast development of strain as observed in the beginning of the loading cycle in Figure 2.20 up to radial displacement ~80 μm (point A). Upon the interlock of the two teeth, reaction forces developed from the RRR start to grow rapidly as demonstrated by the graph of Figure 2.20. This gap arises due to the testing condition where the RRR is held free.

To evaluate the device under circumferentially distributed compressive forces, a condition very similar to actual *in vivo* settings that is likely from the contractions and recoil of the vessel and/or a hosting stent mesh, an *in vitro* stiffness test is conducted in this section wherein the is RRR deployed inside a mock vessel (Figure 2.21). Using a balloon in-

flated at 7-atm pressure, the RRR is expanded resulting in an external diameter 4.9 mm including thickness of the mock vessel. Due to the recoil of the mock vessel, the RRR rests in an expanded state with no gap between the interlocked teeth, unlike the case in the free-holding test.

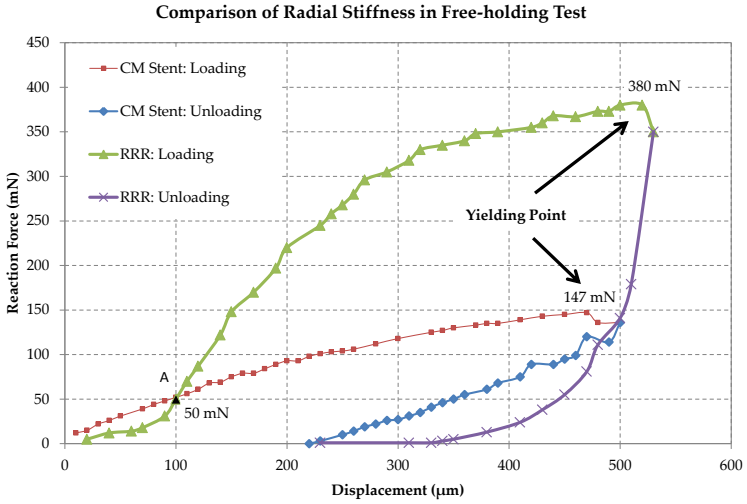

Figure 2.20. Radial loading test results, free-holding. Radial stiffness of the RRR in comparison with a commercial BE stent (CM Stent) made of stainless steel 316L.

This leads to the measurement results presented in Figure 2.21 (c) where reaction forces start to grow rapidly from the beginning of the loading cycle, demonstrating the RRR's full ability to resist external forces and minimize recoil at the expanded state. This can be further confirmed comparing values of reaction forces of the RRR at 100 μm radial displacement in Figures 2.20 and 2.21 (c), denoted by point A. Comparison of reaction forces for similar displacement values from Figures 2.20 and 2.21(c) demonstrates exertion of relatively higher radial forces from the RRR in the *in vitro* case in comparison with the free-holding case. This is likely due to the presence of the additional layer of the vessel around the device increasing the effective stiffness of the assembly. Moreover, upon unloading the RRR exhibits similar elastic recovery observed from the commercial stent[2] in the free-holding test. Considering the easier conformity, higher yielding point against compressive radial forces and comparable elastic recovery of the RRR (comparing Figures 2.20 and 2.21), it clearly outperforms the commercial stent in these aspects despite utilizing the softer martensitic Nitinol compared to the stainless steel in the commercial stent. The above results verify the effectiveness of the developed RRR device as a poten-

[2] TAXUS Liberte coronary stent, Boston Scientific, Boston, USA

tial add-on to the existing stents to improve their recoil resilience while minimally affecting longitudinal flexibility and deployment procedures.

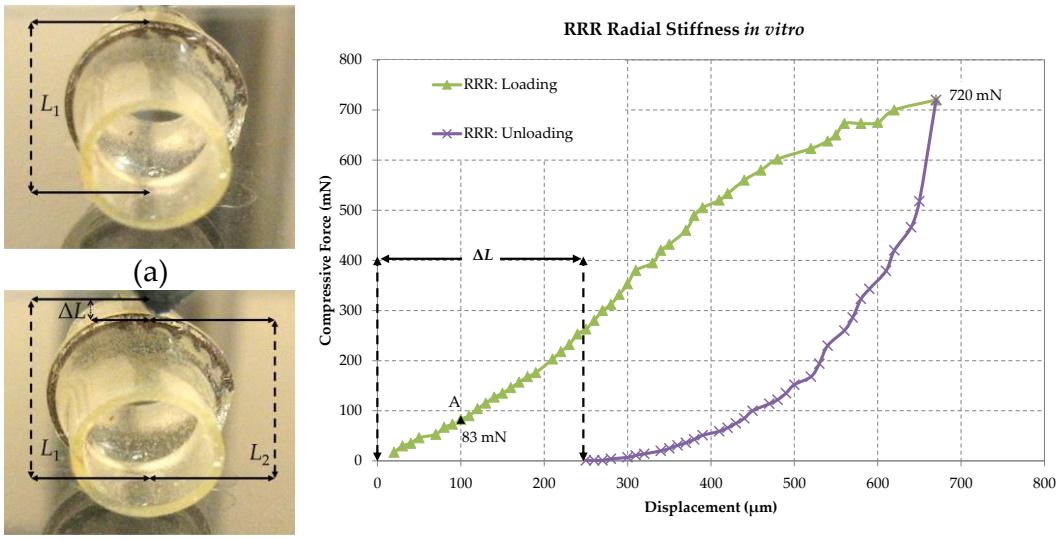

Figure 2.21. Radial loading test results, *in vitro*. Radial stiffness measurement of the RRR deployed in an artificial (mock) vessel, a) overview of the sample under force probe before loading, b) overview of the deformed sample after completion of the load-unload cycle, c) reaction force values vs. probe displacement.

2.5 Chapter Summary

In this chapter, design modelling and fabrication of a viable recoil resilient luminal support for stenting applications was investigated. The proposed structure called recoil resilient ring (RRR) is fabricated by μEDM technology cutting planar shapes from Nitinol sheets of 200 μm in thickness. The simple planar design and subsequent shaping and training methods used, facilitates batch processing and mass production of the structures. To be compatible with today's standard stenting tools and procedures, first-order simple geometries of the RRR were modelled to demonstrate expandability using an angioplasty balloon while maintaining structural integrity. Under circumferential compressive pressures, the FEA results indicated only 3.4% loss of CSA for the RRR that is 13× less than that of a typical balloon expandable stent. After removal of the pressure the balloon expandable stent lost 34% of its CSA due to plastic deformations while the RRR recovered completely.

The fabricated RRR was then subjected to experimental *in vitro* expansion and stiffness tests. The free radial stiffness test measurements indicated 2.8× higher radial rigidity of the RRR compared to that of a two-column stainless steel commercial stent. Considering the lower modulus of elasticity of Nitinol in martensitic state compared to stainless steel, and the comparable thickness and width of the RRR and commercial stent, the higher radial strength of RRR is delivered by the proposed design and interlocking mechanism.

The *in vitro* radial stiffness tests also demonstrated comparable elastic recovery of the RRR to the commercial stent. The proposed RRR is balloon expandable *in vitro* by 5–7 atm pressure, well in the range of recommended *in vivo* pressures. The change in mean CSA after balloon deflation, showed to be < 3% for the RRR compared to the reported mean value of 13–30% associated with commercial stents.

Given RRR's attractive specifications such as low deployment footprint (low width and thickness) and its high radial strength, a series of RRRs can potentially integrated inside a stent mesh through single connection points, providing further scaffolding to specific areas and to the stent as a whole, while not sacrificing expandability or longitudinal flexibility. Considering these benefits compared to the added local thickness inside a stent due to the RRR's profile, the proposed structures bring a good trade-off between flexibility, deliverability, and resilience.

Investigation of the detailed study of the hemodynamic changes of the deployment area after deployment of the proposed structure in comparison with a commercial stent and their effect on increasing neointimal hyperplasia, are the next important subjects. These subjects are discussed extensively in Chapter 3 utilizing computational fluid dynamics (CFD). Furthermore, use of SMA in the martensitic temperature range opens a path to other actuation and expansion methods such as application of heat or electric current as an extension of this work that are discussed in Chapter 4 of the thesis.

Chapter 3

Hemodynamic Risk Assessment by Computational Fluid Dynamics

Acute luminal gain after percutaneous intervention comes with the price of risk of later restenosis. Hemodynamic changes due to the presence of a stent play a key role in occurrence of restenosis. In particular low wall shear stress levels at the treated lesion site have been associated with increased risk of neointimal hyperplasia. In this chapter, the proposed recoil resilient ring (RRR) of Chapter 2 is extensively studied utilizing capabilities of computational fluid dynamics (CFD). Comparisons are then made between the proposed structure and a commercial stent to provide further insight into the hemodynamic performance indicators of the RRR. Moreover, dimensional analysis studies are conducted to demonstrate the efficacy of an RRR-integrated stent to deliver a hemodynamic response comparable to current stent technology. These results provide an insight into the effect of dimensional changes of fluid domains on the hemodynamic response of luminal scaffolds.

3.1 Abstract

Stents that are one of the most prevalent biomedical implants that provide permanent scaffolding as a treatment to constricted lumens. Lumen refers to the cavity inside a vessel that is normally filled with flowing blood. In Chapter 2, a novel recoil resilient ring (RRR) to reduce stent recoil and its subsequent side effects is introduced. The RRR is an overlapped open ring with asymmetrical interlocking sawtooth structures. Teeth from opposite ends of the ring can slide against each other during expansion while interlock step by step to keep the expanded structure upon compression. In Chapter 2, high radial strength of the RRR is demonstrated via numerical and experimental studies outlining its potential to reduce recoil. Particularly, RRR's superior radial resilience is demonstrated in comparison with a commercial stent.

Apart from the acute changes and effects such as luminal gain and vascular wall injury, following their deployment, stents introduce changes to the fluid regime. These effects can potentially result in abnormal biological effects leading to restenosis as outlined in Chapter 1. In this chapter, 3D CFD models are utilized to study and compare the effect of deployment of three different luminal supports that are subject to a physiological pulsatile fluid flow. These supports include a nominal balloon-expandable (BE) stent, a standalone RRR and an RRR-integrated BE stent. The supports are first studied in two fluid domains including a straight domain with no side branches and a branched domain consisting of a proximal and a distal branch. The results are then compared with corresponding fluid domains of unscaffolded healthy arteries with uniform inner diameters through the deployment area. The fluidic response of the healthy vessel represents the reference behaviour of a vessel that may be used as a general benchmark for assessment of new luminal supports.

Utilizing a transient analysis framework, hemodynamic indicators including spatial and temporal distribution of wall shear stress, fluid drag force and flow supply of the branching arteries are investigated. In all these indicators, oscillatory behaviours are observed. Compared with the other two supports, the standalone RRR demonstrated a super hemodynamic response with the least extension of region subject to low wall shear stress (LWSS) (< 0.5 Pa) and the least deviation of the outlet flow rates from a healthy fluid domain. Although, marginal differences between the transient LWSS distribution results of

the RRR-integrated stent and the standalone stent are observed in a straight vessel, the temporal average values show minimal difference in the deployment area (< 3%) and the entire fluid domain (< 1%). In a branched fluid domain these transient differences become minimal. Fluid drag force results show efficacy of the withholding forces by at least 14 times greater than drag forces to cease migration or displacement of any of the supports. Dimensional analysis results in the branched fluid domains demonstrated even slight improvement of the LWSS in the deployment area of the RRR-integrated stent in smaller-diameter lumens and with longer overlap lengths from the two end of the RRR (higher strut thickens to luminal diameter ratios) compared to similar standalone stent deployment cases by 1%. Branching and main outlet flow results of the RRR-integrated and the standalone stents show close correspondence with a cumulative difference of 2%. These results demonstrate the merit of the standalone RRR and RRR-integrated stent as viable luminal implants with minimal potential fluidic penalties compared to the current state-of-the-art stenting devices.

3.2 Introduction

Since the introduction of coronary stenting in 1990, it has received significant praise and attention from both the medical and engineering communities [43]. Providing a chronic support against luminal constrictions, stents, which mostly resemble tubular meshes, have found their way in numerous ducts and lumens through the body [46-48] and more specifically in coronary arteries [213]. Despite their widespread use, these implants often fail to achieve 80–60% of the cross sectional area (CSA) of their expanding balloon [101]. This phenomenon, referred to as stent recoil, is one of the leading risk factors of in-stent restenosis [102, 187].

To address stent recoil, a recoil resilient luminal support is introduced in Chapter 2. The new scaffold called the recoil resilient ring (RRR) [103] is an overlapping open ring with asymmetric sawtooth structures that facilitate expansion in one direction and interlock upon compression. This device may be utilized either as a standalone support or integrated with the current state-of-the-art stents to provide further resilience against recoil while not sacrificing the stent's longitudinal flexibility. The merit of the proposed RRR for decreasing recoil, henceforth recoil related complications, has been demonstrated in

Chapter 2 and [103] through extensive numerical modeling and experimental evaluations.

Optimum scaffolding and minimal stent profile, thus minimal alterations of hemodynamics after deployment, are competing objectives that present a significant challenge in stent design. Physiological recurrence and progression of atherosclerotic plaques in the stented lesions is a complicated phenomenon yet to be understood properly [158, 214]. Despite these facts, a number of studies have demonstrated the effect of geometrical properties of stents as a critical indicator in occurrence and development of restenosis [162, 165, 215, 216].

Factors such as distribution of low wall shear stress (LWSS) after deployment of stents appear to present viable initiation causes for the development of atherombose and atherosclerotic formations [158, 217, 218]. Stent struts that protrude against the flow of blood into the lumen may introduce vortices and stagnation zones that directly influence the spatial and temporal distribution of wall shear stress. As reported by the significant amount of research in the literature [158, 161, 214, 219-222] these changes are highly dependent on the geometrical properties of stents such as the length and most importantly the struts dimensions and configuration, among others. Upon approach of fatty cells to the vessel walls, the shear stress, which is dictated by the fluid regime, determines adherence of these cells to the walls. As a result, regions with lower shear stress are more prone to accumulation of fatty tissue [222-224]. Particularly, a correlation between LWSS (< 0.5 Pa) and early intimal thickening leading to restenosis has been discovered [204, 205, 216]. On the other hand, high and moderate wall shear stress is considered to be beneficial against proliferation of intimal cells [225-227]. The *in vivo* and *in vitro* studies further confirmed the influence of stent structures on wall shear stress distribution, which can result in restenosis and thrombus formation in the deployment area [159, 164, 216, 228]. Consequently, with any new stent structure, the study of its effect on the fluid regime after deployment is of paramount importance.

Computational fluid dynamics (CFD) modeling has the advantage of flexibility and repeatability compared to the experimental methods. Moreover, it can provide detailed insight into critical flow parameters at the deployment region close to the stent struts and the arterial walls where it is very hard, if not impossible, to acquire such data experimen-

tally. These benefits led to a growing number of studies investigating the effect of different stent designs on the distribution of LWSS as a primary predictor of restenosis utilizing CFD [158, 160, 214, 218-220, 229]. Among the aforementioned studies, to the best of our knowledge, only one studied the distribution of LWSS in a healthy vessel as a benchmark while their comparisons were made in a flat and limited geometry [222]. In contrast, other studies were solely dedicated to the comparison between different stent designs and their effect on LWSS. Furthermore, study of hemodynamic alterations such as changes to flow supply of branches before or after a deployment site, in comparison with a healthy domain, may provide useful information that can be used for future structural improvement of stents [230].

Therefore, to study the hemodynamic effects of the proposed RRR in Chapter 2 [103], potential restenosis risk factors such as distribution of wall shear stress and fluid supply to different paths after deployment of the RRR as a stand-alone or integrated luminal support, are extensively investigated in this chapter through transient 3D CFD models.

3.3 Materials and Methods

In this study, the luminal fluid of choice is blood whose flow is considered laminar and incompressible with density $\rho = 1060$ kg/m^3. Due to relatively low magnitudes of flow velocity arteries with respect to the luminal diameter and composition of water, these are reasonable assumptions. The flow is governed by the equations of conservation of mass and momentum expressed by Equations (3.1) and (3.2) respectively.

$$\nabla . \mathbf{V} = 0 \qquad \textbf{(3.1)}$$

$$\frac{\partial \mathbf{V}}{\partial t} + \mathbf{V} . \nabla \mathbf{V} + \frac{\nabla p}{\rho} - 2\frac{\mu}{\rho} \nabla . \mathbf{D} = 0 \qquad \textbf{(3.2)}$$

where $\mathbf{V}$ denotes the fluid velocity, ρ is the fluid density, p is fluid pressure, μ is dynamic viscosity and $\mathbf{D}$ is the tensor of rate of deformation [230]. These equations are solved by the commercial CFD package ANSYS CFX (ANSYS Inc., Canonsburg PA, USA) that allows for coupling the velocity and pressure fields in a transient analysis framework accounting for changes in blood flow during cardiac cycles.

In order to account for the non-Newtonian characteristics of the blood, the Carreau model is employed [214, 229, 231]. Viscosity of the blood approaches the constant Newtonian

value at high shear rates by this model and it provides adequate information for modelling the blood behaviour [229]. Using this model, the dynamic viscosity, μ, is expressed by:

$$\mu = \mu_{\infty} + \left(\mu_0 - \mu_{\infty}\right)\left(1 + \left[\lambda \dot{\gamma}\right]^2\right)^{(n-1)/2} \tag{3.3}$$

where μ_0 and μ_{∞} are the viscosities at zero and infinite share rates respectively, whereas λ and n are material dependent constants. For blood, these parameters are determined by fitting the fluidic flow experimental data to the Carreau model [214, 229, 231], resulting in μ_0 = 0.25 kg/ms, μ_{∞} = 0.0035 kg/ms, λ = 25 s and n = 0.25. In Equation (3.3), $\dot{\gamma}$ is the shear rate calculated by the solver using the second invariant of the strain rate tensor expressed by:

$$\dot{\gamma} = \left[2\left\{ \left(\partial u/\partial x\right)^2 + \left(\partial v/\partial y\right)^2 + \left(\partial w/\partial z\right)^2 \right\} + \left(\partial u/\partial y + \partial v/\partial x\right)^2 + \left(\partial u/\partial z + \partial w/\partial x\right)^2 + \left(\partial v/\partial z + \partial w/\partial y\right)^2 \right]^{1/2} \tag{3.4}$$

where u, v and w are the corresponding x, y and z components of the velocity vector **V** in equations (3.1) and (3.2). As mentioned before, there is a strong relation between late restenosis and the distribution of LWSS that is adopted as the primary criterion for prediction of risk of restenosis in our analyses. Having solved for equations (3.3) and (3.4), the wall shear stress magnitude is calculated by multiplication of shear rate and dynamic viscosity.

The studies in this chapter are divided into three major parts, each seeking to investigate and compare hemodynamic response of the three types of luminal supports shown in Figure 3.1. These three luminal supports as shown in Figure 3.1 include: a) a standalone RRR, b) a standalone BE stent referred to as the standalone stent for the rest of this chapter, and c) an RRR-integrated BE stent referred to as the RRR-integrated stent for the rest of this chapter. In Part 1, transient studies are conducted in unbranched fluid domains with a uniform reference luminal diameter of 4 mm. This value is consistent with the mean luminal diameter of human coronary arteries ranging from 1.5 to 5.5 mm [8, 9]. Performance measures such as LWSS distribution and fluid drag forces are investi-

gated in this section. Results of the deployment of the supports of Figure 3.1 are then compared with those of an unscaffolded fluid domain representing a healthy vessel.

In real conditions, stents can potentially be deployed in any area including before, after, in between or even inside branching areas, affecting the fluid regime inside their preceding or succeeding branches. To account for these effects, the analysis is further extended into Parts 2 and 3, where each seeks to explore the effect of a luminal scaffold on the wall shear stress distribution in the deployment area (as well as the entire fluid domain) and flow rate changes in branching vessels. Part 2 investigates the impact of deploying three different luminal supports of Figure 3.1 into a section of a vessel with the reference luminal diameter of 4 mm for the main branch where the deployment area is preceded and succeeded by two hypothetical branching vessels. Referred to as proximal and distal branches respectively, both these branching vessels maintain a luminal diameter ratio of ¾ with respect to the main branch. This selection criteria is deemed reasonable and also has been adopted in the literature before [230].

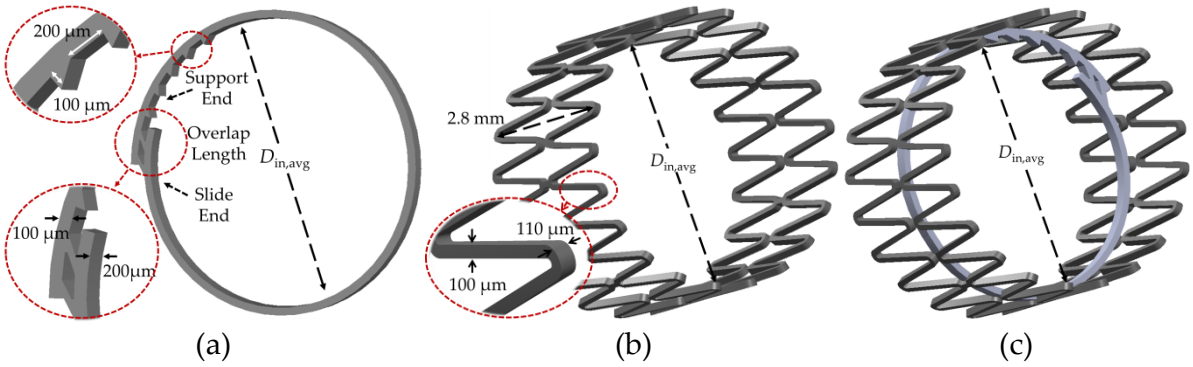

Figure 3.1. Geometry of the three different supports. a) Standalone RRR, b) standalone two-column BE stent (standalone stent), c) RRR-integrated BE stent (RRR-integrated stent). The first two are expanded so the provided inner diameter matches the lumen's reference diameter. The third support is expanded to the point where the inner diameter of the BE stent mesh is equal to the lumen's reference diameter.

The proximal branch creates a -45 ° angle whereas the distal branch creates a 45 ° angle with the longitudinal axis of the main branch. Results of the scaffolded fluid domains including distribution of LWSS and flow supply of the main and side branches are then compared with those of an unscaffolded branched domain representing a healthy vascular domain. To further investigate sensitivity of the results to the dimensional assumptions of the scaffolds and the deployment area, typically in smaller arteries, a comparative dimensional analysis study is conducted in Part 3. In this part, results of

deployment of an RRR-integrated stent with different fluid domain and RRR overlap configurations are compared with those of a standalone stent deployment. This is to investigate the effect of integration of an RRR into a stent in comparison with the use of a standalone stent that is the current state-of-the-art modality. Table 3.1 presents the dimensional and material characteristics of the three different supports. In this table, Avg. Diameter ($D_{in,avg}$) refers to the mean inner diameter of the support after deployment.

Table 3.1. Material and geometrical characteristics of the three luminal supports.

	Standalone RRR	Standalone Stent	RRR-Integrated Stent
Material	Nitinol	Stainless Steel 316L	Nitinol & Stainless Steel 316L
Structure	Overlapping Ring with asymmetric teeth	Slotted tube mesh, W-shaped struts with bridges	Overlapping ring implanted inside the stent mesh
Num. of Columns	1	2	RRR x1, Stent columns x2
Strut Width (W_s)	0.2 mm	0.11 mm x2	0.2 mm x1 , 0.11 mm x2
Strut Thickness (T_s)	0.1 mm	0.1 mm	0.1–0.2 mm
Avg. Diameter ($D_{in,avg}$)	4 mm	4 mm	3.8–4 mm

3.3.1 Models Development

Expanded computational geometries of the supports and the vascular domains are developed using the computer-assisted design (CAD) tool SolidWorks (Solidworks Corp., Velizy, France). Next, the fluid domains are constructed by filling all luminal cavities with volumetric solids which are then meshed by ANSYS. Figure 3.2 shows the fluid domains and the corresponding deployment areas of corresponding with the three supports of Figure 3.1. The arterial walls are all considered as rigid solids with even surfaces and uniform thickness disregarding atherosclerotic formations. Domains before and after the deployment areas are extended to result in fully developed flows for all cardiac velocity profiles before entering the deployment area (Parts 1) and distal branches (Parts 2 and 3). At all the outlets a zero-gauge pressure boundary condition is specified with a no slip boundary condition for external surfaces of the scaffolds and the luminal walls.

Flow simulations are carried out using a transient analysis framework while applying a pulsatile blood flow to the inlet. The ANSYS CFX solver is utilized to solve tions (3.1) and (3.2) based on a three-dimensional finite volume method. To increase accuracy of the final results, convergence criterion for the residuals of continuity and velocity is set at 10^{-5} that is an order of magnitude lower than that of the solver's default. The time-varying inlet blood flow waveform is adopted from literature [219], that was

acquired from velocity measurements in a canine coronary artery at resting conditions. For all simulations the three-cycle waveform shown in Figure 3.3 is applied to the inlet. Nevertheless, due to the oscillatory nature of the results shortly after the completion of first cycle, results of the last cycle are reported here.

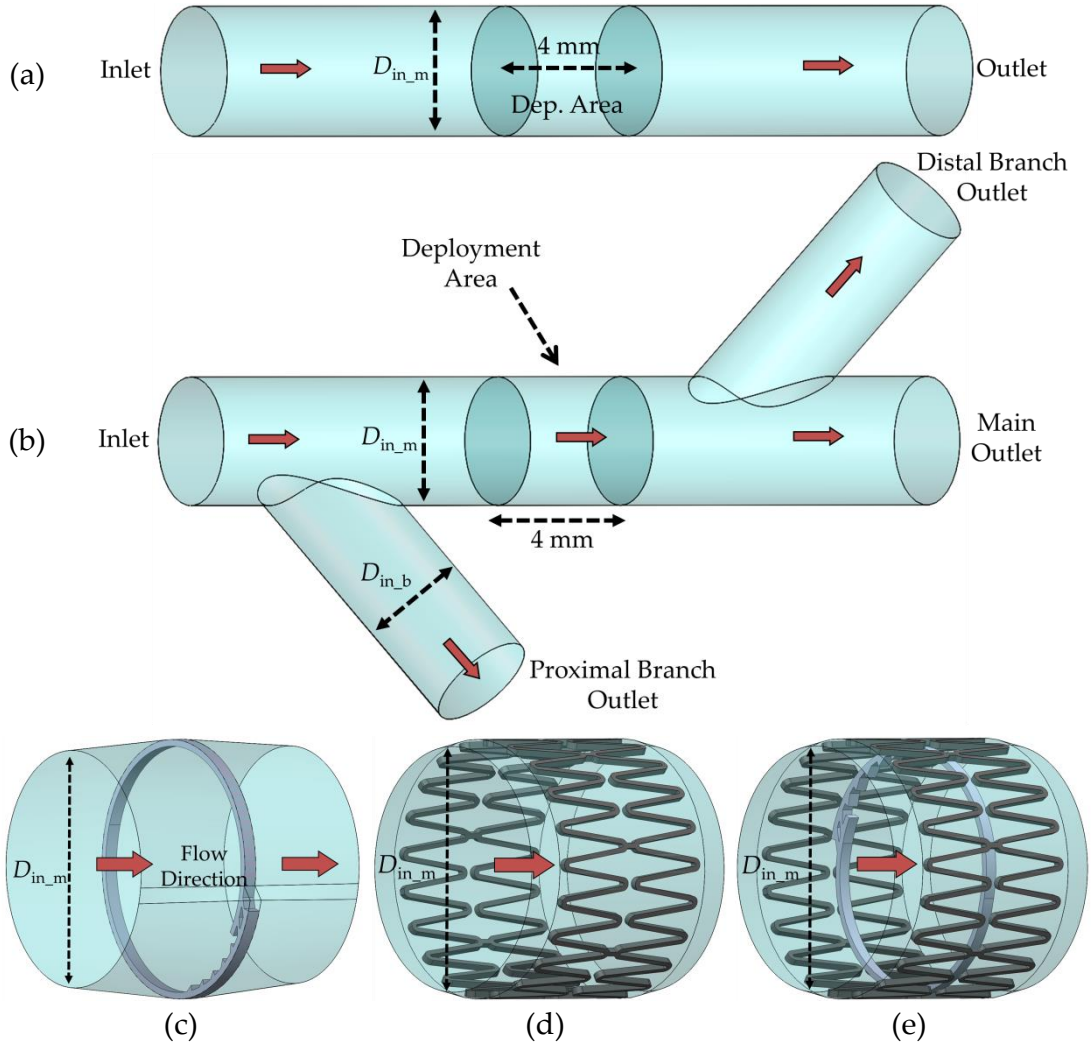

Figure 3.2. Fluid domain configurations of the CFD analysis. a) Straight and, b) branched fluid domains with healthy deployment areas, c) standalone RRR deployment area, d) standalone two-column stent deployment area, e) RRR-integrated stent deployment area. Domains at the inlet and outlet of main branch are extended to form a fully developed flow, full extent of these areas are not shown here.

3.3.2 Discretisation

The mesh in the deployment area, specifically close to the vascular and stent walls is more refined than those of the rest of the fluid domain. All vascular walls are first meshed with thin layer hexahedral elements close to the walls, while the rest of the do-

main, including the deployment area, is meshed with a combination of hexahedral and free tetrahedral elements. To acquire a reliable mesh density, in three separate steady-state studies three velocity magnitudes including the highest, the lowest and the time-average velocity of the waveform in Figure 3.3 are applied to the inlet respectively.

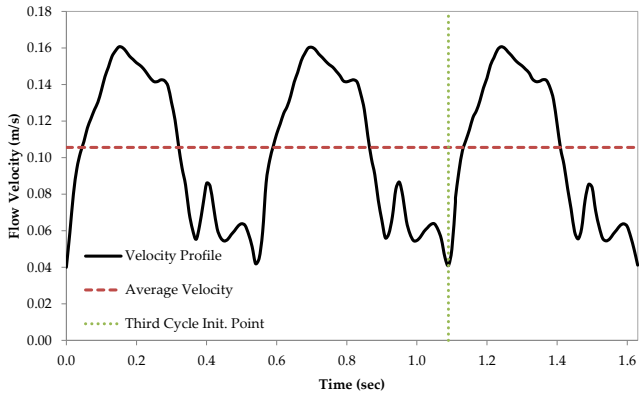

Figure 3.3. Inlet flow profile. Simulations are performed for three cycles and the results of the last one are reported. The average value is used for mesh sensitivity analysis.

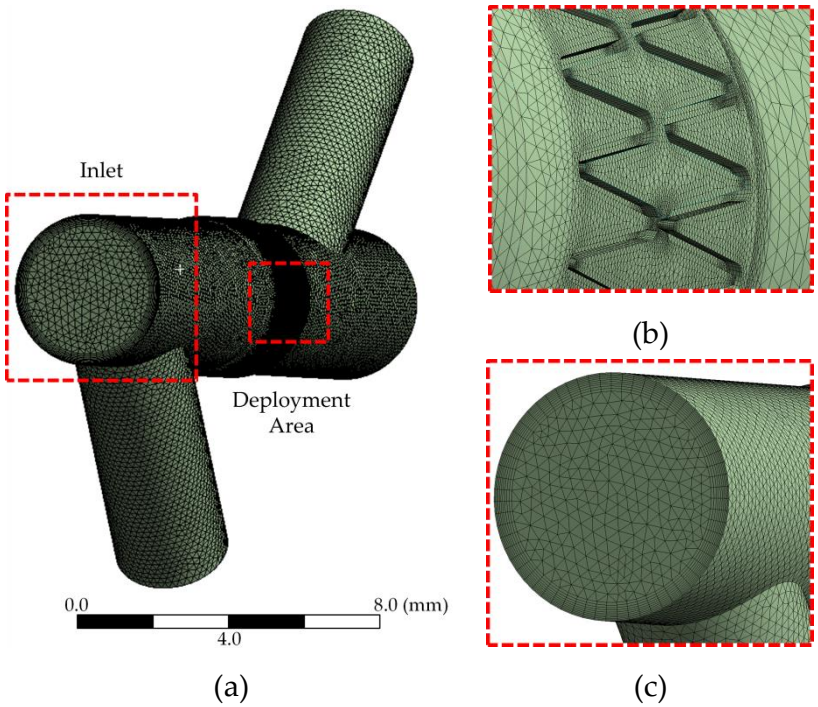

Figure 3.4. Discretization of the fluid domain. a) Entire domain preview, b) close-up view of the refined mesh at the deployment area, c) close-up view of the inlet and the boundary layer hexahedral elements close to the luminal walls. Majority of the domain is meshed using conformal tetrahedral elements due to the curved and sharp angled geometries.

In each study, starting from a base mesh density, multiple refinement levels were defined wherein any subsequent level increased the number of elements by a factor of 2 compared to its preceding level. Should the difference between the wall shear stress re-

sults of two consecutive levels fall below 3%, the last refinement level was chosen as the new base refinement level for further analysis using the aforementioned three velocity magnitudes. Next, using the refined mesh, in a transient analysis timesteps were reduced in multiple iterations till the wall shear stress values difference in corresponding timesteps from one refinement to the next was less than 3%. This approach resulted in around 3.8 million elements for each model with a timestep size of 0.03 sec. Figure 3.4 shows the discretisation of the fluid domain after meshing of the branched domain of RRR-integrated stent using ANSYS meshing utility highlighting the use of hexahedral layer elements close to the walls and the refined meshing in the deployment area. The rest of the domain is discretised by the highly conforming tetrahedral elements. Use of these elements is more pronounced around the curved geometries of the stent mesh and the sharp angles of the sawtooth structures of the RRR.

3.3.3 Dimensional Analysis

The RRR is designed to match a range of different luminal and target lesion diameters reducing the costly custom production runs and resizing for every specific vessel. This resizing capability of the RRR leads to partial expansions, thereby overlapping of the the two end of the RRR, in vessels or lesions with reference luminal diameters smaller than that of a fully expanded RRR. To further investigate the hemodynamic changes made by the integration of a stent with an RRR in vessels with different diameters and different overlap lengths from the two ends of the RRR (Figure 3.5) further comparative CFD studies are conducted in Part 3. Table 3.2 presents the dimensional characteristics of these models. Overlap length in this table refers to the remaining number of teeth from the support end of the RRR to its fully expanded state.

Table 3.2. Dimensional configurations of the fluid domain for sensitivity study.

Characteristic	Configuration Case							
	1	2	3	4	5	6	7	8
Luminal Support	*RRR-Stent*			*Stent*	*RRR-Stent*			*Stent*
Main Branch Diameter (D_{in_m})	2.6 mm				3.2 mm			
Prox. & Dist. Branch Diameters (D_{in_b})	1.95 mm				2.4 mm			
Overlap Length (Steps)	6	3	1	--	6	3	1	--

In the smallest interlocked expanded state of the ring, 6 teeth from the support end are overlapped by the slide end, while in a fully expanded state of the RRR, an overlap of

one step is maintained. This is to ensure a safe interlock and resilience against recoil. These states of the RRR and the configuration cases of Table 3.2 are shown in Figure 3.5.

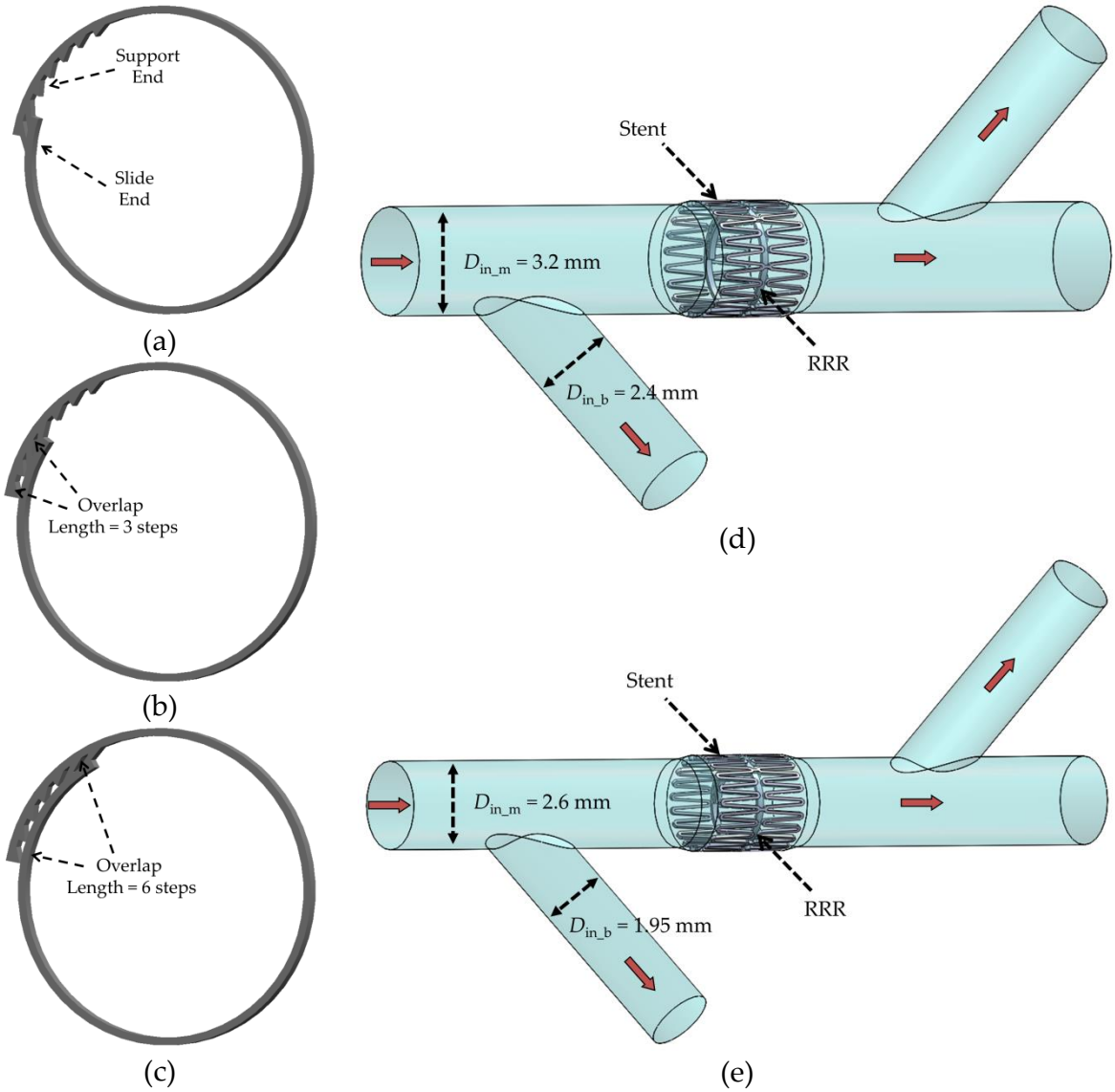

Figure 3.5. Dimensional configurations of the dimensional analysis. a) RRR in the fully expanded state, overlap length of 1 step, b) RRR partially expanded and interlocked with overlap length of 3 steps, c) RRR partially expanded and interlocked with overlap length of 6 steps, d) fluid domain with reference luminal diameter of the main branch and the expanded stent mesh equal to 3.2 mm, e) fluid domain with reference luminal diameter of the main branch equal to 2.6 mm. In all these cases, the diameter ratio of ¾ between diameter of side and main branches is maintained.

Due to the considerably high time and performance costs of these studies, only a limited number of all possible configurations are studied. The ¾ ratio between the inner diameters of the side branches with respect to the main branch is maintained in all these cases. Results from these studies are compared with those of the deployment of a standalone

stent as the current state-of-the-art percutaneous intervention standard. In all configuration cases of Table 3.2, the support structures (standalone stent or RRR-integrated stent) are expanded to the extent that the inner diameter of the expanded stent mesh matches that of the lumen's reference diameter in the main branch. All models are run on a Dell Precision workstation with two quad-core Xeon processors and 20 GB of RAM. On average, every simulation run finished in 24 hours for three cardiac cycles. The post processing time required 3 hours of operation, on average, to extract data of interest for all time instances and around 40 GB of disk space to store each model.

3.4 Results and Discussion

3.4.1 Part 1 – Unbranched Fluid Domain

In this section hemodynamic performance measures such as LWSS distribution and fluid drag force as a result of deployment of the three supports of Figure 3.1 into unbranched fluid domains, Figure 3.2 (a), are presented.

I. LWSS in Unbranched Fluid Domains

Wall shear stress results are reported for the walls, on the luminal side of the vessel, that are not covered by the support struts. For better comparison, the ratio of the wall area subject to LWSS (< 0.5 Pa) to the total wall area is presented for both the deployment area and the entire fluid domain. The results after completion of simulations for three consecutive waveform cycles demonstrated the sufficiency of one cycle to allow for stabilisation of changes in the initial conditions. Therefore, the results for the last cycle are presented henceforth.

Transient ratio of areas subject to LWSS in the deployment area and the entire fluid domains of Figure 3.2 (a) in the third cardiac cycle are shown in Figure 3.6. As observed from these figures, the lowest ratios of areas subject to LWSS, for all deployment scenarios, are more prevalent at higher velocity magnitudes. This is expected as an increase in the velocity translates into an increase in the velocity gradient close to the walls, thereby increasing shear rate and shear stress. Moreover, at these higher velocities, greater differences between the LWSS ratios of all the cases in the deployment area are observed compared to other time instances with lower velocity magnitudes. Of the three supports, the

RRR exhibits the closest correspondence to the LWSS distributions of the healthy vessel profile while the stent and the RRR-integrated stent show a similar trend with marginal difference between the two during the first half of the cycle.

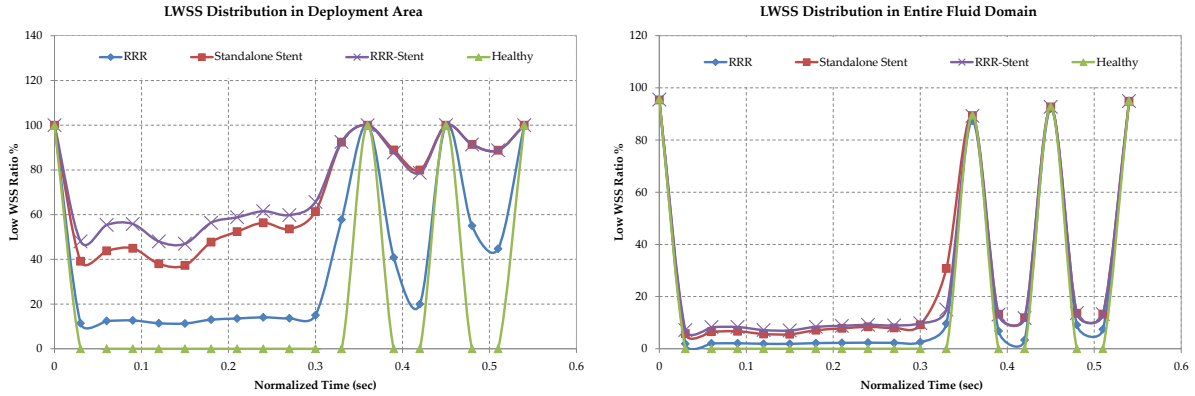

(a) (b)

Figure 3.6. LWSS distribution in unbranched fluid domains. a) Ratio of area subject to low wall shear stress in the deployment area, b) ratio of area subject to low wall shear stress in the entire fluid domain of the unbranched fluid domains.

Temporal average values of the LWSS ratios in the deployment area and the entire fluid domain in a cardiac cycle are presented in Figure 3.7. Given the high radial resilience of the RRR as demonstrated in Chapter 2 [103], it also exhibits a superior hemodynamic behaviour compared to the standalone stent by decreasing the LWSS ratios in both the deployment area and the entire fluid domain as indicated by Figures 3.6 and 3.7.

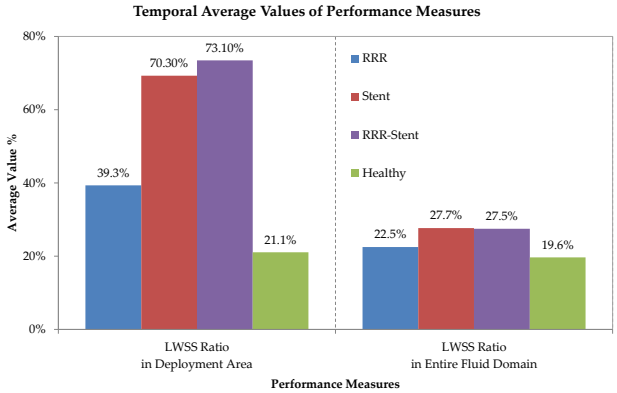

Figure 3.7. Temporal average of LWSS in unbranched fluid domains. RRR exhibits ratios closest to the healthy lumen. RRR-integrated stent and the standalone stent show similar behaviours in the entire fluid domain with marginal increase for the RRR-integrated stent compared with the standalone stent in the deployment area.

Moreover, an RRR-integrated stent, with an effective inner diameter less than that of a standalone stent (due to the addition of the RRR's profile) and higher recoil resilience

(due to the presence of RRRs with high radial resilience) exhibits a similar ratio of LWSS in the deployment area (increased by 3%) and in the entire domain (decreased by 1%). Figures 3.11 to 3.14 present spatial distribution of LWSS (< 0.5 Pa) in the deployment area and the entire domain of the three supports and the healthy vessel at selected time instances of the third cardiac cycle as denoted in Figure 3.8. As demonstrated in these figures, wall shear stress at time instances (1), (2), (3) and (5) exceeds 0.5 Pa in the healthy domain providing a protective mechanism against deposition of fatty cells. This trend is similar in both deployment and the entire area of the healthy domain that is represented by empty wireframes in Figures 3.11 to 3.14. Spatial contour plots from these figures are in agreement with the LWSS ratio values presented in Figure 3.6.

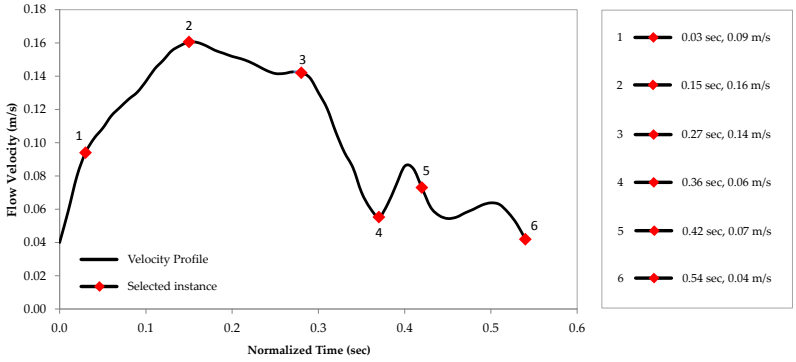

Figure 3.8. Selected time instances of third cardiac cycle. Selected instances are used for spatial contour plots.

A justification for the difference between the LWSS ratios of the RRR-integrated and the standalone stents in the unbranched fluid domains may be given using the definition of the shear stress as a result of multiplication of the dynamic viscosity and the shear strain rate. Given the non-Newtonian shear thinning behaviour of the blood as expressed by Equation (3.3), magnitudes of the shear strain rate and dynamic viscosity are inversely proportional. This relation results in areas with lower values of shear strain rate become mainly adjacent to portions of the fluid with higher values of dynamic viscosity as shown by Figure 3.9 demonstrating contour plots of the dynamic viscosity and shear rate for the standalone stent at time 0.15 sec (time instance 2 of Figure 3.8). Distribution of dynamic viscosity and shear rate strain for time 0.15 sec, in the deployment area of the RRR-integrated stent is presented in Figure 3.10. Comparison between this figure and Figure 3.9 clearly indicates an increase in the average value of shear strain rate in the standalone stent deployment area compared to the RRR-integrated stent.

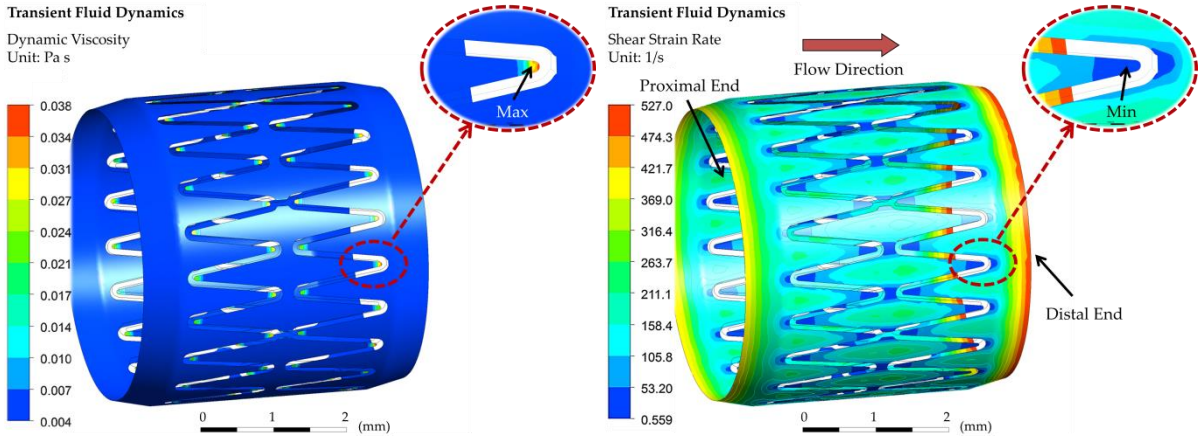

(a) (b)

Figure 3.9. Inverse relation of the dynamic viscosity and shear rate, standalone stent. a) Distribution of dynamic viscosity and, b) shear strain rate in the deployment area of the standalone stent at time instance 2. Higher shear rates occur at unscaffolded regions away from the stent struts with the highest values at the proximal and distal ends.

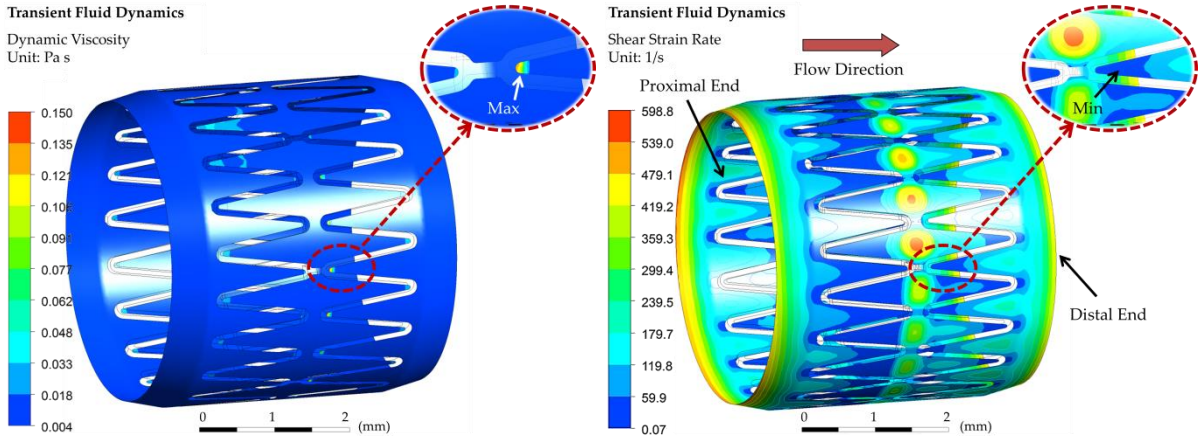

(a) (b)

Figure 3.10. Inverse relation of the dynamic viscosity and shear rate, RRR-integrated stent. a) Distribution of dynamic viscosity and, b) shear strain rate in the deployment area of the RRR-integrated stent at time instance 2. Higher values of shear rate occur at areas with the least amount of scaffolding closer to the distal end. Highest shear rates appear in the area close to outer surface of the RRR due to high velocity gradient at this region.

This is despite the increase in the highest values of shear strain rate in the RRR-integrated stent in comparison with the standalone stent. The shear strain rate in Equation (3.4) is inversely proportional to the length of the velocity boundary layer that translates into direct proportionality to the velocity gradient in the radial direction. To study the effect of the boundary layer and the velocity gradient, two virtual planes at the radial cross-section of the deployment area, one close to the proximal end and the other close to the distal end of the deployment area as marked in Figure 3.10 (b) are considered.

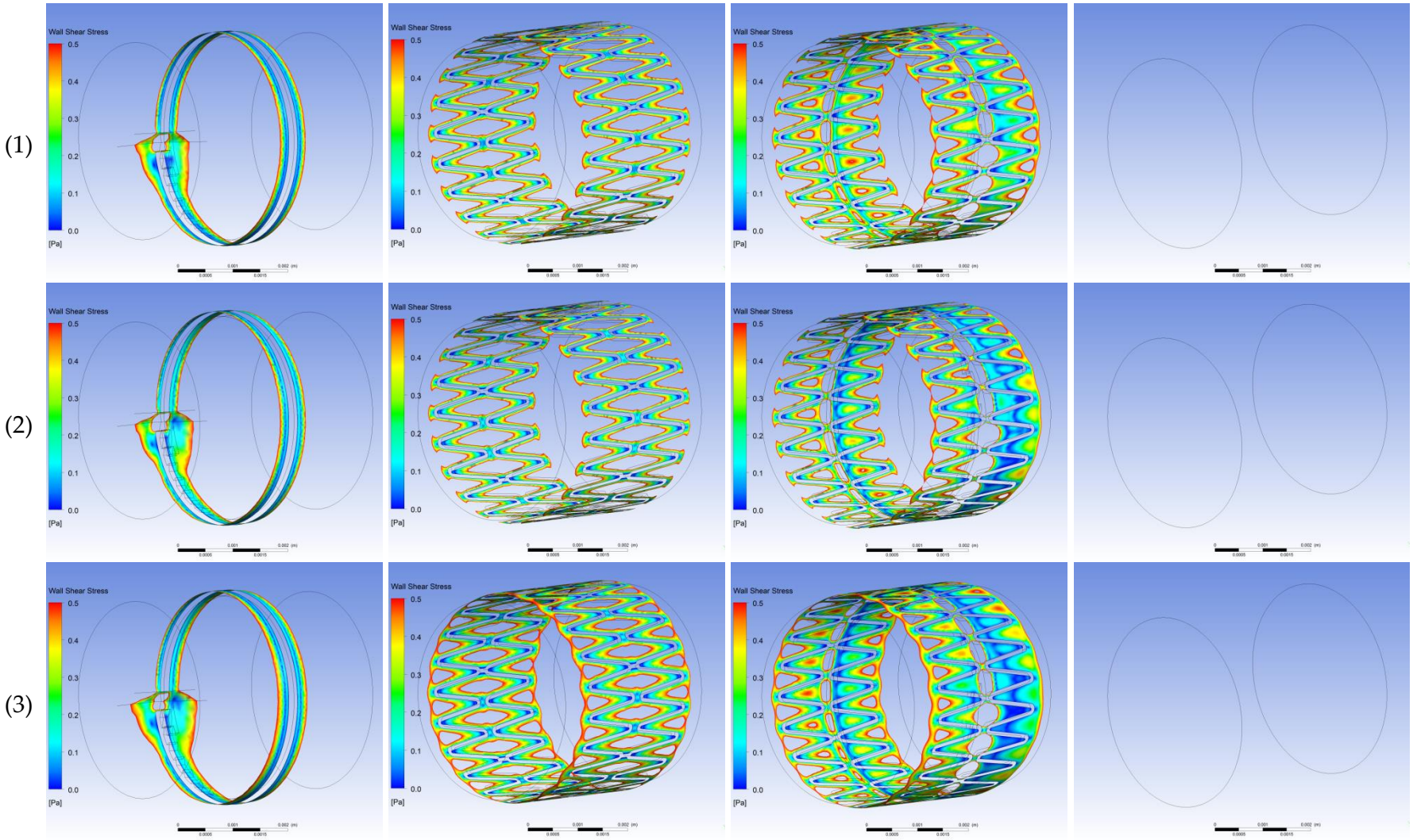

Figure 3.11. LWSS contour plots, deployment area of unbranched domains, instances 1–3. LWSSS distribution in the deployment area of, a) the standalone RRR, b) the standalone stent, c) the RRR-integrated stent and, d) the unscaffolded domain representing a healthy vessel. Inlet is in the left for all images. Empty wireframes in column (d) denote wall shear stress > 0.5 Pa in the healthy vessel.

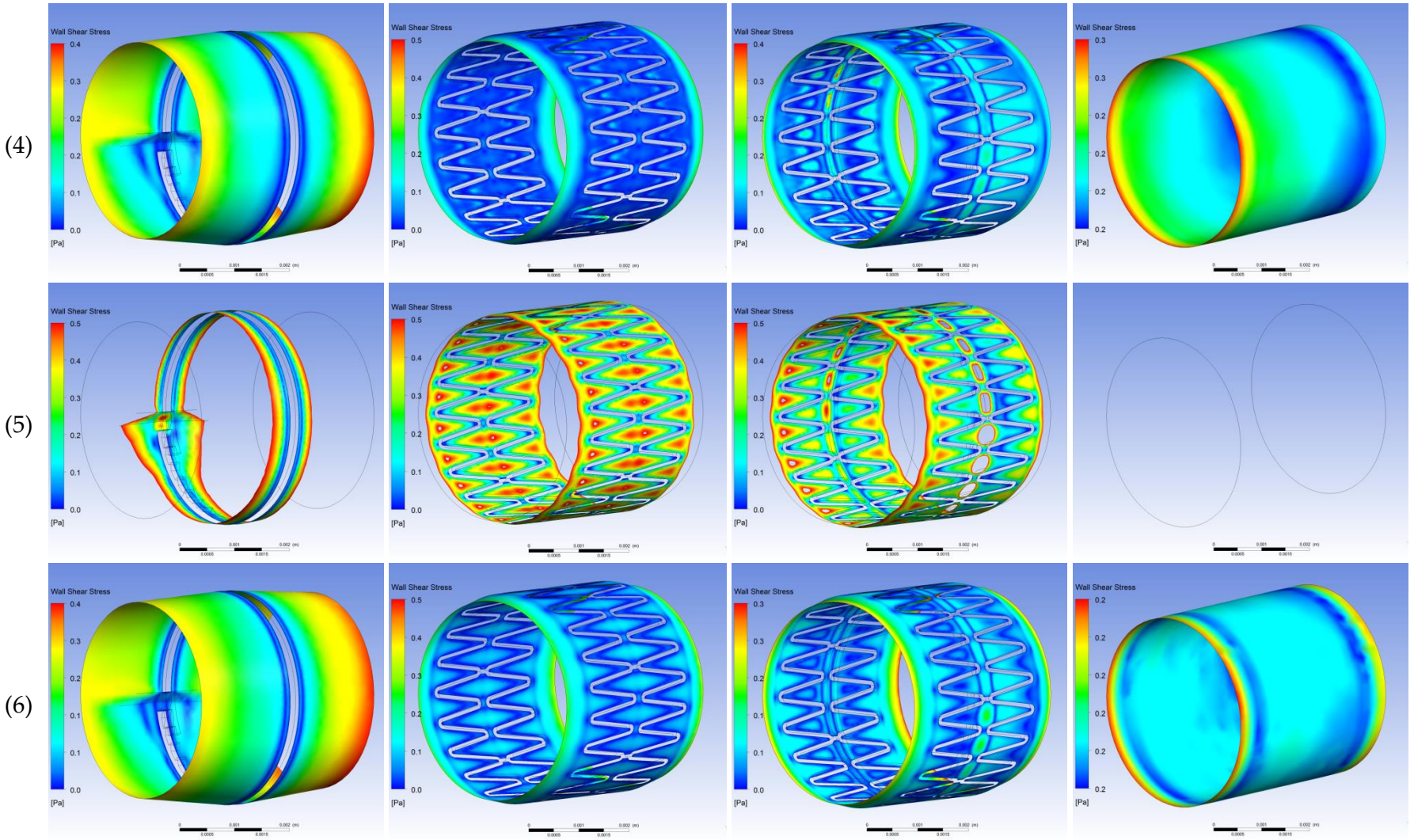

Figure 3.12. LWSS contour plots, deployment area of unbranched domains, instances 4–6. LWSSS distribution in the deployment area of, a) the standalone RRR, b) the standalone stent, c) the RRR-integrated stent and, d) the unscaffolded domain representing a healthy vessel. Inlet is in the left for all images. Empty wireframe in (5,d) denote wall shear stress > 0.5 Pa in the healthy vessel.

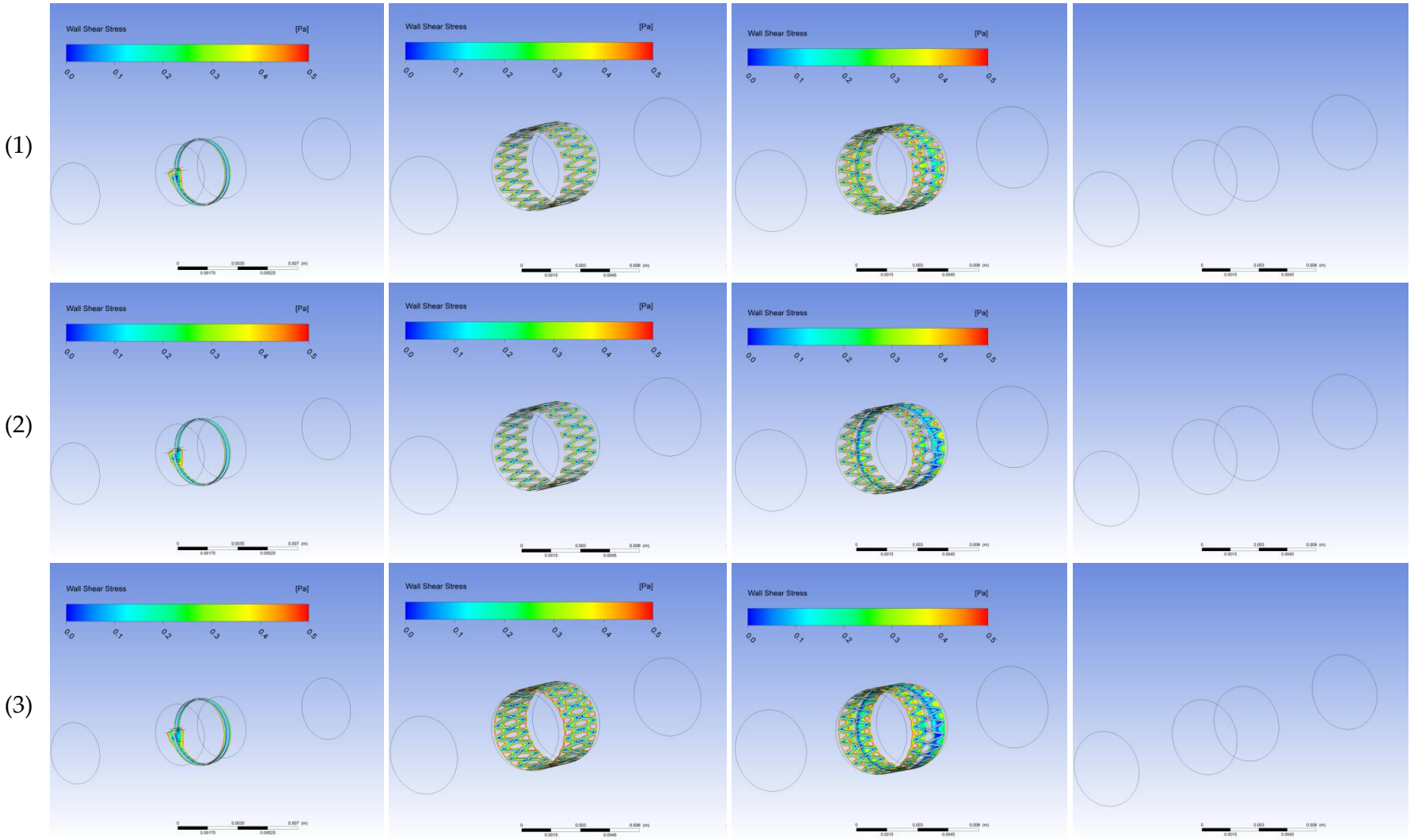

Figure 3.13. LWSS contour plots, entire area of unbranched fluid domains, instances 1–3. LWSS distribution in the entire domain of, a) the standalone RRR, b) the standalone stent, c) the RRR-integrated stent and, d) the unscaffolded domain representing a healthy vessel. Inlet is in the left for all images. Empty wireframes in column (d) denote wall shear stress > 0.5 Pa in the healthy vessel.

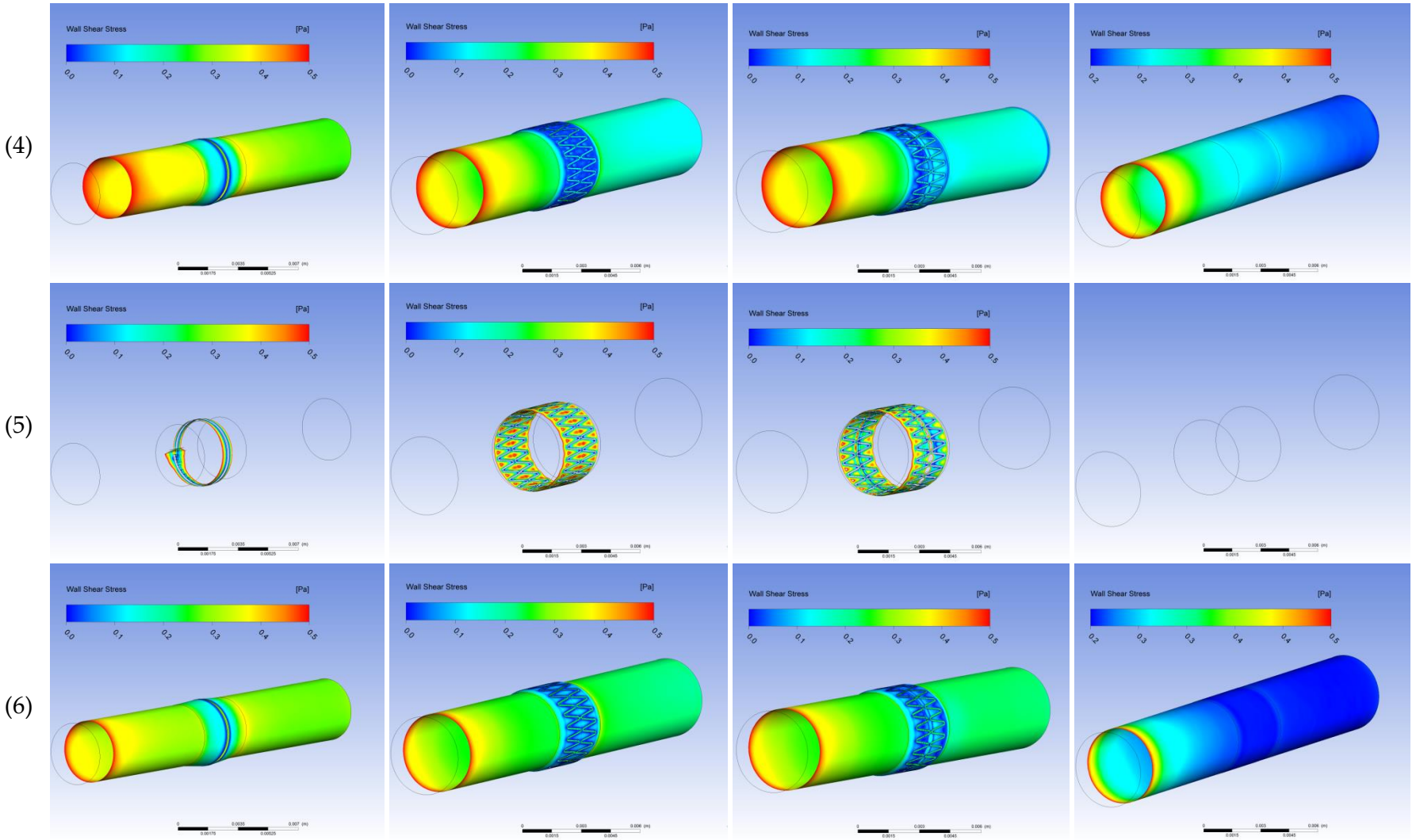

Figure 3.14. LWSS contour plots, entire area of unbranched fluid domains, instances 4–6. LWSS distribution in the entire domain of, a) the standalone RRR, b) the standalone stent, c) the RRR-integrated stent and, d) the unscaffolded domain representing a healthy vessel. Inlet is in the left for all images. Empty wireframes in (5,d) denote wall shear stress > 0.5 Pa in the healthy vessel.

Contour plots of the velocity profile distribution in these two cross-sectional planes for the standalone and RRR-integrated stents at time 0.15 sec are shown in Figure 3.15. In this figure, $L_{\text{Prox,Stent}}$ and $L_{\text{Dist,Stent}}$ refer to initial length of the boundary layer close to the vascular walls at the proximal and distal ends of the standalone stent respectively. Moreover, $L_{\text{Prox,RRR-Stent}}$ and $L_{\text{Dist,RRR-Stent}}$ refer to the similar corresponding parameters at the RRR-integrated stent ends. To further elucidate changes in the velocity magnitudes, a path starting from the luminal wall extending to the centroid of the lumen is defined on the distal planes as shown in Figure 3.15. Velocity magnitudes along this path at time instance 0.15 sec are presented in the graph of Figure 3.16.

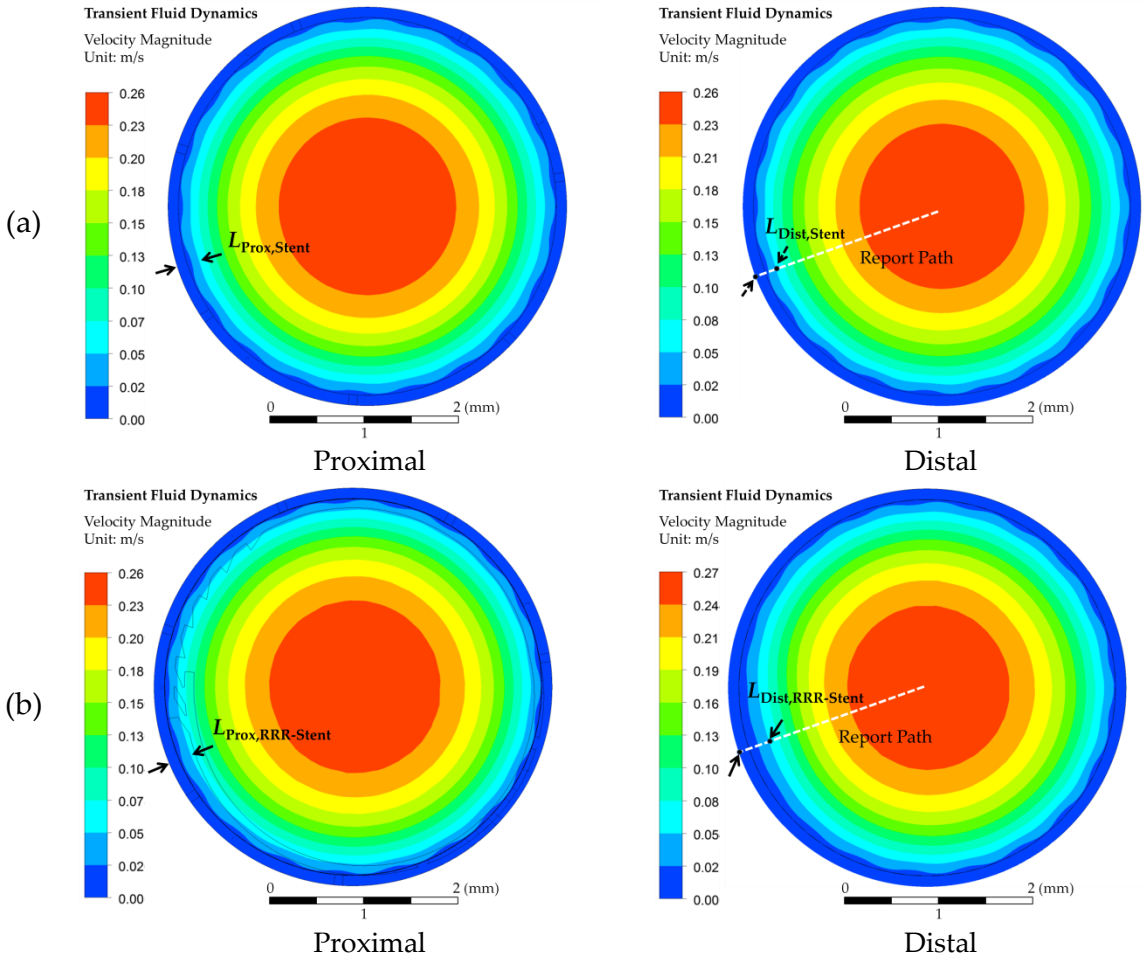

Figure 3.15. Radial gradient of velocity and shear strain rate. a) Velocity contour plots at the proximal and distal ends of the standalone stent and, b) the RRR-integrated stent. All results are reported at time instance 0.15 sec.

From Figure 3.15, it is clear that the initial phase of the boundary layers at the proximal and distal ends of the standalone stent are of equal distance and equal to that of the proximal end from the RRR-integrated stent. In contrast, this length is relatively longer

at the distal end of the RRR-integrated stent resulting in lower velocity gradient in the radial direction as demonstrated in Figure 3.16, thus lower shear strain rates.

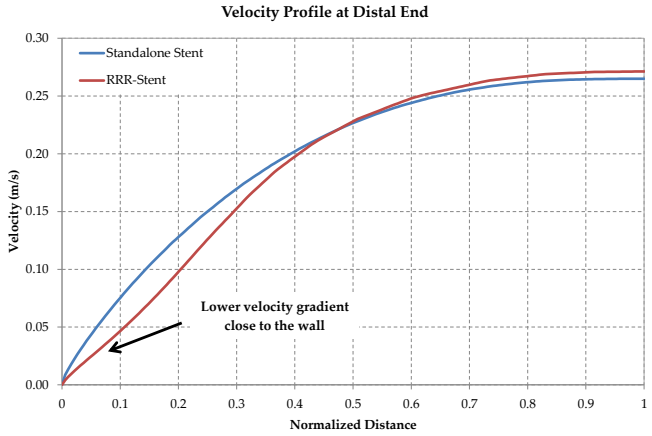

Figure 3.16. Velocity magnitudes along a radial path. Selected radial path starts from luminal wall and extends to the centre of lumen. This path lies on the radial cross-sectional plane at the distal end of deployment area denoted by the dashed line in Figure 3.15.

As mentioned before, by increasing shear strain rate, values of dynamic viscosity start to decrease. Nevertheless, the decay rate of dynamic viscosity is lower than the growth rate of the shear strain rate that effectively results in a marginal increase in the values of the wall shear stress in the standalone stent deployment area at this time instant. This effect can be observed by the relatively lower ratio of area subject to LWSS in the standalone stent deployment area compared with the RRR-integrated stent at time 0.15 sec as shown in Figure 3.11 (2). The difference between the values of shear rate, consequently dynamic viscosity, start to vanish after time instance 3 (0.27 sec) resulting in closely matched trends of the LWSS ratios and distributions as indicated by Figure 3.6. The convergent trends after time 0.27 result in relatively close correspondence of the temporal average ratios of LWSS for the standalone and the RRR-integrated stents as demonstrated in Figure 3.7.

II. Drag Force in the Unbranched Domains

Stents that are implanted in vessels are always exposed to drag forces experienced from the flow of fluid inside the lumen. On the other hand, the frictional forces between the stent and the vascular walls, namely the withholding forces, keep the stent in place. It is important to keep the withholding forces higher than the drag forces at all times to eliminate chances of stent displacement or migration and subsequent related complications

[232]. The importance of these forces is even more emphasized in aortic aneurysms and stent-grafts implantation [233].

Figure 3.17 (a) shows the comparative results of the fluid drag force experienced by the three luminal supports in the primary direction of the flow velocity. This direction is along the longitudinal axis of the fluid domain. In order to evaluate the significance of these forces in comparison with the withholding forces for each of these supports, the reference vessel in Figure 3.2 (a) is gradually expanded up to 0.1 mm radially in order to accommodate a support with mean inner diameter of 4 mm and strut thickness of 0.1 mm as demonstrated by Figure 3.17 (b). Computational model of the vessel consists of a uniform hollow cylinder with the reference inner diameter of 4 mm, thickness of 0.5 mm and an isotropic linear elastic material model with modulus of elasticity of 1.5 MPa [234]. The final pressure, 15 KPa, represents the pressure exerted on a support by the vascular walls after deployment. We refer to this pressure as the withholding pressure.

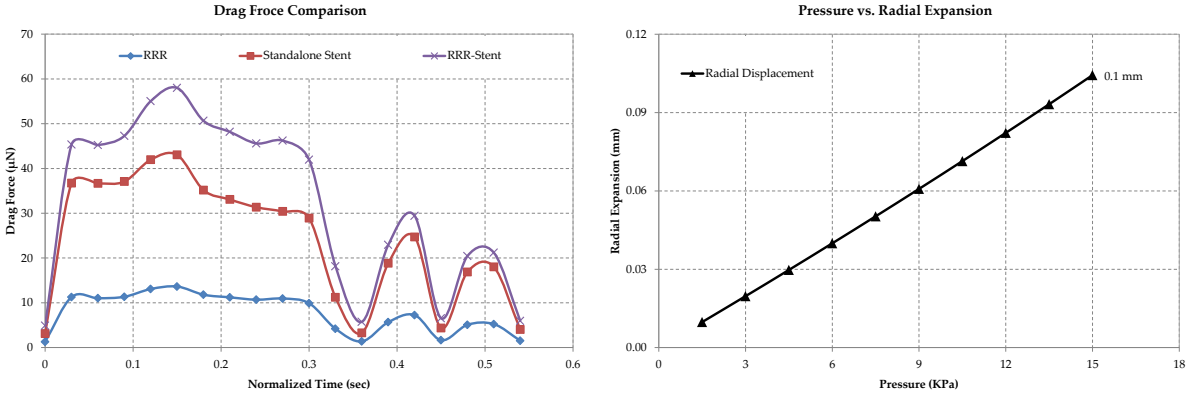

(a) (b)

Figure 3.17. Drag force comparison in a unbranched fluid domain. a) Drag forces experienced by the supports in a cardiac cycle, b) pressure vs. radial displacement of the vessel during expansion to accommodate the supports, at 0.1 mm radial expansion, the average inner diameter of deployment area is equivalent to the reference inner diameter of the vessel. The vessel exerts a 15 KPa pressure on the deployed support at this state.

Adopting a generic uniform frictional coefficient of 0.06 between the vessel and scaffolds [232, 235], withholding forces are calculated multiplying the contact surface areas by the withholding pressure. Safety margin results of all supports, Table 3.3, derived from division of the withholding force by the maximum drag forces, show margins at least by an order of magnitude large. This ensures, strong adherence of all the supports to the deployment region even at the highest velocities of the blood flow.

Table 3.3. Drag and withholding forces comparison in an unbranched fluid domain.

	Standalone RRR	Standalone Stent	RRR-integrated Stent
Contact Surface Area (mm²)	0.25	9.77	9.77
Withholding Force, F_{wh}, (mN)	0.2	8.8	8.8
Max. Drag Force, F_d, (μN)	13.6	43	58
Safety Margin = F_{wh}/F_d	x17	×204	×151

3.4.2 Part 2 – Branched Fluid Domain

In this part, in addition to the hemodynamic indicators discussed in Part 1 and their comparison, other indicators such as flow supply changes to different branches due to the presence of supports are presented.

I. LWSS in Branched Fluid Domains

Figure 3.18 (a) presents the ratio of vessel area subject to LWSS over time for both the deployment area and the entire branched fluid domains (Figure 3.2 ,b) of the three supports of Figure 3.1. As indicated by these trends, the standalone RRR stands out among the other two supports exhibiting the lowest ratio of area subject to LWSS thus reducing risk of restenosis. The healthy vessel LWSS results provide a reference for optimal fluidic performance of a support in these comparisons. In Figure 3.18 (a), the largest difference between ratios of areas subject to LWSS between the scaffolded and healthy cases occur at the time intervals where the flow adopts high velocity magnitudes and velocity gradients such as at time 0.16 sec (the diastolic perfusion) and 0.4 sec (systolic heart injection). Moreover, compared with the trends of an unbranched domain in Figure 3.6 (a), it is noticed that the difference between the RRR-integrated and the standalone stents subsides to lower values in the branched fluid domain. Resultantly, the integration of the RRR with the BE stent does not show a significant effect on the LWSS distribution factors as indicated by the closely intertwined trends of LWSS ratio for these two supports. Comparison between the LWSS results from an unbranched domain and the ones from the branched vessel in this section reveals elevated ratios of LWSS in both the deployment and entire area of the latter for all cases. This indicates more tendency of treated lesions close to or at branching areas to subsequent neointimal hyperplasia and restenosis in comparison with lesions of unbranched domains. These results are in very good agreement with conclusions made in previous studies [230, 236-238]. At low inlet velocities, all

the eight trends of Figure 3.18 converge to significantly higher ratios of areas subject to LWSS. Moreover as shown by Figure 3.18 (b), of the three supports, LWSS ratios in the entire domain associated with the standalone RRR and the RRR-integrated stent exhibit minimal deviation from the trend in a healthy vessel compared with a standalone stent.

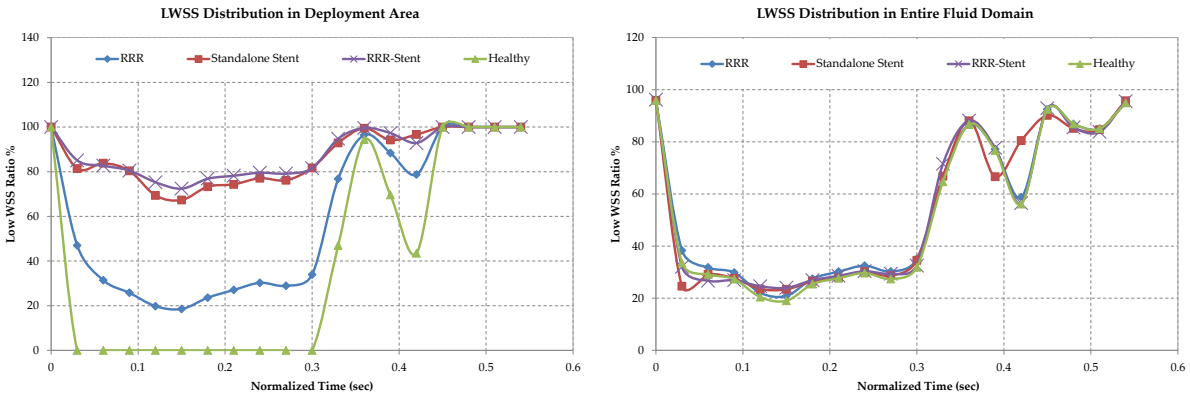

(a) (b)

Figure 3.18. LWSS distribution in branched fluid domains. a) Ratio of area subject to LWSS in the deployment area and, b) the entire fluid domain. RRR-integrated stent and standalone stent show very similar profile in the deployment area with better conformance of the RRR-integrated stent to the healthy vessel behaviour in the entire domain.

Figures 3.20 to 3.23 present the spatial distribution of LWSS (< 0.5 Pa) in the deployment area and the entire fluid domains of the three supports and the healthy vessel at time instances of Figure 3.8. Comparison between these plots and those of Figures 3.11 to 3.14 reveal closer spatial distribution of the LWSS between the RRR-integrated stent and the standalone stent in the branched domains. Moreover, as observed in Figure 3.21, at time instance 5, the RRR-integrated stent exhibits areas of higher WSS between the struts (delimited by the stent struts where the ring is implanted) compared to the standalone stent. This resulted in a less ratio of areas subject to LWSS as is also indicated in Figure 3.18 (a). This is likely due to the increased velocity of the flow capped between the RRR and the luminal wall at lower inlet velocities.

Empty wireframes of the unscaffolded domain at time instances (1), (2) and (3) of Figure 3.20 (d) indicate WSS > 0.5 Pa that is the reference behaviour of the healthy vessel. Once again, comparison between LWSS distribution plots of Figures 3.20–3.23 and those of Figures 3.11–3.14 indicates higher extension of areas with LWSS in branched-domain deployment scenarios compared with the unbranched-domain deployment counterparts. These results are in agreement with the reported values in Figure 3.18.

II. Drag Force and Output Flow Rate

Axial fluid drag forces experienced by each of the supports in a cardiac cycle are shown in Figure 3.19. Given the constant withholding forces in Table 3.3, the resultant safety margins for the RRR, standalone stent and the RRR-integrated stent are increased to ×29, ×339 and ×243 respectively. These values demonstrate the efficacy of the withholding forces to cease any migration or displacement of all the supports.

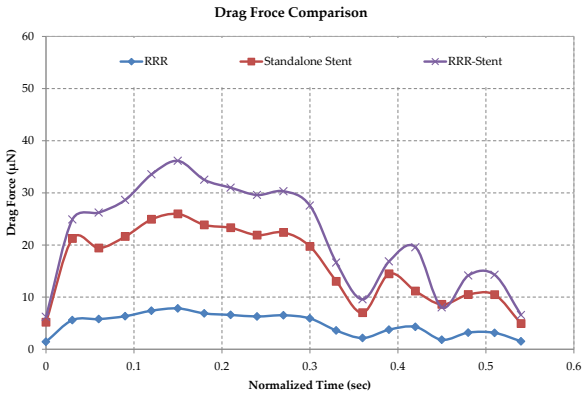

Figure 3.19. Drag force comparison of the scaffolds in branched domains. High ratios of withholding force to drag force in all supports ensure no displacement or migration of the supports over time.

As mentioned before, one of the most important performance measures of stents in branching vessels is the change in the flow supply of main and side branches after deployment. In order to compare flow rate deviation in the main, proximal and distal branches the of the scaffolded domains of Figure 3.2, in comparison with the healthy case, first output flow ratio of the main and side branches are shown in Figure 3.24 (a). Output flow ratio of a branch is express by:

$$\mathrm{FR}_i = \frac{f_{i,\mathrm{support}}}{f_{\mathrm{in}}} \times 100 \qquad \textbf{(3.5)}$$

where $f_{i,\mathrm{support}}$ for i = 1, 2 and 3 refers to the output flow rate of the proximal, distal and main branches respectively and f_{in} refers to the inlet flow rate. The deviation of flow rate of each of these cases from the healthy case, as expressed by Equation (3.6), is presented in Figure 3.24 (b). In this equation, $f_{i,\mathrm{healthy}}$ for i = 1, 2, and 3 refers to the output flow rate of the proximal, distal and main branches of the healthy vessel.

$$\mathrm{FD}_i = \frac{f_{i,\mathrm{support}} - f_{i,\mathrm{healthy}}}{f_{i,\mathrm{healthy}}} \times 100\,. \qquad \textbf{(3.6)}$$

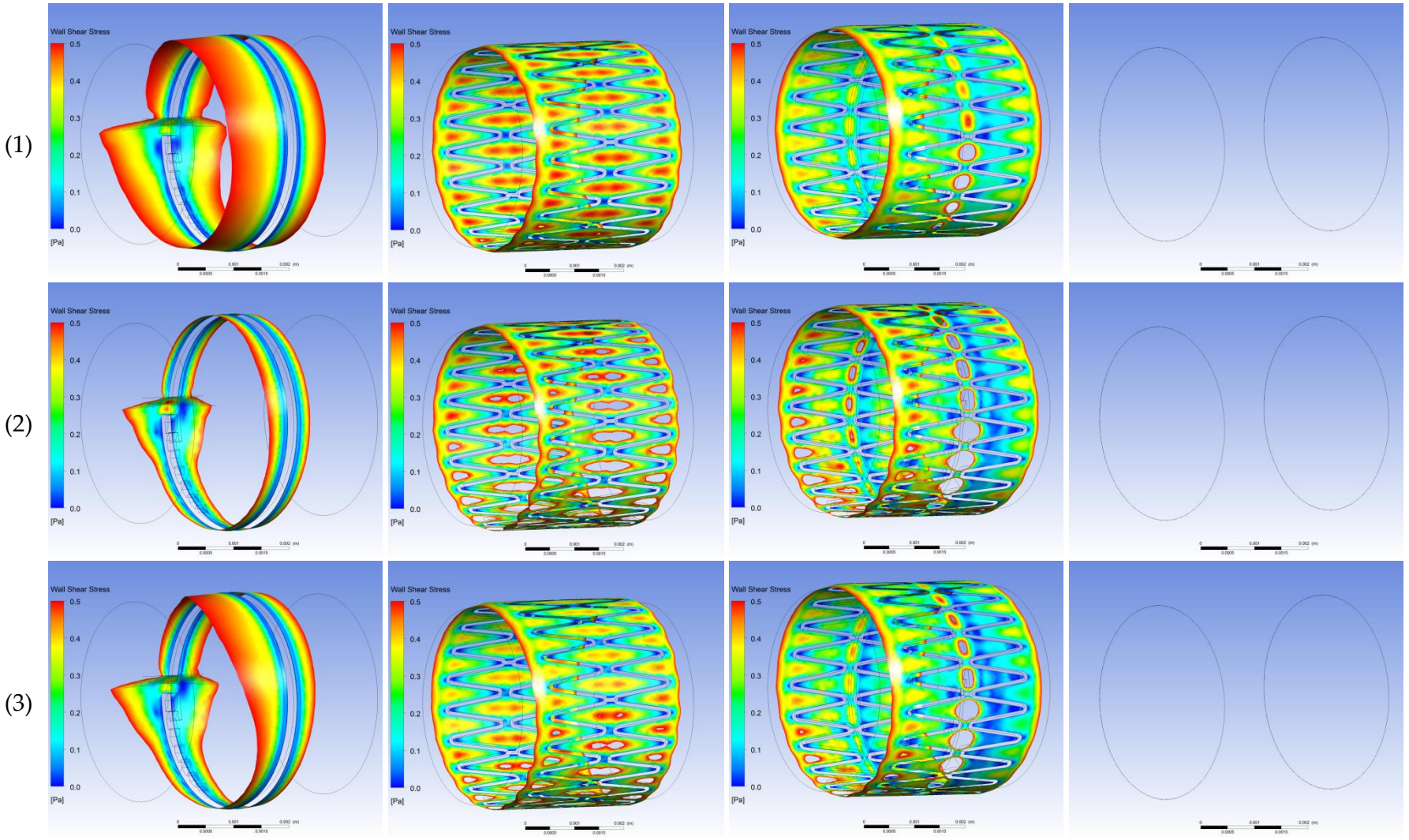

Figure 3.20. LWSS contour plots, deployment area of branched domains, instances 1–3. LWSS distribution in the deployment area of, a) the standalone RRR, b) the standalone stent, c) the RRR-integrated stent and, d) the unscaffolded domain representing a healthy vessel. Inlet is the left for all images. Empty wireframes in column (d) denote wall shear stress > 0.5 Pa in the healthy vessel.

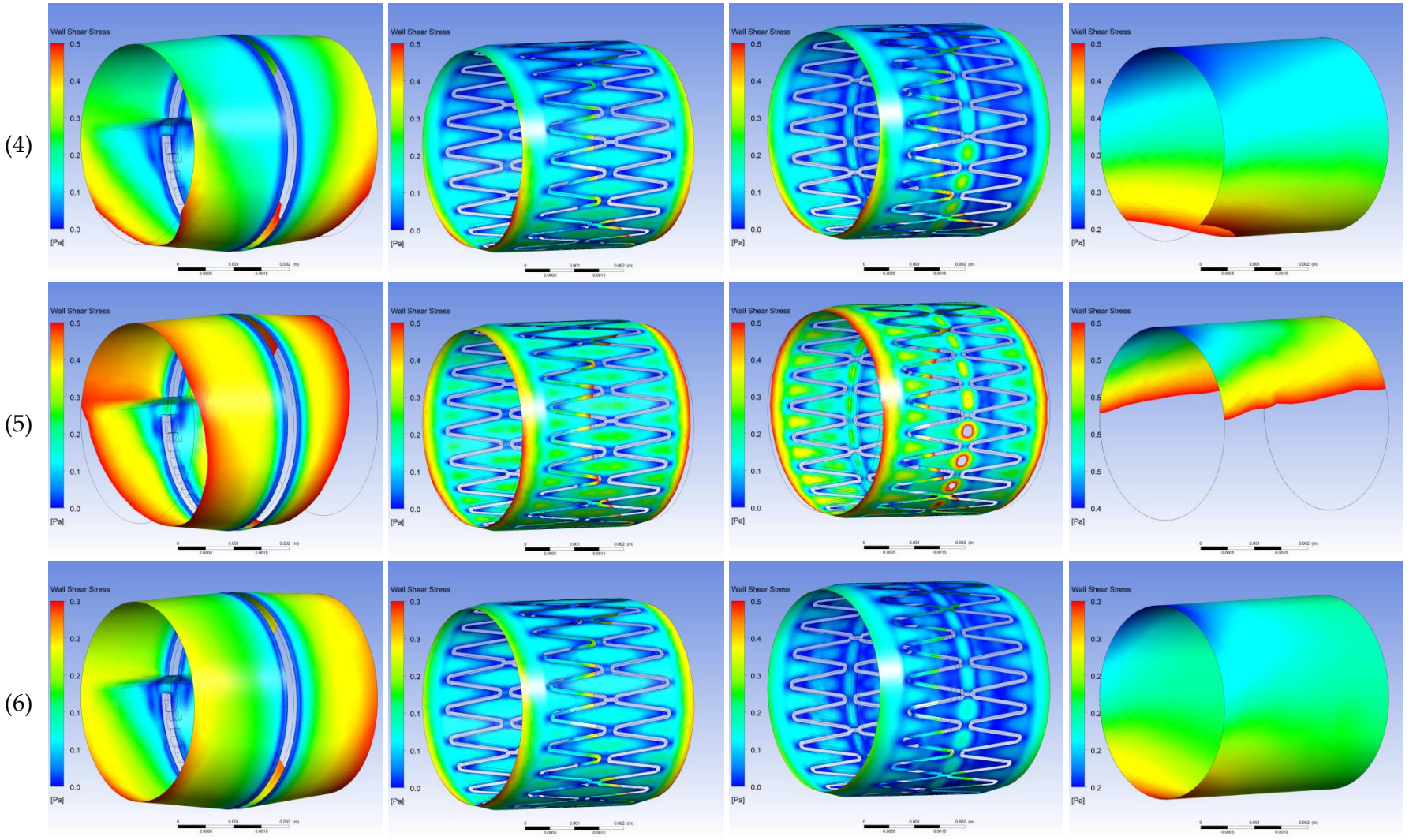

Figure 3.21. LWSS contour plots, deployment area of branched domains, instances 4–5. LWSS distribution in the deployment area of, a) the standalone RRR, b) the standalone stent, c) the RRR-integrated stent and, d) the unscaffolded domain representing a healthy vessel. Inlet is the left for all images.

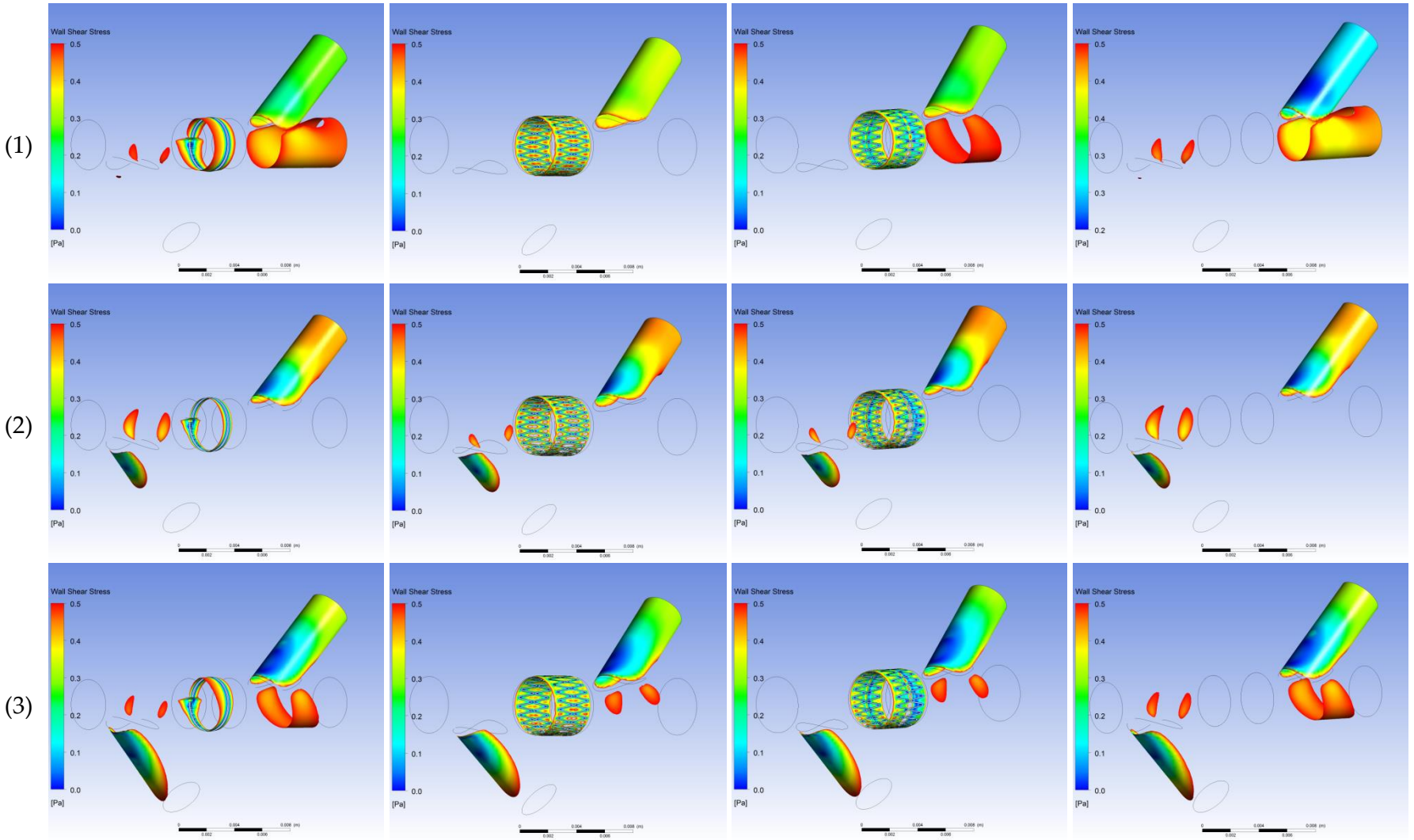

Figure 3.22. LWSS contour plots, entire area of branched fluid domains, time instances 1–3. LWSS distribution in the entire domain of, a) the standalone RRR, b) the standalone stent, c) the RRR-integrated stent and, d) and the unscaffolded domain representing a healthy vessel. The inlet is the left for all images.

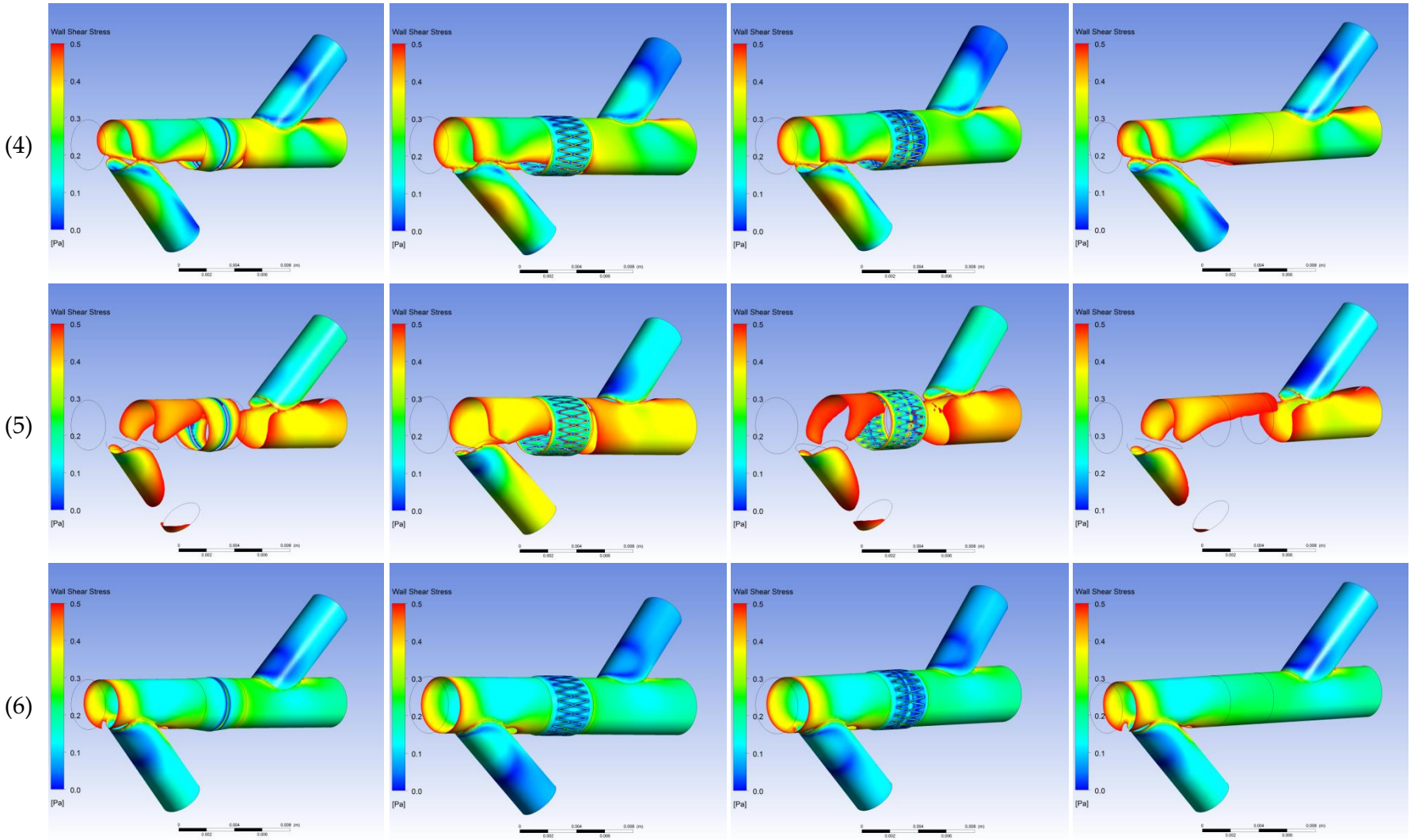

Figure 3.23. LWSS contour plots, entire area of branched fluid domains, time instances 4–6. a) LWSS distribution in the entire domain of, a) the standalone RRR, b) the standalone stent, c) the RRR-integrated stent and, d) and the unscaffolded domain representing a healthy vessel. The inlet is the left for all images.

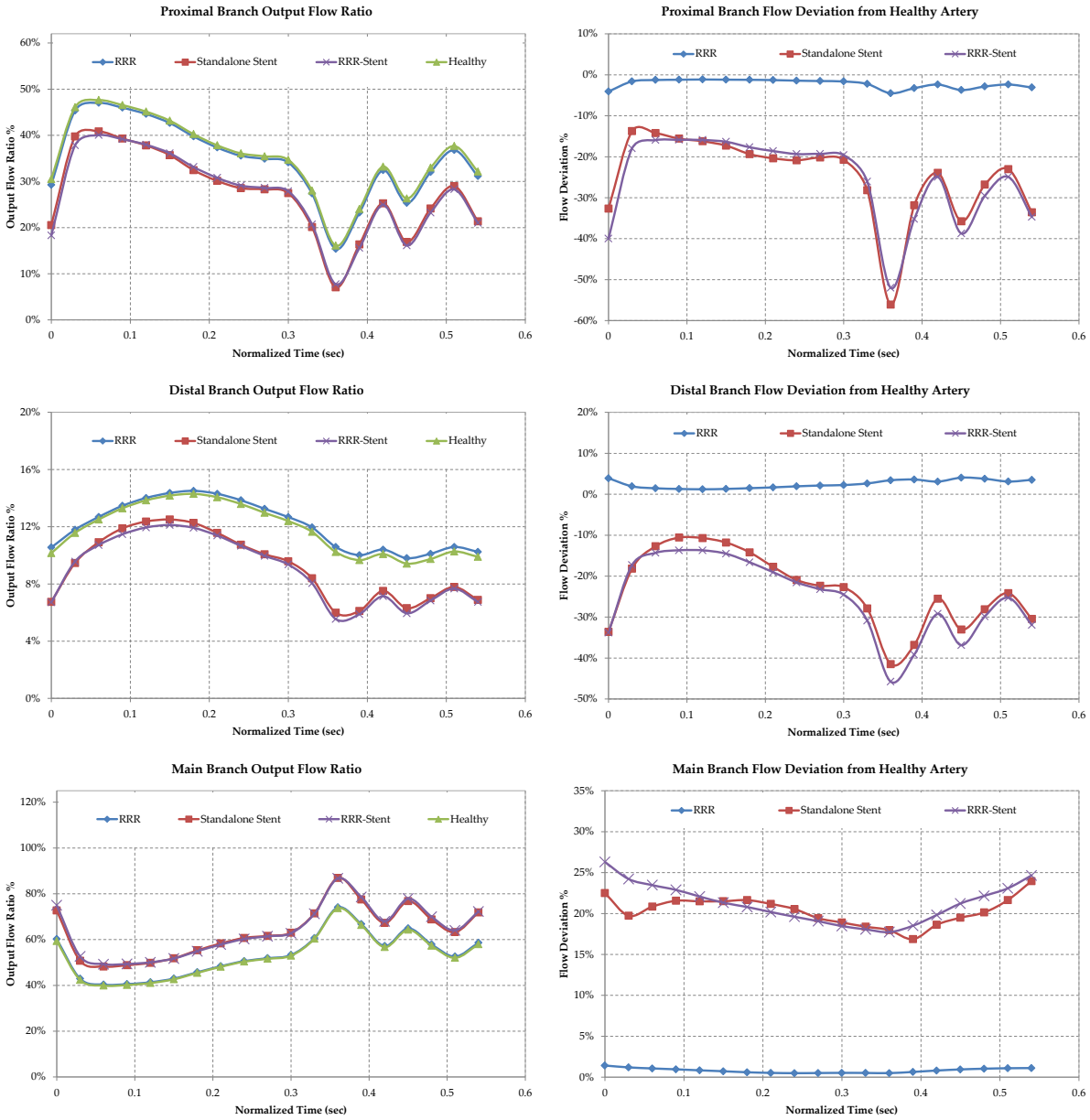

(a) (b)

Figure 3.24. Flow rate comparison of proximal, distal and main branches. a) Output flow ratio of proximal, distal and main branches, b) output flow rate deviation of proximal, distal and main branches from similar corresponding branches of a healthy vessel.

A lower output flow ratio compared to the healthy case in Figure 3.24 (a), thus a negative flow deviation in Figure 3.24 (b), indicates a reduction in the blood supply of the corresponding branch whereas a higher ratio (a positive deviation) indicates an increase in the blood supply of the corresponding branch. For instance, in the majority of scaffolded cases except for the standalone RRR, reductions in the proximal branch output flow ratios are observed that are accompanied by the slight reductions, yet not with the same ratio, in the output flow ratios of the distal branches. Consequently, due to the

conservation of mass, the flow supply to the main branches are slightly elevated as observed by the comparison of flow rate deviation trends in Figure 3.24 (b).

Apparently, any deviation from the healthy case, supplying more or less blood to a branch, is an undesired effect and is to be minimized in the design of luminal scaffolds. The cumulative (mean of absolute values) deviation of the flow supply of all branches of a scaffolded vessel from the corresponding branches of a healthy vessel is defined by:

$$\mathrm{FD}_{\mathrm{ma}} = \frac{1}{3}\sum_{i=1}^{3}\frac{\mathrm{abs}(f_{i,\mathrm{support}} - f_{i,\mathrm{healthy}})}{f_{i,\mathrm{healthy}}} \times 100 \qquad \textbf{(3.7)}$$

where $f_{i,\mathrm{support}}$ and $f_{i,\mathrm{healthy}}$ represent the parameters defined in Equations (3.6) and (3.7). These values, shown vs. time in Figure 3.25, are to provide the reader with an overall perspective of the blood supply changes resultant of the deployment of the aforementioned three scaffolds and more specifically to draw a comparison between the RRR-integrated stent and the standalone stent as the current state-of-the-art luminal implant.

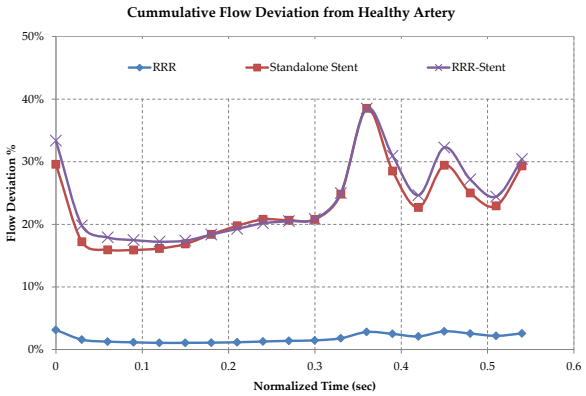

Figure 3.25. Mean absolute flow deviation from a healthy branched vessel. Transient values over a cardiac cycle, RRR-integrate stent (RRR-Stent) and the standalone stent trends correspond closely over the entire cycle.

As observed, once again the standalone RRR demonstrates its hemodynamic superiority over the other scaffolds causing the least amount of disturbance in the flow supply of different branches. Moreover the intertwined trends of the standalone and RRR-integrated stents shows minimal effect of integration of the RRR into the stent mesh in terms of flow obstruction.

Figure 3.26 summarises the temporal average values of the performance indicators discussed in this section over one cardiac cycle. As confirmed by the previous results, and

observed by the time-averaged values in this figure, the standalone RRR proves its hemodynamic superiority over the other two scaffolds exhibiting minimal difference between its hemodynamic indicators and those of the unscaffolded (healthy) vessel. Moreover, the RRR-integrated stent shows a hemodynamic performance that closely matches that of the standalone stent. This is further confirmed by the small difference (< 2%) in the average LWSS ratios in the deployment areas and absolute mean flow deviations between these two structures.

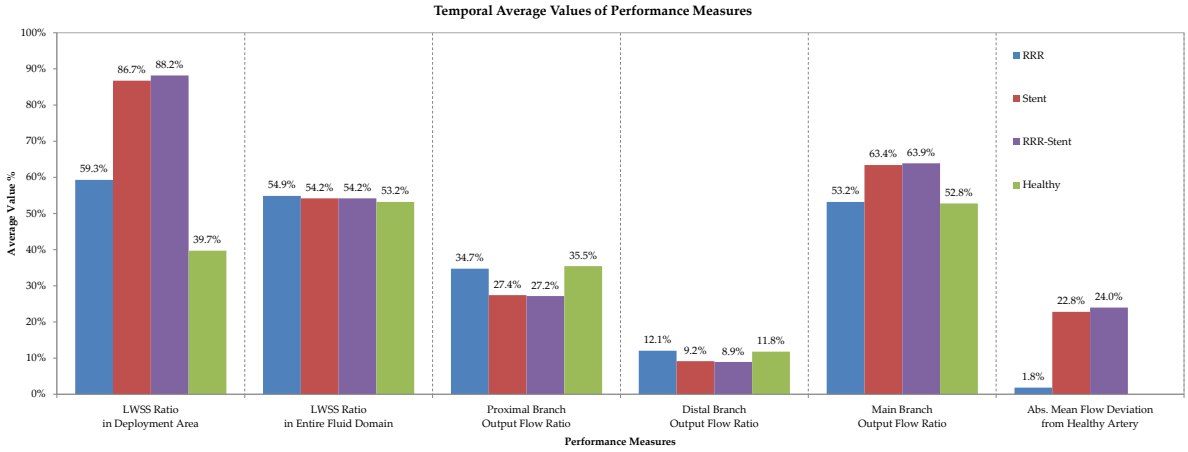

Figure 3.26. Temporal average values of hemodynamic indicators. Absolute (Abs.) mean flow deviation results are reported in comparison with the healthy vessel flow outputs. Of the three supports, RRR (standalone RRR) shows the least changes compared to the healthy vessel while the RRR-Stent (RRR-integrated stent) shadows the Stent (standalone stent) behaviour closely.

3.4.3 Part 3 – Dimensional Analysis

In Part 2 a detailed comparison between three luminal scaffolds including a standalone RRR, a standalone stent and an RRR-integrated stent was presented in a branched fluid domain with fixed dimensional assumptions for the scaffolds as well as the fluid domains. To further investigate the sensitivity of hemodynamic performance measures to dimensional assumptions of the scaffolds and the fluid domains, further comparative studies are conducted in this section. The hemodynamic superiority of the standalone RRR in lowering the extension of areas subject to LWSS, decreasing fluid migration force, and lowering flow deviation compared with the other two scaffolds is predicted to carryover despite the vascular size changes due to its smaller deployment footprint. On the other hand, in this section the emphasis is on the effect of integration of a regular stent

with the proposed RRR with different reference luminal diameters and different overlap lengths of the RRR. This objective is met through a comparative study between hemodynamic performance indicators of the standalone stent as the current state-of-the-art vascular scaffold and the proposed RRR-integrated stent. This is to provide more insight into the potential trade-offs of this new structure given its mechanical benefits detailed in Chapter 2 [103].

First the results associated with the two general groups of cases of Table 3.2, cases 1–4 and cases 5–8 are presented and compared. Next, the aggregated results from combination of all cases of 1–8 are presented. These studies, while provide a framework for comparison of the performance of the proposed RRR-integrated stent with a standalone stent in different deployment diameters, they can also benefit researchers by providing a further level of insight into the effect of dimensional assumptions of the fluid domains in the deviation of hemodynamic responses.

I. Dimensional Assumptions and LWSS

Ratios of luminal area subject to LWSS for the two separate groups of cases 1–4 and cases 5–8 of Table 3.2 are shown in Figure 3.27 (a) for a cardiac cycle. As indicated, all the RRR-integrated cases, cases 1–3 and 5–7, exhibit almost identical behaviours with very close to, sometimes even slightly less, ratios of areas subject to LWSS compared to those of the standalone deployment cases, cases 4 and 8. To provide a better comparison between the RRR-integrated cases and the standalone stents, the deviation of the area exposed to LWSS in RRR-integrated cases from the standalone stent cases can be expressed by:

$$\mathrm{AD}_{\mathrm{LWSS}} = \frac{A_{\text{RRR-Stent}} - A_{\text{Stent}}}{A_{\text{Stent}}} \times 100 \qquad \textbf{(3.8)}$$

where $A_{\text{RRR\_Stent}}$ is the amount of area (in the deployment area or entire fluid domain) that is subject to LWSS in an RRR-integrated stent deployment case (cases 1–3 or 5–7), and A_{Stent} refers to the amount of area (correspondingly in the deployment area or entire fluid domain) subject to LWSS in a corresponding standalone stent deployment case (case 4 or 8). Figure 3.27 (b) shows the values expressed by relation (3.8) in the deployment area of the two groups of cases 1–4 and 5–8 in a cardiac cycle. These results are in good agreement with the ones given in [158]. In this work, the authors conducted a parametric study on a commercial stent design modifying the strut thickness while assuming the

pulsatile flow used in this chapter and reported a slight reduction in the ratio of the area subject to LWSS by 3% on average as the stent strut thickness was increased from 0.05 mm to 0.15 mm. This conclusion is further confirmed by Figure 3.27 (b). As the ratio of the strut thickness to the reference luminal diameter increases (due to the integration of the RRR with the stent mesh, or increasing the overlap length, or reducing the reference luminal diameter) the LWSS ratio deviation values adopt greater negative values i.e. less luminal surface area is subjected to LWSS thereby reducing chances of restenosis.

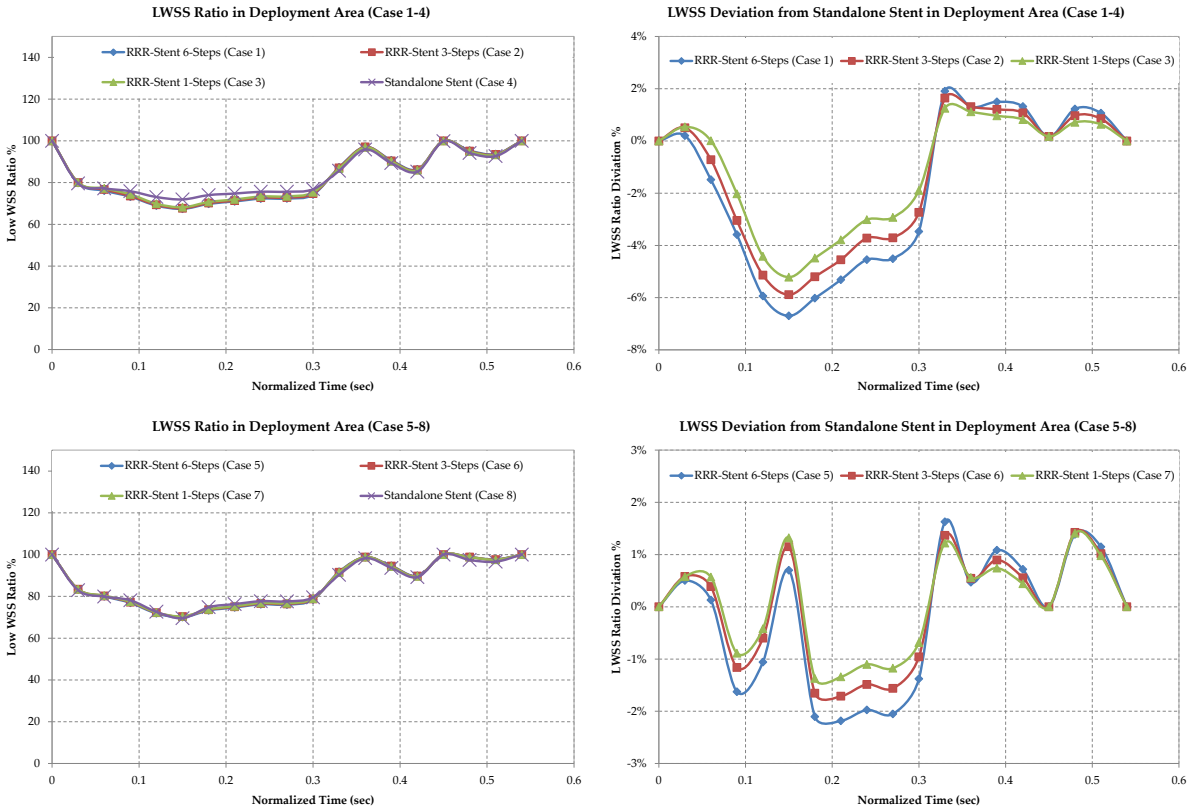

(a) (b)

Figure 3.27. LWSS in the deployment area of cases 1–8. a) Ratio of area subject to LWSS in the deployment area of cases 1–4 and cases 5–8, b) deviation of the ratio of areas subject to LWSS in the deployment area of cases 1–3 and 5–8 (RRR-integrated supports) from cases 4 and 8 (standalone stent) respectively.

As indicated by Figure 3.27 (b), the greatest negative deviation, thus the least LWSS ratio, is observed for the lowest reference diameter (2.5 mm) with the longest overlap length (case 1) at higher magnitudes and higher gradients of the velocity (diastolic perfusion and systolic heart injection). Apparently the extent of these benefits is limited to the point where further increase in the strut thickness starts to significantly alter flow supply to the main and side branches. Results of the effect of dimensional changes to the flow

supply of different branches are discussed in the following sections. Ratio of areas subject to LWSS in the entire fluid domains of the two groups of cases 1–4 and 5–8 are presented in Figure 3.28 (a). Once again, for better comparison of the RRR-integrated cases with the standalone stent deployment cases, deviations expressed by relation (3.8) for the entire fluid domain over time are presented in Figure 3.28 (b). The decreasing trend of areas subject to LWSS still continues for magnitudes of the velocity higher than the temporal average of the flow profile in time intervals 0.1–0.2 sec and 0.24–0.3 sec for cases 1–3. For other intervals of all cases the deviation adopts positive values.

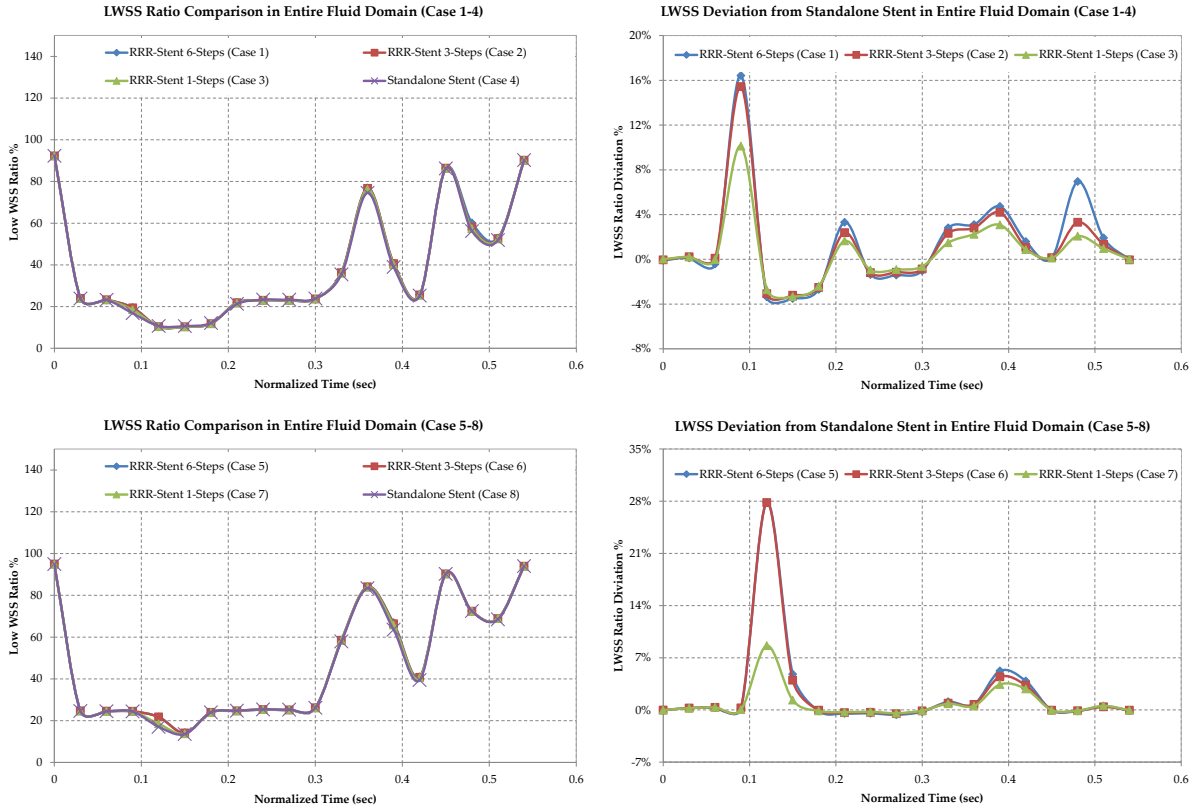

(a) (b)

Figure 3.28. LWSS in the entire fluid domains of case 1–8. a) Ratio of areas subject to LWSS in the entire domain of cases 1–4 and 5–8, b) deviation of the ratio of areas subject to LWSS in the entire domain of cases 1–3 and 5–7 (RRR-integrated stents) from case 4 and 8 (standalone stents) respectively.

II. Dimensional Assumptions, Drag Force and Flow Supply

Figure 3.29 shows the fluid drag force experienced by each of the supports of the two groups of cases 1–4 and 5–8 in a cardiac cycle. Comparing these results with the withholding forces of the standalone stent and RRR-integrated stent in Table 3.3, it is evident that all the structures are ensured from any migration or displacements given the signifi-

cantly higher withholding forces compared to the drag forces. By an increase in the overlap length, thus the deployment footprint, an increase in the fluid drag force is expected as confirmed by Figure 3.29.

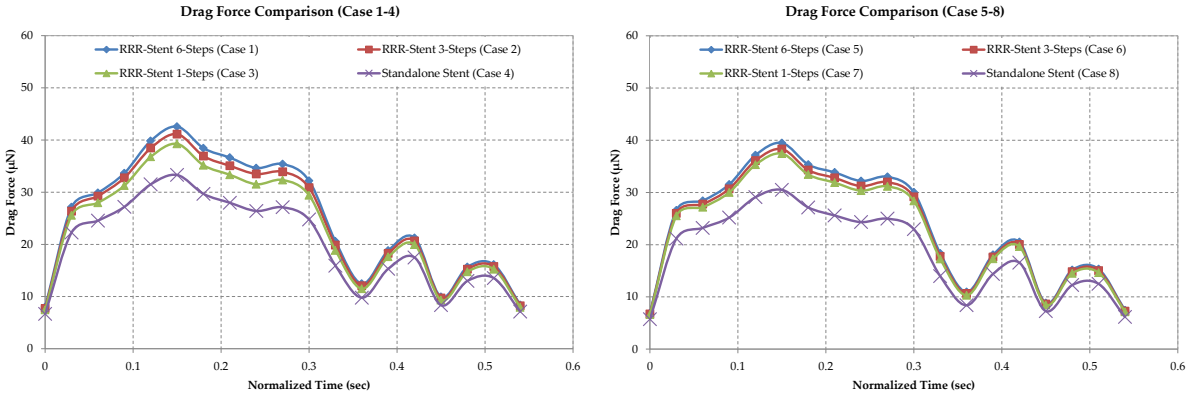

(a) (b)

Figure 3.29. Drag Force Comparison, cases 1–8. By increasing the overlap length, the deployment footprint increases that results in an increase in the drag force by the fluid flow.

As mentioned earlier, performance of luminal scaffolds is also mainly determined by the changes made to the flow supply of the main and side branches [80]. In this section, main and side branch flow supply of the RRR-integrated stent deployment cases of Table 3.2 are compared with the corresponding standalone stent cases. Figure 3.30 (a) presents the output flow ratio, as defined by relation (3.5), of the proximal branch for the two groups of cases 1–4 and 5–8. As shown by these trends, all the RRR-integrated supports exhibit a very close behaviour to those of their corresponding standalone stent counterparts. To provide a better comparison between all these cases, the proximal outlet flow rate deviations of the RRR-integrated stents from those of the corresponding standalone stents in a cardiac cycle are presented in Figure 3.30 (b). Outlet flow rate deviations in these figures are expressed by Equation (3.9):

$$\mathrm{FD}_{i,\text{RRR-stent}} = \frac{f_{i,\text{RRR-stent}} - f_{i,\text{stent}}}{f_{i,\text{stent}}} \times 100 \qquad \textbf{(3.9)}$$

where $f_{i,\text{RRR-stent}}$ for i = 1, 2 and 3 respectively refers to the proximal, distal and main branch output flow rates of a fluid domain deployed with an RRR-integrated stent and $f_{i,\text{stent}}$ refers to the corresponding outlet flow rates of a fluid domain deployed with a standalone stent and identical reference diameters of the fluid domain of the RRR-integrated stent. As indicated by this figure, integration of an RRR with a stent mesh

does not significantly alter blood supply to the proximal branch compared to a standalone stent, while increasing it by less than 6% at most at time interval 0.3–0.4 sec indicated by Figure 3.30 (b). This value is expected to decrease in RRR-integrated supports with shorter overlap lengths that result in lower average thickness of the scaffold as observed in in this figure.

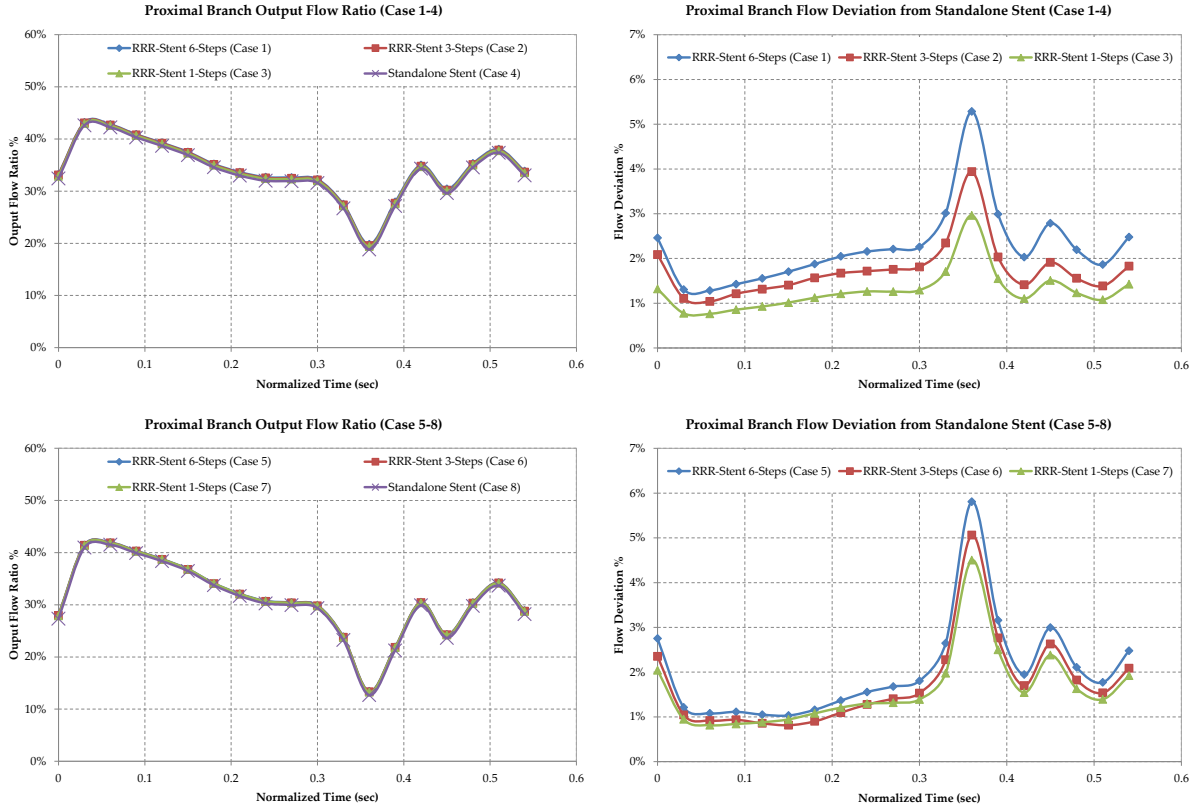

(a) (b)

Figure 3.30. Proximal branch to inlet flow rate ratio, cases 1–8. a) Output flow rate ratio of the proximal branch of cases 1–4 and 5–8 to the inlet flow rate, b) output flow rate deviation of the proximal branch of cases 1–3 and 5–7 (RRR-integrated stent) from cases 4 and 8 (standalone stent) respectively.

The outlet flow ratios of the distal branch in a cardiac cycle for cases 1–4 and 5–8 are presented in Figure 3.31 (a). These results are complemented by the deviational results of the RRR-integrated supports from the standalone stents in Figure 3.31 (b) that are calculated by Equation (3.9) for i = 2 (distal branch). Comparison between Figures 3.30 (b) and 3.31 (b) shows an inverse correlation between the flow supplies of proximal and distal branches where an increase in the flow supply of one results a reduction in the other. Nevertheless this proportionality is not a one-to-one relation. For instance, the reduction

in the flow supply of the distal branch never exceeds 5% while flow surplus of the proximal branch may reach as high as 6% (time interval 0.3–0.4 sec).

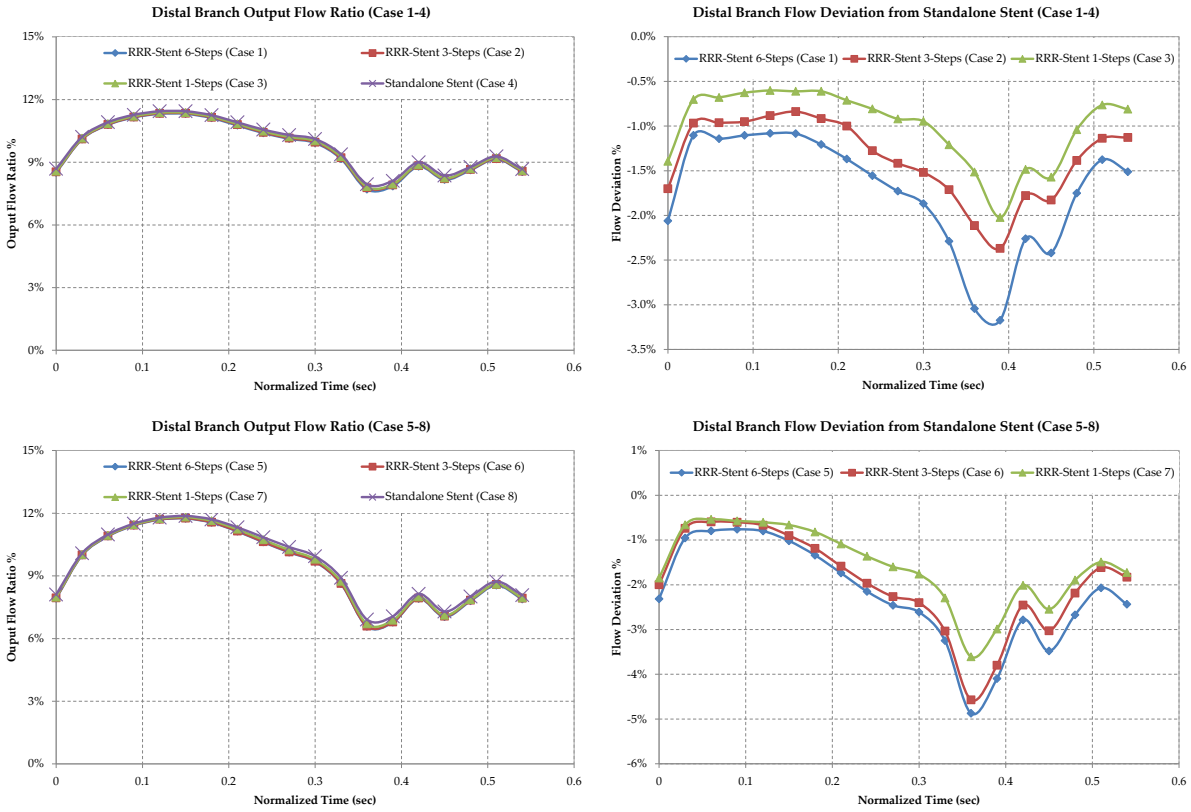

(a) (b)

Figure 3.31. Distal branch to inlet flow rate ratio, cases 1–8. a) Output flow ratio of the distal branch of cases 1–4 and 5–7, b) output flow rate deviation of the distal branch of cases 1–3 and 5–7 (RRR-integrated stent) from cases 4 and 8 (standalone stent) respectively.

As indicated by the main branch output flow ratios in Figure 3.32 (a) and the deviational results in Figure 3.32 (b), it is clear that the main branch flow supply undergoes the least changes compared to the proximal and distal ones. As shown by Figure 3.32 (b), these changes are limited to a maximum of 1.2% reduction in the downstream blood supply where case 1 reaches the end of a cardiac cycle at the lowest velocity of the blood flow. At higher velocities, the deviations for the cases 1–4 stay relatively constant while undergoing changes in the second half of the cardiac cycle. The mean cumulative results of the proximal, distal and main branch outputs of the RRR-integrated cases (case 1–3 and case 5–7) with respect to their corresponding standalone stent case (cases 4 and 8 respectively) are presented in Figure 3.33. In order to capture the overall comparative behaviour of all these structures over a cardiac cycle, temporal average values of the performance measures discussed so far are presented in the histogram of Figure 3.34.

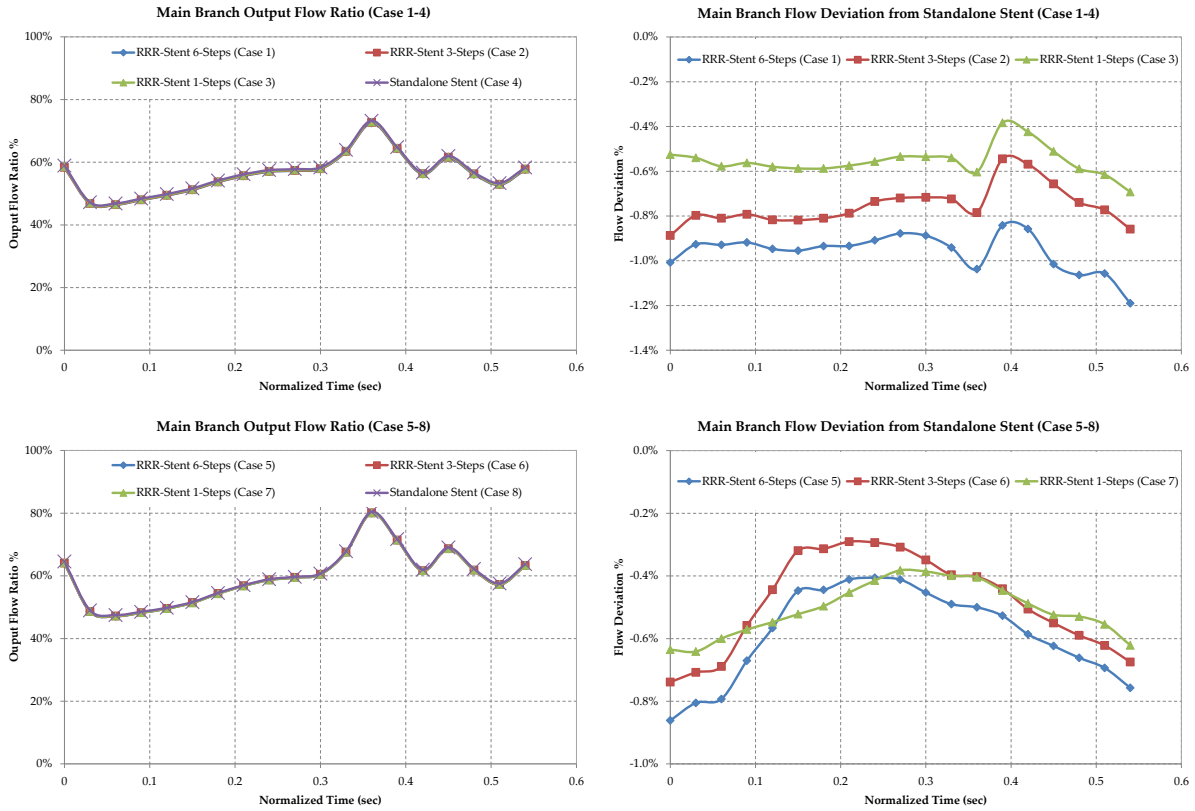

(a) (b)

Figure 3.32. Main branch to inlet flow rate ratio, cases 1–8. a) Output flow ratio of the main branch of cases 1–4 and 5–8, b) output flow rate deviation of the main branch of cases 1–3 and 5–7 (RRR-integrated stents) from cases 4 and 5 (standalone stent) respectively.

The results given so far in Part 2 and 3 all indicate minimal hemodynamic effect of the presence of the RRR in a stent mesh compared to its current standalone stent counterpart assuming a realistic transient cardiac cycle. As mentioned before, in cases 1–8, the introduction of the RRR improved the LWSS distribution in the deployment area by slightly decreasing its average value by at most 1%. This reduction grows gradually as the ratio of strut thickness to the luminal diameter increases by first introducing the RRR, then increasing the RRR overlap length, and finally decreasing the reference diameter of the main branch. These results indicate even the beneficial effect, albeit small, of integration of the RRR in the LWSS distribution in the deployment area of branched lumens with a main branch reference diameter of less than 4 mm.

In turn, the LWSS in the entire fluid domain is slightly increased by at most 0.6%. Moreover, contrary to the trend of the LWSS distribution in the deployment area, in the entire fluid domain, the average value of LWSS faintly increases as the ratio of strut thickness to luminal diameter grows by increasing the overlap length, or decreasing the reference

diameter of the lumen. Transient mean values and standard deviations of these measures over cases 1–8 are further discussed in the next section.

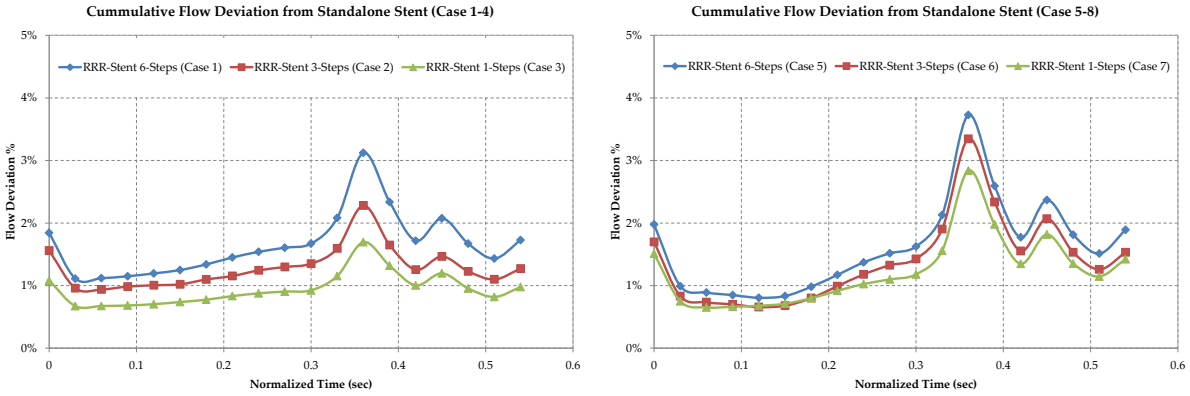

(a) (b)

Figure 3.33. Mean absolute flow deviation. a) Mean absolute flow deviation of cases 1–3 (RRR-integrated stents) from case 4 (standalone stent), b) mean absolute flow deviation of cases 5–7 (RRR-integrated stents) from case 8 (standalone stent).

The absolute mean flow deviation results for cases 1–3 and 5–7 in Figure 3.34 are reported with respect to their corresponding standalone stent counterparts, cases 4 and 8 respectively. Given these values, the effect of integration of RRR with a stent is almost negligible in the blood supply of different branches with a maximum deviation of 1.7% from the standalone stent cases. Moreover, for constant luminal dimensions (case 1–4 or 5–8) increasing the overlap length of the RRR increases mean flow deviation values by at most 0.8%, while maintaining the same overlap profile and increasing the luminal diameter from 2.6 to 3.2, increases the mean flow deviation by at most 0.3%.

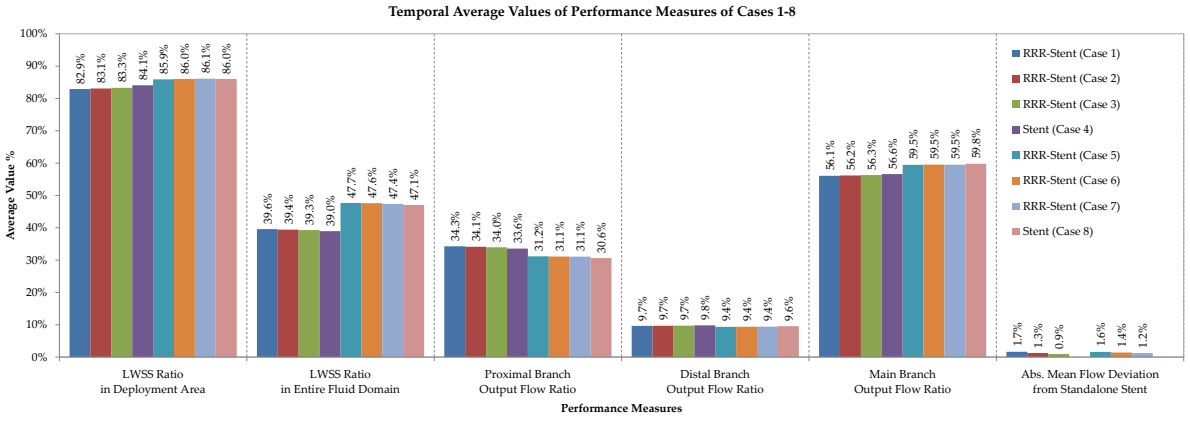

Figure 3.34. Temporal average values of hemodynamic indicators, cases 1–8. Absolute mean flow deviation results of cases 1–3 and 5–7 are reported in comparison with cases 4 and 8 respectively. Scaffolds pertaining to the same groups (cases 1–4 or 5–8) show very similar hemodynamic responses.

III. Dimensional Assumptions, Final Notes

The transient mean values of some of the performance measures discussed above, calculated over results of cases 1–8, vs. time are given in this section. These results are complimented by the standard deviation of these values to provide a predictive guideline on the expected changes in the values of hemodynamic indicators of a scaffolded vascular model in response to the changes in the dimensional properties of the model. As mentioned in the previous section, herein these changes include modifying luminal reference diameter, increasing the effect thickness of the scaffold by introduction of the RRR and changing its overlap length. Figure 3.35 (a) presents the mean value of LWSS ratios in the deployment area as well as the entire fluid domain for cases 1–8 in a cardiac cycle.

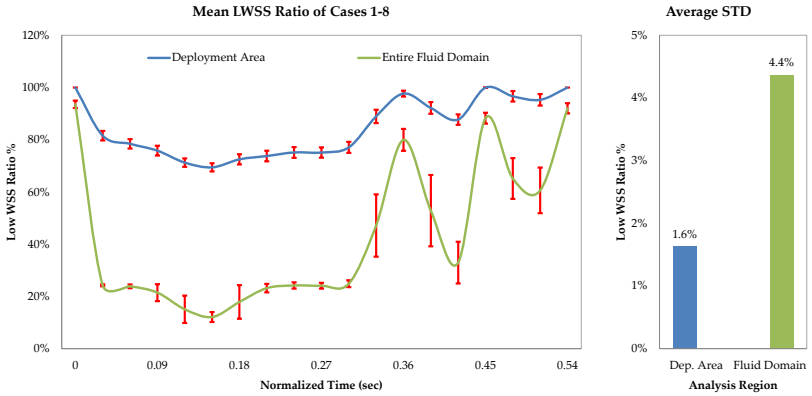

(a) (b)

Figure 3.35. Temporal distribution of the mean LWSS ratios, cases 1–8. a) Trends of the mean values of LWSS ratios for cases 1–8 in the deployment area and the entire fluid domain, vertical bars at each time stamp represent the standard deviation (STD), b) temporal average of the standard deviation for the deployment area and the fluid domain.

Length of vertical bars on each time stamp represent the standard deviation of all these values for cases 1–8 with the temporal average values of standard deviation shown on the histogram of Figure 3.35 (b). As indicated by the low height of standard deviation bards for at the majority of time instances, and confirmed by the small difference between the temporal average values shown in Figure 3.34, the difference between the values of LWSS ratios for all cases 1–8 at different time stamps is almost insignificant remaining unchanged through the cardiac cycle. Conversely, at time intervals with high velocity gradients, the LWSS ratio deviations marginally increase compared to the smaller deviations at intervals with lower velocity gradients.

Mean and standard deviation values of the drag force for cases 1–8 are shown in Figure 3.36 (a) with the temporal average of the standard deviations presented in Figure 3.36 (b). Contrary to the previous results, the differences between different cases are more prevalent during the first half of the cycle where the flow adopts its highest values. Despite these deviations, this trend clearly shows the efficacy of withholding forces to withstand stents against even the highest drag forces.

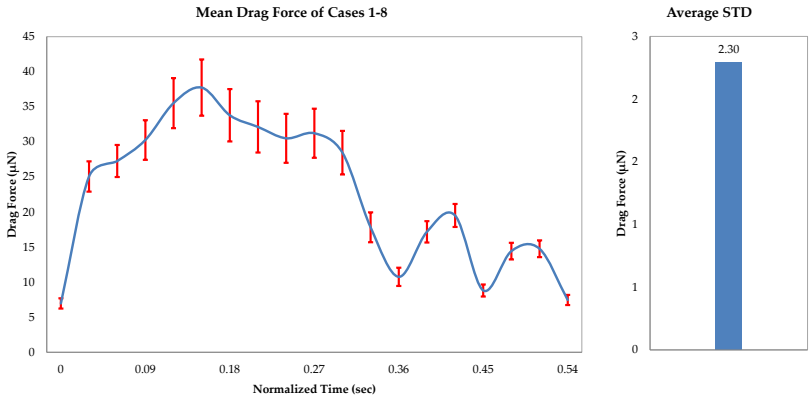

(a) (b)

Figure 3.36. Temporal distribution of mean drag force, cases 1–8. a) Mean values of drag force for cases 1–8 over time. The vertical bars represent the standard deviations at the corresponding time stamps. Highest deviations occur at highest velocities, b) temporal average of standard deviation of drag forces of cases 1–8.

Mean values of output flow rate to inlet flow rate ratio of the proximal, distal and main branches for cases 1–8 over time in a cardiac cycle are plotted in Figure 3.37 (a). A histogram of the temporal average of standard deviations of these values is shown in Figure 3.37 (b). As these trends indicate and confirmed by the temporal average values of Figure 3.34, domain and scaffold dimensional changes have a trivial effect on the flow ratios of the outputs with the highest standard deviations occurring during the systolic phase (0.34–0.54 sec) where flow adopts lower velocities. In contrast, all the trends undergo little change at higher velocities of the flow at the diastolic phase (0–0.34 sec).

3.5 Chapter Summary

In this chapter computational fluid dynamics (CFD) of the new recoil resilient luminal support deployed as a standalone scaffold or integrated with a stent are studied. Hemodynamic indicators such as temporal and spatial distribution of the low wall shear stress (LWSS), the drag force experienced from the fluid flow and the blood supply changes to

the main and side branches are extensively investigated. The results are compared with those of a standalone stent and an unscaffolded (healthy) vessel. Comparison with a standalone stent provides a benchmark, which represents the hemodynamic performance of current state-of-the-art stents, while the results from a healthy vessel provide the reference performance for any luminal scaffold.

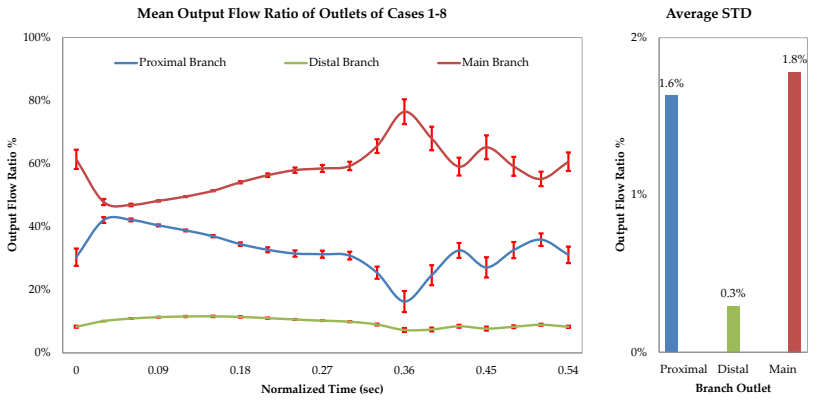

(a) (b)

Figure 3.37. Temporal mean flow ratios, cases 1–8. a) Temporal distribution of the mean ratio of output flow rates of proximal, distal and main branches to the inlet flow rate. The vertical bars represent the standard deviations at the corresponding time stamps. Highest standard deviations occur for lower flow velocities with little changes during the first half of cycle where the flow adopts higher velocities, b) temporal average values of the standard deviations for the proximal, distal and main branch.

A realistic periodic flow profile is applied to the inlet of the models in an extensive series of transient 3D studies first comparing all the aforementioned configurations in unbranched fluid domains followed by the studies in branched fluid domains. From the transient results of the unbranched fluid domains, the standalone RRR prevails having the best hemodynamic performance exhibiting the least ratio of areas subject to LWSS. Despite the slight difference between the LWSS ratios of the standalone stent and the RRR-integrated stent during the diastolic phase of the cardiac cycle (first half), the differences settle to almost zero for the next half of the cycle. This results in close temporal average values of the LWSS in the deployment areas and identical values for the entire fluid domains. Comparisons of the withholding and drag forces for all the scaffolds show the efficacy of the former to keep them in place even for the highest flow velocity magnitudes over time. The standalone RRR remains as the best of the three supports in the branched domains resulting in the least branch flow supplies from the corresponding

branch flow supplies an unscaffolded (healthy) domain and the lowest ratios of areas subject to LWSS compared to the other two scaffolds. The temporal trends of LWSS ratio for the standalone stent and the RRR-integrated stent are closely intertwined through the entire cardiac cycle decreasing the difference to as low as 1% on average in the deployment area and identical values for the entire fluid domain.

Deviation of output flow rates in the side and main branches of the standalone and RRR-integrated stent domains from corresponding branches of a healthy vessel, follow similar trends. These results demonstrate the efficacy of the RRR-integrated stent to deliver a hemodynamic response at least as good as the current state-of-the-art stents considering its superior resilience benefits over the later as demonstrated by the high radial strength of the RRR in comparison to a commercial stent in Chapter 2.

Sensitivity of the results to the dimensional assumptions of the fluid domains and scaffolds in the branched arteries is then studied. In these studies, hemodynamic performance indicators of the RRR-integrated stents, with different overlap lengths from the two ends of the RRR and different reference luminal diameters, are compared with corresponding standalone stents. The results are in good agreement with the ones pertaining to the branched domain analysis conducted earlier once again demonstrating a close resemblance between the hemodynamic behaviour of the standalone and the RRR-integrated stents. Moreover, in the RRR-integrated stent deployment cases in smaller arteries and with longer overlap lengths from the two ends of the RRR, less ratio of area subject to LWSS is observed compared to similar deployment cases of standalone stents. Comparison of all the study cases reveals small standard deviations for the LWSS ratios at the deployment area while becoming relatively greater for the LWSS ratios in the entire fluid domain. Differences of the outlet flow ratios are insignificant for the high flow velocities while relatively increasing for lower velocity magnitudes. Temporal average values of the performance indicators show very little dependence of our results on the dimensional assumptions of the fluid domain and RRR's overlap length showing the merit of both the standalone RRR and the RRR-integrated stent as viable biomedical implants for luminal constrictions.

So far Chapters 2 and 3 demonstrated mechanical benefits of the new RRR and its conformance with the current state-of-the-art stenting standards. High recoil resilience and

radial strength of the RRR in comparison with commercial stents as well as its deployment capability by current angioplasty balloon expansion technique was demonstrated in Chapter 2. Moreover, RRR's hemodynamic implications after deployment and its conformance with current expected hemodynamic response of a luminal support were demonstrated here in Chapter 3. The interlocked, thus incremental, expansion mechanism of the RRR, its high transformation temperature in comparison to its deployment environment (human body) temperature, it thermally trained expanded shape, and the shape memory effect of Nitinol can potentially be utilized for alternative expansion mechanisms. In chapter 4 these actuation mechanisms as alternatives or complimentary to the current expansion by an angioplasty balloon are investigate.

Chapter 4

Thermal Actuation of the Recoil Resilient Ring

Apart from balloon expansion mechanism discussed in Chapter 2, the recoil resilient rings (RRR) have the potential to be actuated by application of heat. This is possible due to the shape memory effect of Nitinol utilized in fabrication of the RRRs. So far, these structures were considered in the more flexible martensite state of their material where plastic deformations are readily achieved. Nevertheless, as Nitinol undergoes microscopic changes in response to thermal stimuli, it can recover high strain rates up to 10% in the austenite state promising alternative expansion mechanisms for the RRR.

Therefore, in this chapter expansion of the proposed RRR in Chapter 2 by application of heat, and later electrical currents is explored. To demonstrate feasibility of such alternative actuation mechanisms, extensive analytical and numerical studies are conducted that are complimented by experimental studies.

4.1 Abstract

In the previous chapters scaffolding and hemodynamic benefits of the new RRR design were discussed through several experimental and numerical studies. The conformity and easy expansion of the RRR using current state-of-the-art angioplasty balloons were demonstrated in Chapter 2 where the superior radial resilience of the RRR was demonstrated and compared to a commercial stent. In Chapter 3, the influence of the presence of the RRR as a standalone or integrated support on the extension of areas with low wall shear stress, as a harbinger of later restenosis, compared to current stent structures was demonstrated. The shape memory properties of Nitinol used for fabrication of the RRR and the specific thermally trained shape of the RRR at its expanded state may further be utilized to explore other methods of actuation such as by heat. Having a transformation temperature, higher than the deployment region's temperature (body temperature), it is possible to force the normally martensite RRR into the austenite phase that can potentially exert high radial expansion forces. In this chapter these possibilities are explored through several studies. First, a heat-induced expansion scenario *in vitro* is studied by initially ensuring safe operation temperature values that are experienced by a mock vessel through theoretical, numerical and experimental studies. Our results indicate that the temperature of all parts of the mock vessel during application of heat to the RRR and before its expansion fall below the recommended operation range. Furthermore, free and *in vitro* expansion of the RRR via application of heat are observed and measured in an experimental study. Secondly, the radial forces exerted by a constrained RRR that is under stimuli of heat are measured experimentally. Finally, using the results from the first two parts, an alternative actuation mechanism by application of an electric potential across the RRR is proposed and examined through theoretical and numerical studies. At the end, further suggestions are given as a continuation of this work.

4.2 Introduction

Shape Memory Alloys (SMA) such as Nitinol are new generations of materials that have the ability to recover a pre-memorized shape when heated beyond a specific temperature referred to as the transformation temperature. At this state of the material, called austenite phase, the crystallographic structure of the material starts to align beyond the starting

transformation temperature (A_s) and reaches its peak at a higher temperature referred to as the finishing temperature (A_f). This range of temperature is a characteristic of the material that heavily relies on the slight changes in the ratio of nickel compound compared to the titanium as well as the preparation conditions of the raw material and the final device [94, 239]. Therefore, A_f may be engineered for specific applications ranging from -200˚C to 110˚C. While cold, or below the transformation temperature, the SMA has a low yield strength rendering it easily deformable into new shapes through a combination of superelastic and plastic strains. This state of the material is called the martensite state. However, upon heating beyond the transformation temperature, the SMA undergoes changes in its crystalline structure that promote the material recover its original shape while reaching the austenite phase. In this process, if the material is constrained, it exerts extremely large forces that may be utilized for actuation [95, 239].

The stress-strain curve of a typical martensite SMA such as Nitinol is shown in Figure 4.1 for both the martensite and austenite phases. Shape memory effect is illustrated by Figure 4.1 (a), when the temperature is well below the transformation temperature. In this state the material is easily deformable due to the low stiffness exhibited by an initial linear elastic curve followed by the superelastic response from point A to B resulting in large deformations for small values of stress. Upon unloading, part of the deformation is recovered through elastic recovery though leaving residual deformations at point C. Raising the temperature of the material above A_f at this stage, induces a martensite to austenite phase shift causing the structure recover the leftover strain from point C to the initial shape. This effect is referred to as the one-way shape memory effect.

Figure 4.1 (b), demonstrates the stress strain response of the Nitinol in the austenite phase while the temperature of the material is maintained above A_f. The forward path upon loading, demonstrates the high stiffness of the material at the early stages of stressing, followed by the stress-induced forward phase transformation from austenite to martensite and the resultant superelastic response from point A to B. In this state, large deformations are achieved with small increases in stress. During unloading, the sample first exhibits an elastic recovery curve from point B to C, after which the stress- relieved reverse martensite transformation (martensite to austenite) is observed from point C to D. After finishing the loading and unloading cycle, Nitinol does not exhibit any residual

strain, nevertheless, due to the different paths of loading and unloading curves, a hysteresis loop is observed.

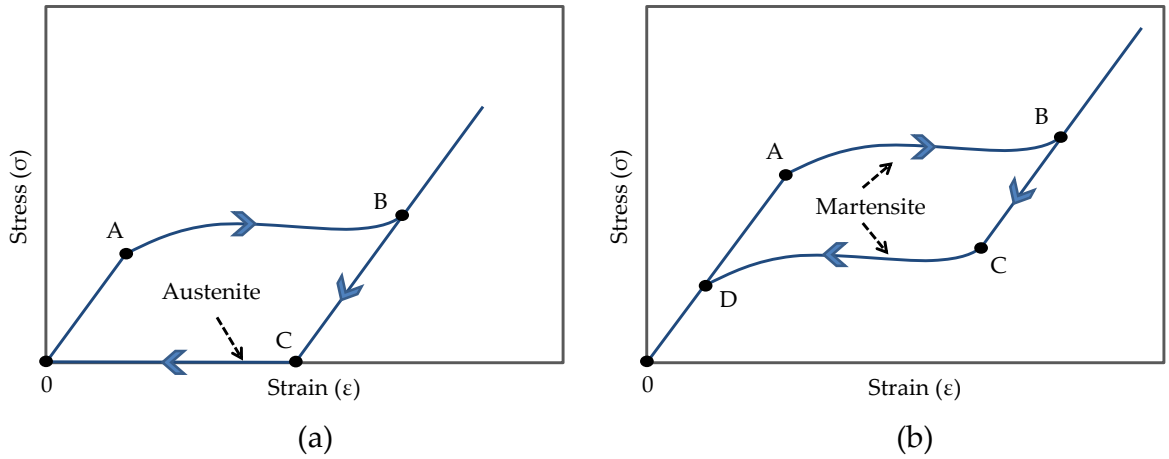

Figure 4.1. Stress-strain curve of a shape memory alloy. a) Shape memory effect, superelasticity from point A to B followed by residual plastic deformations in the martensite state from B to C, by increasing the temperature beyond A_f, the unconstrained material recovers its initial shape resulting in zero residual strains returning to 0 from C, b) superelasticity of the austenite material at temperatures beyond transformation temperature , $T > A_f$, material is stressed elastically to point A, then enters into stress induced martensite phase indicated by the superelastic response from A to B. Unloading from B to C starts the reverse phase transformation from martensite to austenite that is culminated in the superelastic recovery from C to D.

It is important to note the difference between the martensite characteristics (more specifically stress levels) of the material due to temperatures lower than the transformation temperature compared with the stress induced martensite characteristics while the material's temperature is maintained above the transformation temperature.

As discussed in the previous chapters, the flexible martensite operation of the RRR *in vivo* is realized by choosing the transformation temperature of the Nitinol to be well above the human body's temperature, A_f = 45–80 °C. In this state, due to the low values of modulus of elasticity and yielding stress, it is easy to shape the structure by plastic deformations. The benefits of these properties of the RRR are twofold. It makes both the crimping and balloon expansion possible at pressures lower than those required for BE stents as demonstrated in Chapter 2. Resilience of the RRR, on the other hand, is facilitated through the interlock mechanism, detailed in Chapter 2, which provides a strong scaffold after each tooth traversal withstanding forces up to 2.7 times more than those of a BE stent. The RRR's martensite mode of operation necessitates the use of an external

expanding device such as an angioplasty balloon for deployment inside a duct. In contrast, given the high strain recovery of the austenite Nitinol by around 10% [95, 239], further potential actuation and/or adjustment schemes would become beneficial either in conjunction with or as a replacement to the use of angioplasty balloon expansion. This mode of expansion may be used for subsequent radial adjustments after initial deployment, should restenosis or recoil occur in the future.

4.3 Materials and Methods

The RRR prototype introduced in Chapter 2 is micromachined from Nitinol sheets of 0.2-mm thickness with the starting transformation temperature (A_s) ranging 50–60°C and a final transformation temperature (A_f) of 80°C. Both these temperatures are well above the typical human body temperatures of 37°C. It is important to note that the thermal actuation methods described in this section are not unique for any specific SMA and may be applied to Nitinol structures with lower A_f, e.g. 45–50°C, for safe operation *in vivo*. In order to study the actuation of the crimped RRR through thermal excitation and evaluate the capability of the outward forces to expand against vascular walls, two *in vitro* methods are proposed in this chapter.

In the first method, using a heat transfer (HT) rod, temperature of a deformed (crimped) RRR in the martensite state is raised slightly above the transformation temperature A_f while suspended inside a mock vessel. Expansion of the RRR inside the mock vessel as a result of phase change from martensite to austenite followed by teeth interlock and subsequent cooling is confirmed visually and through measurement of the outer diameter of the RRR in a free expansion scenario. Due to the high value of A_f for the Nitinol sample available, and in order to ensure safe operation of the mock vessel in this setup while close to the HT rod, analytical, numerical and experimental studies were conducted to evaluate the distribution of heat in the mock vessel. Moreover, to quantify the radial forces exerted by a constrained crimped RRR, these forces are experimentally measured at different temperatures while Nitinol undergoes phase transformation from martensite to austenite. In the end, an alternative method is proposed for the generation of heat in an RRR utilizing an electric current and Joule heating in electronic components for actuation of the ring.

For heat-induced *in vitro* actuation of the RRR, the setup demonstrated in Figure 4.2 is utilized that is comprised of two major parts, the base and the mock-rod assembly.

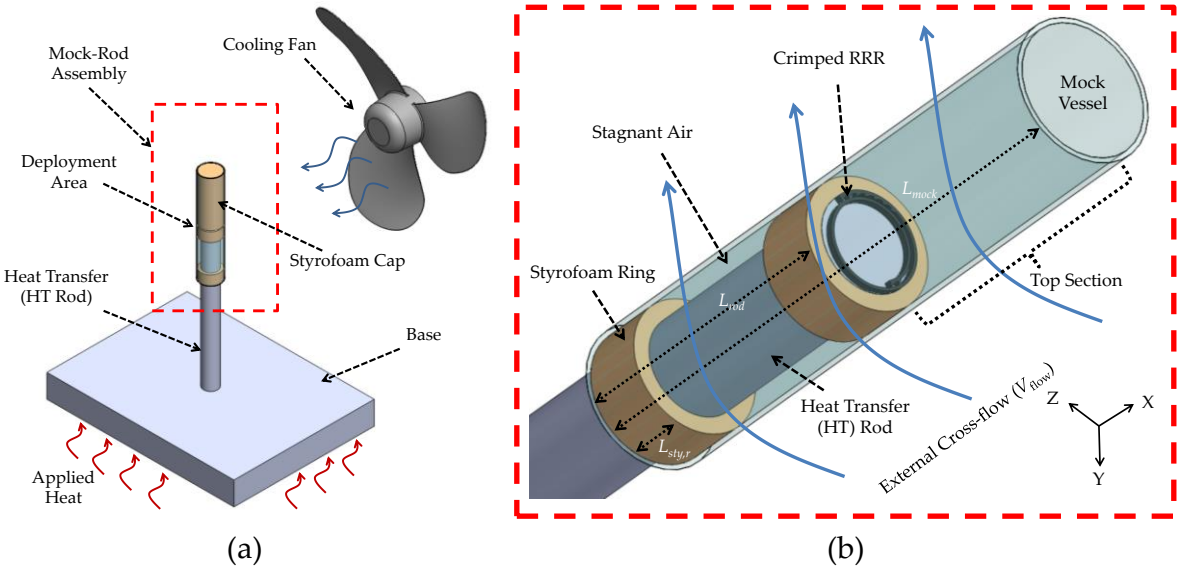

Figure 4.2. Heat transfer setup model. a) Overview of the setup, heat is applied to the base and transferred through the rod to the RRR, separation between the rod and the mock, in addition to the crossflow from the cooling fan keep the mock vessel cool to maintain its properties, b) close-up overview of the mock-rod assembly with the Styrofoam cap removed for better visibility of the RRR. The crimped RRR is mounted on top of the HT rod while suspended inside the mock vessel on top of which the Styrofoam cap is placed. Distance between the internal walls of the mock and the HT rod is maintained by two Styrofoam rings.

The base is composed of a metallic block on top of which a 3-mm-thick HT rod is mounted. Being exposed to heat, the base transfers the heat to the RRR via the rod. The mock-rod assembly includes the 1-cm-long top part of the rod with a crimped RRR at the tip of the rod that are encapsulated by a Styrofoam cap at the top section of the mock-rod assembly as shown by Figure 4.2. This assembly is enclosed by a short section of a mock vessel (Dynatek Dalta Scientific Instruments, MO, USA) while the rod is being separated from the vascular walls for safe temperature margins.

Geometrical and material properties of Figure 4.2 are presented in Table 4.1. In this table, $L_{sty,r}$ and $L_{sty,c}$ and denote the equivalent axial length of the Styrofoam rings and cap respectively. Average thermal conductivity of the RRR is derived from the mean values of thermal conductivity at martensite and austenite phase of Nitinol (Memry Corp., Germany). The RRR is manually crimped and placed inside a short slice of the mock vessel

with an internal diameter of 4 mm and 6–8% compliance that is comparable to the human arteries. The rod thickness (3 mm) has been chosen to maintain a safe distance between the circumference of the rod and the internal walls of the mock vessel. This distance provides a thermal shielding effect against heating of the mock vessel.

Table 4.1. Geometrical and material properties of the mock-rod assembly.

	Geometric Specifications			Material Specifications		
	Property	*Value*	*Unit*	*Property*	*Value*	*Unit*
Heat Transfer (HT) Rod				Material	Structural Steel	
	Length = L_{rod}	10	mm	Density	7854	Kg/m^3
	Radius = r_1	1.5	mm	Specific Heat	434	J/kg.K
				Thermal Conductivity k_{rod}	60.5	W/m.K
Air at 25 °C, 1 atm				Material	Air	
	Length = $L_{air,r}$	0.6	mm	Density	1.185	Kg/m^3
	Length = $L_{air,d}$	0.2	mm	Specific Heat	1004	J/kg.K
	Apprch. Velocity = V_{flow}	7	m/s	Thermal Conductivity = k_{air}	0.026	W/m.K
	Thickness = r_2-r_1	0.5	mm	Prandtl Number (Pr)	0.7	--
				Kinematic Viscosity = ν	15.11	mm^2/s
Styrofoam Insulations	Rings Thickness = $T_{sty,r}$	0.5	mm	Material	Polystyrene	
	Rings Length = $L_{sty,r}$ × 2	0.2	mm	Density	55	kg/m^3
	Radius = r_2	0.4	mm	Specific Heat	1210	J/kg.K
	Cap Length = $L_{sty,c}$	9.8	mm	Thermal Conductivity = k_{sty}	0.027	W/m.K
Mock Vessel	Inner radius = r_2	2	mm	Material	Silicon	
	Outer radius = r_3	2.15	mm	Density	1160	kg/m^3
	Thickness = r_3-r_2	0.15	mm	Specific heat	1670	J/kg.K
	Length = L_{mock}	20	mm	Thermal Conductivity = k_{mock}	0.15	W/m.K
RRR				Material	Nitinol	
	Length = L_{RRR}	15	mm	Density	6450	kg/m^3
	Avg. Thickness = t_{RRR}	0.106	mm	Specific Heat	322.2	J/kg.K
	Width = W_{RRR}	0.2	mm	Avg. Thermal conductivity	15	W/m.K
				Avg. Electrical Resistivity	79	μΩ/cm

The rod and the mock vessel are separated by two rings of expanded polystyrene (Styrofoam, DOW Chemical, Michigan, US). These rings, referred to as Styrofoam rings, provide the support against the displacement of the mock vessel in the axial, radial and circumferential directions in addition to limiting the amount of heat transferred to the mock vessel due to the low thermal conductivity of both the rings and the stagnant air at the separation chamber. In the top section of the mock-rod assembly, the RRR is covered by a solid cylinder of expanded polystyrene, referred to as the Styrofoam cap, inside the mock vessel providing an axial support for the RRR structure. This is to ensure axial alignment of the two overlapping ends of the RRR while at rest and during expansion.

This assembly is then exposed to the forced convection of a cross-flow from a fan installed at a distance of 2 cm.

4.4 Theoretical Analysis

As a first step to demonstrate the thermal shielding effect of this setup for safe use of the mock vessel (temperatures less than 50 °C), the following one dimensional heat transfer analysis has been conducted using the concept of thermal resistance [240]. Assuming a constant rate of heat transfer through a series of media, in such analysis the thermal resistance corresponds to electrical resistance, temperature difference corresponds to electric potential difference, and the heat transfer rate corresponds to electric current. Drawing these analogies, the complex differential heat transfer problems transform into one-dimensional steady-state heat transfer problems.

The general relation of heat transfer for all modes of transfer including conduction, convection and radiation can be expressed using the thermal resistance notation as:

$$\dot{Q} = \frac{\Delta T}{R_{\text{thermal}}} \qquad \textbf{(4.1)}$$

where $\dot{Q}$ is the steady rate of heat transfer through a medium in Watts, ΔT in °C is the temperature gradient through the medium, and R_{thermal} is the equivalent thermal resistance in W/°C calculated as follows for different modes of heat transfer. For conductive heat transfer the thermal resistance R_{cond} can be derived from Fourier's law of conduction resulting in:

$$R = R_{\text{cond}} = \frac{L}{kA} \qquad \textbf{(4.2)}$$

where L is the length of the medium in meters, k in W/m°K is the thermal conductivity of the material and A is the area of the medium through which the heat is transferred. Alternatively for convective heat transfer, thermal resistance is expressed by:

$$R = R_{\text{conv}} = \frac{1}{hA} \qquad \textbf{(4.3)}$$

that follows from the general Newton's law of cooling, where h is the convective heat transfer coefficient of the fluid in W/m²K and A is the surface area exposed to fluid in m².

Finally, where there is a gas surrounding the solid objects, the radiation effects can be significant and may need to be considered. Once again, expressing heat transfer by the general Newton's law of cooling, radiation thermal resistance can be written as:

$$R = R_{rad} = \frac{1}{h_{rad} A} \qquad \textbf{(4.4)}$$

where h_{rad} is the radiation heat transfer coefficient in W/m²K calculated by:

$$h_{rad} = \varepsilon\sigma(T_s^2 + T_{surr}^2)(T_s + T_{surr}). \qquad \textbf{(4.5)}$$

Both the surface temperature (T_s) and the surrounding temperature (T_{surr}) are in Kelvin. In this relation ε denotes the grey-body emissivity of the object and σ is the Stefan-Boltzmann constant. Consider a radial cross-section of the mock-rod assembly as illustrate in Figure 4.3 (a) where the external surface of the mock vessel is exposed to a cross-flow from the fan.

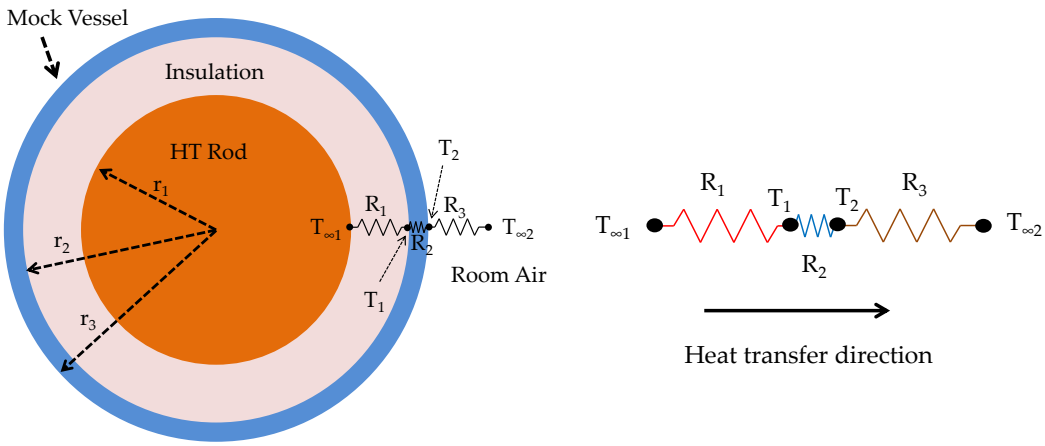

Figure 4.3. Cross-sectional overview of the mock-rod assembly. a) Mock vessel and the rod are separated through a distance of 0.5 mm by a combination of the Styrofoam rings and stagnant air, denoted by the insulation layer, b) the equivalent thermal resistance network, $T_{\infty 1}$, $T_{\infty 2}$ refer to constant temperatures of the rod and the room. Thermal resistance of the insulation layer (R_1) can be derived from a weighted average of the total resistance of the stagnant air and the two Styrofoam rings.

The mock vessel encompasses the HT rod while being separated from it by a cylinder of stagnant air trapped between two low-height rings of Styrofoam. Assuming the effect of heat radiation is very low compared to the conductive and convective heat transfer and taking the circumference of the rod as an isothermal surface along the longitudinal axis of the mock-rod assembly, the equivalent thermal resistance network of the mock-rod

assembly is shown in Figure 4.3 (b). In this figure, R_1 refer to the combined conductive thermal resistance of the stagnant air and the Styrofoam rings (insulation layer), R_2 refers to the conductive thermal resistance of the mock vessel, and R_3 refers to the convective thermal resistance of the crossflow from the fan.

Due to the close thermal conductivity of the stagnant air and the Styrofoam rings as shown in Table 4.1, weighted average value for the thermal conductivity of an insulation layer consisting of the stagnant air and the Styrofoam rings (k_{ins}) is calculated by:

$$k_{ins} \approx \frac{2L_{sty}\,k_{sty} + (L_{rod} - 2L_{sty})k_{air}}{L_{rod}} = 0.26 \text{ (W/m}^{\circ}\text{C)}. \quad \textbf{(4.6)}$$

Therefore the effective thermal resistance of this insulation layer between the rod and internal walls of the mock vessel is:

$$R_1 = R_{cond\_ins} = \frac{\ln\left(r_2/r_1\right)}{2\pi k_{ins} L_{rod}} = 173.13 \text{ (°C/W)}. \quad \textbf{(4.7)}$$

Given the uniform cylindrical shape of the mock vessel, the thermal resistance across this structure is:

$$R_2 = R_{cond\_mock} = \frac{\ln\left(r_3/r_2\right)}{2\pi k_{mock} L_{rod}} = 7.68 \text{ (°C/W)}. \quad \textbf{(4.8)}$$

Note that due to the assumption of one-dimensional heat transfer in the radial direction of the assembly, the heat transfer along the longitudinal axis of the mock vessel is ignored and the effective length has become equal to the length of the portion of the vessel that runs along the rod (L_{rod}). A more detailed analysis considering heat transfer in the axial direction is given later in this section.

As the external surface of the mock vessel is exposed to the forced convection of the fan, first it is necessary to calculate the convective cooling heat transfer coefficient of the air. The entire length of the mock-rod assembly in Figure 4.2 is subject to an external forced convection of a small microprocessor cooling fan providing a uniform approach velocity of around 7 m/s on average. This is when the fan is rotating at 70% of its maximum RPM capacity. These values are typical of current cooling fans mounted on top of microelectronic components heat sinks.

Given the definition of the Nusselt (Nu) number [240], the convective heat transfer coefficient h_{flow}, can be calculated from:

$$\text{Nu} = \frac{\dot{q}_{\text{conv}}}{\dot{q}_{\text{cond}}} = \frac{h_{\text{flow}}\,\Delta T}{k_{\text{air}}\Delta T / L_{\text{chr}}} = \frac{h_{\text{flow}}\,L_{\text{chr}}}{k_{\text{air}}} \qquad \textbf{(4.9)}$$

where $\dot{q}_{\text{conv}}$ and $\dot{q}_{\text{cond}}$ are convective and conductive rate of heat flux (the rate of heat transfer per unit time per unit surface area) respectively. The parameter L_{chr} is the characteristic length of the geometry. In the case of a crossflow over a cylinder, the characteristic length is equal to the external diameter of the radial cross-section of the assembly, in this case the mock vessel. Value of Nusselt number depends on the regime of the fluid that can be determined by the Reynolds (Re) number defined as follows:

$$\text{Re} = \frac{\text{Inertial forces}}{\text{Viscous forces}} = \frac{V_{\text{flow}} L_{\text{chr}}}{\nu} \qquad \textbf{(4.10)}$$

where V_{flow} is the upstream (approach) velocity and ν is the kinematic viscosity of the fluid. The value of Re, mainly describes the fluid flow regime [240]. Given relation (4.9), the average Nusselt number for the laminar flow across the external surface of the mock vessel can be expressed by the empirical relation of Churchill and Bernstein [240]:

$$\text{Nu}_{\text{cyl}} = 0.3 + \frac{0.62\,\text{Re}^{1/2}\,\text{Pr}^{1/3}}{\left[1+\left(0.4/\text{Pr}\right)^{2/3}\right]^{1/4}}\left[1+\left(\frac{\text{Re}}{282000}\right)^{5/8}\right]^{4/5} \qquad \textbf{(4.11)}$$

where Pr is the dimensionless Prandtl Number of the fluid, a characteristic of the material properties of the fluid that is close to 1 for most of the gases. Substituting values given in Table 4.1 into equations (4.10), (4.11) then (4.9) results in the average effective convective heat transfer coefficient of h_{flow} = 136 W/m²K that yields:

$$R_3 = R_{\text{conv}} = \frac{1}{2\pi r_3 L_{\text{rod}} h_{\text{flow}}} = 54.55\ (°\text{C}/\text{W})\,. \qquad \textbf{(4.12)}$$

Due to the presence of the thermal resistors in series, the total thermal resistance is simply the addition of all individual ones resulting in:

$$R_{\text{total}} = R_1 + R_2 + R_3 = 235.35\ (°\text{C}/\text{W})\,. \qquad \textbf{(4.13)}$$

Consequently, assuming the temperature of the rod and the room are kept constant at 80°C and 20°C respectively, the rate of heat transfer though the rod, insulation layer, and mock vessel into the room evaluates to:

$$\dot{Q} = \frac{\Delta T}{R_{\text{total}}} = 0.25\,\text{W}\,. \qquad \textbf{(4.14)}$$

Given the analogy between the electric current and the rate of heat transfer, and the constant rate of heat transfer through all the layers of the media in Figure 4.3 (a), the uniform temperature at the internal walls of the mock vessel T_1 is calculated by:

$$T_{\infty 1} - T_1 = \dot{Q} \times R_1 \qquad \textbf{(4.15)}$$

where $T_{\infty 1}$ is the temperature of the HT rod assumed constant at 80 °C to ensure application of temperatures above the transformation temperature of Nitinol to RRR and R_1 is the conductive heat resistance of the insulation layer evaluated by relation (4.7). This yields $T_1 \approx 36\,°\text{C}$, which is well below the thermal operating range of the mock vessel, up to 50 °C (Dynatek Dalta Scientific Instruments, MO, USA).

The theoretical framework described in this section provides a good first estimate of temperature distribution in the radial direction of the cross-section of the mock-rod assembly, yet it is limited in accuracy due to the following reasons. In an actual setup, the heat flux is fetched through the bottom of the rod resulting in heat dissipation in the longitudinal direction of the assembly as well as the radial direction. This actual scenario turns the heat transfer problem into a multi-dimensional problem governed by more complex differential equations.

A better approximation of the heat transfer problem in this section may be derived from the theory of heat transfer from finned surfaces [240]. Choosing a differential volume along the assembly of Figure 4.2 (b) and adopting a uniform insulation layer with effective thermal conductivity equal to k_{ins}, the following energy balance equations can be written for the bottom section of the rod-mock assembly along the longitudinal axis (x-axis) of the differential volume shown in Figure 4.4,

$$\left[\dot{Q}_{\text{in}}(x) = \dot{Q}_{\text{cond}}(x)\right] = \left[\dot{Q}_{\text{out}}(x) = \dot{Q}_{\text{cond}}(x+\Delta x) + \dot{Q}_{\text{comb}}(x)\right]. \qquad \textbf{(4.16)}$$

In this equation, $\dot{Q}_{\text{in}}(x)$ is the rate of heat transfer into the differential volume from the cross-sectional surface of the rod at distance x, and $\dot{Q}_{\text{out}}(x)$ is the compound rate of heat transfer out of the differential volume in both longitudinal, $\dot{Q}_{\text{cond}}(x+\Delta x)$, and radial, $\dot{Q}_{\text{comb}}(x)$, directions.

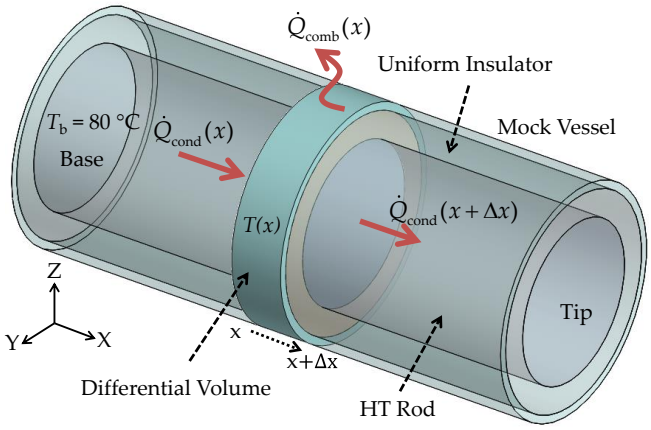

Figure 4.4. Fin analysis of the heat transfer assembly. Heat transfer along a differential volume of the mock-rod assembly. The uniform insulation has a weighted average thermal conductivity of the stagnant air and the Styrofoam rings defined in relation (4.6). Heat transfer in the rod is in both the axial (base to tip) and radial (rod to air) directions while in the insulation layer it is assumed to be dominated in the radial direction.

The thermal resistance network of the differential volume for heat loss in the radial direction is similar to the network described in Figure 4.3 with an equivalent length of Δx that yields:

$$\dot{Q}_{comb}(x) = \frac{T(x) - T_{\infty 2}}{R_{comb}} \qquad \textbf{(4.17)}$$

where R_{comb} is the combined thermal resistance of the differential volume in the radial direction composed of the following components:

$$R_{comb} = R_{cond\_ins} + R_{cond\_mock} + R_{conv}, \qquad \textbf{(4.18)}$$

$$R_{cond\_ins} = \frac{A}{\Delta x}, \quad A = \frac{\ln(r_2 / r_1)}{2\pi k_{ins}}, \qquad \textbf{(4.19)}$$

$$R_{cond\_mock} = \frac{B}{\Delta x}, \quad B = \frac{\ln(r_3 / r_2)}{2\pi k_{mock}}, \qquad \textbf{(4.20)}$$

$$R_{conv} = \frac{C}{\Delta x}, \quad C = \frac{1}{2\pi r_3 h_{flow}}. \qquad \textbf{(4.21)}$$

By substitution and rearranging Equation (4.16), taking the limit when $\Delta x \to 0$ and using Fourier's law of heat conduction along the rod [240], differential Equation (4.22) describes the heat transfer along the bottom section of the mock-rod assembly starting from the base of HT rod up to its tip. In this equation, A_c is the cross-sectional area of the rod and D is the sum of A, B and C from equations (4.19) to (4.21).

$$k_{\text{rod}} A_{\text{c}} \frac{d^2T(x)}{dx^2} - \frac{T(x) - T_{\infty 2}}{D} = 0 \qquad \textbf{(4.22)}$$

To account for the effect of heat loss from the top section of the assembly, extension from the tip of the rod to the tip of the mock vessel, an appended length, L_{added} in tion (4.23), can be added to the length of rod (L_{rod}). This allows for the top of the assembly to be considered as a perfectly insulated surface [240]. Therefore, the total length of the assembly can be expressed by:

$$L_{\text{total}} = L_{\text{rod}} + L_{\text{added}} . \qquad \textbf{(4.23)}$$

The added length can be evaluated by equating the expected rate of heat transfer from the tip of the rod to the rate of heat transfer through the added length of the assembly and considering the tip of the resultant longer assembly as a perfectly insulated tip. This can be expressed by:

$$\left[\dot{Q}_{\text{out,tip}} = \frac{T_{\text{rod}}(x_{\text{tip}}) - T_{\infty 2}}{R_{\text{total\_tip}}} \right] = \left[\dot{Q}_{\text{added}} = \int_{L_{\text{rod}}}^{L_{\text{total}}} \frac{T_{\text{rod}}(x) - T_{\infty 2}}{D} dx \right] \qquad \textbf{(4.24)}$$

where $T_{\text{rod}}(x_{\text{tip}})$ and $T_{\text{rod}}(x)$ respectively refer to the temperature of the rod at the tip of the rod and a coordinate between L_{rod} and L_{total}. An upper, yet close, approximation for $\dot{Q}_{\text{added}}$ may be found by assuming a uniform temperature for the rod along the added length, from L_{rod} to L_{total}, that is equal to $T_{\text{rod}}(x_{\text{tip}})$. This results in:

$$\left[\dot{Q}_{\text{out,tip}} = \frac{T_{\text{rod}}(x_{\text{tip}}) - T_{\infty 2}}{R_{\text{total\_tip}}} \right] \approx \left[\dot{Q}_{\text{added}} = \frac{T_{\text{rod}}(x_{\text{tip}}) - T_{\infty 2}}{D / L_{\text{added}}} \right], \qquad \textbf{(4.25)}$$

$$L_{\text{added}} = \frac{D}{R_{\text{total\_tip}}} \qquad \textbf{(4.26)}$$

where $R_{\text{total\_tip}}$ is the effective thermal resistance of the assembly along the appended length. Value of this resistance may be evaluated considering the following assumptions. Due to the high thermal conductivity of the RRR and its small dimensions in comparison with the rest of the assembly, its thermal resistance can be ignored for these evaluations. From Figure 4.2 (b), it is apparent that the heat dissipation from the tip of the rod is mainly by means of two general media one being the insulation layer above the rod that is composed of the short column of stagnant air surrounding the RRR and the Styrofoam

cap cylinder above it, and the other being the extension of the mock vessel at the top section of the assembly.

Once again, due to the close values of thermal conductivity of the stagnant air and polystyrene, it is reasonable to assume a uniform insulation cylinder for the top section of the assembly by a weighted average value for the thermal conductivity. Using a similar fin analysis for the top section of the assembly and assuming the axial direction of the insulation cylinder as the main direction of heat transfer by conduction in this media, the thermal resistance network of Figure 4.5 can be established from the tip of the rod.

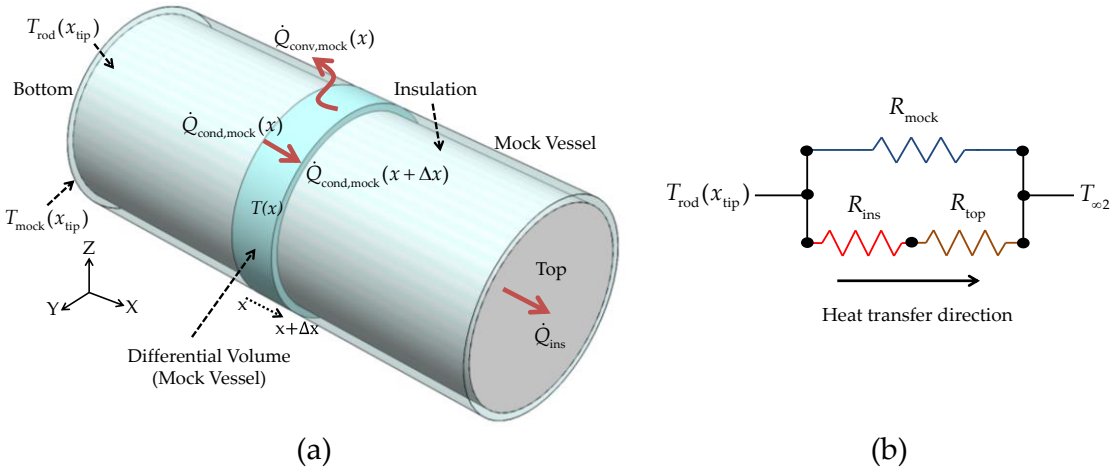

Figure 4.5. Thermal resistance network at the top section of mock-rod assembly. a) Heat is dissipated by the mock and the cylinder of insulation above the tip. Dominant mode of transfer in the insulation zone is conduction in the axial direction followed by the convective heat transfer at the top. Heat transfer through the mock resembles that of a plate fin subject to a flow, b) equivalent thermal resistance network composed of the parallel resistors from the mock and the insulation cylinder. Thermal conductivity of the insulation is from a weighted average of the stagnant air and polystyrene.

As shown by this figure, axial direction is considered as the dominant direction of heat transfer through the insulation cylinder. This is followed by the convective heat transfer from the top of the assembly resulting in two thermal resistors in series R_{ins} and R_{top} as shown in Figure 4.5 (b). Values of these resistors can be evaluated by:

$$R_{ins} = \frac{L_{top}}{k_{ins,top} A_{c,ins}}, \qquad \textbf{(4.27)}$$

$$R_{top} = \frac{1}{h_{top} A_{c,ins}} \qquad \textbf{(4.28)}$$

where L_{top} = 10 mm refers to the length of the top section of the mock-rod assembly in Figure 4.2 (b) and $A_{c,ins}$ refers to the cross-sectional area of the insulation cylinder shown in Figure 4.5 (a).

To find the convective heat transfer coefficient of air at the flat top of the assembly (h_{top}) equations (4.9) and (4.10) can be used. In this case Nusselt number at the top of the assembly, as the result of the laminar flow ($Re < 5 \times 10^5$) over the flat circular cap of the Styrofoam cylinder in Figure 4.5 (a) can be expressed by:

$$Nu_{top} = \frac{h_{top} L_{top}}{k_{air}} = 0.664 \left(Re_{top}\right)^{0.5} \left(Pr_{air}\right)^{1/3}, \quad \textbf{(4.29)}$$

$$Re_{top} = \frac{V_{flow}\left(\pi r_2 / 2\right)}{\nu} \quad \textbf{(4.30)}$$

where $\left(\pi r_2 / 2\right)$ is the average characteristic length of the circular cap at the top of the assembly that is subject to the forced convection of the fan.

To calculate the effective thermal resistance of the mock vessel (R_{mock}) shown in Figure 4.5, the heat transfer analysis in fin structures defined by the differential equation of relation (4.22) can be utilized. In this case, as shown by the differential volume in Figure 4.5 (a), the heat flux that enters at axial distance x, $\dot{Q}_{cond,mock}(x)$, is equal to the sum of the flux that exits through conduction, $\dot{Q}_{cond,mock}(x+\Delta x)$, and convection, $\dot{Q}_{conv,mock}(x)$. Solving for the differential equation and assuming that the mock temperature at the very top reaches the environment temperate ($T_{\infty 2}$), rate of heat transfer through the mock vessel is expressed by:

$$\dot{Q}_{mock} = \left(h_{flow} P_{mock} k_{mock} A_{c,mock}\right)^{1/2} \times \left(T_{mock}(x_{tip}) - T_{\infty 2}\right) \quad \textbf{(4.31)}$$

where P_{mock} and $A_{c,mock}$ refer to the periphery and the cross-sectional area of the mock vessel respectively. Temperature difference between the bottom of the mock (at top section of the mock-rod assembly, Figure 4.2, b) and the room temperature, $T_{mock}(x_{tip}) - T_{\infty 2}$, can be expressed in terms of the temperature of the rod at this point and the thermal parameters A, B and C found using Equations (4.19) to (4.21) resulting in the equalities given in Equations (4.32) and (4.33).

$$\left[\dot{p}_{\text{comb}}(x_{\text{tip}}) = \frac{T_{\text{rod}}(x_{\text{tip}}) - T_{\infty 2}}{A+B+C}\right] = \left[\dot{p}_{\text{mock}}(x_{\text{tip}}) = \frac{T_{\text{mock}}(x_{\text{tip}}) - T_{\infty 2}}{B+C}\right] \quad \textbf{(4.32)}$$

$$T_{\text{mock}}(x_{\text{xtip}}) - T_{\infty 2} = \frac{B+C}{A+B+C}\left[T_{\text{rod}}(x_{\text{tip}}) - T_{\infty 2}\right] \quad \textbf{(4.33)}$$

In Equations (4.32) the newly defined parameter $\dot{p}$ is the rate of heat transfer along a medium per unit length of the medium in the axial direction. Substituting into relation (4.31), the effective thermal resistance of the mock (R_{mock}) is:

$$R_{\text{mock}} = \frac{A+B+C}{B+C}\left(\frac{1}{h_{\text{flow}} P_{\text{mock}} k_{\text{mock}} A_{\text{c,mock}}}\right)^{1/2}. \quad \textbf{(4.34)}$$

Given thermal resistance network of the tip shown in Figure 4.5 (b), total effective thermal resistance from the tip is then expressed by:

$$R_{\text{total\_tip}} = \frac{R_{\text{mock}}(R_{\text{air}} + R_{\text{top}})}{R_{\text{mock}} + R_{\text{air}} + R_{\text{top}}}. \quad \textbf{(4.35)}$$

By substitution into the relations given so far and solving for $T(x)$ and applying the initial conditions the temperature at position x from the base of the rod at the rod surface can be expressed by:

$$T(x) = T_{\infty 2} + (T_b - T_{\infty 2})\frac{\cosh\left[\alpha(L_{\text{total}} - x)\right]}{\cosh(\alpha L_{\text{total}})} \quad \textbf{(4.36)}$$

where T_b is the temperature of the rod at the base of the mock-rod assembly as shown in Figure 4.4 and α is expressed by:

$$\alpha = \left(\frac{1}{k_{\text{rod}} A_{\text{c}} D}\right)^{1/2}. \quad \textbf{(4.37)}$$

In order to find the temperature at different axial distances from the base of the mock-rod assembly along the radial direction, such as the internal surface of the mock vessel, using relation (4.17), the rate of heat transfer per unit axial length of the assembly in the radial direction can be defined by:

$$\dot{p}_{\text{comb}}(x) = \frac{T(x) - T_{\infty 2}}{D} \quad \textbf{(4.38)}$$

where $T(x)$ is temperature of the surface of the rod at axial distance x from the base of the mock-rod assembly as shown in Figure 4.4. Given the steady rate of heat transfer

through all the layers of media in the radial direction, temperature at the internal surface of the mock vessel at axial distance x from the base of the mock-rod assembly can be expressed by:

$$T_1(x) = T(x) - \dot{p}_{\text{comb}}(x)A \qquad \textbf{(4.39)}$$

where A is the thermal resistance per axial unit length of the assembly in the insulation region from the base to the tip of the rod as defined in (4.19).

4.4.1 Results

Figure 4.6 shows the temperature distribution on the internal and external surfaces of the mock vessel along the longitudinal axis of the assembly up to the tip of the rod.

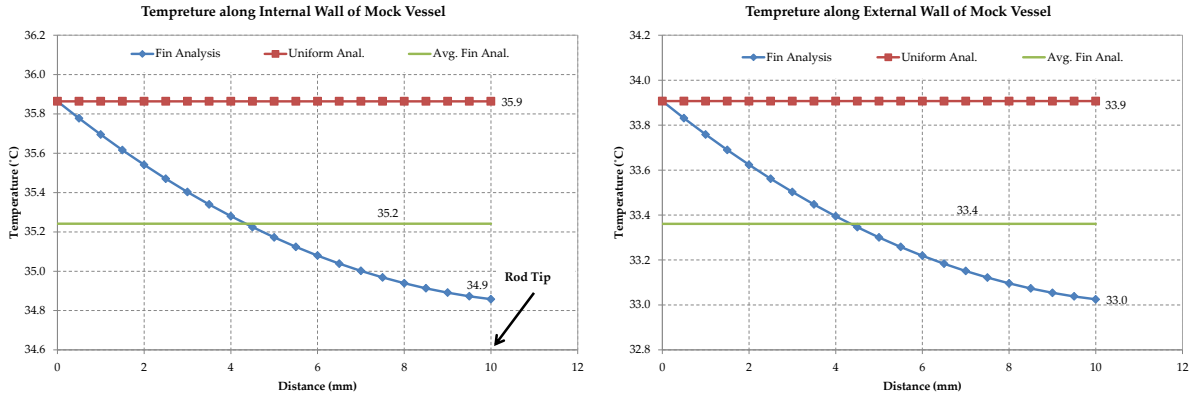

(a) (b)

Figure 4.6. Temperature distribution along walls of mock vessel. a) Temperature distribution along the longitudinal axis of the mock-rod assembly on the internal and, b) external surfaces of mock vessel. The Uniform Analysis overestimates the internal temperature as it gets closer to the deployment area of the RRR at x = 10 mm.

The data is reported for the two approaches adopted in this section. "Uniform Analysis" results refer to the results of the one-dimensional analysis assuming an isothermal surface along the length and circumference of the rod and the "Fin Analysis" results refer to the differential analysis based on the theory of heat transfer in fins. The average line shows the average values over the results of the Fin Analysis. As indicated by this figure, while the uniform analysis overestimates the temperature by at most 1°C at the deployment area of the RRR (rod tip), yet both the internal and external walls of the vessel do not surpass the mock vessel's nominal temperatures (< 50°C).

Figure 4.7 (a) presents the temperature distribution along the longitudinal axis of the HT rod from the base of the mock-rod assembly. As indicated by the tip temperature from

the fin analysis of the assembly, this temperature falls below the A_f of the Nitinol RRR by the applied 80˚C temperature at the base. Therefore, to compensate for this loss, higher temperatures are required at the base. Figure 4.7 (b) shows the temperature of the rod using higher values of T_{base} = 85˚C in the fin analysis and T_{base} = 81˚C in the uniform analysis to ensure raising the temperature of the tip, therefore RRR, above A_f. These results further highlight the importance of considering the axial heat transfer and temperature loss by using the more detailed fin analysis outlined in this section to acquire the adequate mock-rod assembly base temperature for actuation of the RRR.

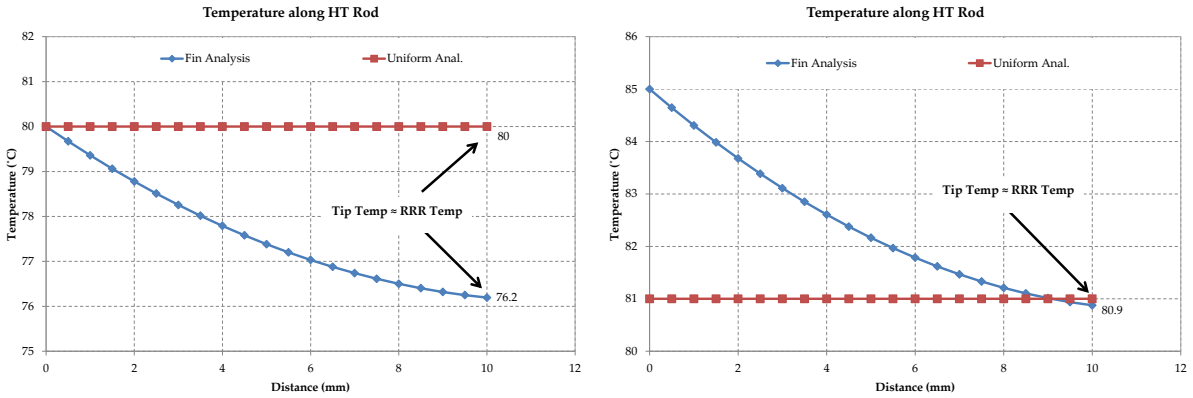

(a) (b)

Figure 4.7. Temperature distribution along heat transfer (HT) rod. a) Temperature distribution along the longitudinal axis of the mock-rod assembly on the outer surfaces of the rod for T_{base} = 80˚C for both the uniform and fin analysis, b) temperature distribution along the longitudinal axis of the mock-rod assembly on the outer surfaces of the rod when T_{base} = 81˚C for the uniform analysis and T_{base} = 85˚C for the fin analysis. Higher temperatures are to ensure that the RRR temperature reaches A_f.

Given these new higher temperatures of the base, temperature distribution on the internal and external surfaces of the mock vessel along the axial direction of the mock-rod assembly are shown in Figure 4.8. As indicates, a safe mock vessel temperature margin by at least 13˚C is still maintained. In the next section rigorous numerical analyses are conducted in order to evaluate the theoretical results presented in this section. First a simplified analysis that readily utilises the convective heat transfer coefficients derived in this section is proposed, followed by a coupled field analysis incorporating computational fluid dynamics and heat transfer wherein the aforementioned parameters are directly calculated by the solver.

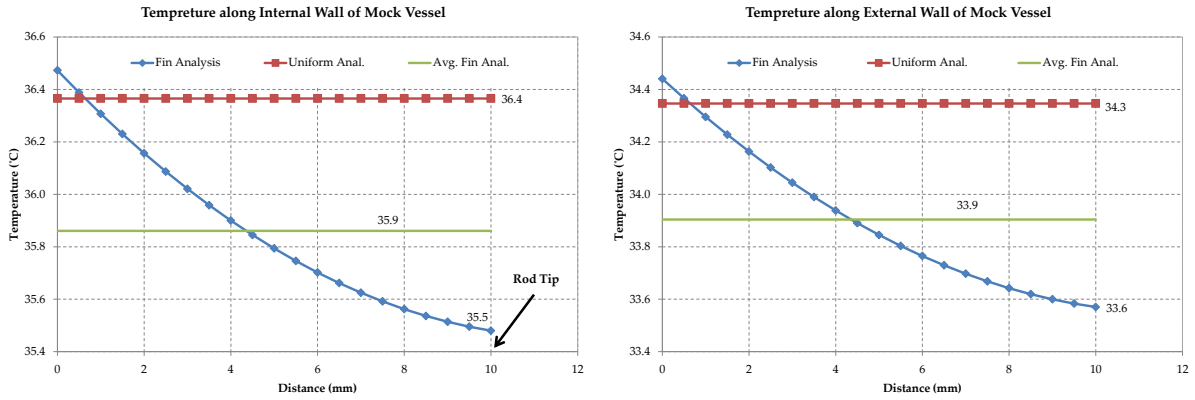

(a) (b)

Figure 4.8. Temperature distribution along walls of mock vessel, high temperature input. Mock-rod assembly base temperature is raised by 1˚C in the uniform analysis and by 5˚C in the fin analysis to ensure martensite to austenite phase transformation of the RRR. These results indicate maintaining the structural integrity of the mock vessel demonstrated by the low temperatures along its internal walls (< 50˚C).

4.5 Numerical Analysis: Uniform Heat Transfer

The theoretical framework that is detailed in the previous section provided a first step towards demonstrating safe operation of the mock vessel in the heat transfer setup shown in Figure 4.2. The limitations of these approaches are as follows: comparison of the uniform and the fin based analysis underlines the importance of inclusion of heat transfer in the axial direction due to the conceivable thermal resistance of structural steel in the axial direction and the localized heat source at the base. Comparison of these results clearly shows overestimation of both the vessel and RRR temperatures by the uniform analysis and necessitated the more elaborate approach of fin analysis. Furthermore, due to the complex fluid regime close to the external walls of the mock vessel, Nusselt number at this area is not always constant.

This is primarily due to the fact that an external flow a across circular shape involves flow separation that is difficult to handle analytically. Particularly, Nusselt number starts with high values at the front side of the cylinder that is straight against the flow (stagnation zone) then drops as the thickness of the boundary layer increases from front to the sides. This trend is then followed by an abrupt increase at the sides where the flow separation and intense mixing occurs (the wake region). The Nusselt numbers calculated in the previous section are average values resultant of numerous experimental attempts

[240]. Moreover, in order to reduce the complexity of the differential equations in the fin analysis a uniform insulation layer was assumed whose thermal conductivity was calculated from the weighted average values of the stagnant air and the Styrofoam rings. Due to the lower thermal conductivity of the stagnant air compared with the polystyrene, it is expected that the temperature of the mock vessel around the Styrofoam rings increases slightly that calls for further analysis. Consequently, in order to account for these details and their effect on the distribution of temperature on both the RRR and the walls of the mock vessel further numerical studies are required.

In this section, a 3D steady-state heat transfer analysis is conducted by means of finite element analysis (FEA). In these studies the energy balance equations of the constant heat transfer are solved by the commercial FEA package ANSYS heat transfer (ANSYS Inc., Canonsburg, PA, USA). For a steady-state thermal analysis in ANSYS, the degrees of freedom are limited to temperatures $\boldsymbol{T}$ that are solved for by the matrix equation:

$$[K(T)]\{T\} = \{\dot{Q}(T)\} \qquad \textbf{(4.40)}$$

where the $[K]$ refers to the matrix of the thermal conductance of materials (reciprocals of thermal resistance). Fixed temperatures applied to a model represent the constraints and boundary conditions on the system [241]. In this case, the general modes of heat transfer are solved for by giving the corresponding parameters such as the convective heat transfer coefficient and thermal conductivity as inputs of the problem. Therefore, the emphasis is more given on the distribution of temperatures and heat flux through different layers of the media in the mock-rod assembly. Due to adoption of a uniform average convective heat transfer coefficient, the study proposed in this section is referred to as the "Uniform Analysis". A more rigorous approach incorporating the computational fluid dynamics (CFD) of the cross flow is presented in the next section referred to as the "Conjugate Analysis".

4.5.1 Materials and Methods

The rod, stagnant air, Styrofoam rings and the mock vessel are modelled as concentric cylinders with the dimensional parameters given in Table 4.1. Extension of the rod from the base of the mock-rod assembly to the base of the heat transfer setup is discarded to simplify the model. Figure 4.9 shows the components of the 3D model for this analysis

along with the applied boundary conditions. Isotropic thermal conductivities of the materials of the model are chosen to be consistent with the values in Table 4.1.

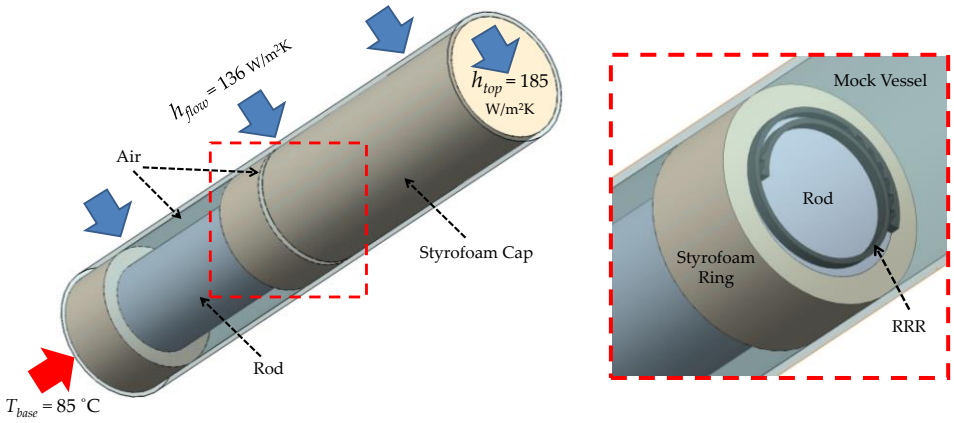

Figure 4.9. Geometry of the 3D thermal analysis model. a) Overview of the model, dimensional and material properties of the model are given in Table 4.1. Convective cooling boundary conditions are applied based values of heat transfer coefficients derived from the theoretical analysis outlined in the previous section, b) closes-up view of the deployment area with the Styrofoam cap removed for better visibility of the RRR.

A base temperature of 85°C is applied to the rod at the base of the mock-rod assembly, where the heat flux is supplied to the assembly in the experimental setting. The external walls of the circumference of the mock vessel are subjected to convective cooling with an effective heat transfer coefficient of 136 W/m²K as calculated by equations (4.9) to (4.11) in the previous section. A planar convective cooling is also applied to the top of the assembly with heat transfer coefficient of 185 W/m²K derived from equations (4.29) and (4.30) of the previous section. The assembly in Figure 4.9 is first developed in SolidWorks (SolidWorks Corp., Velizy, France), then imported into ANSYS. To ensure accuracy of the results and their independence from the mesh size, a mesh sensitivity analysis was conducted before reporting the results. Six levels of mesh refinement were first defined with the mesh size reduced by a factor of two at each level in comparison to the previous one across sensitive areas such as the rod, mock vessel, insulation layers and the RRR. Given that the difference between the maximum values of interest (temperature) from one refinement level to the next fell to less than 3%, the third level comprised of 103,000 elements was chosen to report the final results. All the regular shapes such as the rod, Styrofoam rings and cap, the mock vessel and the stagnant insulating air between the mock vessel and the rod, were primarily meshed with hexahedral elements. In

contrast, due to the non-rectangular sawtooth structures of the RRR, it is meshed with both tetrahedral and hexahedral elements. To better capture temperature gradient across the RRR, a further level of refinement was defined for this domain resulting in four and three elements across its width and thickness respectively. Meshing across the mock vessel's thickness is also further refined compared to the rod and the insulation layers to better capture the temperature gradient across its thickness. Figure 4.10 presents an overview of the meshed geometry.

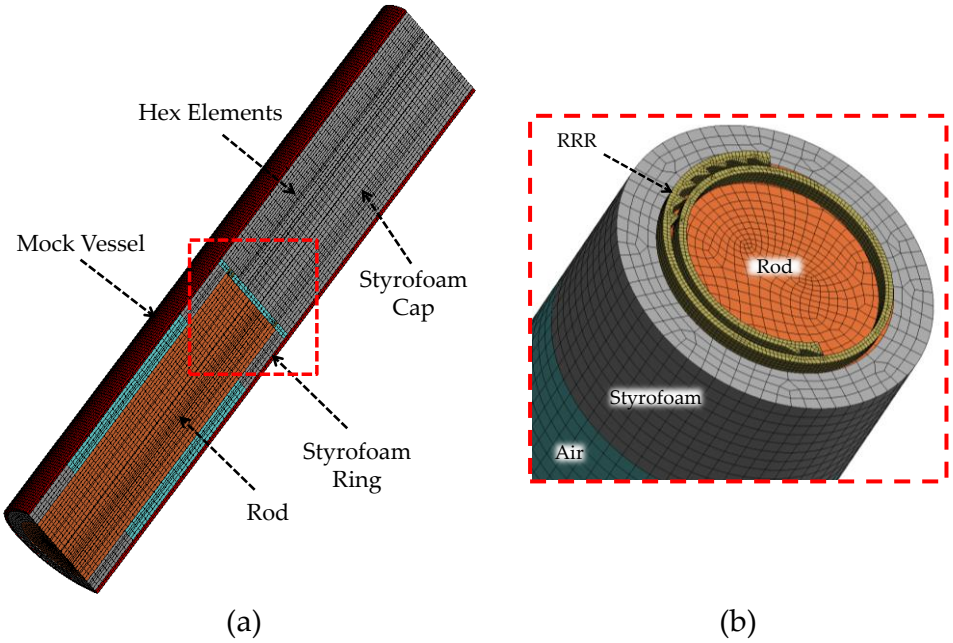

Figure 4.10. Discretised mock-rod domain. a) Axial cross-sectional overview of domain, all the components are meshed with regular hexahedral elements except for the column of air at the top section of the assembly and the RRR, b) detailed view of the refined meshing across the thickness and width of the RRR to better capture the temperature gradient in this region. Mock vessel is hidden for better visibility of the components.

Simulations are run for the full 3D model. This approach was necessary due to the asymmetrical shape of the RRR and its overlapping ends from the two sides as shown in Figure 4.10 (b). Simulations are run on a Dell Precision workstation with two quad-core Xeon processors and 20 GB of RAM.

4.5.2 Results

Temperature contour plots shown in Figure 4.11 (a) demonstrate the uniform distribution of temperature circumferentially at any given radial distance from the centre of the mock-rod assembly while gradually decreasing in the axial direction. Temperature dis-

tribution along the longitudinal axis of the HT rod, from the base of the mock-rod assembly to the rod tip, is presented in Figure 4.11 (b) in comparison with the analytical results from the previous section. As expected, due to the heat loss in the radial direction, the top end exhibits a lower temperature averaged at 82°C. As indicated by this figure, the analytical approach (fin analysis) is able to predict the temperature at the tip with 0.6% accuracy on average, showing its merit for first hand calculations.

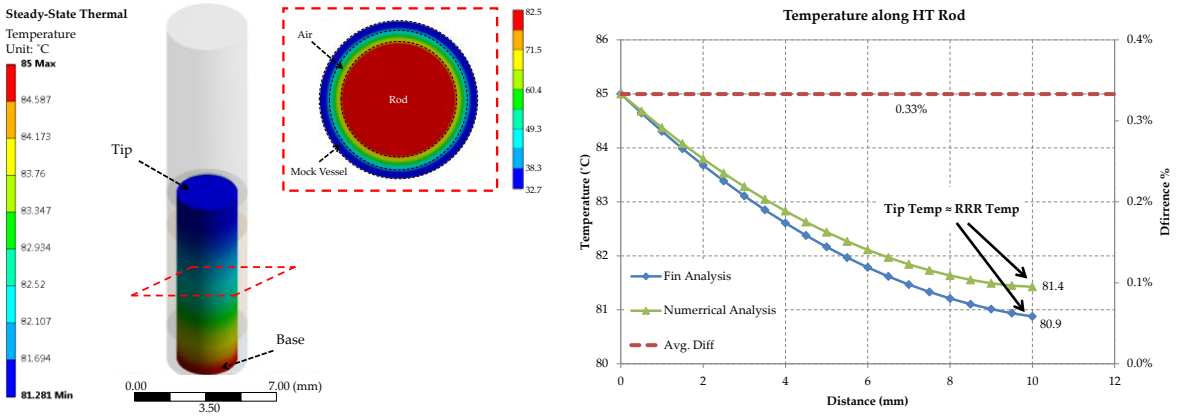

Figure 4.11. Temperature distribution in the axial direction of the rod. a) Contour plots of temperature along the HT rod, temperature distribution in the circumferential direction at any radial coordinate is uniform. The drop towards the tip is due to the fin effect, b) temperature distribution along the longitudinal axis of the rod from the base to the tip in comparison with the fin analysis results. The simulation trend closely follows the analytical trend demonstrating an average accuracy of at least 0.6% for the fin analysis.

Vector plots of the heat flux along the mock-rod assembly are shown in Figure 4.12 (a) with the close-up view near the external layers of the domain (mock vessel). As this figure shows, although the majority of heat being transferred in the rod is in axial direction, in the insulation layers (Styrofoam rings or stagnant air) and mock vessel, heat transfer is dominant in the radial direction. This effect is further confirmed by the flux distribution values in Figure 4.12 (b) that are reported along the radial report path highlighted in Figure 4.12 (a). As demonstrated by the higher flux values along the radial path, the axial heat flux starts with a very high value that is on the surface of the rod then suddenly drops to values close to zero. On the other hand, the radial flux values start with a relatively small value on the surface of the rod followed by higher values along the radial distance. These results further validate the assumption taken in the previous section re-

garding the primary direction of the heat transfer in the insulation and mock vessel layers in the calculation of R_{comb}.

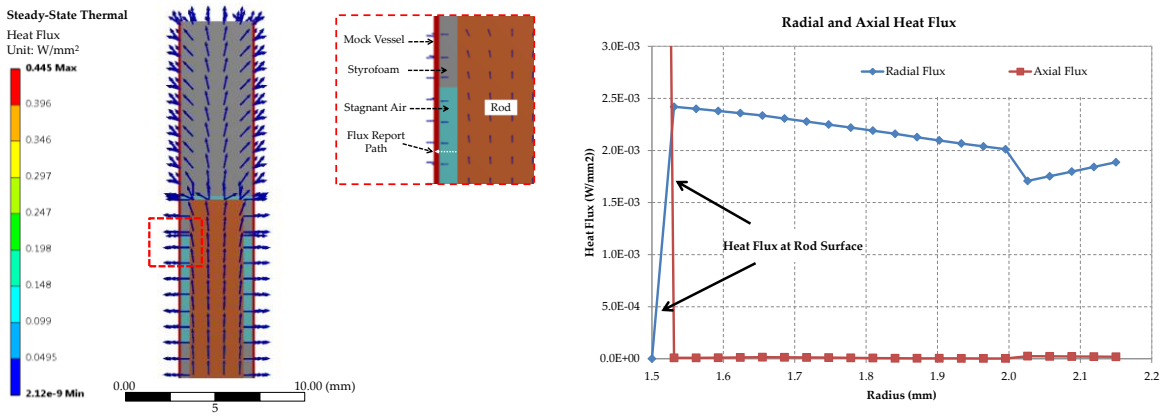

(a) (b)

Figure 4.12. Heat flux in the mock-rod assembly. a) Vector plots of the heat flux along the mock-rod assembly, close-up image at the insulation and mock vessel layers shows primary direction of heat transfer in the radial direction, b) radial and axial heat flux along the flux report path highlighted in part (a), high axial heat flux is observed at the surface of the rod then followed by close to zero flux along the radial path. Radial flux on the surface is first low then becomes the dominant mode of heat transfer along the path in the insulation and mock vessel domains.

Figure 4.13 (a) shows the temperature contour plots on the internal and external walls of the mock vessel. As expected before, the regions of Styrofoam implantation demonstrate higher temperatures relative to the areas at the proximity of stagnant air. That is due to the higher thermal conductivity of polystyrene than that of the stagnant air (Table 4.1). This effect is not reflected in the theoretical results by the assumption of a weighted average value for the entire insulation region between the mock and the rod. These results demonstrate better efficiency of numerical simulations in predicting localized regions of higher temperature. As shown by the radial cross-sectional contour plots of Figure 4.11 (a), temperature distribution in the circumferential direction shows to be uniform. Therefore, temperature values along paths running parallel to the longitudinal axis of the mock-rod assembly on the internal and external walls of the mock vessel are presented in Figure 4.13 (b) in comparison with the analytical results. As demonstrated all the internal temperatures fall below the safe range of mock vessel ensuring its integrity of the structure during application of heat to the crimped RRR.

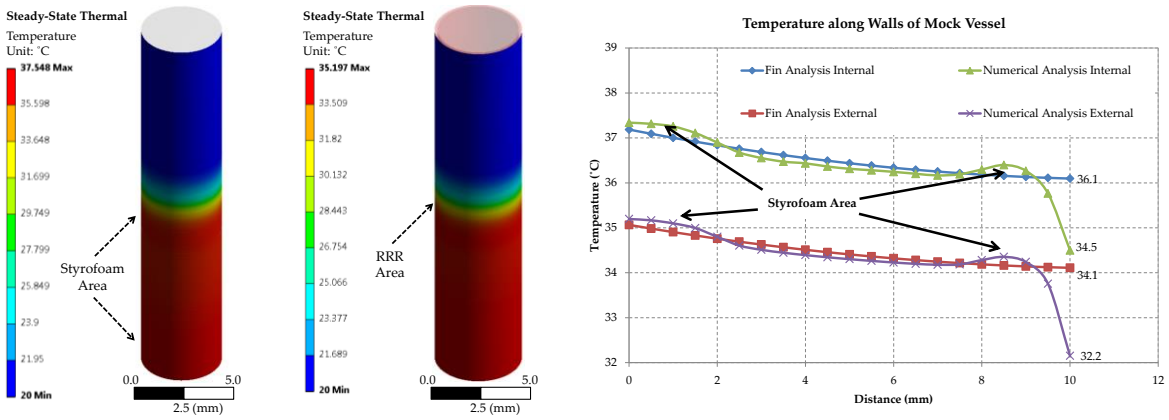

(a) (b) (c)

Figure 4.13. Temperature distribution along internal walls of mock vessel. a) Contour plots of temperature along the internal and, b) external walls of the mock vessel. Styrofoam implantation zones show relatively higher temperatures due to the higher thermal conductivity of polystyrene compared to stagnant air. Temperature in the circumferential direction is uniform with a 0.15˚C standard deviation, c) temperature distribution along the longitudinal axis of the mock-rod assembly. Marginal jumps in the overall trends correspond to the zones of Styrofoam implantation.

Temperature distribution contour plots on the surface of the simplified RRR at the tip of the rod are shown in Figure 4.14 (a). As indicated by these results, the lowest temperature of the RRR is well above the highest transformation temperature (A_f) by at least 1.5˚C ensuring austenite mode of operation of the RRR. To further examine distribution of temperature inside the RRR's body, temperatures along the paths along the circumference, thickness and the width of RRR are reported in Figure 4.14 (b). The horizontal axis in this figure denotes normalized length of the path. As indicated by this figure, high temperatures are uniformly distributed in all directions with standard deviation values of the temperature in the thickness, width and circumferential directions around 0.08, 0.02 and 0.14˚C respectively.

The numerical results in this section provide a better estimation of the temperature distribution along the internal walls of the assembly. In comparison with the analytical model, the numerical model in this section had the advantage of closer examination of the areas at the proximity of the Styrofoam rings. Nevertheless, as mentioned before, use of an average Nusselt number for the flow across the assembly lacks adequate details to find the absolute highest temperatures that can be experienced during the heat-induced expansion tests. Moreover, due to the simplified heat transfer formulations of these anal-

yses, only thermal resistance values are looked into for every element missing other information such as density and specific heat. Therefore, in this section, a more comprehensive model of the assembly in Figure 4.2 including the flow regime and detailed material properties is considered.

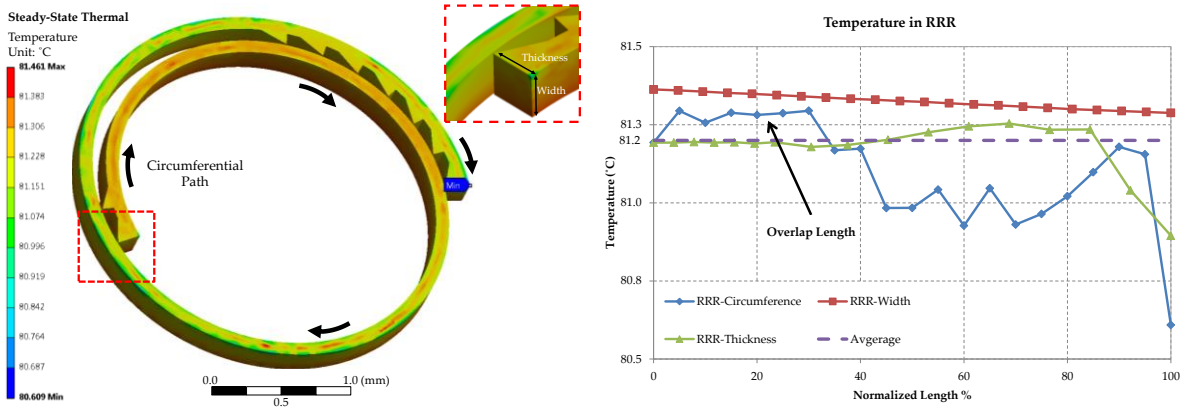

(a) (b)

Figure 4.14. Temperature distribution in the simplified RRR. a) Contour plots of temperature on the external faces of the structure. The lowest temperature observed is higher than the transformation temperature of the Nitinol, which guarantees the austenite phase of operation of the RRR, b) temperature values in the circumferential, thickness and width direction of the RRR. Low deviations from the average value show a uniform distribution of temperature in all directions of the structure.

4.6 Numerical Analysis: Conjugate Heat Transfer

In this study, equations of balance of momentum and energy are solved simultaneously to acquire a more realistic view of heat dissipation, and temperature distribution along the assembly that is subject to the crossflow of the cooling fan in Figure 4.2 (a). Moreover, results from this model provide an opportunity to validate the assumptions made in the previous sections regarding the air stagnation zones between the rod and the Styrofoam insulation bodies.

4.6.1 Materials and Methods

The 3D model of the mock-rod assembly composed of the rod, Styrofoam rings, and the mock vessel are adopted from the previous section with the material and dimensional properties given in Table 4.1. The assembly is then enclosed by a chamber of fluid air. The gap between the Styrofoam rings, the rod and the mock vessel is also filled with flu-

id air. The realistic crimped model of the RRR is laid at the tip of the rod surrounded by the stagnant air and capped by the Styrofoam cap. Figure 4.15 demonstrates the 3D model of conjugate heat transfer setup and the applied boundary conditions.

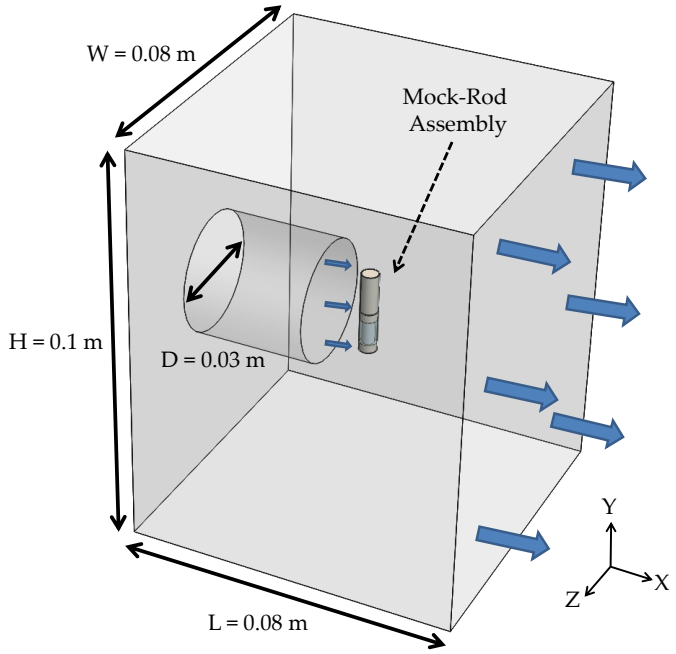

Figure 4.15. FEA model of the mock-rod assembly in a fluid chamber. Air is considered as incompressible. Turbulent models are enabled for the model due to the high values of Reynolds number. Dominant modes of heat transfer include thermal conduction and convection while ignoring effect of radiation. A normal, approach velocity is applied to the inlet with a zero gauge pressure to the outlet.

As shown by this figure, the mock-rod assembly of Figure 4.2 (b), is enclosed by a chamber of air with the height, width, and length of 100 mm, 80 mm and 80 mm respectively that extend the region by 10 times the characteristic dimension (external diameter of mock vessel) of the assembly from all sides. Sensitivity analyses were conducted to investigate the dimensional assumptions of the fluid chamber on the values of critical information of interest such as the RRR's average temperature and the mock vessel's highest temperature values. Our results indicate that a chamber larger than the aforementioned does not incur any changes in these values. To provide a more realistic model of the fan's effect at close proximity of the assembly, a cylinder with a 3-mm diameter is sculpted out of the fluid and extended to a distance of 10 mm from the mock-rod assembly. At this location, the wall facing the assembly is chosen as the inlet that is subject to a flow of air with a normal approach velocity of 7 m/s and a constant temperature of 20°C (room temperature). The opposite face of the inlet is then assigned as the outlet accom-

modating outflow of temperature through convection while all the other surfaces are assigned as fluid walls. All the cavities between the solid bodies of mock vessel, rod, Styrofoam rings, and the RRR are filled with fluid air considering their velocity and temperature as degrees of freedom in calculations. At the contact surfaces (intersection regions) of solid bodies to other solid bodies or fluid domains, interfaces are introduced to account for the wall effect as well as heat transfer through them.

The isotropic material models of Table 4.1 are adopted for the solid materials that are considered as rigid bodies. Rigid body assumption is considered reasonable for this model due to the fact that no solid body deflections or movements were observed during the experimental results.

The flow field is generated by solving for the equations of conservation of mass and momentum in the *x*, *y* and *z* directions expressed by:

$$\nabla.\mathbf{V} = 0, \tag{4.41}$$

$$\rho\left(\frac{\partial \mathbf{V}}{\partial t} + \mathbf{V}.\nabla\mathbf{V}\right) = -\nabla p + \mu_{\text{air}}\nabla^2\mathbf{V} + \mathbf{f} \tag{4.42}$$

where the vector quantity **V** is the velocity of the fluid, ρ is density, p is pressure, **f** represents body forces acting on the fluid, and μ_{air} stands for the dynamic viscosity of air. Simultaneously, the model solves for the thermal balance of the mock-rod assembly and the air flowing in the chamber. Dominant modes of heat transfer are conduction (in the assembly) and convection in the cooling air (via the external walls of the assembly) while ignoring the effect of heat radiation. The temperature field across all the contact surfaces is assumed to be continuous disregarding contact resistance. These equations are solved using stabilized finite volume formulations for fluid flow by the commercial CFD package ANSYS CFX (ANSYS Inc., Canonsburg PA, USA) in a steady-state analysis. Physical properties of air such as thermal conductivity, heat capacity and density are defined by the uniform properties given in Table 4.1. Due to the subsonic velocities, air is modelled as an incompressible fluid, yet because of the high Reynolds numbers (Re ≈ 2000) Shear Stress Transport (SST) turbulence model is enabled for the fluid domain.

At the outlet a zero gauge pressure is applied while a no slip condition is introduced at all solid surfaces (zero velocity at walls). Data of interest in this analysis is the temperature distribution across different parts of the assembly, more specifically on the internal

walls of the mock vessel and surface temperate of the RRR. Independence of the fluid regime from the fluid chamber dimensions is later demonstrated in this section by the low velocity gradients close to the walls of the chamber.

To ensure accuracy of the results, a mesh sensitivity analysis is conducted prior to the final reports. In this study successive mesh refinement levels are defined, each reducing the size of the fluid and solid elements by 50%, thereby increasing the number of elements by a factor of 2. Critical information such as highest temperature of the mock vessel, lowest temperature of the ring, average distribution of temperature along the axial direction of the rod and velocity profile around the circumference of the assembly, more particularly appearance of the flow wake region, were compared from one level to the other. As soon as the highest difference between these values fell below 3%, the corresponding refinement level was chosen for reporting the results. The geometry is meshed with both tetrahedral and hexahedral elements, shown in Figure 4.16, majority of which belong to the former due to different part sizes and irregular shapes around the RRR sawtooth structures. Mesh size was chosen to be smaller in and around the assembly in the fluid region, shown in Figure 4.16 (b), with a slow inflation rate throughout the fluid domain to accommodate smoother convergence of the results and better capture of the fluid flow close to this region. Following this objective, close to the walls of the mock vessel assembly a hexahedral boundary mesh with multiple layers is generated. The final mesh consisting of around 2,000,000 elements is shown in Figure 4.16 with close-up view near the assembly in parts (b) and (c).

Convergence criterion for the residuals of heat, mass, momentum and turbulence are all set to 10^{-5} that is one order of magnitude lower than the solver's default. The total number of iterations for completion is set to 800 and the solver is due to iterate to the last one even if it reaches the target residual accuracy. This is to ensure stability of results over a number of iterations. Models are simulated on a Dell Precision workstation with two quad-core Xeon processors clocked at 2.6 GHz and 20 GB of RAM. Runtime for the final model is about 16 hours to finish.

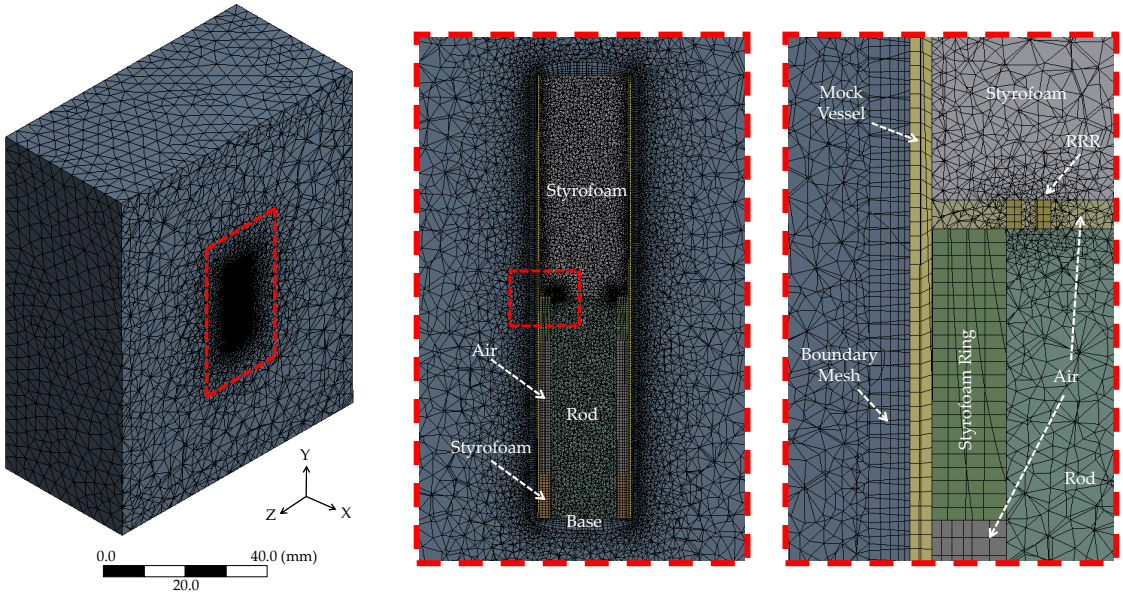

(a) (b) (c)

Figure 4.16. Discretization of the fluid solid domain for conjugate heat transfer. a) Overview of the model consisting of 2,000,000 elements, b) close-up of the mock-rod assembly with refined fluid mesh close to the assembly and the refined mesh of the solids, c) close-up of the assembly around the deployment area with the refined boundary mesh close to the mock vessel walls. The mesh in the RRR domain is further refined to capture temperature gradient across thickness.

4.6.2 Results

Convergence of the residuals of heat, mass, momentum and turbulence to the predetermined target values over computational iterations is demonstrated in Figure 4.17 (a–c). As indicated by these figures, all the residuals fall below the objective error (10^{-5}) after 600 iterations, before completion of the last iteration, and continue to decrease over time. Stability of the final results is further confirmed by the graph of the maximum temperature of the mock vessel presented in Figure 4.17 (d). As indicated by this trend, the mock vessel's highest body temperature levels out after the 300th iteration at 46.4°C with minimal fluctuations till completion of the last iteration. Due to the difference in the values of the local Nusselt number and the resultant non-uniform distribution of temperature at the circumferential direction of any of the radial cross-sections of the mock-rod assembly, four different paths are chosen to report temperature results in the axial direction. These paths that divide the circumference of the assembly into four quadrants include, one facing the inlet (front path), one facing the outlet (rear path), one at 90° angle from

the front path at the right side of the assembly (right path), and one at -90° angle from the front path at the left side of the assembly (left path).

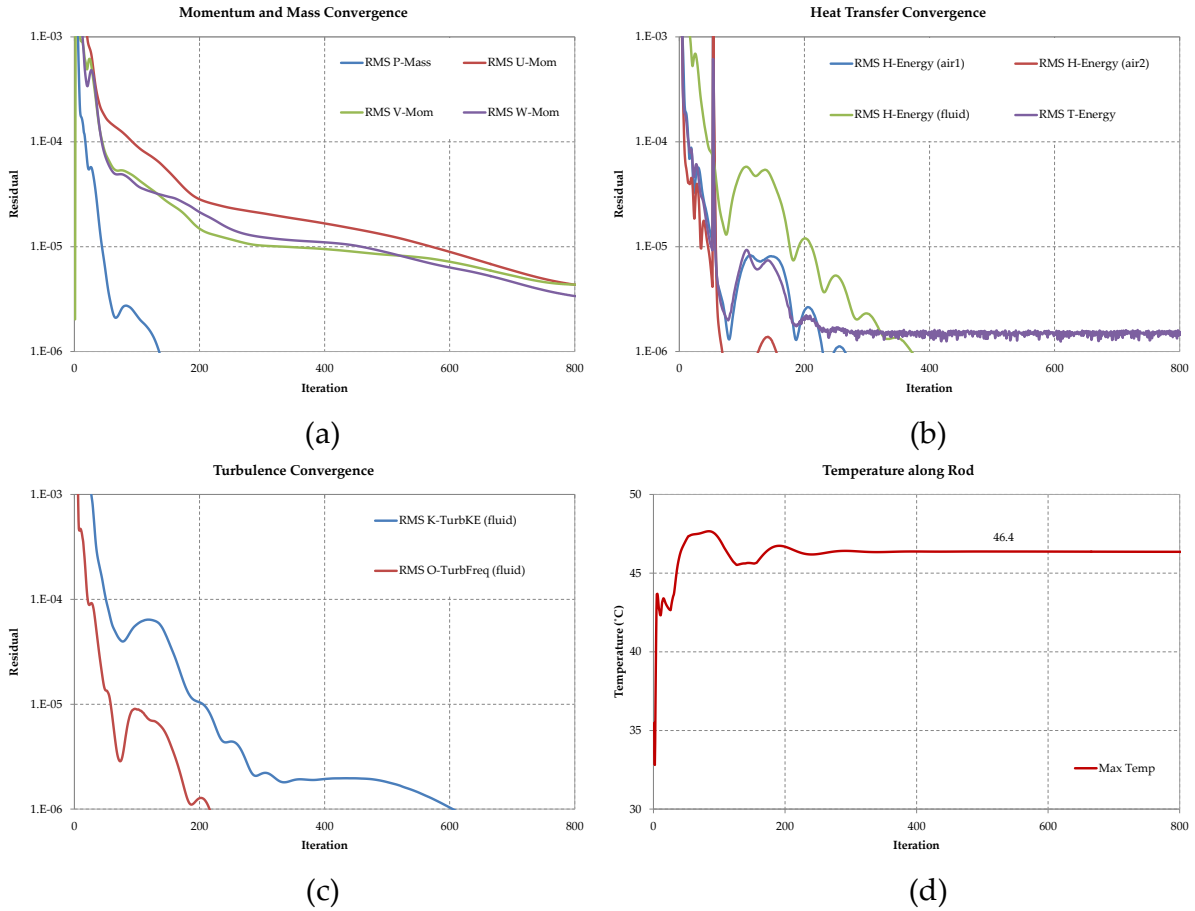

Figure 4.17. Convergence plots of the conjugate heat transfer analysis. a) Mass and momentum convergence plots for the fluid chamber, b) heat transfer residuals for all domains, c) shear stress transport (SST) turbulence residuals for the fluid chamber. All the residuals fall below the objective error (10^{-5}) after iteration 600, d) maximum temperature of the mock over the course of solution converges to a steady value at 46.4°C after the 300th iteration.

Temperature contour plots on the external walls of the HT rod are shown in Figure 4.18 (a) with the values of temperature along the four longitudinal paths presented in Figure 4.18 (b). As indicated by these trends and the radial cross-sectional contour plots at the longitudinal distance of 5 mm from the base, the temperature distribution along the rod, maintains a uniform circumferential distribution highlighted by Figure 4.18 (a). Moreover, compared with the results obtained from the previous sections, particularly Figure 4.11 (b), it is apparent that the analytical and the uniform numerical analysis results both underestimate the tip temperature by at most 1°C while all methods show temperatures

of the tip higher than the final transformation temperature of the RRR ensuring its transformation into the austenite phase in an experimental setup.

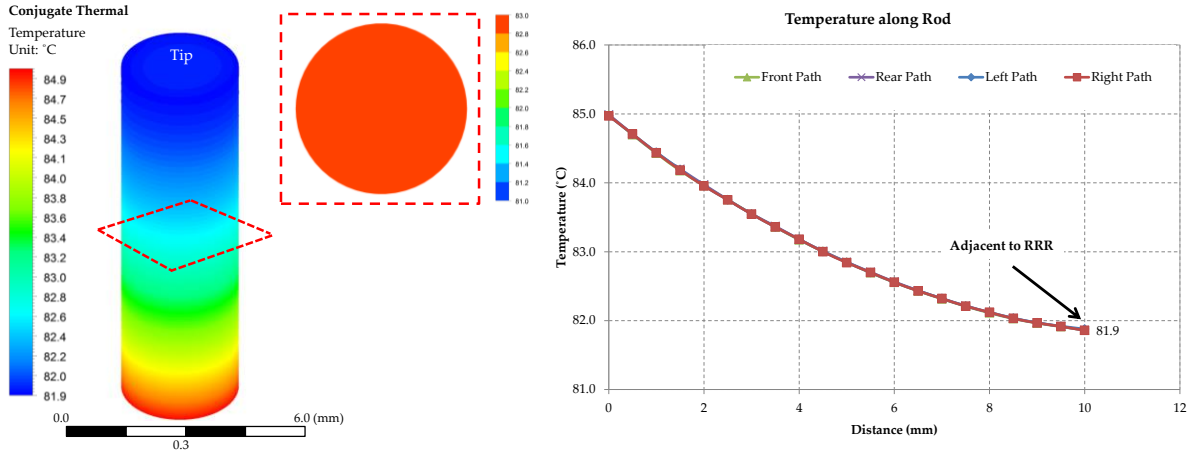

(a) (b)

Figure 4.18. Temperature distribution along the rod, conjugate heat transfer. a) Contour plots of temperature along the HT rod, temperature distribution in the circumferential and radial direction of the rod is uniform, b) temperature values along the four axial paths of front, rear, left and right. Lowest temperature at the tip stands higher than the RRR's final transformation temperature (A_f).

In order to demonstrate the efficacy of the assumed dimensions for the fluid chamber as well as the stagnation of air at the region enclosed between the HT rod, mock vessel and Styrofoam rings and at the region between the HT rod's tip, mock vessel and the Styrofoam cap, velocity contour plots at selected horizontal and vertical cross-sectional planes are presented in the following. Contour plots of the flow velocity in a horizontal plane of the fluid chamber of Figure 4.15 at height Y = 10.1 mm from the base of the assembly is shown in Figure 4.19. At this height, the cross-sectional plane passes through the RRR's deployment site providing insight into the fluid regime of the entrapped air around the RRR. As demonstrated by this figure and confirmed by the velocity values along path 1 in the graph of part (b), the fluid at the RRR deployment region is in complete stagnation and conduction is the dominant mode of heat transfer through this medium. This figure also clearly shows the advent of wake region at the rear end of the assembly after the flow separation region at the sides. More details may be observed from the magnitudes of velocity along the report paths of part (a) vs. the z coordinate as demonstrated in Figure 4.19 (b) from the origin of the coordinate system that is assumed at the centre of the base of the mock-rod assembly.

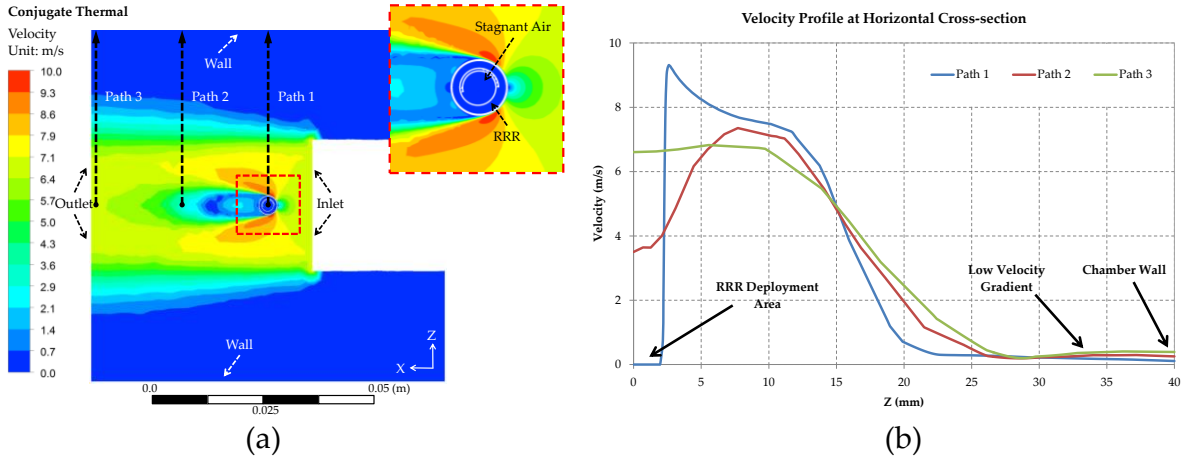

Figure 4.19. Velocity profile at the horizontal cross-section of the fluid chamber. a) Contour plots of velocity magnitudes in the fluid domains, fluid is in complete stagnation at the RRR deployment zone. Fluid exhibits very small velocity magnitudes at a great distance from the fluid boundary walls relative to the chamber's dimensions showing the efficacy of dimensional assumptions in the horizontal direction for this analysis, b) velocity values along paths 1, 2 and 3 from part (a), velocity gradients at distances greater than 30 mm from the centre of the assembly are close to zero, denoted by the horizontal velocity trends that are maintained to the extent of the boundaries of the chamber (walls).

As indicated by these trends, the profile along Path 1 starts with zero magnitudes that correspond with the stagnant air in the deployment zone and the short boundary layer adjacent to the external wall of the mock vessel abruptly followed by higher magnitudes that eventually start to decline at distance 15 mm from the origin. This trend is then followed by very low velocity magnitudes that extend to the walls of the fluid chamber from distance 30 mm, Figure 4.19 (b). The very low velocity gradients for the relatively long distance from 30 mm to the chamber's wall surface indicate adequacy of the fluid region's width to capture the fluid behaviour around the mock in a larger environment such as a room. Wall shear stress values equal to zero at the vertical walls of the chamber that are denoted in Figure 4.19 (a) further complementing this statement.

The velocity profile snapshot at a vertical plane at the centre of the fluid region is demonstrated in Figure 4.20. The close-up image near the mock-rod assembly highlights the stagnant air zones that are trapped between the mock vessel and polystyrene insulation layers as well as the flow wake region at the rear side of the assembly. Differences in the magnitudes of velocity at different circumferential and axial points of the mock-rod assembly denoted by the contour plots of Figures 4.20 and 4.19 demonstrate the expected

fluctuations in the local Nusselt numbers. This highlights the necessity of conjugate heat transfer analysis to better capture circumferential temperature distributions.

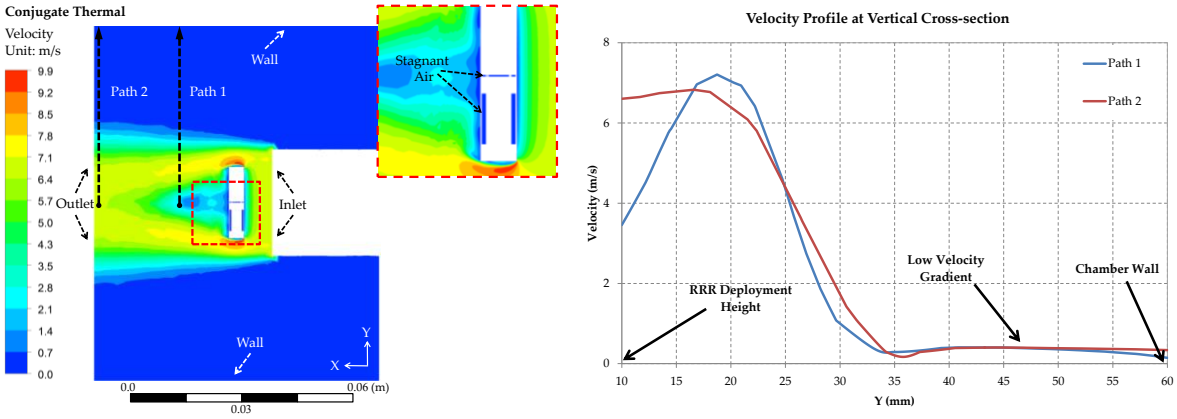

Figure 4.20. Velocity profile at the vertical cross-section of the fluid chamber. a) Contour plots of velocity magnitudes in the fluid domains, stagnant air regions are highlighted in the close-up image. Small velocity magnitudes are observed for a relatively long distance from the chamber walls. These results coupled with zero wall shear stress values at the boundary walls of the chamber show independence of the results to the vertical dimensions of the fluid chamber, b) velocity magnitudes along paths 1 and 2 highlighted in part (a). Low velocity values and near-zero gradients after distance 40 confirm the efficacy of the dimensional assumptions in the vertical direction.

Velocity magnitudes along the two paths in part (a) of Figure 4.20 are plotted in part (b) of this figure. The paths start at a height equivalent to the tip of the rod (Y = 10 mm) and extend to the ceiling of the region at Y = 60 mm. As indicated by the steady trends after distance 40 mm, the velocity exhibits close to zero gradients that are maintained up to the boundaries of the chamber. These observations are further confirmed by the zero wall shear stress values at the floor and ceiling boundary walls denoted in Figure 4.20 (a). The aforementioned results in addition to the horizontal trends of Figure 4.19 (b) further validate the adequacy of the fluid chamber dimensions in capturing the real physical interactions of the mock-rod assembly and the cooling fan in a room.

Distribution of temperature along the internal surfaces of the mock vessel by contour plots and values along the four axial paths of the front, rear, left and right, which are snapped to the internal surface of the mock vessel, are shown in Figure 4.21. As demonstrated by these plots, areas of lower Nusselt number (lower fluid velocity nearby) and close to the heat source at the base, show relatively higher values of temperature. Conse-

quently the temperature at the rear bottom end of the mock-rod assembly reaches the highest values that are still safely below the mock vessel's nominal operating temperatures. Higher temperature values close to the Styrofoam rings are still observed that is due to the lower thermal resistance of these objects compared to stagnant air.

Temperature values along the four axial paths in Figure 4.21 (b), further confirm the non-uniform distribution of temperature in the circumferential direction highlighting the importance of inclusion of fluid effects into the simulations of heat transfer that incorporate convection. Temperature values of Figure 4.21 (b) are reported for the entire length of the assembly where RRR is deployed at distance 10 mm from the base of the assembly that is located at the origin.

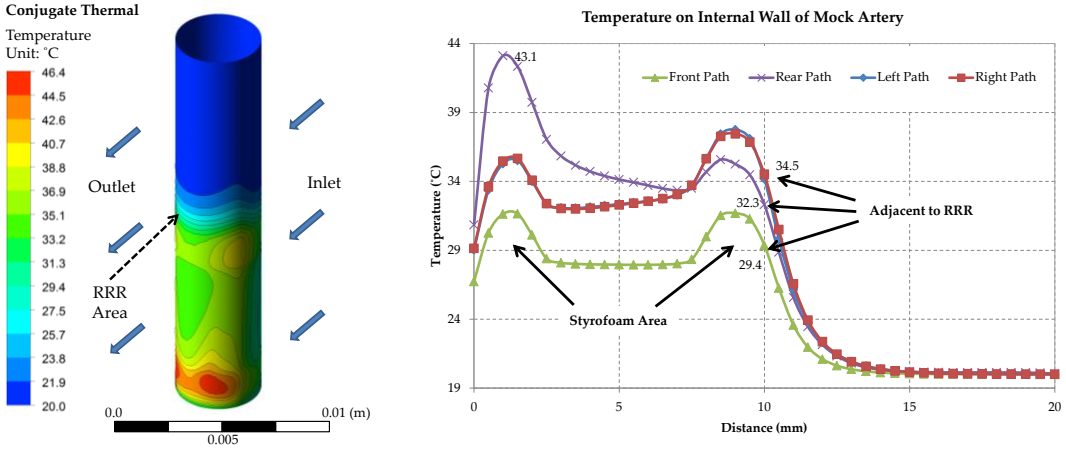

(a) (b)

Figure 4.21. Temperature on mock vessel internal walls, conjugate heat transfer. a) Temperature contour plots along the internal walls of the mock vessel. Subject to the local Nusselt number, circumferential distribution of temperature is not uniform and adopts relatively higher values at the rear end of the assembly, b) temperature values along axial paths at the front, rear, left and right side of the internal walls of mock vessel.

As indicated by these results, the temperature at the top half of the mock vessel (distance 10 mm onwards) drops rapidly to room temperature, validating the assumptions made in the theoretical framework for this section of the mock, refer to page 132. Due to the high convective heat transfer coefficients at the front, temperatures experienced from this regions fall below the uniform temperature values from the previous section. Nevertheless, temperatures adopt relatively higher values at some local points at the rear bottom of the assembly that are at the farthest distance from the deployment area. Temperature distributions on the external walls of the mock vessel are shown in Figure 4.22. These re-

sults, once again confirm the operation of the mock vessel for the short duration of the thermal expansion, 2–3 sec, within its nominal temperature range.

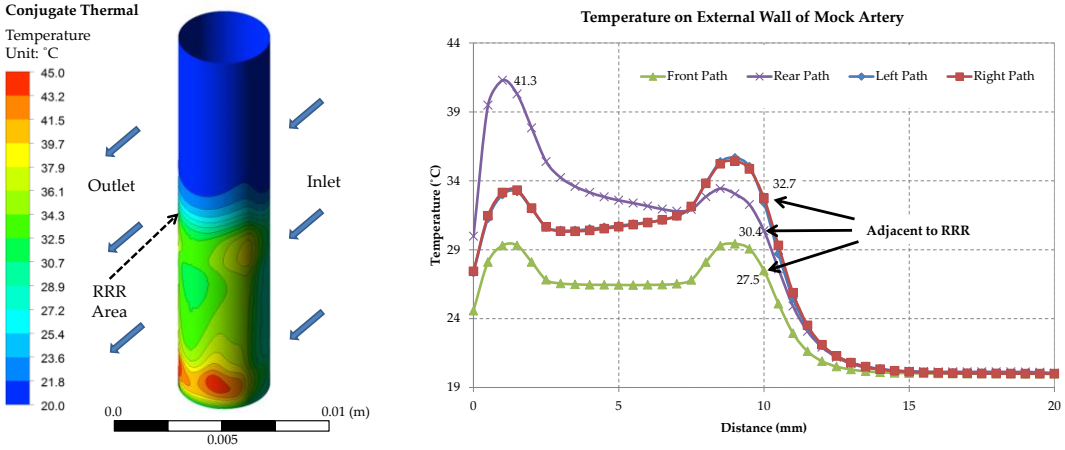

(a) (b)

Figure 4.22. Temperature on mock vessel external walls, conjugate heat transfer. a) Contour plots of temperature distribution along the external walls of the mock vessel, b) temperature values along the front, rear, left and right axial paths.

As mentioned before, one of the most important objectives of these studies is to ensure phase transformation of the crimped martensite RRR into austenite by raising the temperature of this structure above the final transformation temperature (A_f) of Nitinol. Temperature contour plots on the external surfaces of the RRR are shown in Figure 4.23 (a) complimented by the temperature values reported along different paths of the RRR in Figure 4.23 (b). As shown, the RRR, being uniformly heated, is in the austenite mode of operation by its lowest internal temperature being above $A_f \approx 80^{\circ}C$.

The numerical models presented in this section laid the foundation for further investigation of several parameters such as expansion mechanism of the RRR inside the mock vessel, and the radial forces exerted by the crimped RRR while transforming from martensite to austenite. While complementing the previous theoretical and numerical analyses, it is important to note the limitations of the conjugate heat transfer study in this section. As mentioned in the materials and methods section, the effect of thermal contact has been ignored due to lack of such physical information. This simplification is justified by the fact that by the introduction of thermal contact between the solid parts such as the rod, Styrofoam rings, and mock vessel, the desired shielding effect would even further increase, which effectively results in distribution of less temperature values in the mock vessel. Given the higher surface area of the tip of the rod compared to that of the RRR,

and due to the stagnation of the fluid at this region, the assumption to ignore the thermal resistance between the RRR and rod is reasonable as the thermal resistance between these two parts is yet smaller than other means of heat transfer at the region such as the mock vessel and the stagnant air. Moreover, the material properties of the parts in this numerical analysis are mainly derived from literature and datasheets that belong to the tests conducted on the bulk materials. Therefore, it is impossible to acquire the exact values for these properties in different test conditions and shapes of components that might render slight sources of error in the final results.

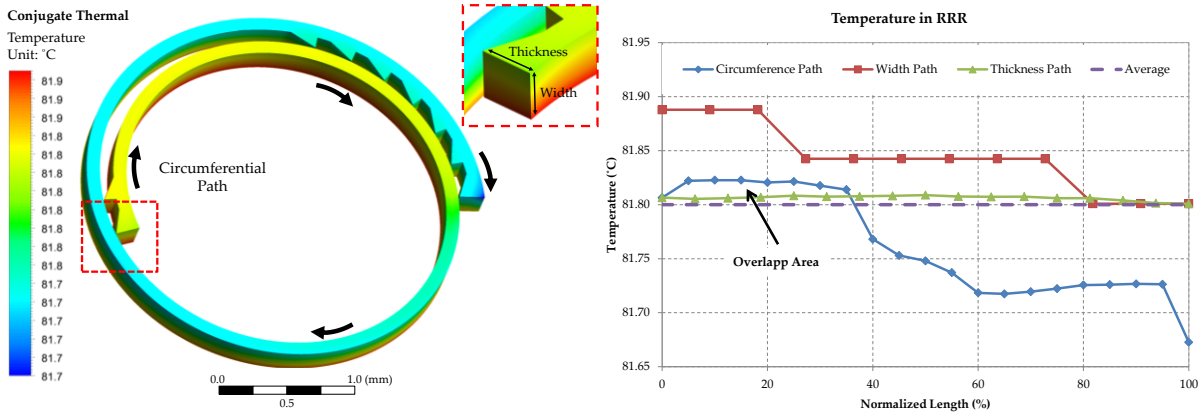

(a) (b)

Figure 4.23. Temperature distribution in the RRR, conjugate heat transfer. a) Temperature contour plots on the external surfaces of the RRR, b) temperature values along the circumference, width and thickness of the RRR.

To complement the numerical results of the conjugate heat transfer study, further experimental studies are conducted in the following sections. In these studies, first the internal and external temperatures of the mock vessel in the setup of Figure 4.2 is measured in a number of accessible points, then the expansion results of the crimped martensite RRR by application of heat and while undergoing phase transformation into austenite are presented. In the end the radial expansion forces exerted by a constrained RRR under the stimuli of heat are measured and presented.

4.7 Experimental Results

In this section heat-induced expansion mechanics of the RRR are experimentally studied and, where relevant, comparisons are drawn with the results of the previous sections. The physical setup of the heat transfer model in Figure 4.2 is shown in Figure 4.24. The base is first laid on top of a hotplate (Cimarec, Barnstead International, Iowa, USA) with-

out the RRR, and the temperature of the rod close to the bottom Styrofoam ring shown in Figure 4.24 (c) is measured using a digital thermocouple (OMEGA HH802U, OMEGA Engineering, INC., Connecticut, USA) while increasing the temperature of the hot plate to reach around 85˚C. This temperature corresponds with the parameter T_b at the base of the mock-rod assembly in Figure 4.2 (b). At this stage the temperature of the hotplate has reached around 100˚C.

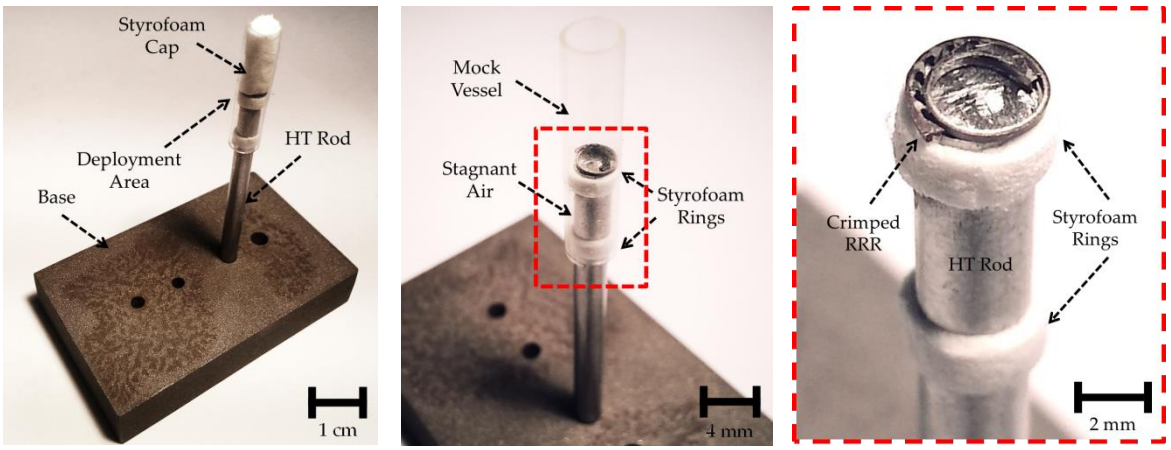

Figure 4.24. Heat transfer setup. a) Overview of the setup, b) close-up view of the mock-rod assembly with the Styrofoam cap removed for better visibility, c) close-up view of the deployment area with the crimped RRR at the tip of HT rod. The mock vessel is removed for better visibility. The RRR is semi-down-crimped to the HT rod diameter.

At this equilibrium state, temperature of the external surface of the mock vessel is measured using the thermocouple at eight different points. Two points per each of the axial paths at the front, rear, left and right of the mock vessel as defined in the previous sections are chosen for these measurements. On each path one point is chosen towards the bottom of the assembly (close to the bottom Styrofoam ring in Figure 4.24, c) while the other is chosen close to the RRR's deployment area (close to the top Styrofoam ring in Figure 4.24, c). The 2-mm-long tip of the sensing probe is fixed axially along the surface using an adhesive tape. Histograms of Figure 4.25 and Figure 4.26 present the measured temperature values at the aforementioned acquisition points on the external surface of the mock vessel in comparison with the numerical and analytical results obtained in the previous sections. Figure 4.25 shows the temperature values at points close to the base of mock-rod assembly, whereas Figure 4.26 shows temperatures at the points close to the deployment area of the RRR (deployment region of the mock-rod assembly). The

Avg. values in these figures refer to the average of a series of values at each acquisition point along a 2-mm axial path (equivalent to the length of the probe tip) on the external surface of the mock vessel.

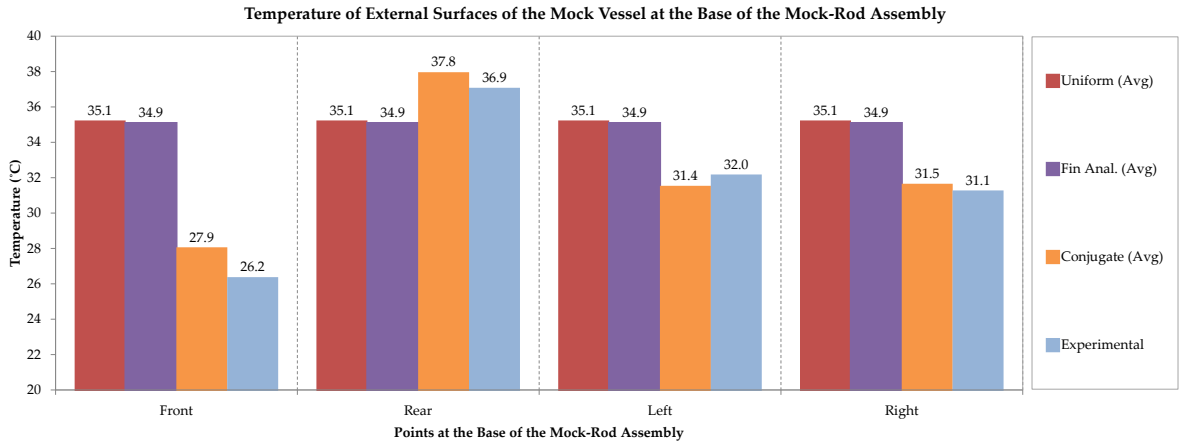

Figure 4.25. Temperature of the external surface of mock vessel, base. The (Avg) values refer to the average of a number of values at the acquisition points at the base along 2-mm axial paths on the external surface of the mock vessel starting from base of mock-rod assembly (from x = 0 mm to x = 2 mm). This axial length is equal to the length of the sensing probe.

In these figures, "Uniform" refers to the results from the uniform numerical analysis in Section 4.5, "Fin Anal." refers to the results from the theoretical analysis using theory of crossflow over finned surfaces in Section 4.4 and "Conjugate" refers to the results from the conjugate heat transfer analysis conducted in Section 4.6. Comparison between the temperature values from the conjugate heat transfer analysis and the experimental measurements in these figures demonstrates the capability of the former to effectively capture the temperature distribution in these acquisition points.

In Figure 4.25, the lower temperate levels at the front, left and right points from the conjugate heat transfer and the experimental measurements in comparison with the results from uniform numerical analysis and the theoretical fin analysis are associated with the high local Nusselt numbers at these areas as discussed in the previous section. Following a similar trend, due to the lower local Nusselt number of the back flow at the rear end of the assembly, higher temperature values are measured form both the conjugate heat transfer and the experimental results in comparison with the other studies where an average convective heat transfer coefficient is used for the crossflow.

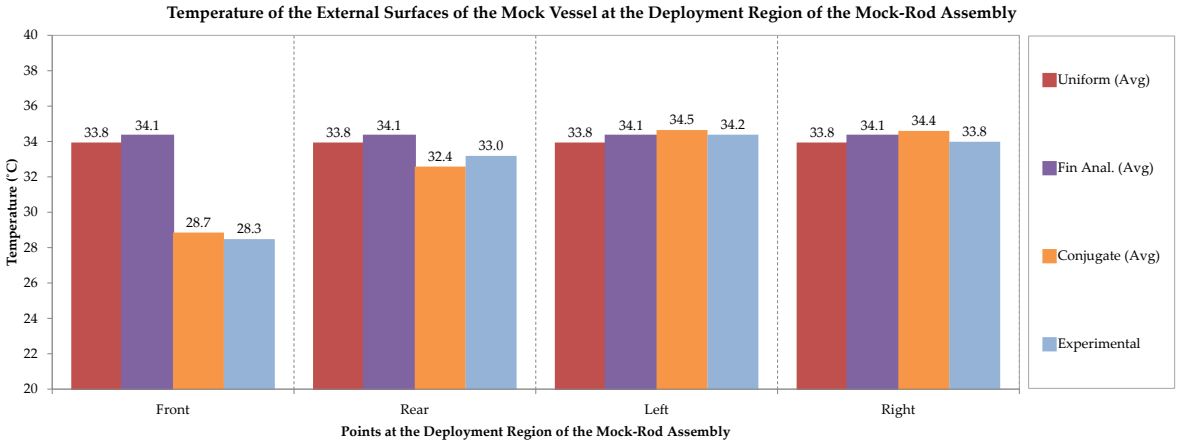

Figure 4.26. Temperature of the external surface of mock vessel, deployment area. The (Avg) values refer to the average of a number of values at the acquisition points at the base along 2-mm axial paths on the external surface of the mock vessel starting from tip of the rod assembly (from x = 10 mm to x = 8 mm). This axial length is equal to the length of the sensing probe.

As indicated by Figure 4.26, the differences between the experimental measurements, uniform numerical analysis, conjugate heat transfer analysis and the theoretical fin analysis studies become markedly lower towards the deployment region of the assembly which is more prominent for the rear, left and right acquisition points. Nevertheless, the relatively high Nusselt numbers at the front side of the assembly results in lower temperature readings from the conjugate heat transfer analysis and the measurements compared with the uniform numerical and the theoretical fin analysis results. Values from Figures 4.25 and 4.26, once again, confirm the operation of the mock vessel within nominal temperature ranges minimizing the effect of temperature in the integrity of the results in the next section.

4.7.1 Heat-induced Actuation *in vitro*

The thermally treated shape of the RRR has a mean inner diameter of 4.1 mm and any deformations causing less than 10% strain in the martensite phase will be retrieved when the temperature is raised above the transformation temperature. One such deformation may be a manual crimping wherein the diameter is decreased for deployment inside a vessel. Mechanics of the expansion by heat are studied in the following sections by three studies. First the expansion of the RRR is visualized inside and outside a mock vessel, and then expansion forces are measured while increasing the temperature of the RRR in the second study. Using the setup shown in Figure 4.24 with the RRR in the deployment

region, when the temperature of the mock-rod base passes around 80˚C (A_f), the RRR fully expands inside the lumen that is demonstrated in Figure 4.27.

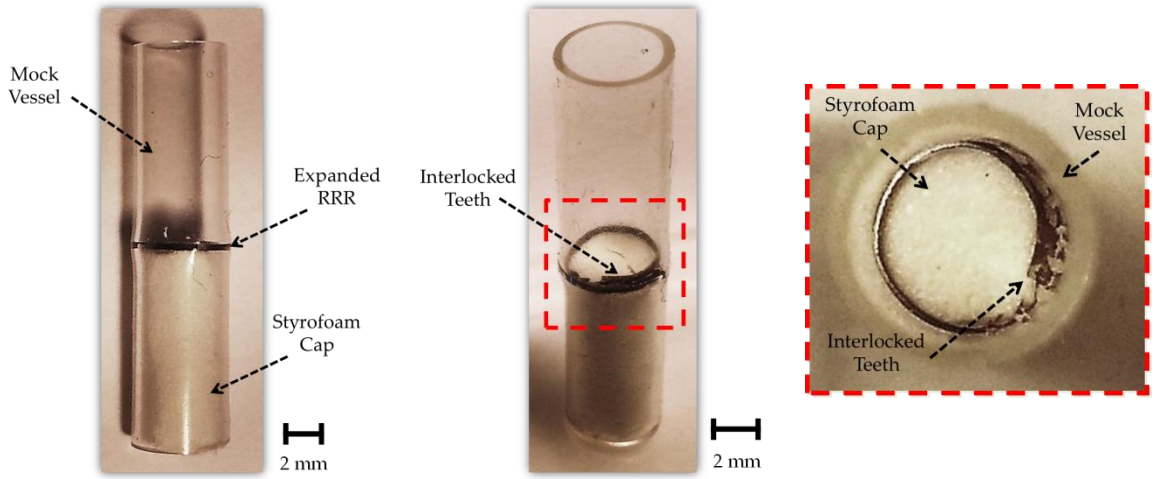

Figure 4.27. *In vitro* thermal expansion of the RRR. a) Front view, the mock is removed from the rod assembly while the Styrofoam cap is left in place. The slight overstretch of the mock vessel at the RRR's deployment area indicates expansion of the RRR and the interlock of sawtooth structures from the two overlapping ends of the RRR, b) ISO view and c) top view of the mock vessel with the expanded interlocked RRR. For a better indication of expansion compare with Figure 4.24.

The slight overstretch of the mock vessel in the deployment region of the mock vessel in Figure 4.27 (a) in addition to comparison of parts (b) and (c) of Figure 4.24 with the corresponding parts of Figure 4.27 clearly indicate expansion of the RRR inside the mock vessel up to a mean inner diameter of 4.1 mm and the interlock of the sawtooth structures from the two ends of the RRR.

4.7.2 Heat-induced Actuation in Free Expansion

To further investigate the mechanics of expansion by heat, free expansion of the ring in response to raising its temperature is investigated. The RRR is first manually crimped to an average external diameter of 3 mm then laid on a hot plate while gradually increasing the temperature from room temperature (20˚C) up to 80˚C in steps of 5˚C. At every step, 10 seconds is lapsed to ensure the RRR reaching equilibrium temperature close to that of the hot plate. Figure 4.28 shows a series of images taken during the heat-induced free expansion of the RRR starting from the crimped state at room temperature ($T = 20$˚C) up to the fully expanded sate at $T = 80$˚C.

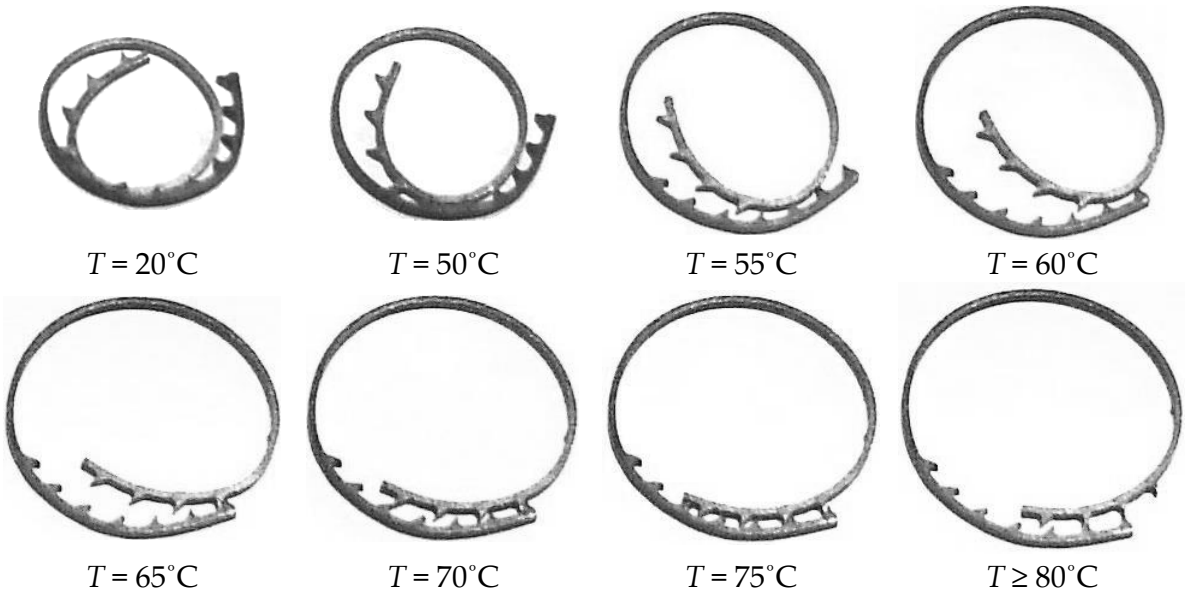

Figure 4.28. Free expansion of the RRR under heat stimuli. RRR is down-crimped to a mean external diameter of 3 mm at room temperature $T = 20^{\circ}C$, then temperature is raised in 5°C steps. Up to 50°C there is no significant change in diameter (less than 10% expansion) after which RRR starts to expand up to 80°C.

External diameter of the RRR at each temperature step is measured by a calliper (ABSOLUTE Digimatic, Mitutoyo, USA) and reported by taking the average of four measurements. Graph of the external diameters of the RRR at different temperatures of the hot plate (thus RRR) is presented in Figure 4.29.

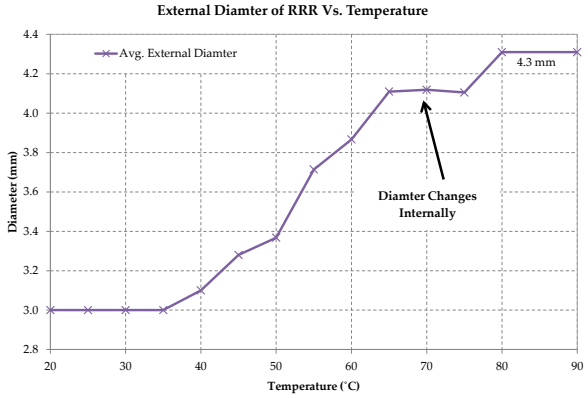

Figure 4.29. Average external diameter of RRR vs. temperate. No significant change in diameter up to 50°C after which the diameter increases steadily up to 65°C. Most of the changes between 65 and 75°C occur at the internal diameter as observed in Figure 4.28. External diameter becomes constant after 80°C.

As indicated by this figure, for $T = 20–45^{\circ}C$ there is very little change in the diameter (less than 3%), then the RRR starts to expand at 50°C where the phase transformation starts to occur. From 50°C up to 80°C the external diameter increases almost constantly in all

temperature steps except between 65˚C and 75˚C where most of the shape changes occur in the internal diameter, more specifically with the tooth traversal and interlock between 70 and 75˚C. Given the situation after deployment of the RRR where it is under compressive forces of a vessel, these intermediate stages of change in the internal diameter manifest themselves as perceivable changes in the external diameter. That is due to the more uniform expansion of RRR from the two overlapping ends as a result of the constraining forces from the vessel. The RRR reaches its maximum external diameter around 4.3 mm at 80˚C with no change after that.

4.7.3 Heat-induced Actuation Force

The free and *in vitro* heat-induced expansion results of the previous section demonstrated the capability of the RRR to respond to thermal stimuli and the sufficiency of expansion forces to overcome the compressive forces of a mock vessel. This was observed by the slight over-expansion of the mock vessel after deployment of the RRR utilizing heat. Nevertheless, to provide the reader with better quantitative results and further characterise the fabricated RRR, the force measurement setup of Figure 4.30 is implemented.

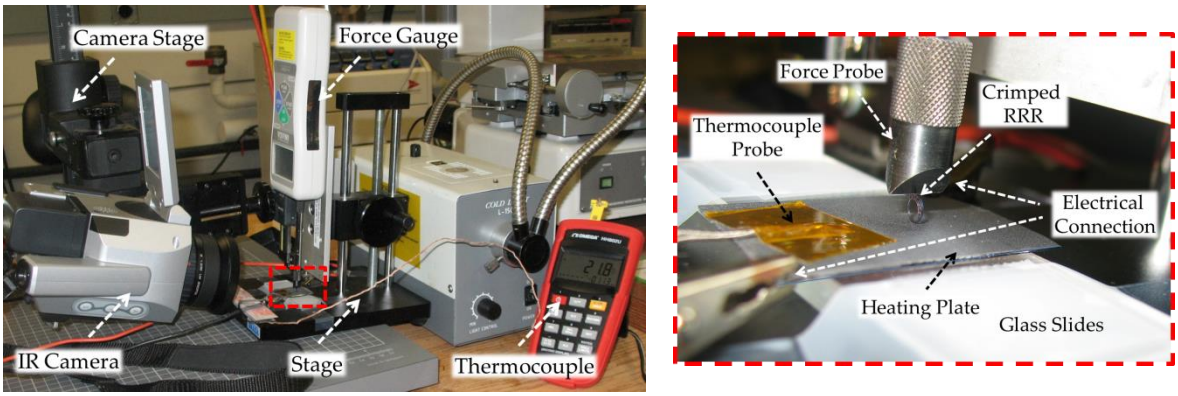

(a) (b)

Figure 4.30. Actuation force measurement setup. a) Setup overview, b) close-up image from the probe area. Heating plate is coated with a conductive copper layer heated by resistive heating. The RRR is mounted on top of the heating plate by an adhesive. At the bottom, the heating plate is separated from the stage by two layers of glass slides to decrease heat dissipation into the stage. RRR is crimped and clamped by the force probe, and the expansion forces as a result of phase transformation are recorded.

This setup is comprised of three major components including, an RRR, a heating plate and a digital force gauge (DS2-2, Imada Inc., IL, USA). The RRR, down-crimped to an external diameter of 3-mm in room temperature, is mounted on top of the heating plate

by an adhesive. The RRR is thermally trained to an expanded shape with mean inner diameter of 4.1 mm that is achieved in the previous section at the final transformation temperature of $A_f \approx 80^{\circ}C$, well above the room temperature (around 20°C). Heating plate, separated from the base of the force gauge by two layers of glass slides, is comprised of a 3×2 cm rectangular block machined from a 100-mm in diameter P-type wafer (University Wafer, Boston, Massachusetts, USA) that is coated with a thin layer of copper (Cu). The 20-μm Cu layer is electroplated on top of the wafer with a 50-nm intermediate adhesive layer of Cr.

Passing a direct current through the heating plate, its temperature starts to rise due to energy loss through the conductive layer governed by Joule's heating law expressed by the balance of rate of energy at equilibrium:

$$\left[\dot{Q}_{\text{electric}} = I^2 R_{\text{electric,plate}}\right] = \left[\dot{Q}_{\text{thermal}} = \frac{\left(T_{\text{plate}} - T_{\text{room}}\right)}{R_{\text{thermal,plate}}}\right]. \qquad \textbf{(4.43)}$$

In this relation, $\dot{Q}$ refers to the rate of generation (consumption) of energy per second. Moreover, $R_{\text{electric,plate}}$ refers to the total electrical resistance of the conductive layer of the heating plate, and $R_{\text{thermal,plate}}$ refers to the total thermal resistance of all the components that are in contact with the heating plate. Variables T_{plate} and T_{room} refer to the average temperature of the plate and room respectively.

At the initial stage, the force probe is lowered in the axial height down to the level of the external diameter of the RRR. At this height, further downward motion of the probe incurs a rapid increase in the reaction forces from the RRR (Figure 4.30, b). Then the probe is elevated slightly by 100 μm by the displacement stage to compensate for the vertical thermal expansion of other components in the setup such as the heating plate, glass slides, the probe tip and base. To show adequacy of this distance, an upper limit for the linear vertical expansion of these components may be calculated by the equation of linear thermal expansion [242] expressed by:

$$\Delta L = L_{\text{initial}} \delta_{\text{linear}} \Delta T \qquad \textbf{(4.44)}$$

where ΔL denotes change in length, L_{initial} represents the initial length in the axis of interest (vertical axis in this case), and δ_{linear} is the linear coefficient of thermal expansion

(CTE). To find an upper limit we may assume the highest average temperature of the heating plate for all the other components in the setup including probe's tip and stage, the glass slides and the heating plate. This is an overestimation of temperatures for all these components due to the high thermal resistance (thus shielding effect) of glass slides and the cooling of the components through natural convection. Nevertheless, such an overestimation ensures reduction of noise data which may incur due to the linear expansion of these components.

According to the results of experimental measurements, outlined below, in order to raise the RRR's temperature up to 85˚C, the heating plate's temperature requires reaching around 113˚C on average. Substituting dimensional and material properties of the components given in Table 4.2 into Equation (4.44), a higher value for the cumulative vertical expansion of the probe tip, probe stage, heating plate and glass slides amounts to around 43 μm. Consequently, the 100-μm separation zone well accommodates for such vertical linear expansions.

Restraining the probe at the specified height above the external surface of the RRR, temperature of the heating plate is gradually increased by increasing the direct current in 0.1-A steps. A 10-sec delay is given at each step to allow all components reach thermal equilibrium then the expansion (reaction) forces from the RRR are recorded by the average value of two readings from the force gauge with 1-mN resolution.

Table 4.2. Vertical expansion of components in heat-induced actuation setup.

	Probe Tip	Probe Stage	Wafer Substrate	Cu Layer	Glass Slide
Material	Stainless Steel	Stainless Steel	Silicon	Copper	Glass
CTE (1/˚C) × 10^{-6}	11 [242]	11 [242]	3.2 [243]	17 [242]	9 [242]
Axial Height (mm)	20	20	1	0.02	1×2
Upper ΔT (˚C)	93	93	93	93	93
Vertical Expansion (μm)	20.5	20.5	0.3	0.03	1.7
			Total Vertical Expansion (μm)		**43**

Temperature of the heating plate at the proximity of an electrical contact is measured by a digital thermocouple (OMEGA HH802U, OMEGA Engineering, INC., Connecticut, USA). Temperature distribution at the surface of the heating plate close to the mounting point and the RRR is recorded by an infrared (IR) camera (Jenoptik VarioCam HiRes 1.2 M, Jena, Germany). The camera is first calibrated with the digital thermocouple by com-

parison of temperature measurements from the Nitinol sheet that the RRR is machined from. Temperature of the ring is reported by the average values of three points whereas temperature of the heating plate close to the RRR's mounting region is reported by the average of values of 2 points denoted in Figure 4.31.

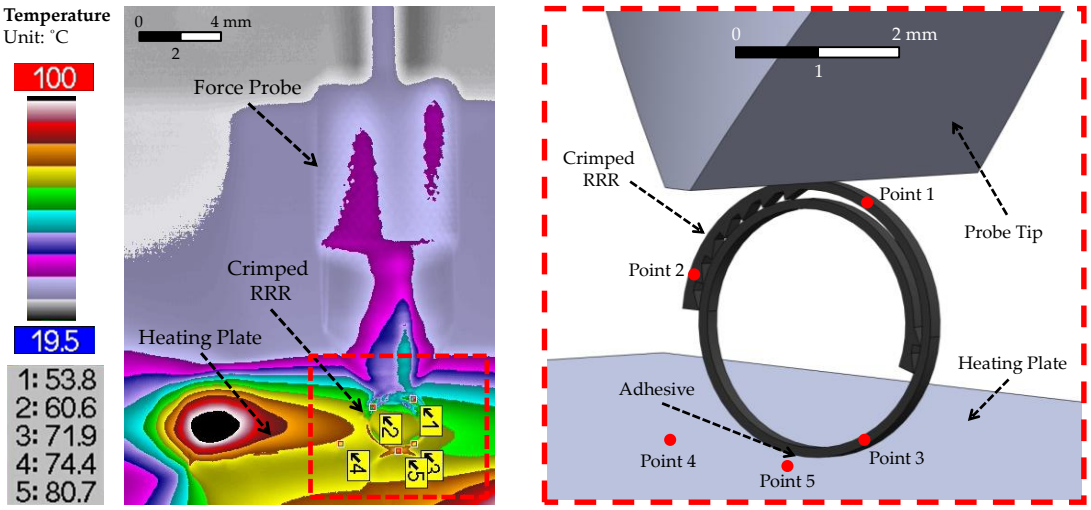

(a) (b)

Figure 4.31. Temperature distribution on the heating plate and RRR. a) Temperature contour plots on the surfaces of the heating plate, RRR and the force probe. Highest temperature values are observed close to the data acquisition point of the digital thermocouple, b) 3D close-up from the RRR region with the highlighted data acquisition points. Points 1, 2 and 3 are used for reporting RRR's temperature and points 4 and 5 are used for reporting heating plate's temperature close to the mounting point of RRR.

The current through the heating plate is increased gradually till the average temperature of the RRR reaches 85°C. After this stage the Cu layer in the heating plate starts to break down due to the high concentration of electrical currents specifically close to the proximity of interconnections. In Figure 4.31 (a) heat distribution on the surfaces of the RRR and the heating plate is shown from the early stages wherein the RRR starts to exert radial forces. The IR camera is initially focused on the RRR. Data acquisition points for both the RRR and the heating plate are denoted in part (b) of this figure. Points 1 to 3 are used to report the temperature of the RRR whereas pints 4 and 5 are to report the temperature of the heating plate at the close proximity of the RRR. Highest temperature values are observed towards the two edges of the heating plate where the electrical connections are. These temperature values are captured by the digital thermocouple.

Figure 4.32 shows values of the RRR's radial force vs. its average temperature. As demonstrated, up to 40°C the radial forces exerted by the RRR are negligible after which

they start to increase slightly up to 55˚C. Then, at the interval of 55–65˚C these forces increase rapidly which are associated with the microscopic transformation of Nitinol from martensite to austenite. This increasing trend of radial forces continues with a relatively lower slope up to 75˚C where it starts to level out by reaching the end of phase transformation (A_f). These results are in good agreement with the free expansion observations of Section 4.7.2. The linear portion of this trend between 55˚C and 65˚C may potentially be utilized for a heat-induced expansion method. This is suggested due to the predictable linear radial force vs. temperature response of the RRR at this region. The high values of forces reported in this section, complemented by the free expansion results of Figure 4.28, confirm capability of the RRR to expand in response to the stimuli of heat as an alternative to the balloon expansion detailed in Chapter 2. Moreover, it proposes new potentials for different *in vivo* expansion mechanisms, one of which is explored in the following section through application of an electric potential across the RRR.

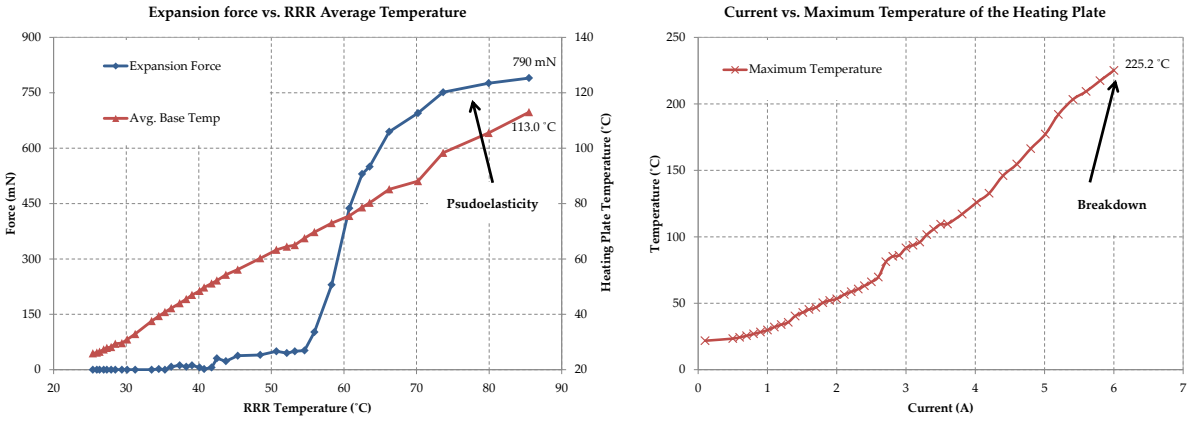

(a) (b)

Figure 4.32. Expansion forces of thermal actuation. a) Expansion forces of the crimped and constrained RRR and average temperature of the heat base close to the RRR mounting point vs. average temperature of RRR. At temperatures of the RRR around 75˚C, the expansion forces start to plateau and reach their highest at 85˚C by 790 mN, b) highest temperature of the heating plate vs. the applied electric current. At 6 A, the Cu layer in the heating plate breaks down.

4.8 Electro-Thermal Actuation

As described before, the thermal actuation methodology detailed in the previous sections is primarily targeted for *in vitro* experiments and to demonstrate the capabilities of the

RRR as an actuator. Gradual expansion of the RRR *in vivo*, on the other hand, first requires a Nitinol compound with a lower, and safer, transformation temperature and secondly it calls for more attractive means of *in vivo* actuation with smaller footprints. The current SMA based stents are primarily made of Nitinol with A_f temperatures that are lower than the human body temperature [95]. Therefore, while outside the body, in room temperature, these stents are in the martensite state wherein they are effortlessly crimped into a constraining sheath. Upon delivery to the lesion site the sheet is retracted and the warmed, thus microscopically transformed, stent retrieves its thermally trained (expanded) shape. Remained in the austenite phase for the rest of its lifecycle, the expanded stent then exerts a low chronic outward force against internal walls of the vessel to maintain patency of the lumen.

The RRR proposed in this thesis, is to operate mainly in its martensite state after deployment. Consequently, thermal actuation (expansion) is to occur at temperatures higher than that of the human body. To devise a safe actuation temperature, lower A_f may be engineered via either changes in the compositional ratio of nickel and titanium or a thermal treatment process [95, 96, 239]. Expansion by a bulky apparatus such as an angioplasty balloon or the heat transfer rod in the previous sections is not desirable in general as outlined under stenting objectives in Chapter 1. However, the conductive properties of Nitinol alloy and Joule heating may further be utilized in a heat-induced actuation method. To explore this potential and to provide recommendations for future work, in this section a theoretical and numerical framework is presented to further investigate the capabilities of the RRR.

4.8.1 Theoretical Framework

The energy dissipated by the electrical resistance of a conductor subject to an electric filed may be expressed by Joule's first law:

$$\dot{Q}_{\text{electric}} = V_{\text{electric}} I_{\text{electric}} \qquad \textbf{(4.45)}$$

where $\dot{Q}_{\text{electric}}$ is the rate of energy dissipated through resistive heating, V_{electric} is the electric potential across the resistive conductor and I_{electric} refers to the current passing through it. Given the conductive properties of the Nitinol alloy (Table 4.1), this phenomenon may be utilized for thermal actuation of the RRR by application of an electric po-

tential across the two ends of the ring (Figure 4.33). Moreover, by conservation of energy and using the constant heat transfer relation of (4.1), the thermal resistance network in Figure 4.33 is established.

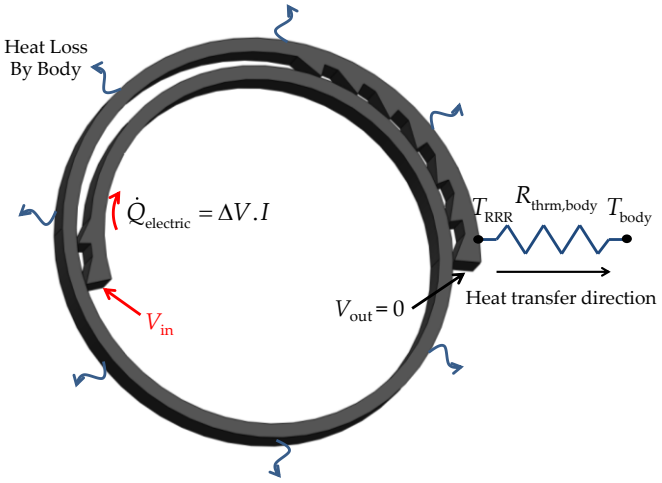

Figure 4.33. Electro-thermal actuation of the RRR. Heat inside the RRR is generated through resistive heating then transferred to the surrounding tissue (mainly blood). Equivalent thermal resistance network with effective thermal resistance. Here T_{RRR} and T_{body} refer to the constant temperature of the RRR and body (typically 37°C) after heat balance.

To increase biocompatibility and hemocompatibility of luminal implants, deposition of thin layers of coating that do not alter bulk properties of stents have been practiced shortly after the advent of alloy based stents [79, 244, 245]. Polymer coatings exhibit a strong adhesion to the stent surface while introducing minimal changes to the mechanical properties of stents. These attributes in addition to high biocompatibility to reduce thrombus formation and inflammatory responses from the body, made polymers as attractive choices for stent coating [87]. Parylene conformal coating boasts a number of properties that render it appealing for a range of biomedical device applications. These properties include providing an excellent moisture, chemical and dielectric barrier, minimal increase in weight and volume, its lubricity, strong adhesion to a wide range of substrate materials, flexibility, hydrophobicity, corrosion resistance and most importantly biocompatibility [111, 125, 246, 247]. More recently, this polymer has been adopted as a vehicle of drug delivery in development of drug-eluting (DE) stents [79, 248].

Therefore, to provide better surface conformance with the blood stream, in addition to add an electrical insulation barrier between the two conductive bodies of blood and RRR, surfaces of RRR may be coated by a thin layer of parylene-C (≈100 nm) by deposition in

vacuum [247, 249]. For the first-hand calculations of this section, blood is considered as a homogenous fluid with the material properties [250, 251] presented in Table 4.3 along with the properties of parylene-C.

Table 4.3. Material properties of blood and parylene-C.

		Blood	Parylene-C
	Unit	*Value*	
Average Viscosity	Pa.s	0.0037	--
Thermal Conductivity	W/m.K	0.5	0.082
Density	kg/m^3	1060	0.0013
Prandtl Number	--	25	--
Specific Heat	J/kg.K	3850	712
Avg. Electrical Resistivity	Ωcm	150	6×10^{16}

Heat dissipation from the RRR is first by means of conduction in the parylene-C layer, and then convective cooling effect of the blood stream. As a result, RRR's equations of balance of energy may be written using equations (4.1), (4.2), (4.3) and (4.45) resulting in:

$$\left[\dot{Q}_{\text{electric}} = \frac{\left(V_{\text{in}} - V_{\text{out}}\right)^2}{R_{\text{elec,RRR}}}\right] = \left[\dot{Q}_{thermal} = \frac{T_{\text{RRR}} - T_{\text{body}}}{\left(R_{\text{thrm,body}} \approx R_{\text{thrm,blood}}\right)}\right], \qquad \textbf{(4.46)}$$

$$R_{\text{thrm,blood}} = R_{\text{cond,parylene}} + R_{\text{conv,blood}}\ , \qquad \textbf{(4.47)}$$

$$R_{\text{cond,parylene}} = \frac{L_{\text{coating}}}{k_{\text{parylene}} A_{\text{RRR,conv}}}\ , \qquad \textbf{(4.48)}$$

$$R_{\text{conv,blood}} = \frac{1}{h_{\text{blood}} A_{\text{RRR,conv}}}\ . \qquad \textbf{(4.49)}$$

Equation (4.46), $R_{\text{thrm,blood}}$ refers to the effective thermal resistance from the RRR to the blood stream. This thermal resistance consists of the two components in series including the conductive thermal resistance of the parylene-C coating expressed by $R_{\text{cond,parylene}}$ in Equation (4.48), and the convective thermal resistance of the blood stream expressed by $R_{\text{conv,blood}}$ in Equation (4.49). Due to the very small thickness of the parylene layer ($L_{\text{coating}} = 100$ nm) relative to the dimensions of the RRR, it is reasonable to assume a constant conduction surface area through its conduction length (thickness). This results in Equation (4.48) where $A_{\text{RRR,conv}}$ refers to the total surface area of the RRR. The variable $R_{\text{elec,RRR}}$ in Equation (4.46) refers to the total electrical resistance of the open ring experienced by the electric current from the two ends of the RRR evaluated by Equation (4.50).

$$R_{\text{elec,RRR}} = \frac{\rho_{\text{elec,Nitinol}}\, L_{\text{RRR}}}{\text{A}_{\text{RRR,cs}}} \tag{4.50}$$

In this equation L_{RRR} and $\text{A}_{\text{RRR,cs}}$ refer to the total length and average cross-sectional area of the RRR in Figure 4.33 respectively and $\rho_{\text{elec,Nitinol}}$ refers to the average electrical resistance of Nitinol given in Table 4.1. In order to find the effective convective heat transfer coefficient of the blood, h_{blood}, average velocity of blood is calculated from the time-varying waveform from Chapter 3 [219] presented in Figure 3.3. The average heat transfer coefficient of the blood stream may be estimated by Churchill and Bernstein relation given in Equation (4.11) where the Reynolds number is evaluated by:

$$\text{Re} = \frac{V_{\text{avg,blood}}\, L_{\text{chr}}\, \rho_{\text{blood}}}{\mu_{\text{blood}}} \approx 6.3 \tag{4.51}$$

where μ_{blood} refers to the average viscosity of the blood given in Table 4.3, $V_{\text{avg,blood}}$ is the time-averaged flow velocity denoted in Figure 3.3. In this equation, L_{chr} refers to the characteristic length of the RRR that may be estimated by a structure of a circular cross-section. This length is estimated equating the periphery of the rectangular cross-section of the RRR to a circular cylinder expressed by:

$$\left[P_{\text{RRR}} = 2\left(W_{\text{RRR}} + t_{\text{RRR}}\right)\right] = \left[P_{\text{cylinder}} = \pi L_{\text{chr}}\right] \tag{4.52}$$

where W_{RRR} and t_{RRR} respectively refer to the width and average thickness of RRR given in Table 4.1. Evaluating the Nusselt number, the convective heat transfer coefficient of blood can be expressed by:

$$h_{\text{blood}} = \frac{k_{\text{blood}}\, \text{Nu}}{L_{\text{chr}}} \approx 12000 \text{ W/m}^2\text{K}. \tag{4.53}$$

For the theoretical and numerical studies of this section, a Nitinol material with a low transformation temperature $A_{\text{f}} = 45^{\circ}\text{C}$ and a narrow offset between A_{s} and A_{f} around 2°C may be adopted as mentioned above. Consequently, substituting h_{blood} into Equation (4.46), the required electrical potential across the RRR to raise its temperature from its initial state (body temperature≈37°C) to A_{f} is approximately 0.64 V. Given this low value of actuation voltage, and current advances in remote radio frequency (RF) actuation schemes, further studies to demonstrate actuation utilizing interrogation methods may be conducted in the future.

The analytical method in this section provided a good first hand estimate on the required amount of electromotive forces to induce thermal actuation in an RRR with a low A_f. Nevertheless, these calculations are prone to inaccuracies due to the following reasons: The empirical formulation of Nusselt number from Churchill and Bernstein is primarily defined for cross-flows over cylindrical structures. Nevertheless, due to the lack of such unique formulation for structures of rectangular cross-sections this model is employed for our estimations in this section. Moreover, the cross-sectional area of the RRR structure is not uniform along its length with differences occurring at the sites of sawtooth structures, whereas uniform assumptions are made here for both calculations of the electrical resistance and Reynolds number. In physiological conditions, blood exhibits non-Newtonian behaviour with a shear thinning effect at areas with high shear rates that is not included in the calculations of this section. Most importantly, as mentioned in the previous sections, local Nusselt number around an object that is subject to cross-flow is variable and depends on the complicated flow patterns around it. These limitations call for a more detailed analysis including these parameters into consideration. As a result, to complement the results of this section, a detailed multiphysics numerical analysis coupling electromagnetics, heat transfer and fluid transfer effects into account is presented in the following section.

4.8.2 Numerical Analysis

Numerical analysis has the advantage of providing a robust approach to highlight information of interest in a problem while taking numerous what-if scenarios into account before any costly fabrication and/or experimental results. The following section outlines the methods and results of electrical heating of a crimped stand-alone RRR inside a vessel that is subject to a blood flow profile.

I. Materials and Methods

The 3D model of a crimped RRR inside the deployment area of a mock vessel is demonstrated in Figure 4.34. The RRR is crimped down to an average external diameter of 3-mm that is subject to the luminal flow of a vessel with a reference internal diameter of 4 mm. As an initial condition, both the blood and the RRR are considered at constant temperature of 37°C.

The 3D model of RRR in Figure 4.34 is developed in SolidWorks (SolidWorks Corp., Velizy, France) then enclosed by the fluid domain. The entrance and exit lengths of the fluid domain are both extended to ensure a fully developed flow regime before it reaches the RRR, and before it exits the domain. Due to the low Reynolds numbers of the internal flow of the lumen and of the cross-flow over the rectangular cross-section of the RRR, the flow is considered laminar and incompressible. At the entrance, an inlet flow with average velocity of 0.11 m/s and constant temperature of 37°C is introduced while the opposite opening is defined at the outlet allowing for the outflow of the heat and fluid with a zero-gauge pressure. A 0.64-V electric potential is applied across the two ends of the RRR as demonstrated in Figure 4.34.

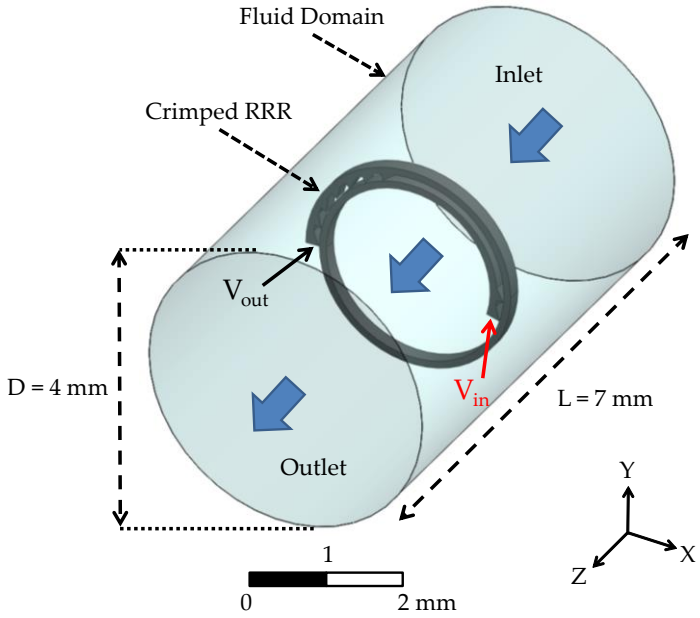

Figure 4.34. Geometry of the electro-thermal analysis, deployment area. The RRR is crimped down to 3-mm in external diameter inside a vessel of 4-mm in internal diameter. The RRR is completely enclosed by the blood passing through the lumen that is subject to an average velocity. Further extension of the fluid domain at the inlet and outlet to form a fully developed flow is not shown here.

The RRR is considered as an electrically insulated body from the blood by the 100-µm-thick layer of parylene-C coating described in the previous section. All the shared surfaces between the RRR and the fluid are introduced as fluid-solid interfaces taking both fluidic and energy interactions into account. At these surfaces the thin material interface model is enabled taking into account the thickness and material properties of the

parylene-C layer. All surfaces other than the inlet and outlet are defined as fluid walls with the no-slip boundary condition for the fluid at these regions.

Equations of the flow and thermal balance are solved by the commercial CFD package ANSYS CFX (ANSYS Inc., Canonsburg PA, USA) as described in the previous section in addition to the electromagnetism balance equation of Joule heating. The non-Newtonian characteristics of the blood is accounted for employing the Carreau model [214]. This model has proved to capture adequate information for modelling the behaviour of blood in CFD models [229] where the dynamic viscosity is expressed by:

$$\mu = \mu_{\infty} + \left(\mu_0 - \mu_{\infty}\right)\left(1 + \left[\lambda\dot{\gamma}\right]^2\right)^{(n-1)/2}. \qquad \textbf{(4.54)}$$

In this equation, μ_0 = 0.25 kg/ms and μ_{∞} = 0.0035 kg/ms refer to the viscosities at zero and infinite shear rates respectively. Furthermore, λ = 25 s and n = 0.25, are material dependent constants where the corresponding values are derived from cross-fitting of experimental data and the Carreau model [214, 229, 231].

Maximum and average temperature values in the RRR and over its surfaces are used as the primary data of interest for the mesh sensitivity study. In this study, multiple levels of element refinement are defined. Each level reduces the size of elements by a factor of 0.5 on average from the previous level then monitors the change in the aforementioned values of temperature in the RRR. The refinement level that results in less than 3% difference in these values compared from the previous level is chosen for final reports.

The mesh in the RRR is refined with a faster pace, reducing the element sizes by a factor of 0.2 at each refinement level. Discretization of this domain starts from a threshold resulting in a minimum number of three elements across the thickness of RRR to capture temperature gradient more accurately. Cross-sectional view of the final mesh consisting of around 1,600,000 elements in the deployment area is demonstrated in Figure 4.35 with the detailed view of the region close to the RRR structure. The fluid domain is primarily meshed by tetrahedral elements that exhibit superior conformance around the angled teeth of the RRR, while the RRR is mainly meshed by the more regularly structured hexahedral elements, Figure 4.35 (b) and (c). As indicated by this figure, the fluid region adjacent to the RRR surfaces is more refined to better capture the effect of velocity gradient on shear rate and the resultant heat transfer rate over these surfaces. Simulations are run

on a Dell Precision workstation with two quad-core Xeon processors and 20GB of RAM. Convergence criterion for electromagnetism, heat, mass and momentum error residuals are all set to 10^{-5} that is an order of magnitude less than that of the solver's default value.

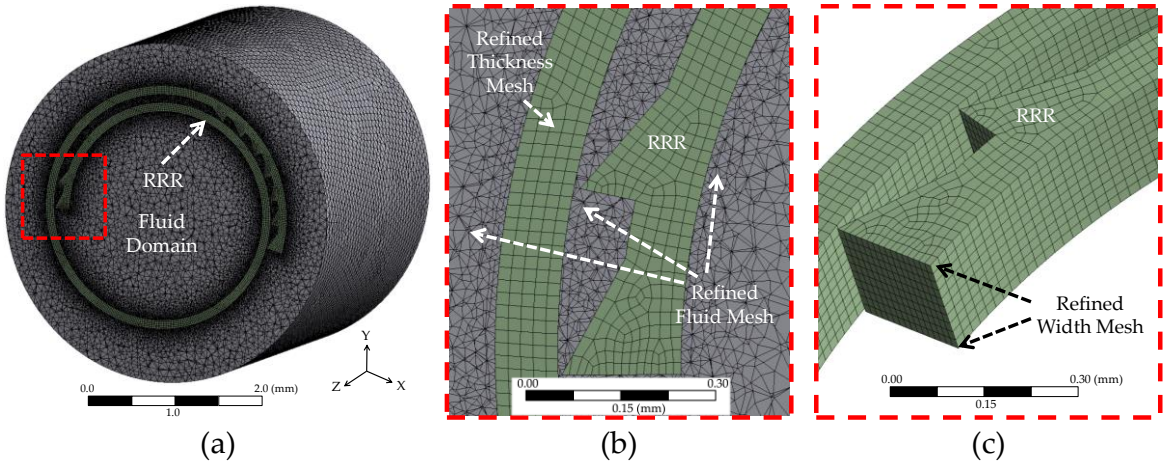

Figure 4.35. Discretization of the fluid solid domain, electro-thermal analysis. a) Overview of the deployment are of the model consisting of 1,600,000 elements, b) close-up image of area close to the slide end of the RRR with the refined mesh close to the RRR surface, c) close-up image of the slide end of the RRR highlighting the refined mesh across the width and thickness of this structure. The fluid and RRR are primarily meshed with hexahedral and tetrahedral elements respectively.

II. Results

As demonstrated by the convergence plots of Figure 4.36, the solution exhibits a stable behaviour with a constant trend of decline in the error residuals and the average RRR temperature plateauing at the very early stages of the process. The average body temperature of RRR vs. iteration number plotted in Figure 4.36 (d) indicates phase transformation in the Nitinol of choice with $A_f = 45^{\circ}C$ that results in heat-induced expansion of the RRR. Temperature distribution contour plots on the external surfaces of the RRR are shown in Figure 4.37. As demonstrated by this figure, the highest temperatures appear at the overlap length of the RRR and away from the outer surfaces of RRR that are adjacent to the internal walls of the vessel. This effect increases the safe operation of the RRR in electro-thermal actuation method.

In order to provide a better assessment of the range of temperatures achievable over different electrical potential values, results of a parametric study are presented in this section. In this analysis, the electric potentials ranging from 0.3 V to 0.9 V with step sizes

of 0.02 V are applied across the RRR while the highest, lowest and average body temperatures in the RRR are reported, Figure 4.38. The average temperature values are presented in comparison with the results from the analytical study, Figure 4.38 (b).

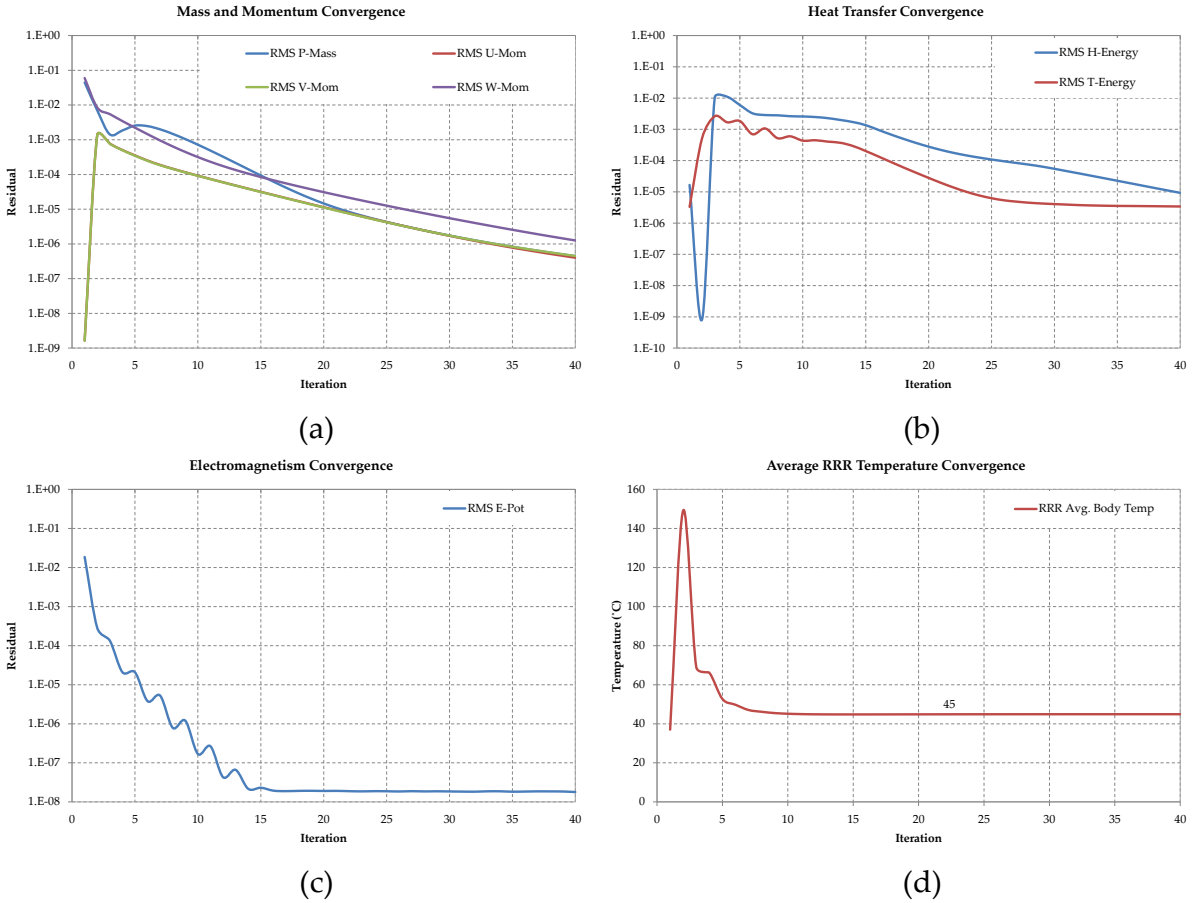

Figure 4.36. Convergence plots of electro-thermal analysis. a) Mass and momentum, b) energy and, c) electromagnetism residuals convergence to the target value of 10^{-5}, d) RRR average body temperature through simulation iterations, it levels out at early stages of the simulation demonstrating stability of the results.

Close correspondence of the average RRR body temperatures between the analytical and numerical results clearly demonstrate the efficacy of the analytical approach to capture the overall performance of the RRR. Despite the increasing trend of difference between the localized highest and lowest temperatures at higher electrical potential values, the average body temperature results indicate the spatially uniform distribution of heat in the RRR structure that ensures reaching targeted final transformation temperatures. The localized temperature differences may be associated with the different local values of Nusselt number as a result of different flow patterns around the RRR's body. The slightly lower average temperatures of RRR from the numerical results in comparison with the

analytical results, at most (0.3% at for 0.9 V electrical potential) is most likely due to the shear thinning effect of blood (reduction in viscosity) close to the RRR walls, that increases the Reynolds number thereby the convective heat transfer coefficient.

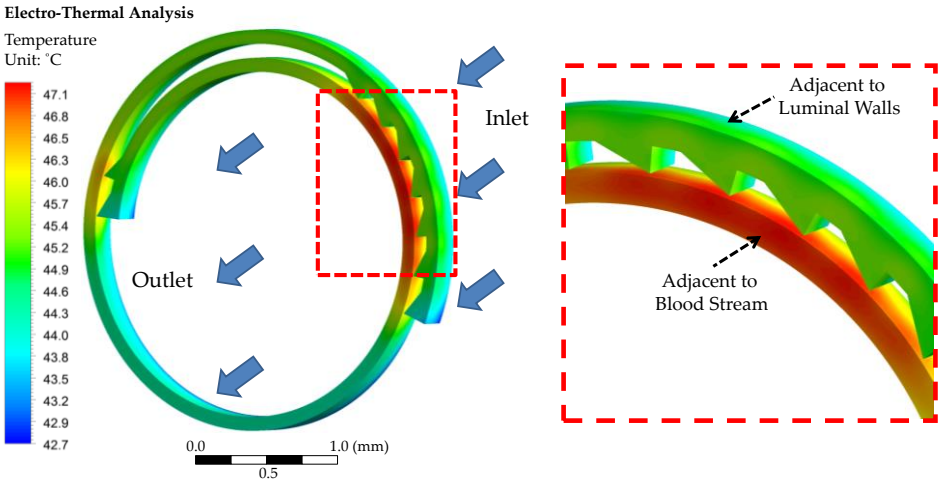

Figure 4.37. Temperature distribution in RRR, electro-thermal analysis. Temperature contour plots on the external surfaces of the RRR, max temperatures appear at the overlap length close to the outlet. Temperature of the surfaces of RRR adjacent to the luminal walls maintains levels within the average temperature values (45°C), thereby not exceeding the nominal values.

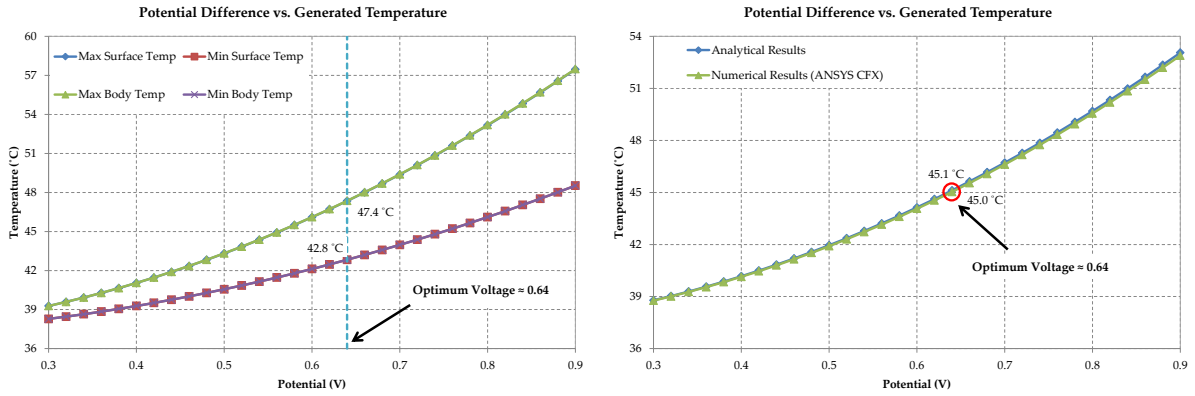

(a) (b)

Figure 4.38. Parametric study of electro-thermal analysis. a) Max and min values on the external surfaces and in the body of the RRR in different potential levels, b) average body temperature of the RRR for different values of electric potential in comparison with the analytical approach. The analytical method is very well capable of predicting RRR body temperature in different potential levels.

This effect is demonstrated in Figure 4.39 where contour plots of shear strain rate and dynamic viscosity at a radial cross-section of the axial centre of the model in Figure 4.34 are presented.

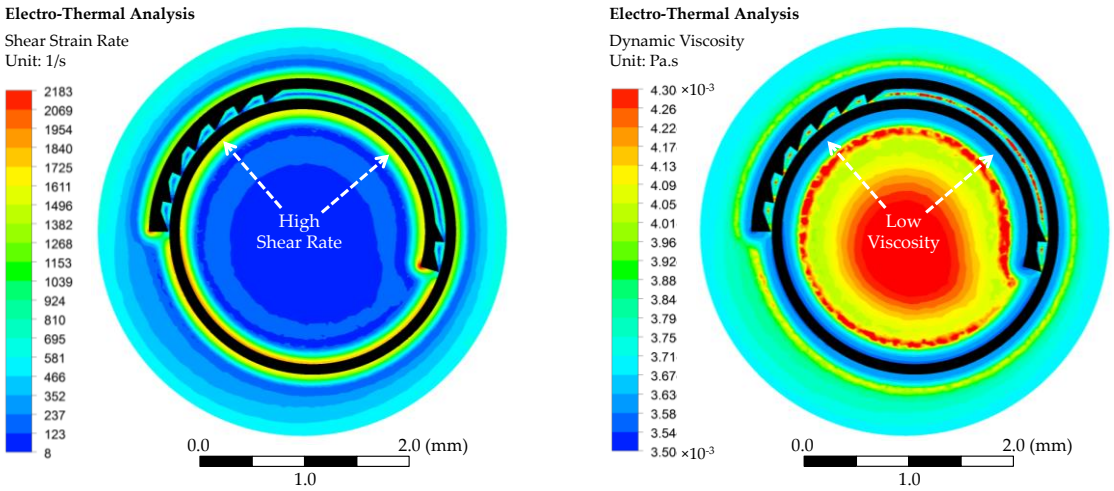

Figure 4.39. Shear thinning effect of blood, electro-thermal analysis a) Max and min values on the surface and in the body of the RRR in different potential levels, b) average body temperature of the RRR for different values of electric potential for both the numerical and analytical approach. The analytical method is very well capable of capturing the overall status of the RRR in different potential levels.

The analytical and numerical studies in this section demonstrated another potential actuation mechanism of the RRR utilizing resistive heating of Nitinol by application of an electrical potential across the length of RRR. These results provide a foundation for future experimental studies including *in vitro* trials. These studies may further extend into characterizing different energy harvesting and delivery methods to the RRR, including but not limited to piezoelectric and wireless energy delivery and interrogation techniques. One, such approach may utilize the Eddy currents generated in a conducting loop (such as the RRR given a conduction path between the interlocked teeth is provided) that are generated by an oscillating magnetic field (RF signal). In such scenario, the efficiency of the fields may be enhanced considering the natural frequency of the RRR. Secure on-demand actuation is a necessity in all these approaches deserving extensive future studies.

Furthermore, the current study is limited in assuming an average velocity value over time that may be improved by a transient analysis adopting the actual waveform of Figure 3.3 for a better understanding of maximum achievable temperatures and their safety *in vivo*. The studies in this section considered the case where the RRR is in its initial stages of expansion where the assumption of no contact with vascular walls is reasonable. Nevertheless, upon expansion of the structure and proximity of the outer

surfaces of the RRR to the luminal walls, both the flow pattern as well as heat conduction parameters may undergo dramatic changes. Where the RRR is in contact with the vascular walls, its outer surfaces will no longer be exposed to the blood stream and heat transfer from these surfaces becomes primarily through conduction into the adjacent vascular tissue. Inclusion of these effects in addition to consideration of different luminal and RRR dimensional assumptions may be performed in several separate studies.

4.9 Chapter Summary

Following the numerical and experimental studies of Chapter 2 on mechanics of the expansion of RRR using an angioplasty balloon, alternative expansion mechanisms were explored in this chapter. Utilizing the shape memory effect of Nitinol that is used in the fabrication of RRR, the RRR's thermally trained shape in the fully expanded state, its incremental interlocked expansion mechanism and choosing the transformation temperature of Nitinol higher than the deployment region's temperature (body temperature), it is possible to accommodate controlled, incremental expansions through application of heat. In this chapter, these possibilities were explored and demonstrated through rigorous theoretical, numerical and experimental studies. To ensure exposure of the mock vessels used in the *in vitro* studies to a controlled and safe range of temperature, first analytical models using the theory of thermal resistance and crossflow over circular patterns were developed. By extension of these models to the more complex analytical models of finned surfaces, boundary conditions to supply adequate transformation, thus actuation, temperature ($> 80^{\circ}C$) to the RRR were calculated, while maintaining temperature of the deployment mock vessel within the recommended range ($< 50^{\circ}C$). In order to evaluate the analytical results, further numerical studies were conducted in multiple steps where each succeeding step validated results of the predecessor while increasing complexity of the models and decreasing the number of known assumptions. Starting from a single field static thermal analysis, these studies were then extended to multi-field analyses including conjugate fluid and heat transfer models.

Close correspondence of the numerical and analytical results, demonstrates the merit of our theoretical analysis in predicting proper initial conditions and their resultant effects. Nevertheless, localised changes to the fluid regime and the resultant temperature distri-

bution, necessitated use of the detailed numerical analysis presented in this chapter to provide more insight into the mechanics of distribution of temperature in the RRR and its surrounding components.

Expansion of the RRR in response to the thermal stimuli is then evaluated by *in vitro* and free expansion experimental results. The incremental expansion of the RRR by application of heat was observed and measured in a free expansion study complimented by the expansion observations from the *in vitro* study. Moreover, radial forces exerted by a constrained RRR under gradually increasing temperature stimuli are measured in an experimental study demonstrating the capability of RRR to exert high radial forces while actuating by heat. The resultant radial force vs. temperature trend demonstrated a region of linear relation between these two parameters, promising a controlled alternative expansion mechanism. That is suggested due to the simplicity and predictability of the force vs. temperature response curve in this linear region.

Finally, using the analytical and numerical foundation from the first sections, a second alternative actuation mechanism utilizing electrical potential is proposed and examined through theoretical and numerical studies. In very good agreement with the analytical results, our numerical results indicated efficacy of a 0.64-V electrical potential, in order to induce adequate temperature increase in the body of an RRR with a transformation temperature $A_f = 45\,^{\circ}\mathrm{C}$ to actuate the RRR while it is subject to *in vivo* thermo and hemodynamic conditions.

In the next chapter, a summary of all tasks, contributions and conclusions is presented. Moreover, recommendations for future continuation of this work are given.

This page is left blank intentionally

Chapter 5

Conclusion and Future Directions

The multidisciplinary journey of the present research project is summarised in this chapter. It draws a summary of the conducted tasks, contributions and conclusions from the work carried out in this research. Furthermore, recommendations for future directions and extension of the proposed luminal structure are given. In the end some concluding remarks are outlined.

5.1 Introduction

Management and treatment of cardiovascular disease (CVD), particularly atherosclerosis as its primary cause, consists of a number of surgical and non-surgical approaches among which balloon angioplasty and stenting are the most common. Short and long-term beneficial results of stents to regain normal blood flow in occluded vessels rendered them as the frontiers of intravascular devices these days. Meeting general biological requirements such as biocompatibility and the more specific and often self-competing stenting imperatives such as high radial strength, low elastic recoil, conformity, trackability and radiopacity led to the current overwhelming number of different stent designs and materials in the market. Despite the promising acute luminal gain after deployment of stents, complications such as in-stent thrombosis (formation of blood clot) and neointimal hyperplasia leading to restenosis (renarrowing) of the treated lesions limit their long-term benefits.

The two most prevalent stenting complications, including restenosis and thrombosis, stem from a number of pre, during and post-interventional conditions. Among these, intravascular trauma during and after stent deployment in addition to the hemodynamic changes after stent deployment play unequivocal roles in occurrence and further development of restenosis and thrombosis. Stent over-expansion techniques compensating for the inherent elastic recoil of stents during deployment or use of self-expanding (SE) stents, that are in fact ever-expanding stents, are attributed with negative effects on increasing intravascular trauma, more specifically in complex and hardened lesions. Current pharmacological approaches to inhibit body's proliferative response, thus restenosis, through systemic or local administration of drugs still overlook the design and mechanical shortcomings of the stenting procedure. Moreover, the often contradictory imperatives of stenting such as easy conformity, easy expansion and on the other hand, high radial strength and low elastic recoil call for a new stent design.

As a result, to address the issue of recoil and extend capability of current stents to controlled and incremental expansion steps with alternative expansion mechanisms to the state-of-the-art balloon expansion, in the current work a novel recoil resilient stent is proposed and developed. Design, development and evaluation of the proposed structure

are extensively elaborated in a multidisciplinary project incorporating tasks, contributions and conclusions as outlined in the following section.

5.2 Contributions and Conclusions

In Chapter 1 after an introduction on atherosclerosis as the primary cause of CVD, its occurrence, development and risk factors were presented in Section 1.2. Then, current treatment options to control and manage luminal occlusions including non-surgical and surgical approaches were discussed and compared in more detail in Sections 1.3 and 1.4. Among the surgical interventional methods and due to its current success, and significance to the current work, a comprehensive review of current stenting technology including its required characteristics and current stent design pros and cons was then given in Section 1.5. In this section, the currently overcrowded market of stents was classified based on: a) materials and expansion mechanism, b) primary material form such as wires, sheets or tubes, c) fabrication methods that are highly reliant on the primary material form, such as weaving, braiding and cutting methods such as laser, water jet and μEDM, d) design and geometrical features as one of the most important features affecting overall performance of stents, and e) some other incremental attributes such as coatings, surface preparation and radiopacity.

In this section, stent design objectives such as high radial strength and low elastic recoil in addition to the opposing imperatives such as high axial flexibility, low pressure expandability and conformity in tortuous paths were iterated, after which the challenge in optimal stent design was recognized. As concluded by this review, despite the numerous attempts and proven stent improvements over the years, thrombosis and restenosis yet remain the most important post interventional complications that are often preceded by an intravascular trauma. Endangering the long-term luminal patency after stenting, exaggerated healing response of the smooth muscle cells to this trauma leads to partial or even total re-occlusion of a treated lesion (restenosis). Induced trauma as a result of high balloon pressure and over-expansion of stents during or after deployment is in fact a natural consequence of current stents limitation to satisfy their self-competing objectives. A plastically deformable material that is also required to exhibit high elastic strength, inevitably exhibits a linear portion of stress-strain response that is natural to the majority

of alloys used in current stents such as stainless steel. Consequently, to compensate for the radial loss due to this linear elastic recoil of the material, high-pressure over-expansion techniques are often adopted by clinicians, which lead to increased trauma of the vessel during deployment. On the other hand, the chronic outward radial force (albeit low) exerted by the ever-expanding SE stents was shown to potentially aggravate vascular trauma. It was then concluded that the current systemic, and localized drug administration, despite their partial success in controlling an emphasised inflammatory response from the body, still overlook the mechanical aspect of the recoil-trauma-restenosis trifecta. As a result, a new stent design paradigm targeting the problem of recoil was necessitated at the end of Chapter 1.

In Chapter 2 after highlighting the two most important complications of stenting, restenosis and recoil and identifying the current stent design gaps, design and development of a novel recoil resilient luminal support for stenting applications was discussed. Development of the proposed structure called recoil resilient ring (RRR) was carried out through multistep numerical analysis, fabrication and mechanical evaluations. The proposed structure aims to minimize the need for high-pressure over-expansion that can induce intra-luminal trauma and excess growth of vascular tissue causing later restenosis. The RRR is an open ring with overlapping ends and asymmetrical sawtooth structures from the two ends that are intermeshed. While radially expanded, these teeth can slide on top of each other, but interlock step-by-step so to keep the final expanded state against compressional forces that normally cause recoil.

Compatibility of the proposed RRR with current balloon expansion mechanics was first investigated via finite element modelling (FEM) of a 3D model in an explicit dynamic simulation framework in Section 2.3. Use of such framework was warranted by the complex geometry of 3D model in addition to the transient nature of the interlocking mechanism that introduced large deformations and abrupt contact changes during expansion. The limited free expansion results from this analysis showed efficacy of pressure levels up to 100 KPa to induce, open ring expansion, tooth traversal and interlock without compromising the structural integrity of the RRR. Such pressured levels, are significantly lower than current *in vivo* pressure levels (up to 1 MPa). Radial strength of the RRR in comparison with a typical balloon-expandable (BE) stent was then studies in a static

structural analysis utilizing FEM. Results from this study indicated superior radial strength of the RRR both in withstanding deformations against compressive forces and in recovery of its initial diameter after removal of these forces compared to the BE stent. Axial strength of the RRR and proposals for improvements were elaborated using FEM at the end of this section.

Following the successful initial numerical analysis results, fabrication of the RRR by linear pattering of Nitinol sheets of 200-μm thickness utilizing μEDM technology was outlined in Section 2.4. The simple planar design and subsequent shaping and training methods used, facilitates batch processing and mass production of the structures. The fabricated RRR was then subjected to experimental *in vitro* expansion and stiffness tests. The free radial stiffness test measurements indicate 2.7× higher radial rigidity of the RRR compared to that of a two-column stainless steel commercial BE stent. Considering the lower modulus of elasticity of Nitinol in its martensitic form compared to stainless steel, and the comparable thickness and width of RRR and the commercial stent, the higher radial strength of RRR is delivered by the proposed interlocking mechanism. The *in vitro* radial stiffness tests also show comparable elastic recovery of the RRR and the commercial stent. The proposed RRR is balloon expandable *in vitro* by 5–7 atm pressure, well in range of recommended *in vivo* pressures. The change in mean cross-sectional area after balloon deflation were shown to be < 3% for the RRR compared to the reported mean value of 13–30% associated with commercial stents. Considering these specifications and the merit of RRR, a series of this structure can potentially be welded by a single point inside a stent mesh, providing further scaffolding to specific areas and to the stent as a whole while not sacrificing expandability or longitudinal flexibility of the stent mesh. Considering these benefits compared to the added local thickness inside a stent due to the RRR's profile (this effect is investigated in Chapter 3), the proposed structures brings an excellent trade-off between flexibility, deliverability, and resilience.

After deployment of stents, apart from their mechanical effect to their surrounding tissue, they introduce changes to the fluid regime. As outlined in Section 1.5, these changes can potentially result in detrimental biological effects such as re-accumulation of fatty deposits leading to restenosis. In particular, numerous clinical and numerical results show a strong relation between increased risk of restenosis and increased extension of

endothelial area that is subject to low wall shear stress (LWSS), less than 0.5 Pa, after deployment of stents. In Chapter 3, investigation of such effects is carried out through extensive 3D computational fluid dynamic (CFD) studies. In these comparative studies three different luminal supports including a nominal balloon-expandable (BE) stent, a standalone RRR, and an RRR-integrated BE stent are subject to physiological pulsatile flows in 3D CFD frameworks.

Hemodynamic indicators such as temporal and spatial distribution of LWSS in the deployment area and the entire fluid domain, fluid drag force experienced by the scaffolds and blood supply changes to the main and side branches, in branched fluid domains, were extensively investigated. Results of the transient studies in unbranched domains in Section 3.4 (Part 1) indicate hemodynamic superiority of the standalone RRR exhibiting the least ratio of area subject to LWSS. Despite the slight differences between the LWSS ratios of the standalone stent and the RRR-integrated stent during the first half of the cardiac cycle, these differences settled to almost zero for the next half resulting in close temporal average values of the LWSS in the deployment areas and identical values for the entire fluid domains of these two scaffolds. High ratio of the withholding forces of all the three scaffolds to the fluid drag forces demonstrated efficacy of the former to keep the supports in place even for the highest values of the latter in a cardiac cycle.

In results of Part 2 of Section 3.4, the standalone RRR remained as the best of the three scaffolds in a branched fluid domain resulting in the least deviation of outlet flow rates from a healthy vessel. Moreover, the standalone RRR was associated with the lowest ratio of luminal areas subject to LWSS compared to the other two supports. The temporal trends of LWSS ratio for the standalone stent and the RRR-integrated stent were closely intertwined through the entire cardiac cycle resulting in a difference as low as 1% on average in the deployment area and identical LWSS ratio values for the entire fluid domains. Deviation of output flow rates in the side and main branches of the standalone stent and RRR-integrated stent domains from corresponding branches of a healthy domain, followed similar trends. These results demonstrated the efficacy of the RRR-integrated stent to deliver a hemodynamic response at least as good as the current state-of-the-art stents considering the superior resilience benefits of the former over the later.

Sensitivity of the results to the dimensional assumptions of the RRR-integrated stent and the branched fluid domains was then studied for different reference luminal diameters and different overlap lengths from the two ends of the RRR. These results were in good agreement with the results of the branched fluid domains demonstrating a close correspondence between hemodynamic indicators of the RRR-integrated and the standalone stents. Moreover, RRR-integrated stents deployed in smaller arteries and with longer overlap lengths demonstrated less area subject to LWSS compared to similar cases of standalone stent deployment. Differences in the side and main branch flow supplies were insignificant for the high inlet flow velocities while relatively increasing for lower inlet velocity magnitudes. Temporal average values of the aforementioned hemodynamic performance indicators show very little dependence of our results on the dimensional assumptions of the fluid domain showing the merit of both the standalone RRR and the RRR-integrated stent as viable biomedical implants for luminal constrictions.

The proposed RRR in the current work is made of Nitinol with a transformation temperature (A_f) well higher (70–80°C) than human body temperature (37°C). This ensures martensite mode of operation of the RRR after and during deployment with an angioplasty balloon. In martensite phase, Nitinol exhibits considerably lower stiffness compared to other materials used for stent fabrication including primarily stainless steel and austenite Nitinol. This characteristic carries benefits such as flexibility, conformity and capability to undergo large plastic deformations that are considered as desirable attributes during deployment as outlined in Chapter 1. High radial strength of the RRR, on the other hand, is provided by its interlock mechanism rendering RRR capable of meeting the opposing stenting objectives simultaneously as demonstrated in Chapter 2. Moreover, thermal treatment of the RRR in the fully expanded state, as discussed in Chapter 2, its incremental interlock mechanism and the shape memory properties of Nitinol while undergoing phase transformation from martensite to austenite, propose new potentials for alternative controlled and incremental actuation and expansion mechanisms to the usual balloon expansion.

In Chapter 4, these alternative expansion potentials, by application of direct or electrically-induced heat were explored and demonstrated through rigorous theoretical, numerical and experimental studies. As a precursor to the *in vitro* experimental results, and to

ensure exposure of the mock vessel, which is used for deployment of RRR in the *in vitro* studies, to a controlled and safe range of temperature, first analytical models using the theory of thermal resistance and crossflow over cylindrical patterns were developed. By extension of these models to the more complex analytical models of finned surfaces, boundary conditions to supply adequate transformation, thus actuation, temperature (> 80°C) to the RRR were calculated, while maintaining temperature of the encompassing mock vessel within the recommended range (< 50°C). Validation of the analytical results was conducted by extensive numerical analyses. Starting from a single field static thermal analysis, these studies were then extended to multi-field analyses conjugating fluid and heat transfer models. Close correspondence of the theoretical and numerical results demonstrated the merit of our theoretical analysis to predict adequate initial conditions for thermal actuation of the RRR and their resultant effects on the domain of the model, most importantly the mock vessel.

In Section 4.7 actuation of the RRR under heat stimuli was experimentally evaluated by *in vitro* expansion, free expansion and constrained actuation studies. First, ability of the RRR to expand against compressive forces of a mock vessel was demonstrated in the *in vitro* expansion study. Next, the incremental expansion of the RRR by direct application of heat was observed and measured in the free expansion experimental study. In the constrained actuation study, capability of a crimped RRR to exert high radial forces while actuated by heat was demonstrated. The linear trend in the resultant radial force vs. temperature response graph suggested an alternative expansion mechanism by application of heat. That is suggested due to the simplicity and predictability of the temperate vs. radial force response curve in this linear region.

In the end and to demonstrate the potentials for extension of current project, using the results and analytical foundation from the previous section, a second alternative actuation mechanism utilizing electrical currents is proposed and examined through multi-field theoretical and numerical studies. In very good agreement with the analytical results, our numerical results indicated adequacy of a 0.64 V electrical potential, in order to induce thermal actuation of an RRR with a transformation temperature $A_f = 45\,^{\circ}\mathrm{C}$ that is subject to physiological thermo and hemodynamic conditions.

Results and observations from the current work led to the identification of other important areas for further improvement of a recoil resilient stent with alternative actuation capabilities.

5.3 Recommendations for Future Work

Attractive material properties of martensite Nitinol such as conformity and biocompatibility and its potential for use as an active material for actuation were the primary drivers for use of this alloy in fabrication of the RRR as outlined in Chapter 2. Nevertheless, other active materials such as piezoelectric polymers may also be considered for fabrication of the RRR. Selection and application of such new materials calls for several studies that may be carried out within the proposed framework in this work.

In Chapter 3 a realistic physiological waveform was adopted for inlet velocities to effectively capture hemodynamic changes over time. Nevertheless, due to the transient nature of blood pressure and velocity depending on factors such as the location (vessel) of measurements, conditions such as at resting or exercising, and pre-existing conditions such as high or low blood pressure, other velocity profiles may be considered. Results from such studies can provide further insight into the effect of these conditions in the success rate of a luminal support after deployment in different groups of patients.

The analytical and numerical framework in Chapter 4 demonstrated actuation capabilities of the proposed RRR in response to non-mechanical stimuli such as heat and electricity. Results from these studies provide a foundation for further future experimental *ex vitro* and *in vitro* studies. One such study may span into exploration and characterization of efficient energy harvesting and delivery methods to the RRR. Examples of such methods include but not limited to piezoelectric and wireless energy delivery and interrogation techniques. In a collaborative attempt with author of the present thesis, a magnetoelectric approach utilizing direct piezoelectric effect is currently under investigation [252]. A potentially viable wireless approach may utilize Eddy currents generated in a conducting loop, such as the RRR, in response to an oscillating magnetic field. Efficacy of thermal excitation in response to a higher electromotive force may be studied considering the natural frequencies of the RRR.

Another possibility is utilization of surface acoustic wave (SAW) technology, to harvest energy from mechanical oscillation of thin piezoelectric layers in response to a radio frequency (RF) signal. This approach has been successfully implemented for actuation of micropumps [253], and its further application to the current work may reap beneficial results.

Irrespective of the actuation mechanism, secure and on-demand actuation is of outmost importance calling for further extensive studies. In this respect, control and study of the unwanted environment causes such as exposure to the strong magnetic field of a magnetic resonance imaging (MRI) scanner is warranted. In the end, like any other biomedical implant, the next major steps towards practical use of the proposed structure include detailed and long-term animal, and subsequently, human clinical studies.

5.4 Closing Comments

In this thesis a new luminal support for stenting applications is proposed. The new device called the recoil resilient ring (RRR) is targeted to address the important issue of recoil and its detrimental consequences to the efficacy of luminal supports. In this thesis, superior mechanical and hemodynamic performance of the fabricated RRR and its compatibility with the state-of-the-art stenting standards are demonstrated through extensive numerical and experimental studies. Moreover, utilizing the shape memory effect of active materials used in the RRR, alternative actuation methods to the current balloon expansion is explored and demonstrated. Carrying out this forefront innovative research, the present thesis facilitated the addition of new contributions to a spectrum of fields incorporating design, analysis and development of biomedical devices.

Bibliography

[1] A. S. Go, D. Mozaffarian, V. L. Roger, E. J. Benjamin, J. D. Berry, W. B. Borden, *et al.*, "Heart disease and stroke statistics—2013 update: A report from the American Heart Association," *Circulation,* vol. 127, pp. e6-e245, 2013.

[2] World Health Organization, *Global Atlas on Cardiovascular Disease Prevention and Control*. Geneva 2011.

[3] R. E. Klabunde, "Cellular structure and function," in *Cardiovascular Physiology Concepts*: Wolters Kluwer Health, 2011, pp. 49-55.

[4] J. A. Berliner, M. Navab, A. M. Fogelman, J. S. Frank, L. L. Demer, P. A. Edwards, *et al.*, "Atherosclerosis: Basic mechanisms oxidation, inflammation, and genetics," *Circulation,* vol. 91, pp. 2488-2496, 1995.

[5] J. Plutzky and P. Libby, "Pathophysiology of atherosclerotic heart disease," in *Atherosclerosis and Heart Disease*, A. M. Tonkin, Ed. UK: Taylor & Francis, 2003, pp. 1-13.

[6] G. K. Hansson, "Inflammation, atherosclerosis, and coronary artery disease," *New England Journal of Medicine,* vol. 352, pp. 1685-1695, 2005.

[7] V. Karagkiozaki, "Nanomedicine highlights in atherosclerosis," *Journal of Nanoparticle Research,* vol. 15, pp. 1-17, 2013.

[8] S. E. Anderson, R. Lahm, and P. A. Laizzo, "The coronary vascular system and associated medical devices," in *Handbook of Cardiac Anatomy, Physiology, and Devices*, P. A. Iaizzo, Ed. New York, USA: Springer, 2010, pp. 109-121.

[9] M. Lüdinghausen, "The lengths and diameters of major coronary arteries," in *The Clinical Anatomy of Coronary Arteries*, Berlin Heidelberg: Springer 2002, p. 32.

[10] Wikipedia. (Sep 2013, Nov 2013). *The Structure of an Artery Wall*. Available: http://en.wikipedia.org/wiki/Tunica_intima

[11] R. J. Esper, R. A. Nordaby, J. O. Vilariño, A. Paragano, J. L. Cacharrón, and R. A. Machado, "Endothelial dysfunction: A comprehensive appraisal," *Cardiovasc Diabetol,* vol. 5, pp. 4-22, 2006.

[12] M. De Beule, "Design van stents met eindige elementen, Finite element stent design," Ph.D. dissertation, Ingenieurswetenschappen: Biomedische Ingenieurstechnieken, Universitet Gent, 2008.

[13] G. M. Chisolm and D. Steinberg, "The oxidative modification hypothesis of atherogenesis: An overview," *Free Radical Biology and Medicine,* vol. 28, pp. 1815-1826, 2000.

[14] A. Tedgui and Z. Mallat, "Cytokines in atherosclerosis: Pathogenic and regulatory pathways," *Physiological Reviews,* vol. 86, pp. 515-581, 2006.

[15] S. Glagov, E. Weisenberg, C. K. Zarins, R. Stankunavicius, and G. J. Kolettis, "Compensatory enlargement of human atherosclerotic coronary arteries," *New England Journal of Medicine,* vol. 316, pp. 1371-1375, 1987.

[16] K. S. Woo and D. Magliano, "Novel atherosclerosis risk factors and management," in *Atherosclerosis and Heart Disease*, A. Tonkin, Ed. UK: Taylor & Francis, 2003, pp. 41-58.

[17] S. E. Humphries and L. Morgan, "Genetic risk factors for stroke and carotid atherosclerosis: Insights into pathophysiology from candidate gene approaches," *The Lancet Neurology,* vol. 3, pp. 227-235, 2004.

[18] J. Frohlich, M. Dobiasova, S. Lear, and K. W. J. Lee, "The role of risk factors in the development of atherosclerosis," *Critical Reviews in Clinical Laboratory Sciences,* vol. 38, pp. 401-440, 2001.

[19] R. Lewis and D. Huang. (2009, Nov 2013). *US Against Athero-Fighting Atherosclerosis with Knowledge*. Available: http://multivu.prnewswire.com/mnr/uaa/37598/

[20] M. A. Pfeffer, "Angiotensin-axis inhibition," in *Textbook of Interventional Cardiology*, E. J. Topol, Ed. USA: Saunders/Elsevier, 2008, pp. 203-221.

[21] V. Rajagopal, "Other adjunctive drugs for coronary intervention: B-blockers and calcium channel blockers," in *Textbook of Interventional Cardiology*, E. J. Topol, Ed. USA: Saunders/Elsevier, 2008, pp. 241-251.

[22] D. P. Chew, "Anticoagulation in percutaneous coronary intervention," in *Textbook of Interventional Cardiology*, E. J. Topol, Ed. USA: Saunders/Elsevier, 2008, pp. 165-181.

[23] K. K. Ray and C. P. Cannon, "Lipid lowering in coronary artery disease," in *Textbook of Interventional Cardiology*, E. J. Topol, Ed. USA: Saunders/Elsevier, 2008, pp. 183-201.

[24] A. Hirohata, K. Yamamoto, T. Miyoshi, K. Hatanaka, S. Hirohata, H. Yamawaki, *et al.*, "Four-year clinical outcomes of the olivus-ex (impact of olmesartan on progression of coronary atherosclerosis: Evaluation by intravascular ultrasound) extension trial," *Atherosclerosis,* vol. 220, pp. 134-138, 2012.

[25] S. Peters, "Inhibition of atherosclerosis by angiotensin II type 1 receptor antagonists," *American Journal of Cardiovascular Drugs,* pp. 1-4, 2013.

[26] American Heart Association, Answers by Heart, *What Are Anticoagulants and Antiplatelet Agents*: Americal Heart Association, 2012.

[27] WebMD. (2010, June 2013). *Coronary Artery Bypass Surgery for Coronary Artery Disease*. Available: http://www.webmd.com/heart-disease/coronary-artery-bypass-surgery-for-coronary-artery-disease

[28] C. J. Mullany, "Coronary artery bypass surgery," *Circulation,* vol. 107, pp. e21-e22, 2003.

[29] M. Pocar, A. Moneta, D. Passolunghi, A. Di Mauro, A. Bregasi, R. Mattioli, *et al.*, "Coronary artery bypass grafting for chronic and acute heart failure," in *Coronary Artery Bypasses*, R. T. Hammond and J. B. Alton, Eds. New York: Nova Science Publishers, 2009, pp. 111-122.

[30] M. Itshida, J. Kobayashi, O. Tagusari, K. Bando, K. Niwaya, H. Nakajima, *et al.*, "Comparison of off-pump and on-pump coronary artery bypass grafting in midterm results," *The Japanese Journal of Thoracic and Cardiovascular Surgery,* vol. 52, pp. 240-246, 2004.

[31] S. Bhimji. (2012, 2013). Heart bypass surgery. *Medical Encyclopedia*. Available: http://www.nlm.nih.gov/medlineplus/ency/article/002946.htm

[32] J. E. Thompson, "The evolution of surgery for the treatment and prevention of stroke: The Willis Lecture," *Stroke,* vol. 27, pp. 1427-1434, 1996.

[33] D. McCrory, L. Goldstein, G. Samsa, E. Oddone, P. Landsman, W. Moore, *et al.*, "Predicting complications of carotid endarterectomy," *Stroke,* vol. 24, pp. 1285-1291, 1993.

[34] A. Indermuehle, R. Bahl, A. J. Lansky, G. M. Froehlich, G. Knapp, A. Timmis, *et al.*, "Drug-eluting balloon angioplasty for in-stent restenosis: A systematic review and meta-analysis of randomised controlled trials," *Heart,* vol. 99, pp. 327-333, 2013.

[35] S. G. Ellis, "Drug-eluting and bare metal stents," in *Textbook of Interventional Cardiology*, E. J. Topol, Ed. USA: Saunders/Elsevier, 2008, pp. 255-271.

[36] University of Rochester Medical Center. (Nov 2013). *Carotid Endarterectomy*. Available: http://www.urmc.rochester.edu/encyclopedia/content.aspx?contenttypeid=92&contentid=p08293

[37] A. R. Grüntzig, Å. Senning, and W. E. Siegenthaler, "Nonoperative dilatation of coronary-artery stenosis: percutaneous transluminal coronary angioplasty," *New England Journal of Medicine,* vol. 301, pp. 61-68, 1979.

[38] D. S. Bain, "Percutaneous balloon angioplasty and general coronary intervention," in *Grossman's Cardiac Catheterization, Angiography, and Intervention*, D. S. Baim, Ed. USA: Lippincott Williams & Wilkins, 2006, pp. 433-466.

[39] H. Token. (Nov 2013). *Balloon Angioplasty*. Available: http://healthtoken.com/balloon-angioplasty

[40] B. N. Potkin, G. Keren, G. S. Mintz, P. C. Douek, A. D. Pichard, L. F. Satler, *et al.*, "Arterial responses to balloon coronary angioplasty: An intravascular ultrasound study," *Journal of the American College of Cardiology,* vol. 20, pp. 942-951, 1992.

[41] G. W. Stone, "Coronary stenting," in *Grossman's Cardiac Catheterization, Angiography and Intervention*, D. S. Baim, Ed. USA: Lippincott Williams & Wilkins, 2006, pp. 492-542.

[42] J. R. Algeria and J. David R. Holmes, "Balloon angioplasty: Is it still a viable intervention?," in *Textbook of Interventional Cardiology*, E. J. Topol, Ed. USA: Saunders/Elsevier, 2008, p. 275.

[43] D. G. Almond, "Coronary stenting I: Intracoronary stents - form, function and future," in *Practical Interventional Cardiology*, E. D. Grech and D. R. Ramsdale, Eds. London, UK: Martin Dunitz, 2002, pp. 63-76.

[44] J. P. Curtis and J. F. Setaro, "Stenting in coronary angioplasty," in *Classic Papers in Coronary Angioplasty*, C. Handler and M. Cleman, Eds. London, UK: Springer, 2006, pp. 115-116.

[45] D. L. Fischman, M. B. Leon, D. S. Baim, R. A. Schatz, M. P. Savage, I. Penn, *et al.*, "A randomized comparison of coronary-stent placement and balloon angioplasty in the treatment of coronary artery disease," *New England Journal of Medicine,* vol. 331, pp. 496-501, 1994.

[46] A.-M. Belli, "Angioplasty and stenting of the superficial femoral artery and popliteal artery," in *Handbook of Angioplasty and Stenting Procedures*, R. A. Morgan and E. Walser, Eds. London, UK: Springer, 2010, pp. 97-111.

[47] N. A. Hamilton and B. D. Matthews, "Minimal access management of pancreatic cancer," in *Minimally Invasive Cancer Management*, F. L. Greene and B. T. Heniford, Eds. New York: Springer, 2010, pp. 129-144.

[48] A. C. Mehta and A. Dasgupta, "Airway stents," *Clinics in Chest Medicine,* vol. 20, pp. 139-151, 1999.

[49] WebMD. (2011, Nov 2013). *Coronary Stent*. Available: http://www.webmd.com/heart-disease/coronary-stent

[50] P. W. Serruys, P. de Jaegere, F. Kiemeneij, C. Macaya, W. Rutsch, G. Heyndrickx, *et al.*, "A comparison of balloon-expandable-stent implantation with balloon angioplasty in patients with coronary artery disease," *New England Journal of Medicine,* vol. 331, pp. 489-495, 1994.

[51] D. S. Baim and D. I. Simon, "Complications and the optimal use of adjunctive pharmacology," in *Grossman's Cardiac Catheterization, Angiography and Intervention*, D. S. Baim, Ed. USA: Lippincott Williams & Wilkins, 2006, pp. 36-75.

[52] M. G. Gunning, I. L. Williams, D. E. Jewitt, A. M. Shah, R. J. Wainwright, and M. R. Thomas, "Coronary artery perforation during percutaneous intervention: Incidence and outcome," *Heart,* vol. 88, pp. 495-498, 2002.

[53] E. J. Topol, F. Leya, C. A. Pinkerton, P. L. Whitlow, B. Hofling, C. A. Simonton, *et al.*, "A comparison of directional atherectomy with coronary angioplasty in patients with coronary artery disease," *New England Journal of Medicine,* vol. 329, pp. 221-227, 1993.

[54] E. Cheneau, L. Leborgne, G. S. Mintz, J. Kotani, A. D. Pichard, L. F. Satler, *et al.*, "Predictors of subacute stent thrombosis: Results of a systematic intravascular ultrasound study," *Circulation,* vol. 108, pp. 43-47, 2003.

[55] K. Fujii, S. G. Carlier, G. S. Mintz, Y.-m. Yang, I. Moussa, G. Weisz, *et al.*, "Stent underexpansion and residual reference segment stenosis are related to stent thrombosis after sirolimus-eluting stent implantation: An intravascular ultrasound study," *Journal of the American College of Cardiology,* vol. 45, pp. 995-998, 2005.

[56] S. Cook, P. Wenaweser, M. Togni, M. Billinger, C. Morger, C. Seiler, *et al.*, "Incomplete stent apposition and very late stent thrombosis after drug-eluting stent implantation," *Circulation,* vol. 115, pp. 2426-2434, 2007.

[57] C. Rogers and D. S. Bain, "Coronary atherectomy, thrombectomy and embolic protection," in *Grossman's Cardiac Catheterization, Angiography, and Intervention*, D. S. Baim, Ed. USA: Lippincott Williams & Wilkins, 2006, pp. 467-491.

[58] E. Cavusoglu, A. S. Kini, J. D. Marmur, and S. K. Sharma, "Current status of rotational atherectomy," *Catheterization and Cardiovascular Interventions,* vol. 62, pp. 485-498, 2004.

[59] D. D. Hansen, D. C. Auth, M. Hall, and J. L. Ritchie, "Rotational endarterectomy in normal canine coronary arteries: Preliminary report," *Journal of the American College of Cardiology,* vol. 11, pp. 1073-1077, 1988.

[60] S. S. Ahn, D. Auth, D. R. Marcus, and W. S. Moore, "Removal of focal atheromatous lesions by angioscopically guided high-speed rotary atherectomy: Preliminary experimental observations," *Journal of Vascular Surgery,* vol. 7, pp. 292-300, 1988.

[61] M. C. Stoner, D. J. Defreitas, S. V. Phade, F. M. Parker, W. M. Bogey, and S. Powell, "Mid-term results with laser atherectomy in the treatment of infrainguinal occlusive disease," *Journal of Vascular Surgery,* vol. 46, pp. 289-295. e1, 2007.

[62] R. T. Strebel, U. Utzinger, M. Peltola, J. Schneider, P. Niederer, and O. Hess, "Excimer laser spectroscopy: Influence of tissue ablation on vessel wall fluorescence," *Journal of Laser Applications,* vol. 10, p. 34, 1998.

[63] J. B. Dahm, J. Ruppert, M. Doerr, N. Bordihn, and W. Maybauer, "Percutaneous laser-facilitated thrombectomy: An innovative, easily applied, and effective therapeutic option for recanalization of acute and subacute thrombotic hemodialysis shunt occlusions," *Journal of Endovascular Therapy,* vol. 13, pp. 603-608, 2006.

[64] G. Borade. (Feb 2013, Nov 2013). *Blocked Arteries: Symptoms and Treatment*. Available: http://www.buzzle.com/articles/blocked-arteries-symptoms-and-treatment.html

[65] I. Moussa, C. Di Mario, J. Moses, B. Reimers, L. Di Francesco, G. Martini, *et al.*, "Coronary stenting after rotational atherectomy in calcified and complex lesions angiographic and clinical follow-up results," *Circulation,* vol. 96, pp. 128-136, 1997.

[66] M. Hoffmann, M. Mintz, S. Gary, M. Kent, M. Kenneth, M. Pichard, *et al.*, "Comparative early and nine-month results of rotational atherectomy, stents, and the combination of both for calcified lesions in large coronary arteries," *The American Journal of Cardiology,* vol. 81, pp. 552-557, 1998.

[67] Y. Kobayashi, J. De Gregorio, N. Kobayashi, T. Akiyama, B. Reimers, I. Moussa, *et al.*, "Lower restenosis rate with stenting following aggressive versus less aggressive rotational atherectomy," *Catheterization and Cardiovascular Interventions,* vol. 46, pp. 406-414, 1999.

[68] M. Buchbinder, R. Fortuna, S. Sharma, T. Bass, R. Kipperman, J. Greenberg, *et al.*, "Debulking prior to stenting improves acute outcomes: early results from the SPORT trial," in *Journal of the American College of Cardiology*, 2000, p. 8A.

[69] R. Mehran, G. Dangas, A. S. Abizaid, G. S. Mintz, A. J. Lansky, L. F. Satler, *et al.*, "Angiographic patterns of in-stent restenosis classification and implications for long-term outcome," *Circulation,* vol. 100, pp. 1872-1878, 1999.

[70] S.-G. Lee, C. Lee, S.-S. Cheong, M.-K. Hong, J.-J. Kim, S.-W. Park, *et al.*, "Immediate and long-term outcomes of rotational atherectomy versus balloon angioplasty alone for treatment of diffuse in-stent restenosis," *The American Journal of Cardiology,* vol. 82, pp. 140-143, 1998.

[71] S. K. Sharma, S. Duvvuri, G. Dangas, A. Kini, R. Vidhun, K. Venu, *et al.*, "Rotational atherectomy for in-stent restenosis: acute and long-term results of the first 100 cases," *Journal of the American College of Cardiology,* vol. 32, pp. 1358-1365, 1998.

[72] J. vom Dahl, P. W. Radke, P. K. Haager, K.-C. Koch, F. Kastrau, T. Reffelmann, *et al.*, "Clinical and angiographic predictors of recurrent restenosis after percutaneous transluminal rotational atherectomy for treatment of diffuse in-stent restenosis," *The American Journal of Cardiology,* vol. 83, pp. 862-867, 1999.

[73] P. W. Radke, H. G. Klues, P. K. Haager, R. Hoffmann, F. Kastrau, T. Reffelmann, *et al.*, "Mechanisms of acute lumen gain and recurrent restenosis after rotational atherectomy of diffuse in-stent restenosis: A quantitative angiographic and intravascular ultrasound study," *Journal of the American College of Cardiology,* vol. 34, pp. 33-39, 1999.

[74] R. Mehran, G. Dangas, G. S. Mintz, R. Waksman, A. Abizaid, L. F. Satler, *et al.*, "Treatment of in-stent restenosis with excimer laser coronary angioplasty versus rotational atherectomy: Comparative mechanisms and results," *Circulation,* vol. 101, pp. 2484-2489, 2000.

[75] S. L. Goldberg, P. Berger, D. J. Cohen, F. Shawl, M. Buchbinder, R. Fortuna, *et al.*, "Rotational atherectomy or balloon angioplasty in the treatment of intra-stent restenosis: BARASTER Multicenter Registry," *Catheterization and Cardiovascular Interventions,* vol. 51, pp. 407-413, 2000.

[76] M. Wholey and E. Finol, "Designing the ideal stent," *Endovascular Today,* vol. 6, pp. 25-34, 2007.

[77] D. Stoeckel, C. Bonsignore, and S. Duda, "A survey of stent designs," *Minimally Invasive Therapy & Allied Technologies,* vol. 11, pp. 137-147, 2002.

[78] R. A. Schatz, "A view of vascular stents," *Circulation,* vol. 79, pp. 445-457, 1989.

[79] G. Mani, M. D. Feldman, D. Patel, and C. M. Agrawal, "Coronary stents: A materials perspective," *Biomaterials,* vol. 28, pp. 1689-1710, 2007.

[80] C. Lally and D. J. Kelly, "Stents," in *Wiley Encyclopedia of Biomedical Engineering*, M. Akay, Ed. Hoboken, New Jersey: John Wiley & Sons, Inc., 2006, pp. 3345-3355.

[81] T. Duerig and M. Wholey, "A comparison of balloon and self-expanding stents," *Minimally Invasive Therapy & Allied Technologies,* vol. 11, pp. 173-178, 2002.

[82] B. O'Brien and W. Carroll, "The evolution of cardiovascular stent materials and surfaces in response to clinical drivers: A review," *Acta Biomaterialia,* vol. 5, pp. 945-958, 2009.

[83] H.-M. Hsiao, Y.-H. Chiu, K.-H. Lee, and C.-H. Lin, "Computational modeling of effects of intravascular stent design on key mechanical and hemodynamic behavior," *Computer-Aided Design,* vol. 44, pp. 757-765, 2012.

[84] K. Jones, B. D. Jensen, and A. Bowden, "Fabrication and testing of planar stent mesh designs using carbon-infiltrated carbon nanotubes," *Journal of Nanotechnology in Engineering and Medicine,* vol. 4, art. no. 020903, 2013.

[85] A. M. Sammel, D. Chen, and N. Jepson, "New generation coronary stent technology-Is the future biodegradable?," *Heart, Lung and Circulation,* vol. 22, pp. 495-506, 2013.

[86] P. Erne, M. Schier, and T. J. Resink, "The road to bioabsorbable stents: Reaching clinical reality?," *Cardiovascular and Interventional Radiology,* vol. 29, pp. 11-16, 2006.

[87] T. Peng, P. Gibula, K. Yao, and M. F. Goosen, "Role of polymers in improving the results of stenting in coronary arteries," *Biomaterials,* vol. 17, pp. 685-694, 1996.

[88] J. A. Ormiston and P. W. Serruys, "Bioabsorbable coronary stents," *Circulation: Cardiovascular Interventions,* vol. 2, pp. 255-260, 2009.

[89] N. Rajendra, B. Wrigley, and A. Gershlick, "Bioabsorbable stents: Nothing from something," *Clinical Investigation,* vol. 2, pp. 1185-1189, 2012.

[90] R. D. Alexy and D. S. Levi, "Materials and manufacturing technologies available for production of a pediatric bioabsorbable stent," *BioMed Research International,* vol. 2013, p. 11, 2013.

[91] Cook Medical. (Jan 2013, Nov 2013). *Formula Renal Balloon-Expandable Stents*. Available: https://www.cookmedical.com/web/peripheral-intervention/article/-/blogs/pad-therapies-program

[92] Meidcal Expo. (2013, Nov 2013). *Endocor Self-expanding peripheral stent*. Available: http://www.medicalexpo.com/prod/endocor-gmbh/self-expanding-peripheral-stents-applicators-nitinol-75348-532161.html

[93] P. H. Grewe, K. M. Müller, T. Deneke, E. Harrer, A. Germing, A. Mügge, *et al.*, "Stents: Material, surface texture and design, in theory and practice," *Minimally Invasive Therapy & Allied Technologies,* vol. 11, pp. 157-163, 2002.

[94] N. B. Morgan, "Medical shape memory alloy applications—the market and its products," *Materials Science and Engineering: A,* vol. 378, pp. 16-23, 2004.

[95] T. Duerig, A. Pelton, and D. Stöckel, "An overview of nitinol medical applications," *Materials Science and Engineering: A,* vol. 273-275, pp. 149-160, 1999.

[96] D. Stoeckel, A. Pelton, and T. Duerig, "Self-expanding nitinol stents: Material and design considerations," *European Radiology,* vol. 14, pp. 292-301, 2004.

[97] B. Ratner, A. S. Hoffman, F. Schoen, and J. E. Lemons, *Biomaterials Science: An Introduction to Materials in Medicine*. San Diego, California: Elsevier Inc., 2004.

[98] M. Niinomi, "Mechanical properties of biomedical titanium alloys," *Materials Science and Engineering: A,* vol. 243, pp. 231-236, 1998.

[99] H. Hermawan, D. Dubé, and D. Mantovani, "Developments in metallic biodegradable stents," *Acta Biomaterialia,* vol. 6, pp. 1693-1697, 2010.

[100] H. Hermawan, D. Dubé, and D. Mantovani, "Degradable metallic biomaterials: Design and development of Fe–Mn alloys for stents," *Journal of Biomedical Materials Research Part A,* vol. 93A, pp. 1-11, 2010.

[101] J. P. Carrozza, S. E. Hosley, D. J. C. MD, and D. S. Baim, "In vivo assessment of stent expansion and recoil in normal porcine coronary arteries: Differential outcome by stent design," *Circulation,* vol. 100, pp. 756-760, 1999.

[102] R. Hoffmann and G. S. Mintz, "Coronary in-stent restenosis—predictors, treatment and prevention," *European Heart Journal,* vol. 21, pp. 1739-1749, 2000.

[103] A. Mehdizadeh, M. S. M. Ali, K. Takahata, S. Al-Sarawi, and D. Abbott, "A recoil resilient lumen support, design, fabrication and mechanical evaluation," *Journal of Micromechanics and Microengineering,* vol. 23, art. no. 065001, 2013.

[104] R. O. Han, R. S. Schwartz, Y. Kobayashi, S. H. Wilson, J. T. Mann, M. H. Sketch, *et al.*, "Comparison of self-expanding and balloon-expandable stents for the reduction of restenosis," *The American Journal of Cardiology,* vol. 88, pp. 253-259, 2001.

[105] A. W. Martinez and E. L. Chaikof, "Microfabrication and nanotechnology in stent design," *Wiley Interdisciplinary Reviews: Nanomedicine and Nanobiotechnology,* vol. 3, pp. 256-268, 2011.

[106] S. Zhao, X. Liu, and L. Gu, "The impact of wire stent fabrication technique on the performance of stent placement," *Journal of Medical Devices,* vol. 6, art. no. 011007, 2012.

[107] Z. M. Hijazi, M. Homoud, M. J. Aronovitz, J. J. Smith, and G. T. Faller, "A new platinum balloon-expandable stent (Angiostent) mounted on a high pressure balloon: Acute and late results in an atherogenic swine model," *Journal of Invasive Cardiology,* vol. 7, pp. 127-1234, Jun 1995.

[108] Y. Yamamoto, D. L. Brown, T. A. Ischinger, A. Arbab-Zadeh, and W. F. Penny, "Effect of stent design on reduction of elastic recoil: A comparison via quantitative intravascular ultrasound," *Catheterization and Cardiovascular Interventions,* vol. 47, pp. 251-257, 1999.

[109] K. Takahata, "Micro-electro-discharge machining technologies for MEMS," in *Micro Electronic and Mechanical Systems*, K. Takahata, Ed. Vukovar, Croatia: InTech, 2009, pp. 143-164.

[110] K. Takahata and Y. B. Gianchandani, "A planar approach for manufacturing cardiac stents: Design, fabrication, and mechanical evaluation," *Journal of Microelectromechanical Systems,* vol. 13, pp. 933-939, 2004.

[111] K. Takahata, Y. B. Gianchandani, and K. D. Wise, "Micromachined antenna stents and cuffs for monitoring intraluminal pressure and flow," *Journal of Microelectromechanical Systems,* vol. 15, pp. 1289-1298, 2006.

[112] S. Mahendran, R. Devarajan, T. Nagarajan, and A. Madji, "A review of micro-EDM," in *International Multiconference of Engineers and Computer Scientists*, Hong Kong, 2010, pp. 981-986.

[113] B. Bhargava, I. De Scheerder, Q. B. Ping, H. Yanming, R. Chan, H. Soo Kim, *et al.*, "A novel platinum-iridium, potentially gamma radioactive stent: Evaluation in a porcine model," *Catheter Cardiovasc Interv,* vol. 51, pp. 364-368, 2000.

[114] J. Hagemeister, F. M. Baer, R. H. Schwinger, and H. W. Höpp, "Compliance of a cobalt chromium coronary stent alloy - the COVIS trial," *Current Controlled Trials in Cardiovascular Medicine,* vol. 6, p. 17, 2005.

[115] M. Peuster, P. Wohlsein, M. Brügmann, M. Ehlerding, K. Seidler, C. Fink, *et al.*, "A novel approach to temporary stenting: Degradable cardiovascular stents produced from corrodible metal–results 6–18 months after implantation into New Zealand white rabbits," *Heart,* vol. 86, pp. 563-569, 2001.

[116] H. Hermawan, D. Dube, and D. Mantovani, "Developments in metallic biodegradable stents," *Acta Biomaterialia,* vol. 6, pp. 1693-1697, 2010.

[117] W. J. Giessen, C. J. Slager, H. M. Beusekom, D. S. Ingen Schenau, R. A. Huijts, J. C. Schuurbiers, *et al.*, "Development of a polymer endovascular prosthesis and its implantation in porcine arteries," *Journal of Interventional Cardiology,* vol. 5, pp. 175-186, 1992.

[118] J. Murphy, R. Schwartz, W. Edwards, A. Camrud, R. Vlietstra, and D. Holmes, "Percutaneous polymeric stents in porcine coronary arteries. Initial experience with polyethylene terephthalate stents," *Circulation,* vol. 86, pp. 1596-1604, 1992.

[119] K. Wilczek, M. Ivan De Scheerder, K. Wang, E. Verbeken, and J. Piessens, "Comparison of self-expanding polyethylene terephthalate and metallic stents implanted in porcine iliac arteries," *Cardiovascular and Interventional Radiology,* vol. 19, pp. 176-180, 1996.

[120] H.-Y. Song, Y.-H. Jin, J.-H. Kim, S.-W. Suh, H. K. Yoon, S.-G. Kang, *et al.*, "Nonsurgical placement of a nasolacrimal polyurethane stent: long-term effectiveness," *Radiology,* vol. 200, pp. 759-763, 1996.

[121] J. S. Lee, G. Jung, B. S. Oum, S. H. Lee, and H. J. Roh, "Clinical efficacy of the polyurethane stent without fluoroscopic guidance in the treatment of nasolacrimal duct obstruction," *Ophthalmology,* vol. 107, pp. 1666-1670, 2000.

[122] X. Wang, S. S. Venkatraman, F. Y. Boey, J. S. Loo, and L. P. Tan, "Controlled release of sirolimus from a multilayered PLGA stent matrix," *Biomaterials,* vol. 27, pp. 5588-5595, 2006.

[123] A. Kotsar, T. Isotalo, J. Mikkonen, H. Juuti, P. M. Martikainen, M. Talja, *et al.*, "A new biodegradable braided self-expandable PLGA prostatic stent: An experimental study in the rabbit," *Journal of Endourology,* vol. 22, pp. 1065-1070, 2008.

[124] W.-J. Fu, Z.-X. Wang, G. Li, F.-Z. Cui, Y. Zhang, and X. Zhang, "Comparison of a biodegradable ureteral stent versus the traditional double-J stent for the treatment of ureteral injury: An experimental study," *Biomedical Materials,* vol. 7, art. no. 065002, 2012.

[125] K. Takahata, A. DeHennis, K. D. Wise, and Y. B. Gianchandani, "Stentenna: A micromachined antenna stent for wireless monitoring of implantable microsensors," in *Proceedings of the 25th Annual International Conference of the IEEE on Engineering in Medicine and Biology Society*, 2003, pp. 3360-3363.

[126] K. Takahata, A. DeHennis, K. D. Wise, and Y. B. Gianchandani, "A wireless microsensor for monitoring flow and pressure in a blood vessel utilizing a dual-inductor antenna stent and two pressure sensors," in *Proceedings of the 17th IEEE International Conference on MEMS*, 2004, pp. 216-219.

[127] S. Chen, C. Tsai, J. Liu, H. Kan, C. Yao, L. Lee, *et al.*, "The biomechanical analysis of the coil stent and mesh stent expansion in the angioplasty," in *13th International Conference on Biomedical Engineering*, 2009, pp. 1592-1594.

[128] C. T. Dotter, R. Buschmann, M. K. McKinney, and J. Rösch, "Transluminal expandable nitinol coil stent grafting: Preliminary report," *Radiology,* vol. 147, pp. 259-260, 1983.

[129] P. N. Ruygrok and P. W. Serruys, "Intracoronary stenting: From concept to custom," *Circulation,* vol. 94, pp. 882-890, 1996.

[130] D. Maass, C. L. Zollikofer, F. Largiadèr, and A. Senning, "Radiological follow-up of transluminally inserted vascular endoprostheses: An experimental study using expanding spirals," *Radiology,* vol. 152, pp. 659-663, 1984.

[131] ELLA-CS. (May 2010, Nov 2013). *SX-ELLA Stent Danis*. Available: http://www.ellacs.eu/danis-procedure-pack.html

[132] A. Antony. (2011, Oct 2013). *Top Ten: Upcoming Products to Benefit the Heart*. Available: http://www.medicaldevice-network.com/features/featuretop-ten-upcoming-projects-to-benefit-the-heart

[133] SNOMED. (Nov 2013). *SUN Bare Metal Stent*. Available: http://en.sinomedical.net/products_detail/&productId=513101b6-8103-4ced-b85a-6fa74ee29249&comp_stats=comp-FrontProducts_list01-1310794394723.html

[134] C. Capelli, F. Gervaso, L. Petrini, G. Dubini, and F. Migliavacca, "Assessment of tissue prolapse after balloon-expandable stenting: influence of stent cell geometry," *Medical Engineering & Physics,* vol. 31, pp. 441-447, 2009.

[135] A. Kastrati, J. Dirschinger, P. Boekstegers, S. Elezi, H. Schühlen, J. Pache, *et al.*, "Influence of stent design on 1-year outcome after coronary stent placement: A randomized comparison of five stent types in 1,147 unselected patients," *Catheterization and Cardiovascular Interventions,* vol. 50, pp. 290-297, 2000.

[136] S. Müller-Hülsbeck, P. J. Schäfer, N. Charalambous, S. R. Schaffner, M. Heller, and T. Jahnke, "Comparison of carotid stents: An in-vitro experiment focusing on stent design," *Journal of Endovascular Therapy,* vol. 16, pp. 168-177, 2009.

[137] Z. J. Shen, S. Brugaletta, H. M. Garcia-Garcia, J. Ligthart, J. Gomez-Lara, R. Diletti, *et al.*, "Comparison of plaque prolapse in consecutive patients treated with Xience V and Taxus Liberte stents," *The International Journal of Cardiovascular Imaging,* vol. 28, pp. 23-31, 2012.

[138] M. Schillinger, M. Gschwendtner, B. Reimers, J. Trenkler, L. Stockx, J. Mair, *et al.*, "Does carotid stent cell design matter?," *Stroke,* vol. 39, pp. 905-909, 2008.

[139] A. Cremonesi and F. Gastriota. (2013, Nov 2013). Do Patients Benefit from Closed Cell Design? Available: www.leipzig-interventional-course.com

[140] S. W. Jordan and E. L. Chaikof, "Novel thromboresistant materials," *Journal of Vascular Surgery,* vol. 45, pp. A104-A115, 2007.

[141] V. Karagkiozaki, P. G. Karagiannidis, N. Kalfagiannis, P. Kavatzikidou, P. Patsalas, D. Georgiou, *et al.*, "Novel nanostructured biomaterials: Implications for coronary stent thrombosis," *International Journal of Nanomedicine,* vol. 7, pp. 6063-76, 2012.

[142] M. Schulz, V. Shanov, and Z. Yin, *Nanotube Superfiber Materials: Changing Engineering Design*: Elsevier Science, 2013.

[143] B. Godin, Y. Hu, S. La Francesca, and M. Ferrari, "Cardiovascular nanomedicine: Challenges and opportunities," in *Molecular and Translational Vascular Medicine*: Springer, 2012, pp. 249-281.

[144] P. Vallance and N. Chan, "Endothelial function and nitric oxide: Clinical relevance," *Heart,* vol. 85, pp. 342-350, 2001.

[145] H. Wieneke, O. Dirsch, T. Sawitowski, Y. L. Gu, H. Brauer, U. Dahmen, *et al.*, "Synergistic effects of a novel nanoporous stent coating and tacrolimus on intima proliferation in rabbits," *Catheterization and Cardiovascular Interventions,* vol. 60, pp. 399-407, 2003.

[146] I. Tsujino, J. Ako, Y. Honda, and P. J. Fitzgerald, "Drug delivery via nano-, micro and macroporous coronary stent surfaces," *Expert Opinion on Drug Delivery,* vol. 4, pp. 287-295, 2007.

[147] W. S. Weintraub, M. V. Grau-Sepulveda, J. M. Weiss, S. M. O'Brien, E. D. Peterson, P. Kolm, *et al.*, "Comparative effectiveness of revascularization strategies," *New England Journal of Medicine,* vol. 366, pp. 1467-1476, 2012.

[148] I. Iakovou, T. Schmidt, E. Bonizzoni, L. Ge, G. M. Sangiorgi, G. Stankovic, *et al.*, "Incidence, predictors, and outcome of thrombosis after successful implantation of drug-eluting stents," *The Journal of the American Medical Association,* vol. 293, pp. 2126-2130, 2005.

[149] J. Daemen, P. Wenaweser, K. Tsuchida, L. Abrecht, S. Vaina, C. Morger, *et al.*, "Early and late coronary stent thrombosis of sirolimus-eluting and paclitaxel-eluting stents in routine clinical practice: Data from a large two-institutional cohort study," *The Lancet,* vol. 369, pp. 667-678, 2007.

[150] I. Moussa, M. Carlo Di Mario, B. Reimers, T. Akiyama, J. Tobis, and A. Colombo, "Subacute stent thrombosis in the era of intravascular ultrasound-guided coronary stenting without anticoagulation: Frequency, predictors and clinical outcome," *Journal of the American College of Cardiology,* vol. 29, pp. 6-12, 1997.

[151] G. D. Curfman, S. Morrissey, J. A. Jarcho, and J. M. Drazen, "Drug-eluting coronary stents — Promise and uncertainty," *New England Journal of Medicine,* vol. 356, pp. 1059-1060, 2007.

[152] A. Kastrati, A. Schömig, J. Dirschinger, J. Mehilli, N. von Welser, J. Pache, *et al.*, "Increased risk of restenosis after placement of gold-coated stents results of a randomized trial comparing gold-coated with uncoated steel stents in patients with coronary artery disease," *Circulation,* vol. 101, pp. 2478-2483, 2000.

[153] B. W. Nolan, M. L. Schermerhorn, R. J. Powell, E. Rowell, M. F. Fillinger, E. M. Rzucidlo, *et al.*, "Restenosis in gold-coated renal artery stents," *Journal of Vascular Surgery,* vol. 42, pp. 40-46, 2005.

[154] P. Urban and E. De Benedetti, "Thrombosis: The last frontier of coronary stenting?," *The Lancet,* vol. 369, pp. 619-621, 2007.

[155] F. Alfonso, "Treatment of in-stent restenosis – past, present and future " *European Cardiology,* vol. 5, pp. 74-8, 2010.

[156] R. Kornowski, M. K. Hong, F. O. Tio, O. Bramwell, H. Wu, and M. B. Leon, "In-stent restenosis: Contributions of inflammatory responses and arterial injury to neointimal hyperplasia," *Journal of the American College of Cardiology,* vol. 31, pp. 224-230, 1998.

[157] R. S. Schwartz, K. C. Huber, J. G. Murphy, W. D. Edwards, A. R. Camrud, R. E. Vlietstra, *et al.*, "Restenosis and the proportional neointimal response to coronary artery injury: Results in a porcine model," *Journal of the American College of Cardiology,* vol. 19, pp. 267-274, 1992.

[158] R. Balossino, F. Gervaso, F. Migliavacca, and G. Dubini, "Effects of different stent designs on local hemodynamics in stented arteries," *Journal of Biomechanics,* vol. 41, pp. 1053-1061, 2008.

[159] C. Kleinstreuer, S. Hyun, J. Buchanan Jr, P. Longest, J. Archie Jr, and G. Truskey, "Hemodynamic parameters and early intimal thickening in branching blood vessels," *Critical Reviews in Biomedical Engineering,* vol. 29, pp. 1-64, 2001.

[160] M. M. Zarandi, R. Mongrain, and O. F. Bertrand, "Non-Newtonian hemodynamics and shear stress distribution in three dimensional model of healthy and stented coronary artery bifurcation," presented at the COMSOL Conference, Boston, 2010.

[161] R. Hoffmann, C. Jansen, A. König, P. K. Haager, G. Kerckhoff, J. Vom Dahl, *et al.*, "Stent design related neointimal tissue proliferation in human coronary arteries; an intravascular ultrasound study," *European Heart Journal,* vol. 22, pp. 2007-2014, November 1, 2001 2001.

[162] A. Kastrati, J. Mehilli, J. Dirschinger, J. Pache, K. Ulm, H. Schühlen, *et al.*, "Restenosis after coronary placement of various stent types," *The American Journal of Cardiology,* vol. 87, pp. 34-39, 2001.

[163] J. A. Ormiston, M. W. I. Webster, and P. N. Ruygrok, "Stent strut thickness and restenosis," *Circulation,* vol. 105, p. e12, 2002.

[164] C. Rogers and E. R. Edelman, "Endovascular stent design dictates experimental restenosis and thrombosis," *Circulation,* vol. 91, pp. 2995-3001, 1995.

[165] Y. Yoshitomi, S. Kojima, M. Yano, T. Sugi, Y. Matsumoto, M. Saotome, *et al.*, "Does stent design affect probability of restenosis? A randomized trial comparing Multilink stents with GFX stents," *American Heart Journal,* vol. 142, pp. 445-451, 2001.

[166] D. McLean and N. Eiger, "Stent design: Implications for restenosis," *Reviews in Cardiovascular Medicine,* vol. 3, pp. S16-22, 2001.

[167] R. Hoffmann, G. S. Mintz, G. R. Dussaillant, J. J. Popma, A. D. Pichard, L. F. Satler, *et al.*, "Patterns and mechanisms of in-stent restenosis: A serial intravascular ultrasound study," *Circulation,* vol. 94, pp. 1247-1254, 1996.

[168] S. L. S. Lung and A. W. S. Pang. (2007, Nov 2013). *Online Clinical Case Study, Clinical Cardiology Series*. Available: http://www.hkma.org/english/cme/clinicalcase/200703a_set

[169] Y. Minami, H. Kaneda, M. Inoue, M. Ikutomi, T. Morita, and T. Nakajima, "Endothelial dysfunction following drug-eluting stent implantation: A systematic review of the literature," *International Journal of Cardiology,* vol. 165, pp. 222-228, 2013.

[170] M.-C. Morice, P. W. Serruys, J. E. Sousa, J. Fajadet, E. Ban Hayashi, M. Perin, *et al.*, "A randomized comparison of a sirolimus-eluting stent with a standard stent for coronary revascularization," *New England Journal of Medicine,* vol. 346, pp. 1773-1780, 2002.

[171] J. W. Moses, M. B. Leon, J. J. Popma, P. J. Fitzgerald, D. R. Holmes, C. O'Shaughnessy, *et al.*, "Sirolimus-eluting stents versus standard stents in patients with stenosis in a native coronary artery," *New England Journal of Medicine,* vol. 349, pp. 1315-1323, 2003.

[172] S. Windecker, A. Remondino, F. R. Eberli, P. Jüni, L. Räber, P. Wenaweser, *et al.*, "Sirolimus-eluting and paclitaxel-eluting stents for coronary revascularization," *New England Journal of Medicine,* vol. 353, pp. 653-662, 2005.

[173] R. Virmani, G. Guagliumi, A. Farb, G. Musumeci, N. Grieco, T. Motta, *et al.*, "Localized hypersensitivity and late coronary thrombosis secondary to a sirolimus-eluting stent should we be cautious?," *Circulation,* vol. 109, pp. 701-705, 2004.

[174] E. Camenzind, P. G. Steg, and W. Wijns, "A cause for concern," *Circulation,* vol. 115, pp. 1440-1455, 2007.

[175] M. Joner, A. V. Finn, A. Farb, E. K. Mont, F. D. Kolodgie, E. Ladich, *et al.*, "Pathology of drug-eluting stents in humansDelayed healing and late thrombotic risk," *Journal of the American College of Cardiology,* vol. 48, pp. 193-202, 2006.

[176] B. Kalesan, T. Pilgrim, K. Heinimann, L. Räber, G. G. Stefanini, M. Valgimigli, *et al.*, "Comparison of drug-eluting stents with bare metal stents in patients with ST-segment elevation myocardial infarction," *European Heart Journal,* vol. 33, pp. 977-987, 2012.

[177] S. Garg and P. W. Serruys, "Drug-eluting stents: A reappraisal," *Heart,* vol. 96, pp. 489-493, 2010.

[178] M. Togni, S. Windecker, R. Cocchia, P. Wenaweser, S. Cook, M. Billinger, *et al.*, "Sirolimus-eluting stents associated with paradoxic coronary vasoconstriction," *Journal of the American College of Cardiology,* vol. 46, pp. 231-236, 2005.

[179] T. F. Lüscher, J. Steffel, F. R. Eberli, M. Joner, G. Nakazawa, F. C. Tanner, *et al.*, "Drug-eluting stent and coronary thrombosis biological mechanisms and clinical implications," *Circulation,* vol. 115, pp. 1051-1058, 2007.

[180] W. Khan, S. Farah, and A. J. Domb, "Drug eluting stents: Developments and current status," *Journal of Controlled Release,* vol. 161, pp. 703-712, 2012.

[181] C. Kaiser, S. Galatius, P. Erne, F. Eberli, H. Alber, H. Rickli, *et al.*, "Drug-eluting versus bare-metal stents in large coronary arteries," *New England Journal of Medicine,* vol. 363, pp. 2310-2319, 2010.

[182] S. P. D Souza and D. M. Seriki, "Aortoiliac angioplasty and stenting," in *Handbook of Angioplasty and Stenting Procedures*, R. A. Morgan and E. Walser, Eds. London, UK: Springer, 2010, pp. 85-95.

[183] S. Mirsa, "Renal artery angioplasty and stenting," in *Handbook of Angioplasty and Stenting Procedures*, R. A. Morgan and E. Walser, Eds. London, UK: Springer, 2010, pp. 153-165.

[184] T. J. Cleveland, "Angioplasty Stenting of the Subclavian and Axillary Arteries," in *Handbook of Angioplasty and Stenting Procedures*, R. A. Morgan and E. Walser, Eds. London, UK: Springer, 2010, pp. 195-205.

[185] G. B. Danzi, L. Fiocca, C. Capuano, S. Predolini, and E. Quaini, "Acute stent recoil: In vivo evaluation of different stent designs," *Catheterization and Cardiovascular Interventions,* vol. 52, pp. 147-153, 2001.

[186] T. Duerig and S. Duda, "Stents: The future," *Minimally Invasive Therapy & Allied Technologies,* vol. 11, pp. 135-136, 2002.

[187] W. J. Cantor, E. D. Peterson, J. J. Popma, J. P. Zidar, M. H. Sketch Jr, J. E. Tcheng, *et al.*, "Provisional stenting strategies: Systematic overview and implications for clinical decision-making," *Journal of the American College of Cardiology,* vol. 36, pp. 1142-1151, 2000.

[188] W. Alvarez and N. K. Kapur, "Drug eluting stent technology," *Journal of Pharmacy Practice,* vol. 18, pp. 461-478, 2005.

[189] H. C. Lowe, S. N. Oesterle, and L. M. Khachigian, "Coronary in-stent restenosis: Current status and future strategies," *Journal of the American College of Cardiology,* vol. 39, pp. 183-193, 2002.

[190] C. M. Nickson, P. J. Doherty, and R. L. Williams, "Novel polymeric coatings with the potential to control in-stent restenosis — an in vitro study," *Journal of Biomaterials Applications,* vol. 24, pp. 437-452, 2010.

[191] V. Spanos, G. Stankovic, J. Tobis, and A. Colombo, "The challenge of in-stent restenosis: Insights from intravascular ultrasound," *European Heart Journal,* vol. 24, pp. 138-150, 2003.

[192] F. G. P. Welt and C. Rogers, "Inflammation and restenosis in the stent era," *Arteriosclerosis, Thrombosis, and Vascular Biology,* vol. 22, pp. 1769-1776, 2002.

[193] B. Lagerqvist, S. K. James, U. Stenestrand, J. Lindbäck, T. Nilsson, and L. Wallentin, "Long-term outcomes with drug-eluting stents versus bare-metal stents in Sweden," *New England Journal of Medicine,* vol. 356, pp. 1009-1019, 2007.

[194] D. Lim, S.-K. Cho, W.-P. Park, A. Kristensson, J.-Y. Ko, S. Al-Hassani, *et al.*, "Suggestion of potential stent design parameters to reduce restenosis risk driven by foreshortening or dogboning due to non-uniform balloon-stent expansion," *Annals of Biomedical Engineering,* vol. 36, pp. 1118-1129, 2008.

[195] L. G. Machado and M. A. Savi, "Medical applications of shape memory alloys," *Brazilian Journal of Medical and Biological Research,* vol. 36, pp. 683-691, 2003.

[196] C. Bonsignore, *Open Stent Design*. Fermont, CA: Nitinol Devices and Components, Inc., 2011.

[197] M. S. M. Ali and K. Takahata, "Wireless microfluidic control with integrated shape-memory-alloy actuators operated by field frequency modulation," *Journal of Micromechanics and Microengineering,* vol. 21, art. no. 075005, 2011.

[198] M. Ali and K. Takahata, "Frequency-controlled wireless shape-memory-alloy microactuators integrated using an electroplating bonding process," *Sensors and Actuators A: Physical,* vol. 163, pp. 363-372, 2010.

[199] B. Kim, M. G. Lee, Y. P. Lee, Y. Kim, and G. Lee, "An earthworm-like micro robot using shape memory alloy actuator," *Sensors and Actuators A: Physical,* vol. 125, pp. 429-437, 2006.

[200] K. H. Ho and S. T. Newman, "State of the art electrical discharge machining (EDM)," *International Journal of Machine Tools and Manufacture,* vol. 43, pp. 1287-1300, 2003.

[201] N. Mohd Abbas, D. G. Solomon, and M. Fuad Bahari, "A review on current research trends in electrical discharge machining (EDM)," *International Journal of Machine Tools and Manufacture,* vol. 47, pp. 1214-1228, 2007.

[202] M. Murali and S. Yeo, "Rapid biocompatible micro device fabrication by micro electro-discharge machining," *Biomedical Microdevices,* vol. 6, pp. 41-45, 2004.

[203] Y. P. Kathuria, "The potential of biocompatible metallic stents and preventing restenosis," *Materials Science and Engineering: A,* vol. 417, pp. 40-48, 2006.

[204] D. N. Ku, "Blood flow in arteries," *Annual Review of Fluid Mechanics,* vol. 29, pp. 399-434, 1997.

[205] D. N. Ku, D. P. Giddens, C. K. Zarins, and S. Glagov, "Pulsatile flow and atherosclerosis in the human carotid bifurcation. Positive correlation between plaque location and low oscillating shear stress," *Arteriosclerosis, Thrombosis, and Vascular Biology,* vol. 5, pp. 293-302, 1985.

[206] M. De Beule, P. Mortier, S. G. Carlier, B. Verhegghe, R. Van Impe, and P. Verdonck, "Realistic finite element-based stent design: The impact of balloon folding," *Journal of Biomechanics,* vol. 41, pp. 383-389, 2008.

[207] N. Li, H. Zhang, and H. Ouyang, "Shape optimization of coronary artery stent based on a parametric model," *Finite Elements in Analysis and Design,* vol. 45, pp. 468-475, 2009.

[208] W. A. James F. Shackelford and W. Alexander, *CRC Materials Science and Engineering Handbook, Third Edition*: CRC PressINC, 2001.

[209] S. Moaveni, "Introduction," in *Finite Element Analysis: Theory and Application with ANSYS,* New Jersey, USA: Pearson Education, Inc., 2008.

[210] K. Takahata and Y. B. Gianchandani, "Batch mode micro-electro-discharge machining," *Journal of Microelectromechanical Systems,* vol. 11, pp. 102-110, 2002.

[211] R. Rieu, P. Barragan, C. Masson, J. Fuseri, V. Garitey, M. Silvestri, *et al.*, "Radial force of coronary stents: A comparative analysis," *Catheterization and Cardiovascular Interventions,* vol. 46, pp. 380-391, 1999.

[212] F. Flueckiger, H. Sternthal, G. E. Klein, M. Aschauer, D. Szolar, and G. Kleinhappl, "Strength, elasticity, and plasticity of expandable metal stents: In vitro studies with three types of stress," *Journal of vascular and interventional radiology,* vol. 5, pp. 745-50, 1994.

[213] S. Garg and P. W. Serruys, "Coronary stents: Current status," *Journal of Amercian College of Cardiology,* vol. 56, pp. S1-42, 2010.

[214] H. M. Hsiao, K. H. Lee, Y. C. Liao, and Y. C. Cheng, "Cardiovascular stent design and wall shear stress distribution in coronary stented arteries," *Micro & Nano Letters, IET,* vol. 7, pp. 430-433, 2012.

[215] H.-M. Hsiao, "Why similar stent designs cause new clinical issues," *Journal of the American College of Cardiology: Cardiovascular Interventions,* vol. 5, pp. 362-362, 2012.

[216] K. Van der Heiden, F. J. Gijsen, A. Narracott, S. Hsiao, I. Halliday, J. Gunn, *et al.*, "The effects of stenting on shear stress: Relevance to endothelial injury and repair," *Cardiovascular Research,* 2013.

[217] P. C. Evans and B. R. Kwak, "Biomechanical factors in cardiovascular disease," *Cardiovascular Research,* 2013.

[218] S. Morlacchi and F. Migliavacca, "Modeling stented coronary arteries: Where we are, where to go," *Annals of Biomedical Engineering,* pp. 1-17, 2012.

[219] J. F. LaDisa, L. E. Olson, I. Guler, D. A. Hettrick, J. R. Kersten, D. C. Warltier, *et al.*, "Circumferential vascular deformation after stent implantation alters wall shear stress evaluated with time-dependent 3D computational fluid dynamics models," *Journal of Applied Physiology,* vol. 98, pp. 947-957, 2005.

[220] A. O. Frank, P. W. Walsh, and J. E. Moore, "Computational fluid dynamics and stent design," *Artificial Organs,* vol. 26, pp. 614-621, 2002.

[221] J. F. LaDisa, L. E. Olson, D. A. Hettrick, D. C. Warltier, J. R. Kersten, and P. S. Pagel, "Axial stent strut angle influences wall shear stress after stent implantation: Analysis using 3D computational fluid dynamics models of stent foreshortening," *Biomedical Engineering Online,* vol. 4, p. 59, 2005.

[222] A. Rouhi, U. Piomelli, and P. Vlachos, "Numerical investigation of pulsatile flow in endovascular stents," *Physics of Fluids,* vol. 25, art. no. 091905, 2013.

[223] C. Caro, J. Fitz-Gerald, and R. Schroter, "Atheroma and arterial wall shear observation, correlation and proposal of a shear dependent mass transfer mechanism for atherogenesis," *Proceedings of the Royal Society of London. Series B. Biological Sciences,* vol. 177, pp. 109-133, 1971.

[224] C. K. Zarins, D. P. Giddens, B. Bharadvaj, V. S. Sottiurai, R. F. Mabon, and S. Glagov, "Carotid bifurcation atherosclerosis. Quantitative correlation of plaque localization with flow velocity profiles and wall shear stress," *Circulation Research,* vol. 53, pp. 502-514, 1983.

[225] A. M. Malek, S. L. Alper, and S. Izumo, "Hemodynamic shear stress and its role in atherosclerosis," *The Journal of the American Medical Association,* vol. 282, pp. 2035-2042, 1999.

[226] O. Traub and B. C. Berk, "Laminar shear stress mechanisms by which endothelial cells transduce an atheroprotective force," *Arteriosclerosis, Thrombosis, and Vascular Biology,* vol. 18, pp. 677-685, 1998.

[227] N. DePaola, M. Gimbrone, P. F. Davies, and C. Dewey, "Vascular endothelium responds to fluid shear stress gradients," *Arteriosclerosis, Thrombosis, and Vascular Biology,* vol. 12, pp. 1254-1257, 1992.

[228] R. Tominaga, H. E. Kambic, H. Emoto, H. Harasaki, C. Sutton, and J. Hollman, "Effects of design geometry of intravascular endoprostheses on stenosis rate in normal rabbits," *American Heart Journal,* vol. 123, pp. 21-28, 1992.

[229] B. M. Johnston, P. R. Johnston, S. Corney, and D. Kilpatrick, "Non-Newtonian blood flow in human right coronary arteries: Transient simulations," *Journal of Biomechanics,* vol. 39, pp. 1116-1128, 2006.

[230] H. Y. Chen, I. D. Moussa, C. Davidson, and G. S. Kassab, "Impact of main branch stenting on endothelial shear stress: Role of side branch diameter, angle and lesion," *Journal of The Royal Society Interface,* vol. 9, pp. 1187-1193, 2012.

[231] E. O. Ofili, A. J. Labovitz, and M. J. Kern, "Coronary flow velocity dynamics in normal and diseased arteries," *The American Journal of Cardiology,* vol. 71, pp. D3-D9, 1993.

[232] A. C. Dunn, T. D. Zaveri, B. G. Keselowsky, and W. G. Sawyer, "Macroscopic friction coefficient measurements on living endothelial cells," *Tribology Letters,* vol. 27, pp. 233-238, 2007.

[233] C. K. Zarins, D. A. Bloch, T. Crabtree, A. H. Matsumoto, R. A. White, and T. J. Fogarty, "Stent graft migration after endovascular aneurysm repair: Importance of proximal fixation," *Journal of Vascular Surgery,* vol. 38, pp. 1264-1272, 2003.

[234] W.-Q. Wang, D.-K. Liang, D.-Z. Yang, and M. Qi, "Analysis of the transient expansion behavior and design optimization of coronary stents by finite element method," *Journal of Biomechanics,* vol. 39, pp. 21-32, 2006.

[235] S. Zhao, L. Gu, and S. R. Froemming, "On the importance of modeling stent procedure for predicting arterial mechanics," *Journal of Biomechanical Engineering,* vol. 134, art. no. 121005, 2012.

[236] S. Chien, "Mechanotransduction and endothelial cell homeostasis: The wisdom of the cell," *American Journal of Physiology-Heart and Circulatory Physiology,* vol. 292, pp. H1209-H1224, 2007.

[237] N. Wang, H. Miao, Y.-S. Li, P. Zhang, J. H. Haga, Y. Hu, *et al.*, "Shear stress regulation of Krüppel-like factor 2 expression is flow pattern-specific," *Biochemical and Biophysical Research Communications,* vol. 341, pp. 1244-1251, 2006.

[238] A. Colombo, J. W. Moses, M. C. Morice, J. Ludwig, D. R. Holmes, V. Spanos, *et al.*, "Randomized study to evaluate sirolimus-eluting stents implanted at coronary bifurcation lesions," *Circulation,* vol. 109, pp. 1244-1249, 2004.

[239] B. O'Brien and M. Bruzzi, "Shape memory alloys for use in medicine," in *Comprehensive Biomaterials*, D. Editor-in-Chief: Paul, Ed. Oxford: Elsevier, 2011, pp. 49-72.

[240] Y. A. Çengel, *Introduction to Thermodynamics and Heat Transfer*, Second ed. New York, USA: McGraw-Hill Higher Education, 2008.

[241] Ansys INC. (2013, Nov 2013). *Ansys Help Guide-V14.5*.

[242] D. Halliday, R. Resnick, and J. Walker, "Temperature, heat, and the first law of thermodynamics," in *Fundamentals of Physics* USA: John Wiley & Sons, Inc., 2011, pp. 481-483.

[243] G. R. Trott and A. Shorey, "Glass wafer mechanical properties: A comparison to silicon," in *Microsystems, Packaging, Assembly and Circuits Technology Conference (IMPACT), 2011 6th International*, 2011, pp. 359-362.

[244] S. H. Hofma, H. van Beusekom, P. W. Serruys, and W. J. van Der Giessen, "Recent developments in coated stents," *Current Interventional Cardiology Reports,* vol. 3, p. 28, 2001.

[245] D. F. Williams, "On the mechanisms of biocompatibility," *Biomaterials,* vol. 29, pp. 2941-2953, 2008.

[246] A. B. Fontaine, K. Koelling, S. Dos Passos, J. Cearlock, R. Hoffman, and D. G. Spigos, "Polymeric surface modifications of tantalum stents," *Journal of Endovascular Surgery,* vol. 3, pp. 276-283, 1996.

[247] T. Stieglitz, S. Kammer, K. Koch, S. Wien, and A. Robitzki, "Encapsulation of flexible biomedical microimplants with parylene C," in *Proceedings of the International Functional Electrical Stimulation Society (IFESS) Conference*, 2002.

[248] K. V. Wolf, Z. Zong, J. Meng, A. Orana, N. Rahbar, K. M. Balss, *et al.*, "An investigation of adhesion in drug-eluting stent layers," *Journal of Biomedical Materials Research Part A,* vol. 87, pp. 272-281, 2008.

[249] G. E. Loeb, M. Bak, M. Salcman, and E. Schmidt, "Parylene as a chronically stable, reproducible microelectrode insulator," *Biomedical Engineering, IEEE Transactions on,* pp. 121-128, 1977.

[250] K. L. Costeloe and D. Hill, "Blood resistivity and its implications for the calculation of cardiac output by the thoracic electrical impedance technique," *Intensive Care Medicine,* vol. 3, pp. 63-67, 1977.

[251] S. A. Victor and V. L. Shah, "Steady state heat transfer to blood flowing in the entrance region of a tube," *International Journal of Heat and Mass Transfer,* vol. 19, pp. 777-783, 1976.

[252] M. K. Kopaei, A. Mehdizadeh, D. C. Ranasinghe, and S. Al-Sarawi, "A novel hybrid approach for wireless powering of biomedical implants," in *Eighth IEEE International Conference on Intelligent Sensors, Sensor Networks and Information Processing* 2013, pp. 455-460.

[253] D. W. E. Dissanayake, "Modelling and analysis of wirelessly interrogated saw based micropumps for drug delivery applications," Ph.D. dissertation, School of Electrical and Electronic Engineering, The University of Adelaide, 2009.

Index

acceleration, 48, 49
angiographic, 10, 12, 19
angioplasty balloon, 1, 2, 8, 9, 10, 11, 12, 14, 17, 18, 19, 22, 33, 35, 37, 39, 42, 43, 44, 46, 47, 49, 50, 51, 62, 65, 67, 69, 70, 72, 73, 117, 120, 164, 176, 180, 181, 182, 183, 184, 185, 188
  deflated, 8, 10, 17, 65
  expanded, 32, 65
  expansion, 44, 46, 47, 117, 120, 164, 182, 185, 188
ANSYS, 47, 49, 75, 78, 81, 137, 138, 145, 171
  CFX, 75, 78, 145, 171
asymmetrical, 37, 42, 47, 72, 182
atherombose, 74
atherosclerosis, 2, 3, 4, 5, 35, 44, 180, 181
  fatty deposits, 3
  hepercholesteromia, 4
  hypertension, 4
  inflammatory response, 4, 17, 21, 22, 32, 33, 34, 36, 182
  low density lipoproteins (LDL), 4
  phospholipids, 4
  stenosis, 4, 5, 6, 8, 32
  treatment, 5
    non-surgical, 5
      pharmacological intervention, 6
        ARB, 6
        beta blockers, 6
        blood thinners, 6
        statins, 6
    surgircal, 2, 5, 6, 35
      invasive, 6
        bypass grafting (CABG), 6, 7, 36
          arrested heart surgery, 7
          beating heart surgery, 7
        endarterectomy, 6, 7
      minimally-invasive, 6
        abrupt closure, 9
        arterial dissection, 9
        atherectomy, 11
          directional atherectomy, 11
          laser atherectomy, 12
            excimer laser, 12
            laser assisted revascularization, 12
          phagocytosis, 11
          rotational atherectomy, 11
        embolic protection, 12
        percutaneous transluminal angioplasty (PCTA), 8
        pseudo-aneurysm, 9
        stenting, 9
          deployment, 9
        thrombectomy, 12, 33
axial integrity, 51
  axial strength, 54
batch processing, 20, 38, 69, 183
behaviour, 76
benchmark, 39, 72, 75, 114
bending compliance, 65
blood vessel, 3
  aorta, 7, 25
  coagulation, 3, 33
  coronary artery, 2, 7, 9, 19, 22, 31, 34, 35, 43, 73, 79
  endothelial cell, 3, 4, 34, 44, 181
  peripheral artery, 24
  tunica adventitia, 3, 4
  tunica intima, 3, 4
  tunica media, 3, 4
  vena cava, 25
body temperature, 24, 39, 44, 118, 121, 165, 172, 173, 174, 175, 176
boundary conditions, 48
boundary layer, 80, 86, 91, 136, 150
branched, 72, 73, 81, 94, 95, 96, 97, 98, 99, 100, 102, 103, 110, 114, 115, 184
calliper, 65
canine, 25, 79
cardiac cycle, 75, 83, 84, 85, 93, 96, 102, 104, 106, 107, 109, 112, 113, 114, 115, 184
cardiovascular disease (CVD), 2
Carreau model, 75, 76, 171
compressive pressure, 52, 69
computational fluid dynamics (CFD), 71, 113, 135, 137

conjugate, 40, 144, 147, 148, 149, 151, 152, 153, 154, 176, 186
constrained, 17, 19, 40, 44, 61, 118, 119, 121, 137, 164, 177
controur, 51, 53, 54, 56, 58, 59, 85, 87, 88, 89, 90, 97, 98, 99, 100, 139, 140, 141, 142, 143, 148, 149, 150, 151, 152, 153, 154, 163, 174
convergence, 49, 56, 78, 146, 148, 172, 173
deformations, 17, 18, 48, 60, 66, 119, 157, 182, 183
deionized water, 65
Dell Precision, 83, 139, 146, 172
density, 15, 21, 48, 50, 75, 80, 143, 145
developed flow, 78, 170
difference time integration, 48
differential volume, 128, 129, 132
dimensional analysis study, 39, 71, 134
discretisation, 79
distal branch, 72, 77, 78, 101, 108, 109
distal end, 13, 24, 86, 91
distal path, 27
drag force, 39, 72, 83, 92, 93, 96, 106, 107, 113, 184
elastic modulus, 15, 17, 18, 21, 22, 43
elastic recovery, 18, 42, 68, 70, 119, 183
electrical potential, 118, 168, 172, 173, 174, 177, 186
electrical resistivity, 123, 167
electro-thermal actuation, 164
endothelialisation, 32, 34
expanded polystyrene, 123
experimental studies, 22, 39, 117, 118, 121, 154, 175, 176, 185, 188
finishing temperature, 119
finned surfaces, 128, 176, 186
flow deviation, 101, 102, 103, 111
flow rate, 72, 77, 96, 101, 108, 109, 110, 113, 114, 115, 184
flow ratio, 96, 101, 107, 108, 109, 110, 113, 114, 115
fluid regime, 39, 72, 74, 77, 136, 146, 176, 183
force gauge, 66, 160, 161
free expansion, 47
free-holding, 67, 68
frictional coefficient, 93
heat flux, 127, 128, 132, 137, 138, 140, 141
heat stimuli, 40, 186
heat transfer, 40, 121, 123, 124, 125, 126, 127, 128, 129, 130, 131, 132, 134, 135, 136, 137, 138, 141, 142, 144, 147, 148, 149, 151, 152, 153, 154, 166, 168, 171, 174, 176, 186
  conduction, 124, 129, 131, 132, 144, 145, 149, 175
  convection, 124, 126, 132, 144, 145, 152
  convective heat transfer coefficient, 124, 125, 126, 127, 132, 135, 137, 138, 152, 168, 174
  radiation, 124, 125, 144, 145
  rate, 124, 127, 128, 130, 132, 133
  thermal conductivity, 122, 123, 124, 126, 128, 129, 130, 137, 141, 142, 145
heat transfer (HT) rod, 121, 122, 125, 140, 148, 155
heat-induced, 118, 122, 142, 154, 158, 160, 172
heating plate, 160, 161, 162
hemodynamic change, 71
hemodynamic response, 71, 76, 111, 115, 184
high wall shear stress, 74
hotplate, 154, 155
hydraulic pressure, 8, 10, 11, 17
hysteresis, 120
implicity analysis, 55
in vitro, 39, 40, 42, 54, 65, 67, 68, 69, 70, 74, 118, 121, 122, 157, 160, 164, 175, 176, 177, 183, 185, 187
in vivo, 39, 42, 46, 70, 74, 120, 121, 164, 165, 175, 177, 182, 183
incompressible, 144, 145, 170
infrared (IR), 162
inlet, 78, 80, 94, 95, 96, 108, 109, 110, 113, 114, 144, 147, 170, 187
interrogation, 24, 175, 187
interventional cardiology, 43
intimal cells, 9, 74
isotropic, 49, 50, 93, 145
Jenoptik VarioCam, 162
Joule heating, 121, 171
kinematic viscosity, 123
Lagrange coordinates, 48
laminal, 127, 132, 170
leapfrog method, 49
lesion, 3, 6, 7, 8, 9, 10, 11, 12, 13, 14, 15, 17, 19, 21, 23, 31, 32, 33, 34, 35, 71, 81, 181
low wall shear stress (LWSS), 71, 72, 84, 113, 118, 184
luminal coverage, 24
luminal cross-sectional area (CSA), 43
magnitude, 44, 49, 76, 78, 93, 146, 172
mean absolute, 111
mechanical evaluation, 41, 46, 182
Memry, 49, 122
meta-analysis, 44

micro electro-discharge machining (μEDM), 20, 38, 42, 43, 46, 47, 60, 61, 69, 181, 183
discharge, 43, 46, 61
patterning, 47
scanning, 60
micro-device, 46
micromachining, 38, 121
missalignment, 54, 56
mock vessel, 40, 42, 54, 65, 67, 118, 121, 122, 123, 124, 125, 126, 127, 128, 130, 131, 132, 133, 134, 136, 137, 138, 140, 141, 142, 143, 144, 146, 147, 150, 151, 152, 153, 154, 155, 157, 158, 160, 169, 176, 186
silicon, 33, 54
mock-rod assembly, 122, 123, 125, 126, 128, 129, 131, 132, 133, 134, 135, 137, 138, 139, 140, 141, 142, 143, 144, 145, 147, 149, 150, 151, 152, 155
momentum, 48, 75, 143, 145, 146, 148, 172, 173
MRI, 21, 22, 188
multiphysics, 169
Newtonian, 75
non-Newtonian, 75, 85, 169, 171
numerical analysis, 37, 40, 47, 148, 169, 182, 183
bonded contact, 57
finite element analysis (FEA), 42, 69, 137, 144
solid mechanics, 48
structural, 47, 53, 183
finite element method (FEM)
explicit dynamics
pseudo-static, 50
frictionless contact, 57
hexaderal elements, 56, 57, 80, 81, 138, 146, 171, 172
mesh sensitivity, 55, 57, 80, 138, 146, 171
substep, 53, 56, 57, 66
tetrahedral elements, 57, 80, 81, 139, 146, 171, 172
transient analysis, 39, 72, 75, 78, 81, 175
Nusselt number (Nu), 127
oesophageal, 25
optical profiler, 62
vertical scanning interferometry (VSI), 63
oscillatory, 72, 79
outlet, 39, 107, 115, 144, 145, 147, 170, 174, 184
outlet flow rate, 39, 72, 107, 184
patency, 36, 63, 64, 181
peripheral artery disease, 5, 19
plastic deformation, 10, 17, 27, 39, 42, 52, 59, 69, 117, 120, 185
Prandtl number, 123, 127
proximal branch, 77, 101, 107, 108
proximal end, 24, 86, 91
radial loss, 54, 182
radial stiffness, 23, 42, 47, 52, 65, 67, 70, 183
radio-frequency (RF), 24
recoil resilient luminal support, 37, 41, 45, 69, 113, 182
recoil resilient ring (RRR), 37, 45, 69, 71, 72, 117, 182, 188
alternative expansion, 40, 121
axial harness, 57, 58, 59
incremental interlock expansion, 40
interlock, 37, 39, 42, 47, 52, 58, 62, 67, 72, 73, 82, 120, 121, 158, 160, 182, 185
overlap length, 39, 73, 81, 104, 108, 115, 185
sawtooth, 37, 42, 47, 52, 56, 72, 73, 81, 139, 146, 158, 169, 182
shaping, 20, 25, 38, 46, 61, 62, 69, 183
slide end, 55, 56, 57, 58, 59, 60, 61, 62, 172
support end, 54, 55, 57, 58, 59, 60, 62, 81
thermal treatment, 38, 46, 61, 62, 185
trained shape, 118
reference behaviour, 39, 72, 95
residuals, 78, 146, 147, 148, 172
restenosis, 3, 9, 10, 11, 13, 18, 23, 31, 33, 34, 35, 36, 37, 39, 42, 44, 47, 71, 72, 73, 74, 75, 76, 94, 103, 105, 118, 121, 180, 181, 183
luminal injury, 24
neointimal hyperplasia, 9, 19, 22, 33, 70, 71, 94, 180
proliferation, 4, 9, 13, 22, 33, 34, 44, 74
Reynolds number (Re), 144, 145, 168, 169, 170, 174
RRR-integrated, 39, 72, 73, 76, 77, 79, 81, 83, 84, 85, 86, 87, 88, 89, 90, 91, 92, 94, 95, 96, 97, 98, 99, 100, 102, 103, 104, 105, 106, 107, 108, 109, 110, 111, 114, 115, 184
sensing, 24, 155
shape memory alloy (SMA), 38, 46, 70, 118, 119, 120, 121, 165
crystallographic phase, 18
Nitinol, 18, 19, 21, 23, 24, 38, 39, 40, 42, 44, 45, 46, 47, 49, 50, 51, 54, 56, 57, 59, 60, 63, 67, 68, 69, 70, 78, 117, 118, 119, 120, 121, 122, 123, 128, 135, 143, 153, 165, 168, 172, 175, 176, 183, 185, 187
martensite, 18, 21, 39, 40, 49, 54, 67, 117, 118, 119, 120, 121, 122, 136, 153, 154, 157, 165, 185, 187

transformation temperature, 38, 40, 44, 45, 118, 119, 120, 121, 128, 142, 143, 149, 153, 157, 165, 168, 173, 176, 177, 185, 186
shape memory effect, 40, 46, 117, 118, 120, 176, 185, 188
one-way, 119
shear rate, 76, 83, 85, 86, 92, 169, 171
shear stress transport, 148
side effect, 72
SolidWorks, 49, 138, 170
spatial, 39, 72, 74, 85, 95, 113, 184
specific heat, 123, 167
stabilisation, 83
starting temperature, 119, 121
state of the art, 15, 45, 73, 78, 83, 102, 104, 114, 115, 118, 184, 188
stent, 13, 43
acute recoil, 10, 18, 31
axial flexibility, 13
balloon-expandable (BE) stent, 17, 18, 21, 24, 25, 36, 37, 39, 43, 44, 46, 49, 50, 52, 53, 54, 62, 63, 72, 75, 76, 77, 83, 94, 120, 183, 184
biodegradable stents, 15
biostable stents, 15
bridge, 23, 26, 27, 28, 67, 78
catheter, 8, 9, 10, 11, 12, 13, 17, 19, 24
classification, 14
coating, 21, 22, 33, 34, 170
carbon, 33
gold, 33
silicon carbide, 33
commercial, 39, 42, 45, 46, 63, 64, 65, 66, 67, 68, 70, 71, 104, 118, 183
complication, 31
crimp, 1, 9, 10, 13, 17, 19, 24, 25, 27, 40, 44, 47, 62, 65, 120, 121, 122, 141, 144, 153, 154, 155, 157, 158, 159, 160, 164, 165, 169, 170
design, 23
coil, 23
modular, 25
closed cell, 23, 26, 29
fish scaling, 28, 29
open cell, 23, 26, 27, 28, 29
peak to peak, 27, 28
valley to valley, 27
spiral, 24
woven, 25
dogboning, 24
drug-eluting (DE) stent
Sirolimus, 34
elastic recoil, 9, 13, 17, 18, 31, 36, 43, 44, 45, 180, 181
fabrication, 20
braiding, 20, 25, 43, 181
chemical etching, 20
coiling, 20
laser cutting, 20
deburring, 20
waterjet cutting, 20
fatigue resistance, 14
foreshortening, 14
geometrical properties, 74
hemocompatiblity, 21, 33
loop, 24, 26, 27, 66, 67
malpositioning, 32
material form, 19
flat sheets, 19
tubes, 19, 20, 43, 181
wires, 19, 20, 25, 43, 181
materials, 15
Co-Cr alloy, 18, 21, 22
corrosion, 14, 21, 22, 33, 46
ductile alloys, 17
Mg Alloy, 18, 22
platinum-iridium, 20
Polyethylene Terephthalate (PET), 22
Polyurethane (PU), 22
Pt-Cr, 22
Pt-Ir alloy, 21
pure Fe, 22
stainless steel, 17, 18, 49, 63, 67
tantalum, 18, 21
Titanium, 21
objectives, 23, 185
over-expansion, 13, 36, 37, 41, 42, 44, 47, 58, 180, 181, 182
perforation, 28
plaque prolapse, 14, 29
radial strength, 13
radiopacity, 14
restenosis, 33
hemodynamic change, 34
inflammation, 4, 17, 21, 22, 32, 33, 34, 36, 182
intraluminal injury, 34
scaffolding, 1, 9, 13, 14, 15, 23, 26, 27, 33, 42, 70, 72, 74, 86, 118, 183
self-expandable (SE) stent, 17, 18, 19, 21, 27, 36, 44, 46, 182
chronic outward force, 19
sheath, 9, 17, 19, 165

slotted tube, 23, 25, 26, 67
strut, 25, 26, 27, 44, 55, 64, 73, 104, 105, 110
superelastic behaviour, 14
thrombosis, 31, 32, 33, 34, 36, 44, 180
endothelial dysfunction, 34
late stent thrombosis, 32
underexpansion, 32
straight vessel, 83, 84, 85, 92, 94
strain, 17, 21, 48, 52, 53, 54, 59, 60, 67, 76, 85, 86, 91, 92, 117, 119, 120, 121, 157, 174, 181
strain-stress curve, 119
structural integrity, 52, 56, 60, 69, 136, 182
Styrofoam cap, 122, 138, 155, 158
Styrofoam rings, 122, 125, 126, 129, 137, 138, 142, 143, 145, 152, 153
superelasticity, 44, 120
surface profile, 62
tangent modulus, 50
temporal, 39, 72, 74, 92, 102, 106, 109, 112, 113, 114, 115, 184
tensile strength, 15, 21, 22, 51, 59
theoretical, 40, 118, 128, 135, 136, 138, 141, 152, 153, 176, 177, 185, 186
thermal conductivity, 122, 123, 124, 126, 128, 129, 130, 137, 141, 142, 145
thermal resistance, 40, 124, 125, 126, 127, 129, 130, 131, 132, 133, 134, 136, 137, 143, 154, 161, 166, 167, 176, 186
convective, 126
thermocouple, 155, 162
time instance, 83, 85, 91, 92, 95, 99, 100, 112
toxicity, 22
transient analysis, 39, 72, 75, 78, 81, 175
trauma, 36, 37, 42, 181, 182
turbulence, 145, 146, 148
uniform, 39, 53, 72, 93, 126, 128, 129, 130, 131, 134, 135, 136, 137, 139, 140, 141, 142, 143, 145, 147, 148, 149, 152, 160, 169, 173
unit length, 133, 134
vessel, 2, 3, 6, 9, 10, 11, 13, 14, 15, 17, 18, 22, 25, 27, 29, 31, 36, 39, 44, 47, 54, 62, 65, 67, 68, 69, 72, 73, 74, 75, 77, 81, 82, 83, 84, 85, 93, 94, 95, 96, 101, 102, 103, 114, 118, 121, 122, 123, 125, 126, 132, 134, 136, 138, 139, 140, 141, 143, 145, 152, 153, 155, 158, 160, 169, 170, 176, 182, 186
compressive forces, 18
viscosity, 75, 76, 85, 86, 92, 127, 145, 171, 174
von Mises, 49, 51, 54, 56, 59
wall shear stress, 34, 39, 72, 74, 75, 76, 77, 80, 81, 84, 85, 87, 88, 89, 90, 92, 97, 151
welding, 20, 45, 55, 62
withholding forces, 73, 92, 93, 94, 96, 106, 113
workstation, 83, 139, 146, 172
yield strength, 21, 119
yield stress, 17, 43, 59
zero-gauge, 78, 170
Z-rings, 25, 26

This page is left blank intentionally

Biography

Arash Mehdizadeh was born in 1982, Kerman, Iran. In 2005, he graduated from Amirkabir University of Technology (Tehran Polytechnic), Tehran, Iran with a first class BSc honours among the top 2% of students at the department of Computer Engineering and IT. Consequently, he was admitted to pursue his studies towards an MSc in his *alma mater* without participating in the nationwide entrance exam. In early 2008 he graduated from the department of Computer Engineering and IT with the highest rank in Computer Systems Architecture. During his BSc and MSc studies, he collaborated in several computer systems design projects including the national Automatic Layout Synthesis Tool (ATLAS) taskforce where he developed multi-layer cross-talk aware detail routing algorithms.

In late 2008 he was awarded an international postgraduate scholarship (ASI) from the University of Adelaide to conduct his doctoral studies where he joined the Centre for Biomedical Engineering (CBME) under supervision of Dr Said Al-Sarawi and Prof. Derek Abbott at the School of Electrical and Electronic Engineering. In 2011 and 2012, he was a visiting scholar at the Microsystems and Nanotechnology (MiNa) research group, University of British Columbia, Vancouver, Canada, hosted by Prof. Kenichi Takahata. For this visit, he was awarded a Research Abroad scholarship, The University of Adelaide, a BUPA Postgraduate Travel grant, and a AUGU/RC Heddle Award travel scholarship. During his studies, he was involved in a wide range of projects spanning from mechanical, chemical, electrical and biomedical engineering. He received a Young Biomedical Engineer award by Engineers Australia for best presentation at the Australian Biomedical Engineering Conference (ABEC) in 2012. Throughout his MSc and PhD studies he also served as a teaching assistant and part time lecturer for a number of courses including VLSI and Data Path Systems, Automated Electronic Design, Digital Microelectronics and Mathematics.

His current research interests span several areas of biomedical engineering with a focus on application of NEMS/MEMS technologies in biomedical devices, targeted drug delivery and active smart implants. Moreover, he has been actively conducting research in development and application of optimization methods as well as VLSI circuits and systems design.

Scientific Genealogy of Arash Mehdizadeh